Analysis of Surface Infiltration Through Acid Generating Waste Rock at Faro Mine Complex

by

Gabriella Anne Wahl

A thesis submitted in partial fulfillment of the requirements for the degree of

Master of Science

In

Geoenvironmental Engineering

Department of Civil and Environmental Engineering
University of Alberta

ABSTRACT

Characterizing infiltration through acid generating waste rock is essential in addressing critical environmental issues attributed to mining activities. At it's peak operation, Faro Mine in Yukon, Canada was one of the world's largest lead and zinc mines, where 320 million tonnes of waste rock was accumulated during operation and has been leaching contaminants over time. In efforts to remediate the existing waste rock, a reactive transport model is planned to characterize geochemical reactions within the waste rock pile. Prevalence of acid rock drainage is a function of available moisture, which is driven by the infiltration of precipitation events. The purpose of this research is to utilize a soil – atmosphere model to determine the boundary condition for a reactive transport model in the form of net percolation.

Field and laboratory investigations were paired with numerical modeling to compute net percolation. The field and laboratory studies aimed to characterize in-situ physical and hydrological properties of the waste rock materials which govern saturated / unsaturated flow. The overall nature of the surface materials were found such that unsaturated flow of water and water vapour contributing to geochemical reactions is predominantly through fine fraction of the waste rock matrix materials.

An existing finite element soil – atmosphere model (SoilCover) was used to compute net percolation for three meteorological scenarios: wet year, average year, and an extreme event. Sensitivity analyses were conducted to understand the effect of saturated hydraulic conductivity and initial matric suction on the predicted net percolation.

For average and wet year simulations, the baseline net infiltration was computed to be 12% and 15 % of the total yearly precipitation respectively. When saturated hydraulic conductivity was altered during sensitivity analyses, a range of net infiltration computed was found to be 2.1% and 20% of total precipitation across all simulations for average and wet year. Net percolation was also computed for an extreme event found within the representative wet year analysis. During the extreme event, baseline infiltration was found to be 47% of the total rainfall event, where minimum and maximum values were computed to be between 25% and 90%. The saturated hydraulic conductivity had a large effect on the infiltration for all scenarios. Increasing the hydraulic conductivity by one order of magnitude doubled the amount of predicted infiltration for the extreme event. Effects were calculated on water balance parameters such as runoff and actual evaporation. Initial matric suction had a larger effect on extreme events than the overall yearly water balance simulations.

Results of net percolation analyses were in good agreement with results of previous in-situ investigations performed on the surface of the Main Dump. Matric suction profiles computed by the soil – atmosphere model showed that the surface soils become saturated to a depth of approximately 1.0 m as a result of large infiltration events, particularly the freshet season. In-situ measurements show that large infiltration events and freshet can reach deeper elevations within the waste rock pile than computed by the water balance model. It is thought that differences between field behaviours and numerical simulations is a result of spatial variability of fines contents, as well as the existence of preferential flow paths beneath the surface of the waste rock storage facility.

DEDICATION

Leonard Wahl at Lynn Lake, MB (1958)

To everyone before me who worked to get me where I am today.

ACKNOWLEDGEMENTS

I would like to start by thanking the generous contributions made by the National Science and Engineering Research Council of Canada (NSERC) through the Toward Environmentally Responsible Resource Extraction (TERRE-NET) program, and by the Crown-Indigenous Relations and Northern Affairs Canada (CIRNAC) for their support and funding of the work completed in this study.

I would like to thank Dr. Wilson for providing me the opportunity of a lifetime to work under his direction & guidance, I am truly thankful for all of the opportunities I have been given. I cherish all of your support and wisdom, and I hope to learn from your positivity to make the world a better place, wherever life takes me. Thank you for teaching me what being a leader truly means and thank you for seeing something in me that I was not able to see myself.

Thank you is also owed to the team at the University of Waterloo who provided invaluable assistance and collaboration on this project. Thank you to Jeff Bain for your wisdom and for your willingness to help and mentor whenever possible. Thank you to Zhongwhen Bao and Esteban Larrea for all of your assistance and guidance on site.

To all of the people that made this research possible, thank you for your hard work and dedication. A huge thank you is owed to David Barsi who dug the holes that my little arms could not, and for all of your help in the lab. I could not have done this without your expertise. Thank you to Dr. Ahlam Abdulnabi for your support as well as our insightful and whimsical discussions on soil science. Thank you to Christine Hereygers & Dr. Louis Kabwe for your generosity of time and ever so needed expertise in the laboratory, this project would not have been possible without you both. Many, many thanks are owed to Vivian Giang and Jennifer Stogowski who have spent countless hours helping myself and all other students in our group. Thank you Kwaku Amoako for all of your time spent discussing my project and for keeping the lab fun and upbeat. Thank you to Saulo Castro who has been a giant support and resource. I would also like to thank my colleagues at the University of Alberta Geotechnical Centre, our group is filled with amazing

people, and I am thankful for each and every one of you. Your positivity and friendship carried us through some of the most challenging times of our lives.

I want to thank from the bottom of my heart, all of the essential workers that jeopardized their health and safety during one of the most profound times my generation has faced, and the impact it has had on our global community. Thank you for risking your health and safety so we could come back and continue to do what we love safely. We owe you everything.

I would like to thank my all of my parents, family, and friends for the unconditional love, support, and encouragement you have given me through one of the toughest, yet most rewarding times of my life. This could never have happened without you all.

To my mom, Michelle, you have sacrificed more than I will ever know to provide me the opportunity to achieve this goal. You are my standard of strength, courage, and perseverance. I cannot thank you enough for all you have done and taught me.

To my partner, Laurence, I cannot express enough gratitude. You have not only believed in me the many times I did not, but you constantly provided me unconditional love which allowed me to chase my dreams, and for that I owe you the world. Thank you for all you have sacrificed and I hope I made you proud.

LAND ACKNOWLEDGEMENT

It is a great honor to acknowledge the land we stand on and the Peoples of the land we both live and conduct our research on. The University of Alberta is situated on the traditional territory of Treaty 6, and we live and use land that carries the footsteps and the hearts of many First Nations including the Cree, Blackfoot, Nakoda, Tsuu T'ina, and Dene. This land also carries the footsteps and hearts of many Metis people. Furthermore, my research was conducted on the traditional territory of the Ross River Kaska Dena First Nation and has an impact on the traditional territory settled under the Final Agreements with Selkirk First Nations. All Indigenous Peoples have been on these lands for thousands of years and many generations before settler occupation.

I would like to acknowledge our and their relationships with Mother Earth, which is an interconnected relationship. We are all relations and have an obligation to respect that this land has nourished, healed, protected, and embraced us. We are grateful to the Indigenous Peoples that have been the stewards of the land, and this interconnected relationship. We are all relations and as such we all respect each other and our beliefs, as well as our own individual relationships with Mother Earth. From my heart and spirit to yours.

A large thank you is owed to Jessica Vandenberghe at the University of Alberta for developing and sharing this land acknowledgement.

TABLE OF CONTENTS

LIST OF TABLES

LIST OF FIGURES

LIST OF SYMBOLS

K_{fsat} - Field Saturated Hydraulic Conductivity

K_{sat} – Saturated Hydraulic Conductivity

G_s – Specific Gravity

θ_w – Volumetric Water Content

D_{10} – Effective Particle Size

C_u – Coefficient of Uniformity

C_c – Coefficient of Curvature

LL – Liquid Limit

PL – Plastic Limit

PI – Plasticity Index

W – Moisture Content

LIST OF ACRONYMS

AE – Actual Evaporation

AEV – Air Entry Value

ARD – Acid Rock Drainage

CAC - Climate Atlas of Canada

GDP – Gross Domestic Product

HRU – Hydrological Response Unit

LEL – Local Evaporation Line

LMWL – Local Meteoric Water Line

PBSM - Prairie Blowing Snow Module

PCIC - Pacific Climate Impacts Consortium

PDE – Partial Differential Equation

PE – Potential Evaporation

PR – Precipitation

RCP – Representative Concentration Pathway

RO – Runoff

SWCC – Soil-Water Characteristic Curve

SWE – Snow Water Equivalent

UA – University of Alberta

UW – University of Waterloo

LIST OF EQUATIONS

CHAPTER 1. INTRODUCTION

1.1. MOTIVATION FOR RESEARCH

Mining is an essential component of economic development and provides society the materials needed to maintain their current standard of living. The Mining Association of Canada (MAC) estimates that the direct contribution of the mining sector to Canada's real Gross Domestic Product (GDP) was approximately $69.5 billion, which includes extraction and manufacturing processes (Marshall, 2019). A growing demand for innovative smart technology and green infrastructure such as solar panels still require metals mined from earthen materials. As the consumer demand grows and the quality of ore remaining decreases, amount of waste generated is predicted to increase 10-fold every 30 years based on historical trends (Robertson, 2019). Waste rock piles are one of the largest of these waste structures and also one of the largest liabilities facing the industry today. Environmental impacts of residual waste rock are primarily a concern in the form of acid rock drainage (ARD).

A series of geochemical reactions, known as ARD, generate low pH seepage due to the oxidation of mainly pyrite minerals when exposed to oxygen and water. The resulting seepage then has the potential to strip the surrounding waste rock of the remaining metals, carrying them into the environment where they can come into contact with sensitive environmental receptors. ARD can persist in the environment for hundreds of years with a potential long-term liability of hundreds of millions of dollars (Price, 2003). Financial commitments and environmental damage associated with mine waste structures make remediation and reclamation planning key to mitigating long term release of potentially toxic contaminants.

Faro Mine serves as an example of what can happen when ARD is not addressed in the planning and assessment stage of mine development. Currently there are water diversion and treatment infrastructure that was installed as a reactive measure to years of uncontrolled discharge. These facilities and control measures will have to operate as long as the chemical reaction governing ARD continues to persist, which could easily be thousands of years. It is in the best interest of mining operations to investigate mitigation measures during the planning and assessment stage of new mining operations. This will provide a better chance of achieving decommissioning

certificates in the future, and to reduce costs associated with perpetual treatment options and environmental cleanup.

Several technical advancements and tools can be used at the development stage of a mine to help predict the performance of several mine waste materials over the life of the mine. Reactive transport models are multifaceted tools that combine the effects of biological and geochemical processes driving acid generating reactions within waste rock storage facilities. These tools can be used to estimate the rate and quantity of contaminant loading to the environment over time. Boundary conditions can be applied to these models to reflect changes made during reclamation, such that the contaminant loading can be quantified and qualified over time. Previous estimates of contaminant loading from the Main Dump East alone at Faro Mine suggested approximately 317 tonnes of heavy metals are discharged annually, which include iron, lead, nickel, zinc and manganese (Robertson Geoconsultants, 1996a). By modelling potential closure options, contaminant loading can be limited, where total discharge over time is lowered to a manageable level that is economically feasible to treat with water treatment facilities.

One of the most important factors in the geochemical reactions is the exposure of active minerals to moisture, in the form of rainfall and snowmelt. Although not traditionally considered by geotechnical engineers, the properties and behaviors of the unsaturated zone are critical in mine waste management. Typical applications of a designated hydraulic head and/or impervious (zero-flux) along geometric boundaries do not reflect accurate processes of unsaturated soils at ground surface (Fredlund et al., 2012). Site-specific boundary conditions that account for the interactions between soil and atmospheric moisture provide a more accurate measurement of unsaturated flux over time (Wilson, 1990). Water balance modelling provides a breakdown of the fate of water through the soil-atmosphere system to understand how much rainfall and snowmelt can contribute to geochemical reactions within waste rock storage facilities.

1.2. HISTORICAL OPERATIONS

Faro Mine Complex (FMC) is located in the southwest region of Yukon, Canada, which is approximately 20 km northwest of the Town of Faro, YT and is shown in Figure 1.2.1. The mine site is situated approximately 300 km upstream of Pelly Crossing, which is home to the Selkirk First Nation (Nahir, 2019).

Figure 1.2.1 - Location of the Faro Mine Complex (Adapted from Koester 2015)

FMC was once recognized as the largest open pit lead and zinc mine in the world where excavation, extraction and storage of precious metals and waste materials were carried out from 1969 until 1998 (Robertson Geoconsultants, 1996a). Operations were eventually ceased due to the bankruptcy of the Anvil Mining Corporation, and the site was left abandoned. Several mine

waste structures remain that have yet to be reclaimed, including a tailings storage facility and several waste rock piles scattered throughout the site. Current liability for the contaminated mine waste lies with the Canadian Government, where the current remediation plan is set to be implemented in 2023-2024. Current estimations suggest that the site carries approximately $997 million in liability due to environmental risks (Nahir, 2019).

Operations at FMC consisted of both the Vangorda Plateau mine site and the Faro mine site. Vangorda Plateau mine site is located approximately 9 km southeast of Faro Mine Site and consists of Vangorda and Grum Pit waste rock dumps as well as the currently operating water treatment facility (Robertson Geoconsultants, 1996b). Faro mine site consists of tailings impoundments on the west, both the main and intermediate waste rock dumps, Faro Pit and the abandoned mill site (Robertson Geoconsultants, 1996b). Currently, there are 320 million tonnes of waste rock and 70 million tonnes of tailings between the Faro mine site and the Vangorda Plateau site, which have yet to be remediated.

1.2.1. Construction of the Main Waste Rock Dump

During operations, waste materials were distributed between various different waste rock piles located at both Vangorda Plateau and the Faro Mine site. This study is focused on the Main Dump at Faro mine site; therefore, only the construction of the Main Dump will be detailed.

Construction of the Main Dump East section commenced in 1972 and was followed by the West section of the Main Dump two years later in 1974 (Robertson Geoconsultants, 1996b). Both were completed in 1990 and contained an approximate total of 46.4 million m^3 (92.8 million tonnes) of sulphide-bearing waste rock (Robertson Geoconsultants, 1996b). The surface area exposed for potential infiltration totals approximately 656,926 m^2, with Main Dump East accounting for 436,065 m^2 (Robertson Geoconsultants, 1996b). To minimize geochemical reactions and interactions between sulphide-rich waste rock and the atmosphere, it was thought that a centrally located sulphide cell was constructed within the surficial layers of Main Dump East until 1991 (Robertson Geoconsultants, 1996b). The sulphide cell was constructed with interbedded layers of calc-silicate and schist to provide a buffering capacity of any acid drainage that may occur over time (Robertson Geoconsultants, 1996b; Bao et al. 2020). Current geochemical investigations of the Main Dump by Bao et al. (2020a) show that the West portion of the waste rock pile is most

likely to contain the higher sulphide content materials, which were originally thought to be contained within the centre of the pile.

1.2.2. HYDROLOGY

Layering and orientation of material placement can have a great influence on how contaminants and water flow through waste rock piles. Both Main Dump East and Main Dump West were constructed at their angle of repose (Robertson Geoconsultants, 1996b), which was achieved using both end dumping and push dumping (Janowicz et al., 2004). These deposition methods resulted in two main topographic textures present on the surface of the waste rock dumps as described by Janowicz et al. (2004). End dumping was used to create a hummocky surface on the tops of the Main Dump, which is referred to as the bubble dump surface topography (Janowicz et al., 2004). The hummocks of waste rock were created by dumping materials from the end of large dump trucks, which created piles 3-4 meters high and resulted in depressions 2-3 m deep between each pile (Janowicz et al. 2004). These features are observed in Figure 1.2.2. Push-dumping was used to create smooth lift surfaces or trafficable access roads, which resulted in flat topography. The flat surface at the top of the Main Dump is regularly graded and trafficked, which impacts the infiltration of water through the surface. The steep slopes at the angle of repose were constructed using both end-dumping and push-dumping methods. The combination of end dumping and push dumping creates preferential flow paths that facilitate air circulation within the pile which encourages acid rock drainage production (Herasymuik, 1996; Cash, 2014; Lahmira et al., 2016).

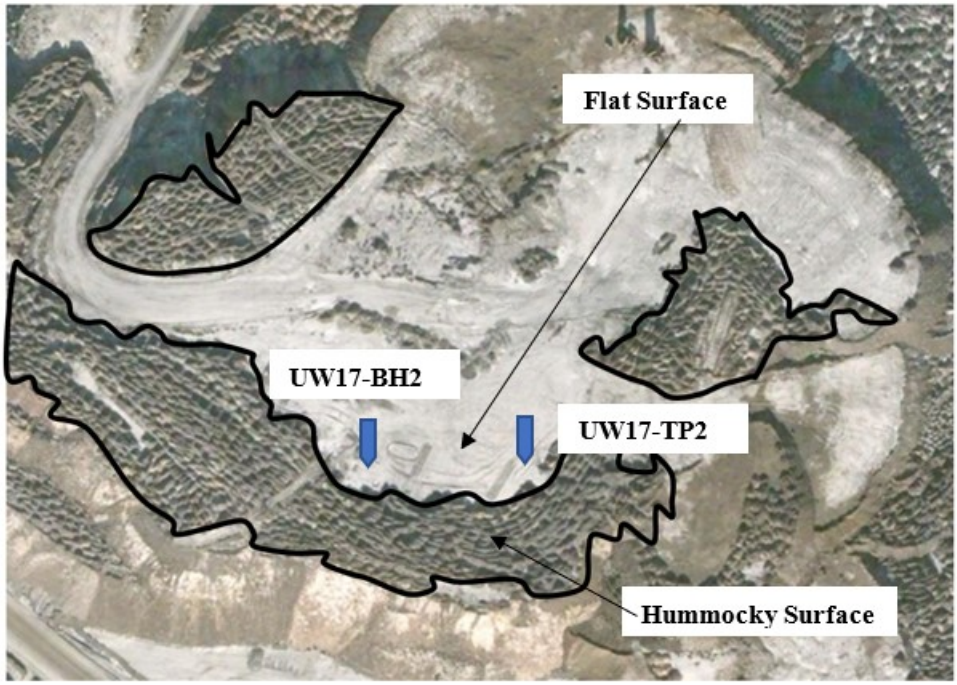

Figure 1.2.2 - Aerial View of Surface Topography on the Main Dump East

The Main Dump also acts as a landform to facilitate local and regional recharge due to net percolation through the pile. The resulting contaminant loading from Main Dump East is distributed between the North Fork of Rose Creek, which receives approximately 30% of internal drainage, and an area designated X23 based on studies completed by Robertson 1996b. The same investigation found that Main Dump West reports all of its internal drainage to X23, which is a water quality monitoring station located in the former Faro Creek Channel, which samples surface water from the toe of the Main Dump (Robertson Geoconsultants, 1996a).

1.2.3. CLIMATE

Faro Mine is located within the Boreal Cordillera ecozone, which is characterized by strong climate gradients of temperature and precipitation with elevation and lateral distance (Macdonald, 2007). On a regional level, the ecoregion's climate ranges from sub-humid to semi-arid but can be described overall as sub-artic within the discontinuous permafrost zone (Macdonald, 2007). The nearby Town of Faro lies at an elevation of 716.6 meters above sea level (masl), where the surface of the Main Dump exists at 1156 masl. Meteorological

parameters such as wind speed, net radiation, and relative humidity were available from the Main Dump meteorological station for 2017 - 2018. Climate normals for the Faro Airport were taken from the Environment Canada records for that location.

This section presents the local climate trends from the Faro Airport and Main Dump meteorological stations. Detailed climate inputs for the numerical model will be discussed in more detail in Section 3.3.5 and 3.3.6 in this thesis. Figure 1.2.3 shows the meteorological parameters recorded on the Main Dump during the years 2017 and 2018.

Daily precipitation data from 2000 – 2020 showed that annual precipitation had a geometric mean of 357 mm. These records showed that the lowest annual precipitation was captured in 2019 with 213 mm, and the highest annual precipitation was recorded in 2016 with 507 mm total. Records from Faro Airport, located in a valley 15 km south of Faro Mine recorded an annual average precipitation of 320 mm, based on 20 years of previous records. 101 mm of the Faro Airport annual precipitation falls as snow water equivalent (SWE). SWE values and snowpack data were not reliable from the tipping bucket gauge used to measure precipitation at the Faro Mine meteorological station; therefore, an SWE cannot be inferred directly from site data. Chapter 4 details the process of further estimating SWE for the Main Dump. Previous water balance reports conducted by Janowicz et al. (2004 & 2006) used an energy budget method to estimate the development of a snowpack on the surface of the Main Dump from both 1994 to 1995 and 2004 to 2005 data. Losses due to sublimation, transport by wind, and saltation were also considered by adopting the Prairie Snow Blowing Module (PBSM) (Janowicz et al. 2006). A total of 75 mm and 100 mm of SWE was predicted to establish for the end of March in 1995 and 2005, respectively. Only approximately 1.4 % of the SWE was predicted to be lost due to sublimation and transport as predicted by the PSBM results.

Temperature records for the Faro Airport indicate a maximum and minimum average daily temperature of 25.3°C and -26.5°C in July and January of 2017, respectively. Faro Main Dump records from 2018 indicate a maximum and minimum average daily temperature of 19.6°C and -28.3°C respectively. Temperature extremes ranged from -31°C to 25.3°C in 2017. For 2018, temperature extremes were recorded as -31.7°C and 24.4°C respectively. Colder winter

temperatures at the Faro Airport may correspond to the 350 m difference in elevation between the Main Dump and the bottom of the valley.

Hourly relative humidity records were available for the year 2017 and 2018, with data missing for the month of June 2017. In 2017, daily average relative humidity ranged from 27% to 93.5% respectively, where the average daily maximum was 82%, and average daily minimum was 49%. Relative humidity recorded in 2018 showed an average maximum and minimum of 81.7% and 49% respectively. Daily average relative humidity ranged from 28.9% to 94.7%. Airport values for maximum and minimum readings were 81.2% in November and 41.4% in June, considering airport records for April and May were not available.

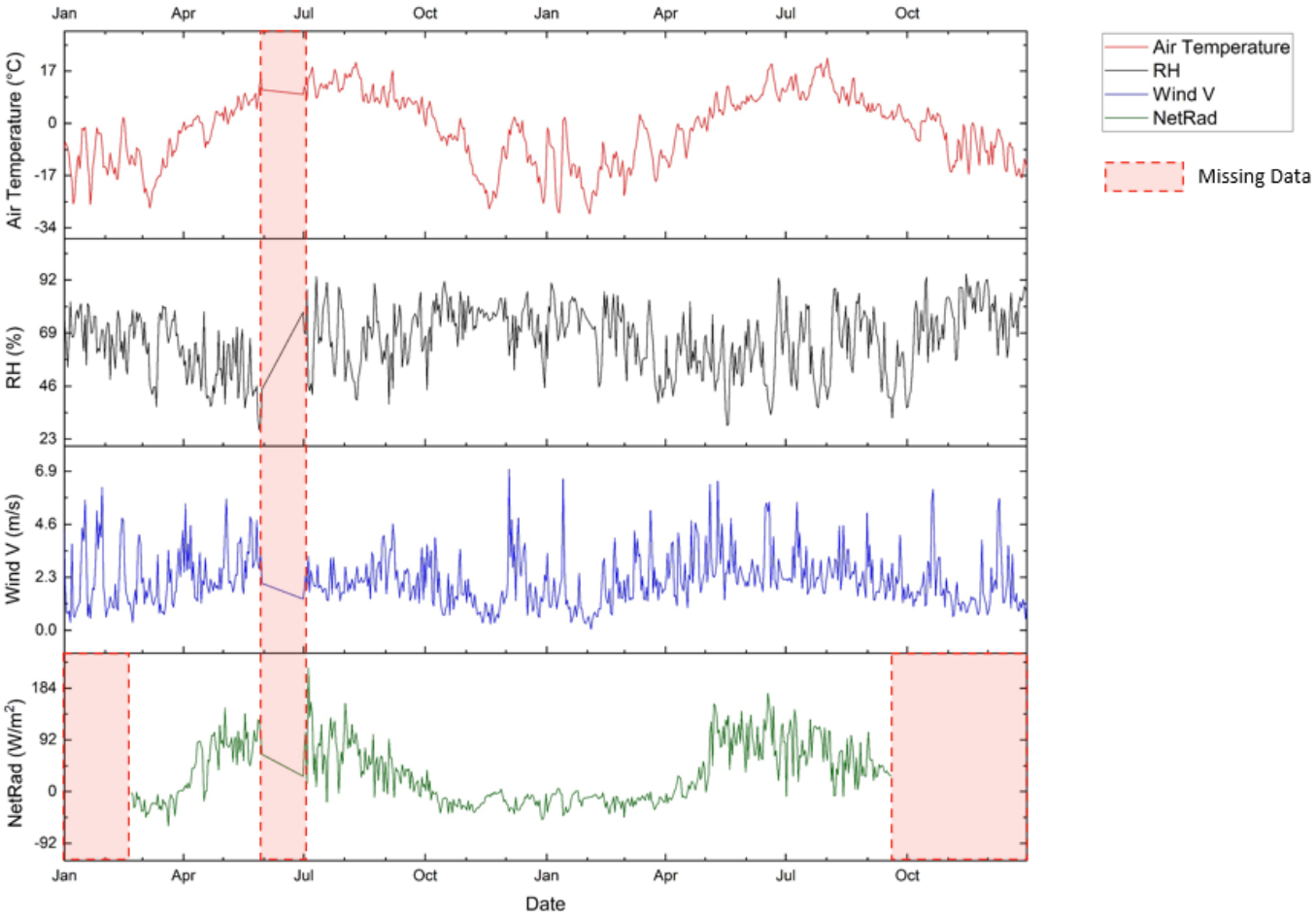

Figure 1.2.3 - Daily Meteorological Data from the Main Dump Station in 2017 and 2018

Daily average wind speed records were not available from the Faro Airport, but hourly wind speed records were available for the surface of the Main Waste Rock Dump. Average daily wind

speed was recorded to be 2.14 m/s in 2017 and 2.21 m/s in 2018. Extreme wind events recorded during 2017 reached peak wind speeds of 11.3 m/s, and 2018 saw maximum wind speeds of 12.1 m/s. Previous water balance reports by Janowicz et al. (2004 & 2006) indicated similar wind speed data from both 1994 to 1995 and 2005 to 2006 on the surface of the Main Dump. Both report findings and records were consistent in terms of average daily wind speed rarely exceeding 6 m/s.

Net radiation was also recorded on the Main Dump East. Records from 2017 and 2018 contained instrumentation reading errors during periods identified in Figure 1.2.2. The maximum daily average net radiation of 174.8 W/m^2 was recorded in June 2018, where the minimum was recorded in December at -23.6 W/m^2. Extreme readings were captured in July 2017 (220 W/m^2), and March 2017 (-61.7 W/m^2).

1.2.3.1. CLIMATE CHANGE

Effects of climate change are important to consider when evaluating water balances on soil-atmosphere systems. Increased average annual temperatures and changes in snowpack depth during winter months can increase or decrease infiltration over time. Efforts have been made to predict changes in climate reaching to the year 2095. The main source of data used by the Climate Atlas of Canada (CAC) is from the Pacific Climate Impacts Consortium (PCIC). The PCIC uses data from 24 climate models, where CAC is able to downscale projections of daily precipitation and data. This data is provided for two different carbon emissions scenarios or representative concentration pathways (RCP's) the first being the RCP8.5 (high carbon) and RCP4.5 (low carbon scenario) in Table 1.2.1. Each RCP considers variations in socioeconomic conditions that effect emissions production.

Each model or scenario provides data resolution for all of Canada at a 10 km x 10 km from the years 1950 – 2095. Different climate scenarios are the same for the years 1950 – 2005, where the data for each carbon scenario starts to deviate at the year 2006. Average annual temperature and precipitation are considered for further analysis, using both RCP4.5 and RCP8.5 scenarios. Table 1.2.1 contains a summary of the predicted changes for each climate parameter between the years 2030 and 2095. Each value was taken as the average of predictions from all 24 models.

Table 1.2.1 - Climate Change Predictions Between 2030 and 2095

Model Scenario	Average Annual Temperature (°C)			Average Annual Precipitation (mm)		
	10th Percentile	Mean	90th Percentile	10th Percentile	Mean	90th Percentile
RCP4.5	+1.9	+1	+1.4	+41	+38	+91
RCP8.5	+4	+4	+5	+3	+68	+99

Climate change predictions are not made for additional input parameters such as net radiation; With this assumption, it may be that net radiation increases between 2030 and 2095, which could reduce snowpack depth and increase evaporation. Further numerical modelling and assessments need to be performed for this trend to be verified.

1.2.4. GEOLOGY

Faro Mine Complex is situated within the Anvil district of the Yukon Plateau physiographic subdivision (Bond, 2001). Within this district lies the Anvil Mountain Range, which reaches upwards of 1800 m above median sea level (abmsl), with the peak elevation at the top of Mount Mye reaching 2060 masl (Pigage, 2004).

The regional geology of the Anvil District comprises three major geological units: the Menzie Creek formation, Mount Mye Formation and the Vangorda formation (Bond, 2001; Pigage, 2004). Two surfacing and dominant formations are the Mte Mye and Vangorda formations (Robertson Geoconsultants, 1996a). Both formations are described to be formed by metamorphic events which resulted in prominent folds within the Anvil District. This formation resulted in sulphide bearing geological units concurrent with orientations of folds (Robertson Geoconsultants, 1996a). The Mount Mye formation comprises non-calcareous phyllite and schist containing interbedded layers of marble and calcite lenses and other minor components. The Vangorda formation is dominated by calcareous phyllite and schist, and interbedded marble and calc-silicate lenses (Robertson Geoconsultants, 1996b; Bond, 2001; Pigage, 2004) Previous field

investigations and ore body exploration describes the location of the ore body at the interface between these two major formations, leading to waste rock piles with varying composition. Surficial deposits were generated through the last glaciation event that resulted in glaciofluvial, alluvial, morainal, colluvial and organic soils (Robertson Geoconsultants, 1996a).

1.3. SCOPE AND OBJECTIVES

This project is a component of a larger effort to develop a reactive transport model that aims to characterize dominant transport mechanisms for oxygen diffusion and moisture flux contributing to geochemical reactions. Reactive transport models provide insight into the complexity of geochemical reactions within heterogeneous porous media by coupling interactions of physical and biogeochemical reactions governed by proven physical models. Rigorous field investigations are needed to provide geochemical and hydrological properties of waste rock materials to properly predict the dominant geochemical reactions at each diverse site. The first phase of field investigations conducted on the Main Dump was completed by University of Waterloo (UW) in 2017. Investigations focused on determining geochemical and physical properties of sub-surface waste rock samples. Activities on site included a drilling and test-pitting program completed in 2017, which was followed with instrumentation that monitors the Main and Intermediate Waste Rock Dumps (Bao et al. 2020b). Measurements of volumetric water content, O_2 and CO_2 pore gas concentrations, temperature, and air permeability have been monitored since 2017.

The purpose of this research project is to characterize infiltration through the surface of the Main Waste Rock Dump at Faro Mine. To contribute to a larger research initiative, the water balance in the form of net percolation will serve as surface flux boundary conditions for a site-specific reactive transport model. This was achieved through the following:

- Completing field and laboratory analysis to characterize in-situ infiltration capacity and key unsaturated soil parameters that control moisture migration,
- One dimensional transient saturated-unsaturated flow analysis based on established soil-atmosphere models for both a typical year, a wet season and for an extreme precipitation event,

- Perform sensitivity analyses for each meteorological scenario to understand the effect of in-situ variability on the overall water balance.

Results of this research are aimed to provide input parameters for the calibration stage of the reactive transport model. All water balance simulations are conducted with no cover in order to provide insight into existing conditions.

1.4. THESIS OUTLINE

This study is presented over a series of Chapters. A review of theory surrounding unsaturated soils and the underlying workings of the soil-atmosphere model is presented in Chapter 2.

Chapter 3 contains the methodology used to conduct the supporting field and laboratory investigations. Details on each material property are provided for context on how each parameter was derived and under which conditions. Additionally, Chapter 3 also provides an outline of the methodology used to develop the assumptions and conditions for the soil-atmosphere model used in this study.

Chapter 4 presents the results of both the field and laboratory investigations to provide a summary of geotechnical parameters that will be used for further numerical modelling. A discussion of each result is also contained within this Chapter.

Chapter 5 presents water balance and net infiltration results found using the soil-atmosphere model. Discussion surrounding the results of net infiltration, runoff, and actual evaporation are provided to compare numerical results to in-situ measurements completed by additional studies.

Conclusions and recommendations based on the results are provided in Chapter 6.

Appendix A and B contain water balance charts and matric suction profile figures for each computation respectively.

CHAPTER 2. THEORETICAL APPROACH TO INFILTRATION

In Geotechnique, one of the most important parameters within a water balance analysis is infiltration. Formally, infiltration can be defined as the process of meteoric water entering an unsaturated porous medium and moving downwards due to gravitational flow (Freeze, 1969; Wilson, E. M., 1974). Infiltration can also be defined using a fairly simple arithmetic relationship between different parameters of the well-known water cycle. This relationship was derived from the water balance equation applied to large watersheds in traditional hydrological applications (Freeze & Cherry, 1979):

$$S = P - E - R \quad [1]$$

where:

S = Change in storage of water within a soil matrix

P = Precipitation

E = Evapotranspiration

R = Surface Runoff

The change in storage term (S) describes the amount of infiltration for an engineered soil-atmosphere system rather than the sum of all loss terms within an entire watershed. In physical terms, when rainfall comes into contact with the soil surface, it can either continue to migrate through pore space within soil, or it can be shed as surface runoff (Horton, 1933; Swanson & O'Kane, 1999). Water that infiltrated into the vadose zone, or the unsaturated zone, can be released to the atmosphere through evapotranspiration with the help of atmospheric conditions and established vegetation. Rainfall can also remain as storage within soil matrix, or can continue to flow through the soil matrix when soil storage capacity has been reached (Horton, 1933; Swanson & O'Kane, 1999). This process is illustrated in Figure 1.4.1.

Although the water balance equation portrays itself as a simple arithmetic relationship, it is often more difficult to achieve accurate results than one might initially assume. Looking at the water balance equation, it can be shown that precipitation can be measured fairly well, and runoff can be measured to a certain degree of accuracy, but directly measuring actual evaporation (AE) has proven to be difficult. Furthermore, the process of predicting both AE and runoff is computationally intensive and time consuming in some simulations. Values of each parameter within the water balance equation depend on many site-specific characteristics which are interconnected by coupled soil and atmospheric processes (Wilson, 1990). Infiltration alone depends on several parameters that include (Smith & Beckie, 2003):

1) Type and density of vegetation

2) Site specific climate

3) Rainfall intensity

4) Physical properties: in-situ density, moisture content, SWCC, field saturated hydraulic conductivity (k_{fsat})

5) Surface texture and topography (slope gradient)

6) Soil moisture content

The mechanics of infiltration are extremely interconnected by moisture demands in both the soil and atmospheric systems, making the governing mechanisms behind infiltration a complicated, non-linear, and hysteretic system (Fredlund et al. 2012). The following sections outline several critical concepts related to the performance of unsaturated soil systems. Materials for these sections were based on the works of Fredlund et al., 2012 and the review conducted by Abdulnabi 2018 if not otherwise stated.

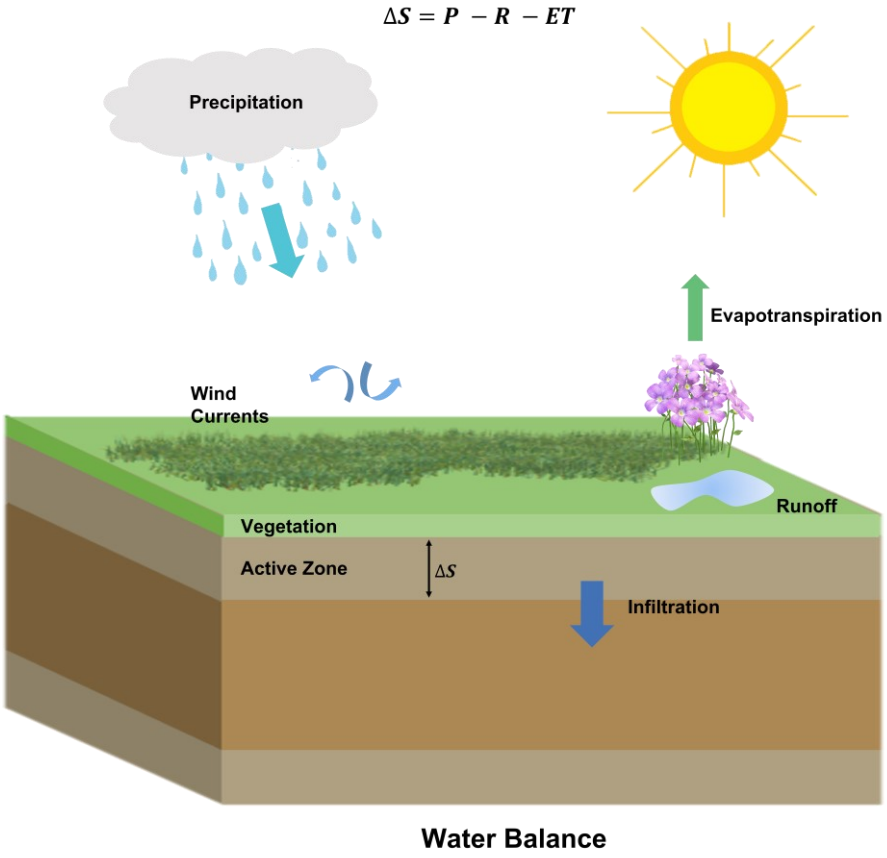

Figure 1.4.1 - Concept of Net Infiltration and the Water Balance Equation

2.1. Mechanics of Infiltration

Various physical models have been developed to describe infiltration over many years in response to the needs of various disciplines such as agricultural and environmental sciences. The discipline of Geotechnique is strongly focused on considering the effect of unsaturated water flow on the strength and compressibility of mine wastes such as tailings. Infiltration through these anthropogenic materials can have very different effects on the geotechnical properties of these materials. In the context of this research, the focus of infiltration is to describe the movement of unsaturated flow through porous media, such as waste rock, and to represent infiltration as a surface flux boundary condition.

One of the first physical models of infiltration is Darcy's Law (1856), which mathematically described the rate at which water could move through soils as a function of both the hydraulic conductivity of the soil and the hydraulic head gradient, as taken from Fredlund et al. (2012):

$$v_w = -k_w * \frac{\partial h_w}{\partial y} \quad [2]$$

where:

v_w = flow rate of water phase

k_w = hydraulic conductivity of the water phase

$\partial h_w / \partial y$ = hydraulic head gradient of the water phase in the y-direction

Darcy's Law is widely used in both saturated and unsaturated systems, where this relationship is used to define the movement of the water phase within soil-atmosphere models.

Green and Ampt (1911) developed another basic constitutive model that aimed to determine the rate of water flow in saturated, homogeneous soil systems. This method employed the measurement of a sharp, piston-like wetting front through the soils which used the saturation to drive infiltration rather than the hydraulic head gradient that was employed in Darcy's Law (Kale & Sahoo, 2011; Assouline 2012).

Following the Green and Ampt equation came the Richard's equation (Richard 1931), which incorporates the relationship between matric suction and volumetric water content and considers the impact this relationship has on the infiltration and unsaturated flow of soils (Assouline, 2013). The one-dimensional equation for vertical infiltration can be seen below:

$$\frac{\partial \theta}{\delta t} = \frac{\delta}{\delta z}\left[K(\varphi)\left(\frac{\delta \varphi}{\delta z} + 1\right)\right] \quad [3]$$

where:

$\partial \theta / \delta t$ = change in water content with time

$K(\varphi)$ = unsaturated hydraulic conductivity function with respect to matrix suction

$\partial \varphi / \delta z$ = change in matric suction with depth

Although this method was a step forward, it requires different boundary conditions for a variety of meteorological conditions and does not directly use the hydraulic gradient as the driving force behind moisture flow. Moisture content gradients should not be used as the driving force behind moisture flow due to the effects of hysteresis on many soil systems (Fredlund et al. 2012). A Dirichlet boundary condition is used for ponding conditions, and a flux or Neuman boundary condition is used when the rainfall intensity is less than the infiltration capacity (Assouline 2013). These do not accurately reflect the complex interaction of moisture inputs and losses as a result of environmental interactions (Fredlund et al. 2012). Richard's equation is also limited computationally by the highly non-linear nature and can only be solved with a certain combination of initial boundary conditions and soil properties (Assouline 2013).

Furthermore, Horton (1933) put forth the concept of infiltration capacity, which describes the process of infiltration as the partitioning of rainfall into two different quantities (1) a portion that successfully infiltrates into the porous medium and (2) the remaining rainfall that is shed as surface runoff. The mathematical relationship describing this process is shown below (Ohja et al., 2008):

$$f(t) = f_c + (f_o - f_c)e^{-kt} \qquad [4]$$

where:

$f(t)$ = infiltration capacity at t = 0

f_c = final infiltration capacity

f_o = initial infiltration capacity

k = constant determining how quickly the infiltration capacity decreases over time

As rainfall moves through the soil matrix, the rate of infiltration decreases over time to reach a steady-state condition, where the soil's field saturated hydraulic conductivity is achieved (Freeze & Cherry 1979). If the rainfall intensity ever exceeds the infiltration capacity at any point in time, the excess rainfall will be shed as overland flow, or runoff (Freeze & Cherry 1979). The capacity of soil to allow for infiltration varies with both soil properties and initial conditions such as the degree of saturation.

Traditional physical models of infiltration have considered many factors such as the hydraulic head gradient, and the effect of saturation and matric suction on the permeability of soils. Some of the important assumptions made in most of the aforementioned models is that the soil is homogeneous, isotropic, and is not a layered system. For popular mine waste remediation strategies such as soil covers, the ability to handle a layered system is crucial. Furthermore, most of these early models of infiltration lack the ability to address atmospheric moisture demands on the soil-atmosphere boundary. Evapotranspiration is an essential component of predicting the amount of infiltration through soils, which is why soil-atmosphere models are the most appropriate for predicting in-situ infiltration.

2.1.1. UNSATURATED SOILS

Traditional geotechnical practice considers saturated soil systems as a two-phase system, where pore space is completely filled with moisture, and the remainder of the soil matrix is the solid phase. Unsaturated soil systems are commonly thought to be a three-phase system consisting of the solid, water, and air phase (Fredlund et al. 2012). Although this three-phase system is a commonly accepted model, it is more appropriate to understand unsaturated soils as a four-phase system, where this fourth phase is the contractile skin at the air-water interface (Fredlund et al. 2012). This contractile skin forms a membrane that separates the air and water phases. Any changes in this air-water interface will affect the degree of saturation, which is comprised of both the volume of air and water within the voids (Fredlund et al. 2012). This concept is demonstrated in Figure 2.1.1. The contractile skin is a key concept when evaluating unsaturated soils and can be explained using the capillary model of matric suction, which relates the matric suction of soils to the rising surface tension caused by capillary rise.

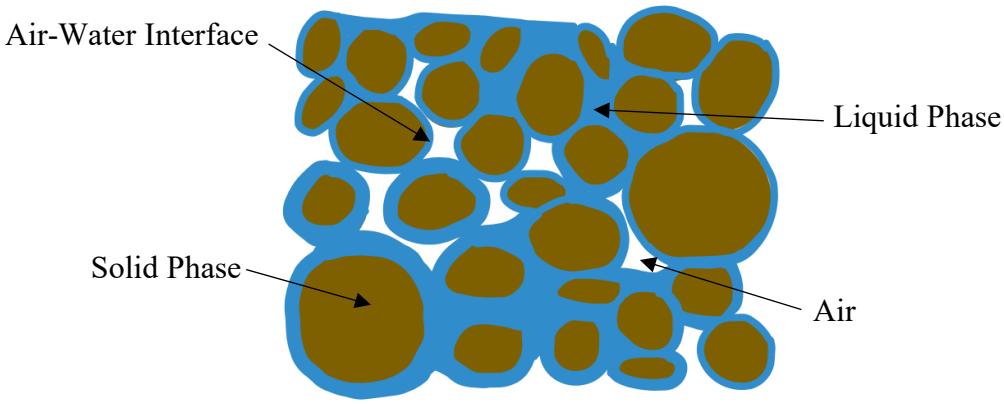

Figure 2.1.1 - Contractile Skin in Unsaturated Soil Systems

Matric suction can be mathematically defined as the difference between pore air pressure and pore water pressure within a soil matrix. Although unsaturated soil mechanics focuses on matric suction, total suction is the most accurate measure of suction within a soil system, which is the effect of both matric suction and osmotic suction. Osmotic suction is a result of migration of solvents passing from solutions of lower solute concentrations to those of a higher solute concentration by passing through a semipermeable membrane (Barbour & Fredlund, 1989). Although it has shown to affect the validity of Darcy's law in several studies, the magnitude of the osmotic suction when compared with that of the matric suction is assumed to be minimal, therefore unsaturated systems are typically evaluated using matric suction (Tami 2004).

2.1.2. Capillary Theory

The capillary phenomenon has been used to describe the relationship between matric suction and water content within unsaturated soils. The contractile skin separating the air and water phase experiences a tensile force in order to maintain a force equilibrium within the unsaturated system, which is possible due to the surface tension of the contractile skin (Fredlund et al. 2012). The contractile skin experiences a larger air pressure than water pressure, and the pressure difference between these two phases is the resulting matric suction previously described. Matric suction forces the contractile skin to be shaped in a concave curvature show in Figure 2.1.2, and can be described using the following mathematical equation:

$$u_a - u_w = \frac{2T_s}{R_s} \qquad [5]$$

where:

$u_a - u_w$ = matric suction

T_s = surface tension

R_s = radius of curvature

In this model of soil suction, we can equate the radius of curvature to the radius of pore spaces between the solid phase within an unsaturated soil system. So as the radius of the pore spaces decreases, the corresponding matric suction increases. In fined grained soils with smaller pore radii, there will be a greater matric suction associated with those materials compared with coarser grained materials which contain larger pore diameters. Variations in matric suction within soils depend on many factors such as density, water content, and grain size. Laboratory measurements of this relationship are routinely conducted by measuring the soil-water characteristic curve of various soil samples.

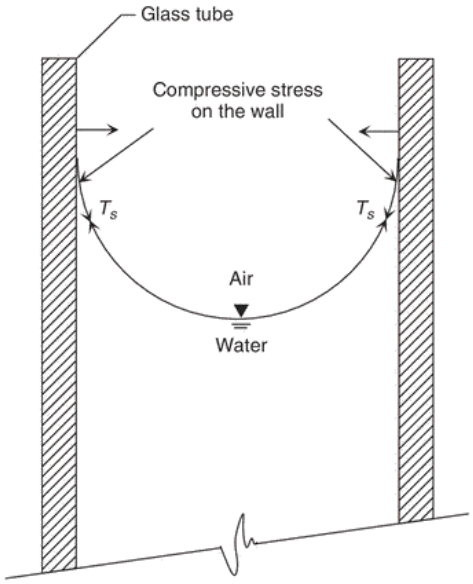

Figure 2.42 Forces acting on capillary tube.

Figure 2.1.2 - Surface Tension at the Air-Water Interface for Unsaturated Soil Systems (Fredlund et al. 2012)

2.1.3. SOIL-WATER CHARACTERISTIC CURVE

The relationship between water content and matric suction is an essential component of unsaturated flow and is a bounding relationship of volume-mass conservation in unsaturated systems. The SWCC has also been used to determine the permeability function which is essential for assessing the flow through unsaturated soils (Fredlund et al. 2012). Soil-water characteristic curves relate the variation in water content with changes in matric suction. The form of the water content being measured can vary between the gravimetric or volumetric water content, or the degree of saturation, depending on the soil type and the amount of volume change (Fredlund et al. 2012). Figure 2.1.3 shows the general shape of a soil-water desorption curve, where several important features can be identified.

First on the desorption trend are the saturated water content, the air entry value (AEV), and the residual water content. Starting from a saturated state, as increasing matric suction is applied, the water content will essentially remain at the saturated state until the point where air can enter into the pore space. This matric suction value is the suction needed to overcome the surface tension of the water phase within a pore of specific radius. The value of the air entry value changes based on the grain size distribution, density, and the void ratio. Clayey soils have a larger air entry value due to the inverse relationship between matric suction and pore radius. Coarse soils such as silty sands will have a smaller AEV due to their overall larger pore size.

Various shapes of the SWCC can be related to the grain size distribution of materials being tested. Figure 2.1.4 shows the difference in typical SWCC curves for various soils which include sand, silt, and clayey soils. As the soil becomes finer grained, the air entry value increases, and the trend towards residual water content becomes less sharp.

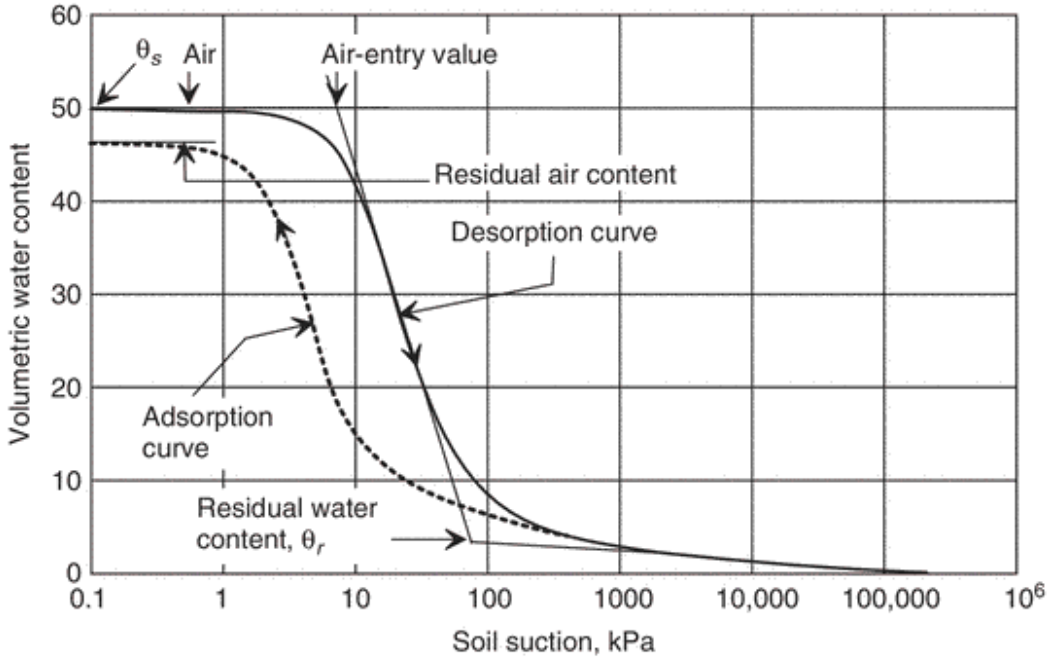

Figure 2.1.3 - Soil-Water Characteristic Curve for Typical Silt Sample (Fredlund et al. 2012)

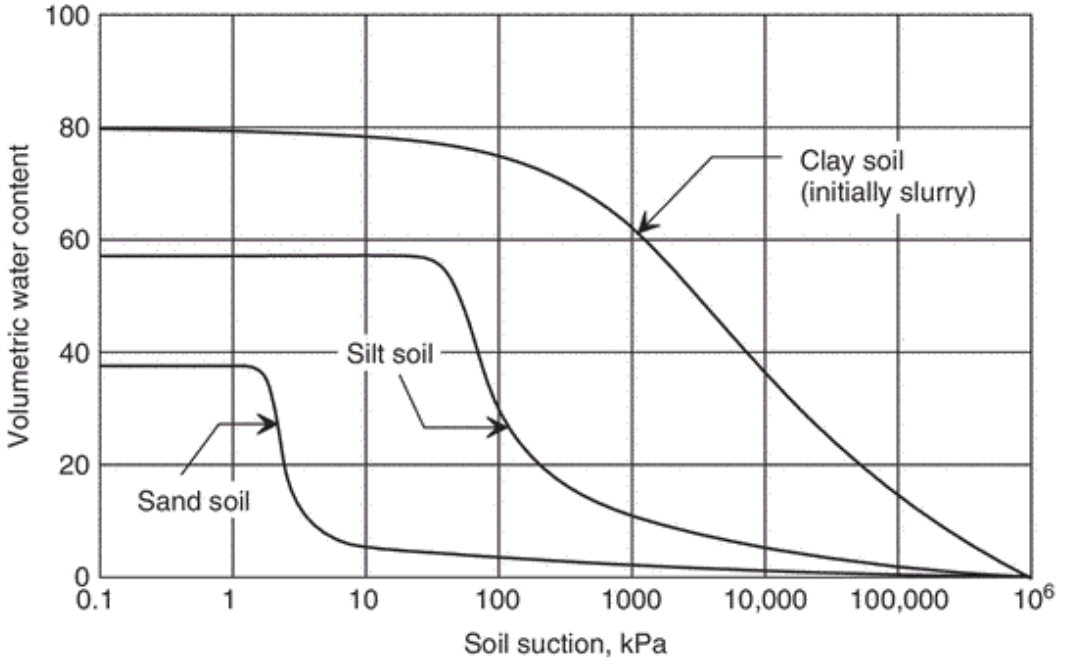

Figure 2.1.4 - Desorption Trends for Sand, Silt, and Clay Soil Samples (Fredlund et al. 2012)

The shape of various SWCC's is also affected by the shape of the grain size distribution. Well graded soils will have a shallower trend towards residual water content due to the large range of particle sizes. In a well graded soil, pore water stored in larger diameter pore spaces will drain first at lower measures of matric suction, where the remaining smaller pores will require larger matric suction to drain, resulting in a shallower trend towards the residual water content. In uniformly graded soils, all pore spaces are of similar size, so at a particular value of matric suction, uniformly graded soils will drain faster and have a sharper trend towards the residual water content. It is also necessary to note that this relationship is also heavily influenced by hysteresis, where it is seen that there is no one single SWCC for one material; it is a non-unique property of soils and there exist infinite wetting and drying curves of which a soil can experience (Fredlund et al. 2012).

2.2. NUMERICAL MODELS OF INFILTRATION

There is a great need in the geoenvironmental engineering discipline to predict the water balance for various saturated-unsaturated soil systems. Numerical models provide engineers the tools to help inform engineering judgement on contaminant transport, the effect of water balances, and the design and response of various waste retention structures to climate extremes (Scanlon et al. 2002). The later has become more important as climate change has had a greater impact on our most northern regions.

There are numerous codes available to perform such tasks, and each has their own method for calculating different components of the water balance. Scanlon et al. (2002) provide an excellent overview of several numerical models that aim to predict the flow of moisture, heat, and contaminants through saturated-unsaturated soil systems. Among those discussed were HELP (Shroeder et al. 1994), HYDRUS-1D (Simunek et al. 1998), SoilCover (Wilson 1990; Wilson et al. 1994, GEO2000 1997), SHAW(Flerchinger and Saxton 1989; Flerchinger et al. 1996), SWIM (Verburg et al. 1996), UNSAT-H (Fayer 2000), and VS2DTI (Healy 1990). More recent additions to the market include SVFLUX (SoilVision 2014) which is now incorporated in PLAXIS LE, which have similar models of infiltration to those already mentioned. The following sections provide a comparison of various codes and their underlying conceptual models of infiltration.

2.2.1. Approaches to Water And Heat Flow Through porous Media

HELP (Hydrologic Evaluation of Landfill Performance) is a quasi-two-dimensional hydrologic based model developed by Shroeder et al. (1994). Vertical percolation through the soil is governed two different ways. When the soil has a greater moisture content than the field capacity, downward flow is controlled by gravity. When the soil suction of the current layer is less than the underlying layer, moisture flow is governed by principles of moisture retention (Schroeder et al. 1994; Allbright et al. 2002). Water retention properties of the input material are assessed using the Cambell (1974) modification of the Brooks and Corey (1964) relationship. Unsaturated permeability is determined using the relationship reported by Cambell (1974), which requires the saturated/unsaturated volumetric water contents in addition to the saturated hydraulic conductivity (Schroeder et al. 1994, Allbright et al. 2002). A different approach is taken by the HELP model to predict actual evaporation. This code uses a method of evaluating an evaporation coefficient which is empirically measured using the unsaturated hydraulic conductivity of varying soils at 0.1 bar capillary pressure (Schroeder et al. 1994). This coefficient is calculated in each simulation where upper and lower limits are used to ensure that evaporation cannot exceed the flux outside of values reported by Kinsel (1980) (Schroeder et al. 1994). HELP also utilizes empirical relationships developed by the U.S. Soil Conservation Service that relate the precipitation input to the resulting runoff (Scanlon et al 2002).

The HYDRUS 1.0 code was developed by Simunek et al. (1998) to simulate water, heat, and contaminant transport through porous media. This software uses the van Genuchten equations to solve the one-dimensional Richard's equations of water movement through unsaturated soils (Simunek et al. 2006). The form of the Richard's equation employed by HYDRUS does not consider the air phase as a significant factor in the liquid flow process; therefore, an additional equation to account for non isothermal liquid and vapour flow is employed (Simunek et al. 2009). Versions following HYDRUS 1.0 expanded its capability to handle multiple dimensions of moisture flow. Prescribed heat and flux boundary conditions can be used to reflect soil-atmosphere interactions, and water flow can be handled in dual-porosity soils (Simunek et al. 2006). Both conductive and convective heat and solute transport for both liquid and gaseous phases are also considered when simulating contaminant and water transport (Simunek et al. 2006).

SoilCover software was developed using the findings of a collaborative effort made by Wilson (1990), Joshi (1993), Machibroda (1994), Tratch (1994), Swanson (1995), and Newman (1996). Each study built upon the previous to result in a one dimensional transient saturated/unsaturated moisture and heat flux model. Moisture and vapour flow are represented by Darcy's Law and Fick's Law respectively (Geo-Analysis 1997). Water retention properties of soil are assessed using the Fredlund and Xing (1994) method for soil-water characteristic curves, and the Fredlund, Huang, and Xing (1994) method to estimate the permeability function (Allbright et al. 2002). One of the most notable abilities of the SoilCover code is that of the atmospheric coupling which uses the Wilson-Penman method to estimate actual evaporation. Compared with most models discussed in this section, it has one of the most computationally demanding estimates of actual evaporation. A review of the SoilCover theoretical model is present in Section 2.3 of this thesis.

UNSAT-H is a computer code with an underlying theoretical model that describes the movement of water, vapour, and heat through a one-dimensional soil profile, where this system also includes the effects of transpiration on the water balance (Allbright 2002, Fayer 2000). Underlying principles of heat and moisture flow are very similar to that present in SoilCover. One of the main advantages of UNSAT-H is that the user can choose the method which describes the water retention equation the user would like, where the choices include either the van Guchten or the Brooks and Corey (Allbright 2002).

The SHAW (Simultaneous Heat and Water) code is a one-dimensional soil-atmosphere model created to simulate heat, moisture, and solute flux through snow, residue, and soil (Flerchinger and Saxton 1989). Richard's equation in the finite-element form is used to predict water migration through soil, and water retention characteristics of soils is determined using the Brooks and Corey (1966) equations added to by Cambell (1974) (Flerchinger and Saxton 1989). SHAW has the most rigorous snowmelt evaluation process compared with the listed codes (Allbright 2002). In terms of estimating the evaporation from soil-atmosphere boundaries, this software uses the energy budget method to simulate the actual evaporation (Scanlon et al. 2002).

Although these models can be very helpful tools, it is important to note that there is a great need for calibration before utilizing results in the design and operation of remediation structures. Comparing the predicted components of the water balance to field measurements is critical to

ensure the results of each modelling scenario reflect in-situ behaviours. Rather than thinking of a numerical model as a static system, it should be continuously updated based on site observations, and be considered a dynamic system (Nordstrom 2012).

2.3. SOIL-ATMOSPHERE CONCEPTUAL MODEL: SOILCOVER

Net percolation, or infiltration, is a process governed by the interaction between atmospheric processes and saturated-unsaturated soil mechanics (Wilson et al., 1994; Fredlund et al., 2012). Moisture flux through unsaturated soils is a complex interaction driven by several coupled processes including (Wilson 1990):

a) Thermal gradients

b) Atmospheric processes (total precipitation, net radiation, and wind speed)

c) Diffusion and gravity flow of water and water vapour

SoilCover is an established unsaturated – saturated seepage software that uses well-known physical laws to characterize both water and vapour flow; these include Darcy's Law, Fick's Law, and Fourier's law. All physical laws are bound using mass conservation principles within a representative element volume (Geo-Analysis 1997). This one-dimensional transient seepage model operates on several fundamental assumptions that must be identified (SoilVision 2019):

1) "Soil phases can be described using a continuum mechanics approach",

2) Pore air and water vapour both behave as ideal gases,

3) Thermodynamic equilibrium is achieved between the liquid and vapour phases throughout the duration of the simulation and exists at every point within the soil system,

4) Atmospheric pressure gradients have a negligible impact on seepage.

The following sections of this thesis describe the fundamental laws governing the soil-atmosphere model and present how it is used to assess and predict the amount of infiltration given a variety of meteoric scenarios.

2.3.1. MASS CONSERVATION

Concepts governing the flow of water, water vapour, air, and heat through porous media is derived using mass conservation equations. Partial differential equations (PDE) used to carry out mass conservation of water in porous media can be derived from the representative element volume seen in Figure 2.3.1. The conservation of mass principle is derived by knowing the rate of flow in and out of the REV in one dimension. It is assumed that the variables used to derive the mass conservation are mathematically continuous and valid at a macroscopic standpoint (SoilVision 2019).

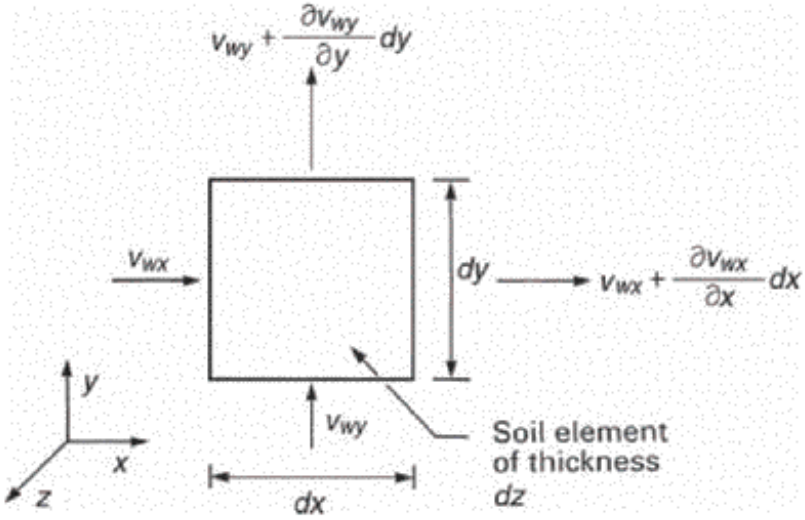

.

Figure 2.3.1 - Representative Element Volume Showing Mass Conservation of Water Flow (Fredlund et al. 2012)

The following equation is the overall heat and mass transfer equation based on the principle of mass conservation (SoilCover 2000):

$$\frac{\partial h_w}{\partial t} = C_w^1 \frac{\partial}{\partial y}\left(k_w \frac{\partial h_w}{\partial y}\right) + C_w^2 \frac{\partial}{\partial y}\left(D_v \frac{\partial P_v}{\partial y}\right) \quad [6]$$

where:

h_w = Total head (m)

t = Time (s)

C_w^1 = Coefficient of consolidation with respect to liquid water phase

$= \frac{1}{\rho_w g}$

ρ_w = Mass density of water (kg/m^3)

g = Acceleration due to gravity (m/s^2)

y = Position (m)

k_w = Hydraulic Conductivity (m/s)

C_w^2 = Coefficient of consolidation with respect to the water vapour phase

$= \frac{(P+P_v)}{P*\rho_w^2 g m_2^w}$

m_2^w = Slope of the moisture retention curve (1/kPa)

P = Total gas pressure in the air phase (kPa)

P_v = The partial pressure due to water vapour (kPa)

D_v = Diffusion coefficient of water vapour through the soil (kg*m/kN*s)

$= \alpha\beta(D_{vap}\frac{W_v}{RT})$

α = Tortuosity factor of soil

$= \beta^{\frac{2}{3}}$

β = Cross sectional area of soil available for vapour flow

D_{vap} = Molecular diffusivity of water vapour in air (m^2/s)

2.3.2. CONSTITUTIVE LAWS

Various constitutive laws are needed to define the laws of volume change and flow of both water and water vapour as well as the laws of heat flow through porous media. (Fredlund and Gitirana, 2005). It is when these constitutive laws are combined with the mass conservation laws that we can reasonably assess the flow of water through unsaturated soils. Fredlund and Gitirana (2005) provide a comprehensive overview of both constitutive and mass conservation laws. The following discussion is an overview of the aforementioned paper unless otherwise stated.

2.3.2.1. FLOW OF WATER AND WATER VAPOUR THROUGH POROUS MEDIA

Pore water can be free flowing through the soil matrix or exist as water vapour in the gaseous phase. Each phase of water that exists within the unsaturated system has different transport mechanisms, which are described using constitutive laws taken from well established water and heat flow principles.

The first constitutive law used is the flow of liquid water, which is captured using Darcy's Law. Hydraulic head is used as the driving potential, which considers the flow of water due to hydraulic gradients and gravitational flow. The one-dimensional version of this mathematical relationship according to the cartesian coordinate system in Figure 2.3.1 is shown in Equation 7 (SoilVision 2019):

$$v_{wy} = -k_{wy}(\varphi)\frac{\delta h}{\delta y} \quad [7]$$

where:

v_{wy} = liquid pore water flow rate in the y-direction

$k_{wy}(\varphi)$ = hydraulic conductivity in the y-direction as a function of matric suction

$\frac{\delta h}{\delta y}$ = hydraulic head gradient in the y-direction

This equation is slightly different than that shown in Section 2.1 of this thesis, as the permeability is now specifically defined as a function of the matric suction within the REV and is taken from the permeability function of the material.

Water vapour flow, or water vapour diffusion, is described mathematically using a modified form of Fick's Law, where the corresponding driving potential is the mass concentration gradient of vapour. Water vapour also has a second driving force, which is due to bulk air flow within unsaturated pores. This is represented using another modified form of Fick's Law, where the driving potential is considered to be the mass concentration of air per unit volume of soil. Both mechanisms are accounted for in Equation (8) (SoilVision, 2019):

$$v_{vy} = -\frac{k_{vd}}{\gamma_w}\frac{\delta u_w}{\delta y} \quad [8]$$

where:

v_{vy} = rate of vapour flow in the y-direction

$k_{vd} = \gamma_w \frac{W_v p_v}{\rho_w R(T + 273.15)} \frac{D_v^*}{\rho_w} =$

W_v = molecular weight of water vapour

p_v = partial pressure of water vapour

R = universal gas constant

T = temperature

$D_v^* = \frac{(1-S)nD_v W_v}{R(T+273.15)}$ = vapour diffusivity through the soil accounting for molecular and concentration gradient transport

D_v = molecular diffusivity of vapour through soil

In order to facilitate mass transfer between the liquid pore water phase and water vapour phase, it is assumed that there is constant equilibrium between these two states. When there are changes in fundamental parameters such as the soil suction and temperature, there is an immediate response within the system, which allows for continuous mass transfer to be evaluated. SoilCover uses the

relationship derived by Edlefsen and Anderson (1943) to calculate the vapour pressure at the soil surface and is shown as Equation [9] below (Geo-Analysis 1997):

$$P_v = P_{sv} * h_r \quad [9]$$

where:

P_v = partial vapour pressure

P_{sv} = Saturation vapour pressure of the soil at it's corresponding temperature, T

h_r = Relative humidity of the soil surface as a function of total suction and temperature

$= e^{\frac{(\varphi g W v)}{RT}}$

φ = Total suction in the soil (m)

R = Universal gas constant

T = Temperature

2.3.2.2. Flow of Heat Through Porous Media

There are various mechanisms of heat transfer within porous media which include convection, conduction, and latent heat changes. Compared to heat flow generated through conduction, convection has relatively small significance within the total heat flow; therefore, this is not considered going forward. The remaining heat flow parameter is latent heat, which is the product of phase changes resulting from vaporization or condensation. As water changes state, either from water-to-water vapour, or vise vera, heat can be released or consumed in exothermic or endothermic processes. Equation 10 contains the mathematical relationship describing the change in temperature as a result of conductive and latent heat transfer (Geo-Analysis 1997):

$$C_h \frac{\partial T}{\partial t} = \frac{\partial}{\partial y}\left(\lambda \frac{\partial T}{\partial y}\right) - L_v \left(\frac{(P + P_v)}{P}\right) \frac{\partial}{\partial y}\left(D_v \frac{\partial P_v}{\partial y}\right) \quad [10]$$

where:

T = Temperature (°C)

C_h = Volumetric specific heat of the soil as a function of water content (J/m^3/°C)

$= C_v \rho_s$

C_v = Specific heat of the soil (J/kg/°C)

ρ_s = Mass density of the soil (kg/m^3)

λ = Thermal conductivity of the soil (W/m/°C)

L_v = Latent heat of vaporization of water (J/kg)

2.3.3. Actual Evaporation and Atmospheric Coupling

Accurate estimations of infiltration are dependant upon the quality and accuracy of each term within the water balance calculation. Evaporation is one of the most important terms to quantify and is typically not estimated using conservative methods. The soil-atmosphere model put forth by (Wilson, 1990) provides a method that accounts for the actual evaporation estimation in a manner than reflects actual atmospheric water demands. Traditional hydrological relationships such as the Philip & de Vries (1957) and the Penman method (1948) make various assumptions that are fundamentally incorrect when applied to a soil-atmosphere interface, which include the following (Wilson et al.1994):

1) Completely saturated conditions (i.e. a free water surface or saturated soils)
2) Flow is controlled by volumetric water content gradients (Philip & de Vries 1957)
3) Flow of water is solely controlled by atmospheric conditions (Penman 1948)

Within mine waste, unsaturated conditions are most prominent and tend to control the migration of contaminants through the unsaturated waste rock. Assuming completely saturated conditions will over-estimate the amount of actual evaporation happening within the active zone. Figure 2.3.2 shows the relationship between the ratio of actual and potential evaporation, and the amount of moisture available within the porous media. In general, atmospheric demands such as increased wind speed, reduced RH, and increased temperature reduce the amount of moisture available within the soil over a certain period of time. With the reduction of pore water, the remaining water becomes isolated within the pore space, making it difficult for moisture to move through the porous matrix due to increasing atmospheric demands as water can only flow where other water exists. As a result, the rate of evaporation is greatly reduced at lower values of moisture availability. This is not captured within traditional methods of estimating evaporation.

Potential evaporation is often used which severely over-estimates the amount of evaporation that can take place within the porous media.

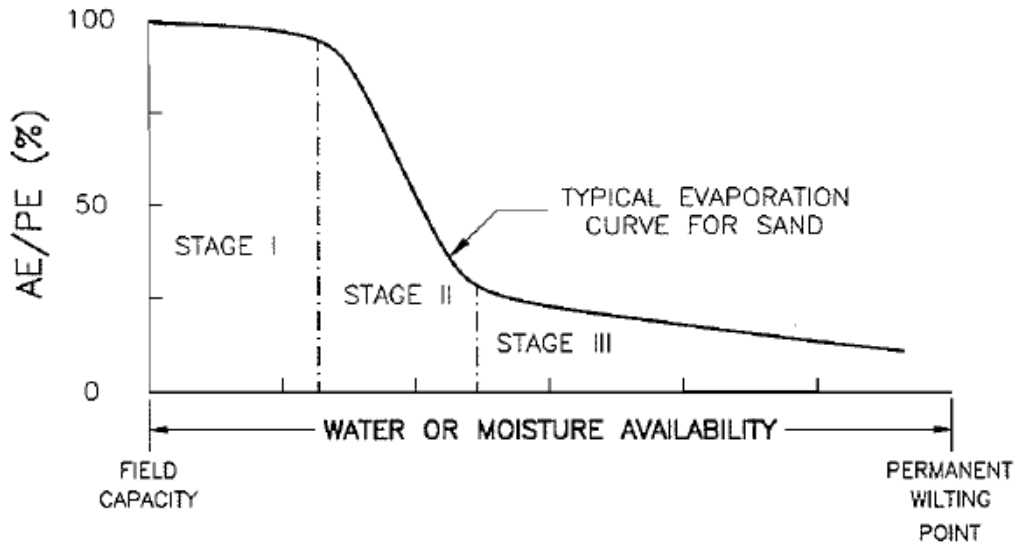

Figure 2.3.2 - Effect of Moisture Availability in Porous Media on the Ratio of Actual and Potential Evaporation (Wilson et al. 1994)

Furthermore, it is well established that the flow of water through soils is governed by a hydraulic head gradient, rather than the volumetric water content or atmospheric conditions alone (Wilson et al. 1994, Fredlund 2012). Therefore, the theoretical model put forth by Wilson et al. (1994) remains the most representative of moisture interactions at the soil-atmosphere interface and is used within SoilCover to estimate actual evaporation within each simulation. The modified Penman formulation that is used to calculate the soil evaporative flux is as follows (Geo-Analysis 1997):

$$E = \frac{\Gamma Q + vE_a}{\Gamma + Av} \quad [11]$$

Where:

E = Vertical evaporative flux (mm/day)

Γ = Slope of the saturation vapour pressure versus temperature curve evaluated at mean air temperature

Q = Net radiant energy available at the surface (mm/day)

v = Psychrometric constant

E_a = f(u)P_a(B-A)

f(u) = Function dependant on wind speed, surface roughness, and eddy diffusion

= 0.35(1 + 0.15U_a)

U_a = wind speed (km/hr)

P_a = Vapour pressure in air above the evaporating surface

B = Inverse of the relative humidity of the air = 1/h_a

A = Inverse of the relative humidity at the soil surface = 1/h_r

This relationship considers the net radiation, wind speed, and relative humidity of both the air and soil surface to directly estimate the actual evaporation released from the soil matrix. When the soil is completely saturated, the modified Penman formulation reverts back to the original Penman method. By accounting for the relative humidity of both air and soil surface, the modified Penman method also provides atmospheric coupling, which connects the soil matrix to atmospheric conditions (Swanson et al. 2003). SoilCover solves for the relative humidity of the soil surface by solving the moisture flow equation and the modified Penman equation simultaneously (Geo-Analysis 1997). Furthermore, to solve the moisture flow equation, soil temperatures are needed, which then requires simultaneous solving of the heat flow equation (Geo-Analysis 1997). The surface temperature of the soil can be estimated in SoilCover using Equation [12] (Geo-Analysis 1997):

$$T_s = T_a + \frac{1}{v * f(u)}(Q - E - G) \quad [12]$$

where:

T_s = Temperature at the soil surface (°C)

T_a = Temperature of the air above the soil surface (°C)

v = Psychrometric constant

$f(u) =$ Function dependant on wind speed, surface roughness, and eddy diffusion

$Q =$ Net radiant energy available at the surface (mm/day)

$E =$ Vertical evaporative flux (mm/day)

$G =$ Ground heat flux (mm/day of equivalent latent heat).

2.3.4. Calculation of Runoff and Cumulative Water Balance

SoilCover has a specific built-in procedure to calculate runoff and the subsequent cumulative water balance. During each iteration of water balance calculations, SoilCover performs the following checks and corresponding operations (Geo-Analysis 1997):

1) If the surface is not saturated, precipitation minus internally calculated actual evaporation is applied at the top mode as a liquid flux boundary condition.
2) If the surface is saturated, runoff equals the precipitation minus the actual evaporation minus the Darcy flux infiltration.
3) If the calculated runoff is negative, this means the top node is passing enough infiltration to desaturate the surface and the calculation reverts to the first step.

CHAPTER 3. METHODOLOGY

3.1. FIELD RESEARCH PROGRAM

From August 29 to September 1, 2019, a field investigation was completed in order to conduct in-situ testing and collect samples for further laboratory analyses. Locations near previous test pits and boreholes completed by the University of Waterloo in 2017 (UW17-TP2 and UW17-BH2) were chosen in order to compare in-situ measurements to results of this study. A third test location near UW17-TP2, named UA19-TL1, was also assessed. All test locations are shown in Figure 3.1.1 (Bao et al. 2020).

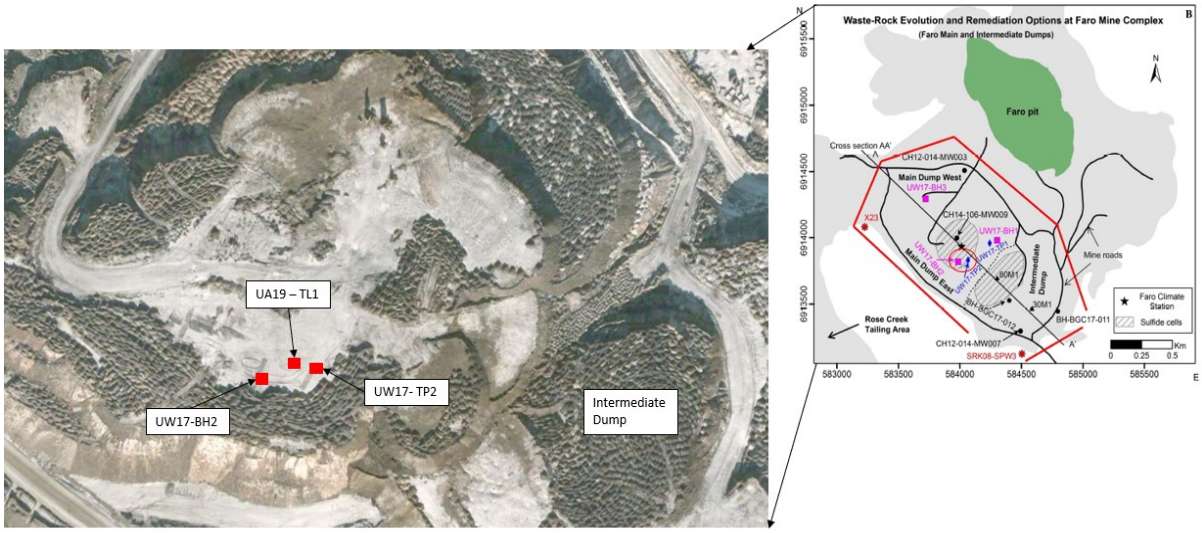

Figure 3.1.1 - Location of In-Situ Testing on the Main Waste Rock Dump (Adapted from Bao et al. 2020)

At each test location, four Guelph permeameter tests were completed, one measurement of in-situ density was taken, and one jet fill tensiometer was monitored throughout the duration of the field investigation. Two 20L pail samples were collected from UW17-BH2, UW17-TP2, and UW17-TL1 to provide representative samples for further laboratory analyses. These samples were taken from the first 25 cm of the waste rock surface in order to characterize the physical and hydrological properties governing initial surface infiltration.

3.1.1. Site Observations

Evidence of acid rock drainage is abundant in the many piles of exposed waste rock on site. Several smaller piles of severely weathered and oxidized rock exist on the outer edge of the Main Waste Rock Dump and are distinguishable by their color. Progression of ARD reactions can result in the generation of precipitates over time, which were visible in numerous piles. Severe degradation of the rock structure can be observed as a paper-like appearance on some specimens. Figure 3.1.2 captures this phenomenon on highly degraded waste rock.

Figure 3.1.2 - Highly Degraded Waste Rock on Main Dump East

Further observations on site indicated variability in material properties, as shown in Figure 3.1.3. Gravitational segregation has resulted in the deposition of course materials at the base of the slope, while allowing finer material to remain at the top of the pile. In addition, surface erosional features were observed on the slope, where differences in these features provide evidence of variation in physical composition. Varying colors of matrix materials can also be seen in Figure 3.1.3, suggesting that there is also geochemical variability in the waste rock on the Main Dump East. Distribution of waste rock throughout the site during operations in combination with the geology of the formation likely resulted in this mixture of different waste materials.

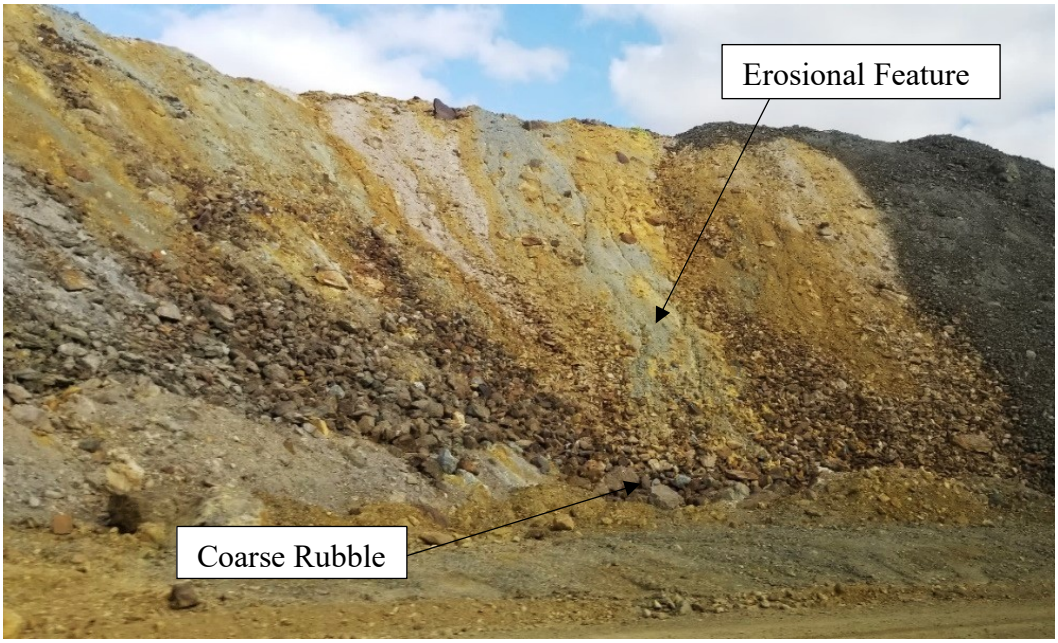

Figure 3.1.3 - Variable Physical Properties Observed on End Dumped Pile of Waste Rock

Additional observations were made on the surface of the Main Dump East which indicated preferential flow paths that begin at the surface. Physical features observed near UW17-BH2, captured in Figure 3.1.4 a) show large-scale surface flow features on Main Dump East. Surface flow patterns indicated concentrations of runoff towards this feature, where fines have started to form sedimentary layers. The diameter of this feature was approximately 2-3 meters and was located approximately 8-10 m South of Guelph permeameter tests conducted near UW17-BH2.

Desiccation of silty fines on the surface of the flow feature indicates surface evaporation during periods of high actual evaporation. This also indicates possible ponding of water at the surface of this feature during periods of high rainfall.

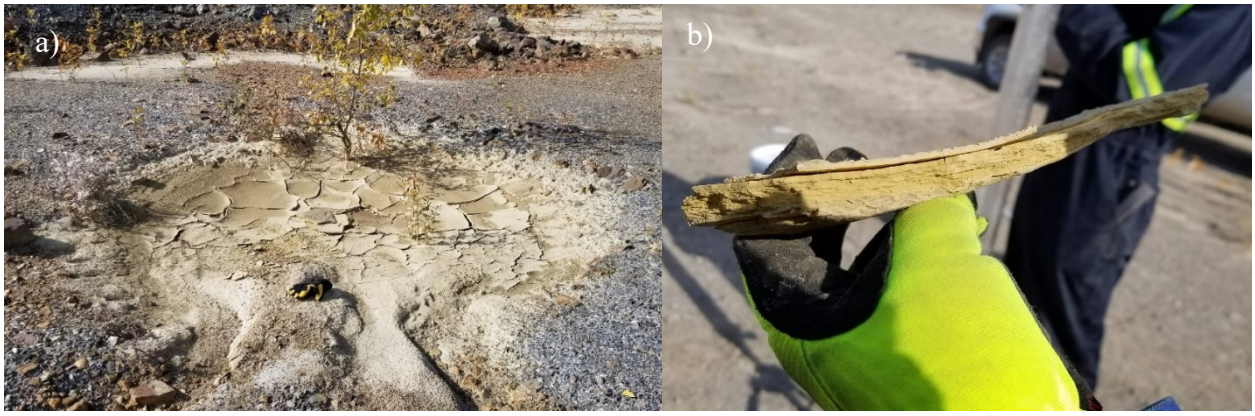

Figure 3.1.4 - a) Preferential Flow Near UW17-BH2 on the Main Dump East, b) Layered Fine Sediment Forming on the Flow Feature

Furthermore, small amounts of vegetation were present on the outer edge of the Main Dump East. Most vegetation did not have many leaves, indicating any transpiration accounted for in a water balance would be minimal to negligible. These observations are contained in Figure 3.1.5 which also provides evidence of ponding captured after a flash rain event on the top of the Main Dump East. Additional preferential flow areas were also identified near the UW17-BH2 test location. Previous site investigations conducted by Bao et al. captured similar observations of preferential flow, surface evaporation and ponding during heavy meteoric events (Bao et al. 2020).

Figure 3.1.5 - Surface of the Main Dump East Near UW17-BH2

3.1.2. GUELPH PERMEAMETER TESTS

One of the most important parameters in a water balance analysis is the field saturated hydraulic conductivity (k_{fsat}). To determine k_{fsat}, an in-situ constant head permeameter test was conducted using a Guelph permeameter (SoilMoisture 2800K1). A hand auger was used to excavate suitable holes for insertion of the permeameter. To capture any variation in permeability with depth, shallow and deep tests were conducted at each test location. Shallow tests were conducted between 180 mm – 230 mm and deep tests were conducted between 380 mm – 600 mm. All measurements were taken within an acceptable range of 150 mm – 700 mm (SoilMoisture, 2012). Consistency of well hole depth was challenging to maintain as larger rock fragments were frequently encountered during the well hole excavation. The diameter of each hole was approximated to be the width of the hand auger (50 mm), plus 10 mm on each side for disturbance upon removal of deep materials, resulting in a total diameter of 70 mm.

When the depth of the well hole was greater than 380 mm, the tripod bushing was used to support the reservoir throughout the test. Well holes shallower than 380 mm required a tripod to support the apparatus. During periods of high winds, the tripod was used to stabilize the reservoir. At each test location, two hydraulic conductivity tests were performed, each at varying depths, yielding 12 permeameter tests in total. Figure 3.1.6 shows the experimental set up at test location UW17-BH2.

The two-head method using combined reservoirs was used to measure k_{fsat} during each test. This method provides a more accurate determination of the steady-state flow rate for materials expected to have larger saturated hydraulic conductivities (SoilMoisture 2012). During each test, initial measurements of the water level were taken at 1-minute intervals followed by 2- and 5-minute recording intervals. Longer time increments decreased the effect of small inconsistencies on the measurement of flow rate at smaller time increments. Each test was conducted until 3 equal flow rates were recorded consecutively. Additional readings were taken to verify that steady state had been reached. Each steady-state flow rate was used to determine the field saturated hydraulic conductivity at each location and depth.

Figure 3.1.6 - Guelph Permeameter Test Conducted at UW17-BH2

3.1.3. IN-SITU DENSITY

In-situ density measurements were determined using a sand cone density apparatus following (ASTM D1556). This standard is applicable for test volumes of less than 0.1 m^3, and samples with less than appreciable amounts of soil with grain sizes larger than 38mm. Although some soil particles were found to be larger than 38 mm, the amount found was small enough to be considered accurate (ASTM D4914). Test locations were based on practical and representative locations that were flat enough to conduct an accurate test. One in-situ density test was conducted per test site, for a total of three in-situ density measurements on the surface of the Main Waste Rock Dump. Figure 3.1.7 shows the sand cone density test in progress at test location UA19-TL1.

Figure 3.1.7 - In-Situ Density Measurement at UA19-TL1

3.1.4. SUCTION

One jet-fill tensiometer was installed at each test location to measure suction values from August 30 to September 1, 2019. The installation distance from each permeameter test and depth of installation varied for each location due to encounters of large rock fragments. All tensiometers were installed between 0.25 – 0.45 m. Initial installation methods used for locations UW17-BH2 and UW17-TP2 were completed using rebar to create a starter hole, where the tensiometer was then installed. Contact with fine-grained materials may not have been optimum compared with the tensiometer installed at UA19-TL1, which was installed in a hole excavated using a hand auger. Fine-grained materials were filled in around the tensiometer, ensuring proper contact with the porous stone. Despite varying installation methods, all tensiometers had comparable peak in-situ suction measurements.

3.2. LABORATORY PROGRAM

Samples were shipped by ground from Faro Mine Complex and arrived at the University of Alberta (UA) on September 17, 2019. Testing of samples was completed from October 2019 to July 2021.

The laboratory analysis program aimed to evaluate the moisture contents, grain size distribution, soil classification parameters, and the soil water characteristic curve of the fine fraction. All waste rock samples were stored at room temperature which is within the acceptable range of 3 – 30°C (ASTM D2216-19).

University of Waterloo (UW) provided grain size and SWCC results for a sample taken during the 2017 field investigation from UW17-TP1 at a depth of 1.5 m. These results will be compared to UA surface samples for validation of numerical results for UA samples.

3.2.1. MOISTURE CONTENTS

In-situ moisture contents of waste rock samples were determined in accordance with (ASTM D2216-19). Additional moisture contents were assessed from the in-situ density test samples, which have a more accurate assessment of in-situ moisture content. Each density sample's initial mass was weighed on site and was not affected by time delays between transport and initial analysis.

Measurement of the moisture contents from in-situ density test samples was completed per ASTM D2216 – 19 Method A. Although there were somewhat appreciable amounts of materials greater in particle size than 3/8 inch, the volume of materials tested was too small for application of Method B.

3.2.2. SIEVE ANALYSIS

Traditionally, soil has few large coarse-grained portions, but waste rock is a unique material due to the large range of particle sizes observed. A significant portion of the coarse fraction contained rock fragments larger than 19.0 mm; therefore, a composite sieve was conducted using (ASTM D6913-17).

One 20L pail of dried sample from each test location was further separated into 4 representative sub-samples using a chute splitter. One representative sample was used for grain size distribution analysis, while the three remaining representative samples were used for hydrological classification, including saturated hydraulic conductivity and SWCC, hydrometer analysis and a specific gravity test. Sample splitting was conducted carefully to eliminate loss of fines, but it was not practically possible to prevent all loss of fines.

Composite sieve analysis was carried out by splitting the representative sub-sample into the coarse fraction and finer fraction. A dry sieve was completed using a sub-sample derived from the outlined procedure while a wet sieve was conducted using a sand cone density sample taken from the surface. Previous investigators have shown that the difference between wet and dry sieves can be substantial (Shokouhi & Williams 2017; Le Bissonnais 2016). The dry sieving method is known to contribute to increased loss of fines during the sieving and splitting procedure and cannot separate silts and clays from the surface of coarser grain size fractions. Wet sieving allows for separation of fines from the surface of coarser fractions, and therefore can provide insight into the relative proportions of silt and clay sized particles within a soil matrix. Results of both the wet sieve and dry sieves are discussed in Section 4.2.2 of this thesis.

The coarse fraction considered for each sieve contained particles larger than and including 9.5 mm, and the fine fraction contained particles less than 9.5 mm. The coarse fraction of each subsample was measured using the Gilson TS-1 Mechanical Sieve Shaker. The coarse fraction was characterized using the 75 mm, 50 mm, 37.5 mm, 25 mm, 19 mm, and 9.5 mm sieves. Each sub-sample designated for grain size distribution testing was split into two batches in order to prevent overwhelming the sieve shaker. Each batch of sample was shaken for 10 minutes before weighing the weight of material retained on each sieve. The apparatus used for coarse fraction sieving is displayed in Figure 3.2.1.

The finer fractions of the dry sieves were mechanically sieved using the 4.75 mm, 2.00 mm, 1.18 mm, 0.425 mm, 0.250 mm, 0.150 mm, 0.106mm, and 0.075mm sieves. Fine fractions of the wet sieve were measured using the 4.75 mm, 2.00 mm, 0.850 mm, 0.425 mm, 0.30 mm, 0.150 mm, 0.106 mm, and 0.075 mm sieves. Fine fraction samples were split into 150 g sub-samples as stipulated by ASTM D6913-17 to prevent overloading of sieves. Each sub-sample was shaken for 10 minutes in the mechanical sieve shaker, which was followed by measuring the mass of

material retained on each sieve. Data collected from each subsample was combined to generate the total grain size distribution for each location according to the USCS classification system.

Figure 3.2.1 - Coarse (Left) and Fine Fraction (Right) Mechanical Sieve Shakers

3.2.3. HYDROMETER

To further characterize fine soil particles smaller than 0.075 mm, hydrometer tests were conducted using (ASTM D7928-17). In this experiment, Stokes' Law is used to relate the settling velocity of spherical soil particles to their particle diameter. Assuming there is no interference between particles, theoretically larger diameter particles will settle faster than the smaller particles that stay suspended in solution longer. Mathematically, the soil particle diameter is proportional to the square of the settling velocity, but many assumptions make this possible. Soil particles are assumed to be spherical in shape, interference caused by larger particles are not considered, and particles are assumed to all have the same density (ASTM D7928-17). Fluid

mechanics is also important to consider in this experiment. Stokes' law considers the internal flow regime constant between the center and walls of the settling column, and it assumes that the flow regime remains laminar during the entire experiment (ASTM D7928-17).

Before the experiment was conducted, the soil sample was soaked in a dispersing agent that prevents smaller particles from remaining on the surface of larger particles. This is important to ensure that a representative amount of fine material is captured during settling. The dispersing agent sodium hexametaphosphate was used at a concentration of 40 g/L. 125 mL of this solution was used to soak a 50.0 g sample for 16 hours before testing began.

Correction factors are necessary to interpret results correctly. 125 mL of the sodium hexametaphosphate solution was added to 875 mL of distilled water in order to account for the effects of the dispersing solution in the distilled water when measuring the appropriate correction factors. Correction factors were then measured from this mixture using a 152H hydrometer at room temperature of 20.0 °C. Hydrometer readings were taken at 2, 5, 15, 30, 60, 240, and 1400 minutes according to the requirements of ASTM D7928-17. Additional temperature readings were taken after each hydrometer reading to accurately correct for temperature effects on the slurry. The typical setup for these experiments is shown in Figure 3.2.2.

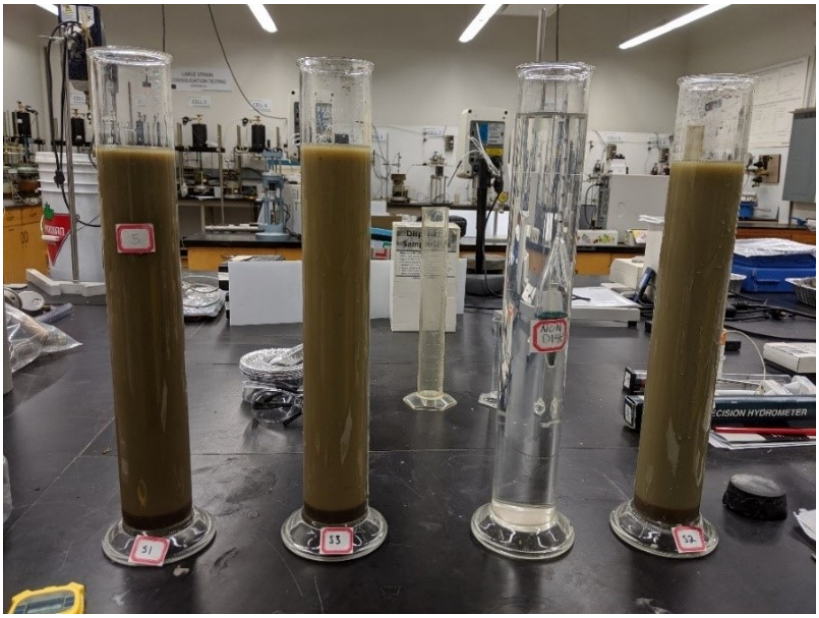

Figure 3.2.2 - Hydrometer Experiments Conducted on Fine Matrix Materials

3.2.4. SPECIFIC GRAVITY

The specific gravity of the solid soil mass is essential for infiltration modelling and to complete the hydrometer analysis. The specific gravity of the waste rock samples was determined for the fraction smaller than 4.75 mm. The samples were prepared in accordance with (ASTM D854-14). Pycnometers were calibrated before testing. The experimental setup is captured in Figure 3.2.3.

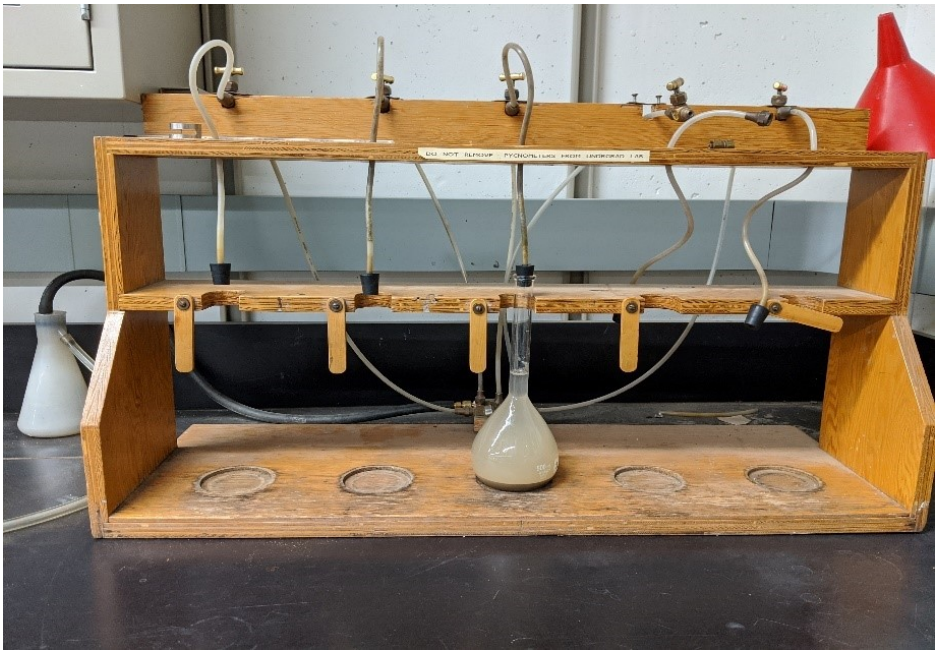

Figure 3.2.3 - Water Pycnometer Used for Specific Gravity Testing

3.2.5. ATTERBERG LIMITS

Atterberg limits were conducted on materials finer than 0.075 mm and were sieved according to ASTM D6913-17. Test procedures for determining the plastic and liquid limit of these materials was followed according to (ASTM D4318-17).

Liquid limits for each sample were determined using the Casagrande apparatus. Samples were assessed using 5 unique blow counts between 15 and 35 to determine a linear trend of blow counts with moisture content. The moisture content corresponding with 25 blow counts is taken as the liquid limit of the sample (Das & Sivakugan 2015).

Plastic limits were determined by rolling waste rock fines until a cracking appears at a particular diameter. Three separate trials were completed to obtain an average value for the plastic limit of each sample.

3.2.6. SATURATED HYDRAULIC CONDUCTIVITY

Traditionally, the saturated hydraulic conductivity is determined using a constant or falling head permeameter in a laboratory setting. Due to COVID-19, this was not possible as lab closures continued; therefore, Guelph permeameter results were assigned as the saturated hydraulic conductivity. Using in-situ values may be more appropriate than lab-derived values, as hydraulic conductivity is severely influenced by soil structure, which includes the in-situ density and presence of preferential flow paths. Having multiple readings for each location allows for a sensitivity analysis to be performed using field-derived values, which may better reflect site conditions.

3.2.7. SOIL-WATER CHARACTERISTIC CURVE

The soil-water characteristic curve (SWCC) is essential to characterize unsaturated moisture flow through the soil matrix. Results from grain size distribution showed that the waste rock samples had a range of 56- 65 % of the overall sample finer than 4.75 mm, which is significant when assessing moisture flux through these materials. Soil classification from the grain size distribution analysis showed that the waste rock is likely to behave as “soil-like”, where the unsaturated flow is controlled by hydraulic properties of the fine matrix (Herasymuik, 1996, Cash, 2014). SWCC tests were performed on materials less than 4.75 mm to reflect this “soil-like” behavior.

Laboratory analysis of the soil-water characteristic curve was performed using both the hanging column method for small matric suction values, and by applying positive air pressure to each sample to reach larger values of suction. Sample preparation for both methods included compacting each sample to a reasonable estimation of the in-situ density. This was achieved by measuring a dry 400g sample of a representative grain size distribution for each sample location. Each sample was moistened to a representative in-situ moisture content of approximately 5% using distilled water. A strip of plastic wrap was used to contain the sample within the TEMPE-cell casing, where approximately 3 equal lifts were placed and compacted using the arbor press and additional head weight seen in Figure 3.2.4.

Figure 3.2.4 - SWCC Sample Compaction Method to Achieve In-Situ Density

Before additional lifts were added, previous lifts were scarified to promote continuous contact and avoid macropores within the sample. The maximum density achieved before saturation was 2156 kg/m^3 with a moisture content of 5%. The discrepancy between the achieved SWCC sample density and in-situ bulk density may be due to large rock fragments included in the in-situ density measurements. Without the inclusion of clast density, the fines may not completely achieve field-derived density; therefore, the density achieved during laboratory compaction was deemed acceptable within practical limits.

Samples were saturated bottom upwards through porous stones with air entry values of 1 bar and were left to saturate for 24 hours before testing was completed. Small increments of suction were applied to each sample using the hanging column method. Negative water pressure was applied to the sample by reducing the elevation of the outlet tube, where each centimeter of elevation loss was equal to 0.1 kPa. Initial increments from 0 – 4 kPa were applied using the hanging column method, and additional suction values were achieved by applying positive air pressure up to the 95 kPa pressure increment.

3.3. NUMERICAL MODEL

Soil-atmosphere models have been used to couple existing physical principles of soil mechanics with atmospheric demands on moisture within saturated – unsaturated soil systems. Several modern software packages are available to calculate net percolation using the theoretical principles described earlier in this thesis.

Initially, a more modern seepage software was used for water balance simulations. It was found that the solving method was not capable of overcoming large discontinuities created during large precipitation events; therefore, the software SoilCover was used for all simulations. SoilCover software has proven to have a robust solving method that is able to handle larger changes in soil properties due to changes in soil moisture.

SoilCover is a transient one-dimensional finite element model developed by Wilson (1990) that determines the water balance while employing more accurate methods of estimating actual evaporation, of which the mechanics are detailed in Section 2.3.3 of this thesis. Various studies on soil cover systems have shown that SoilCover has the ability to reasonably predict the water balance in heterogeneous soil systems when compared to data collected during field investigations. (Jubinville 2013, Abdulnabi et al. 2016). Swanson et al. (2003) saw that there was accurate prediction of field observations with laboratory derived soil parameters being calibrated to field results. Although it has been seen to be reliable, SoilCover operates on a limited data resolution where only daily meteorological data can be used.

During all simulations, underlying assumptions will be used to simplify the scope of this project. It is assumed that when the average daily temperature is below 0°C, infiltration is negligible. The effects of freeze/thaw and vegetation on infiltration are also not considered.

Each assumption was applied to the numerical model, SoilCover, was used to provide a range of surface flux boundary conditions for the surface of the Main Dump East. contains a visualization of the model configuration.

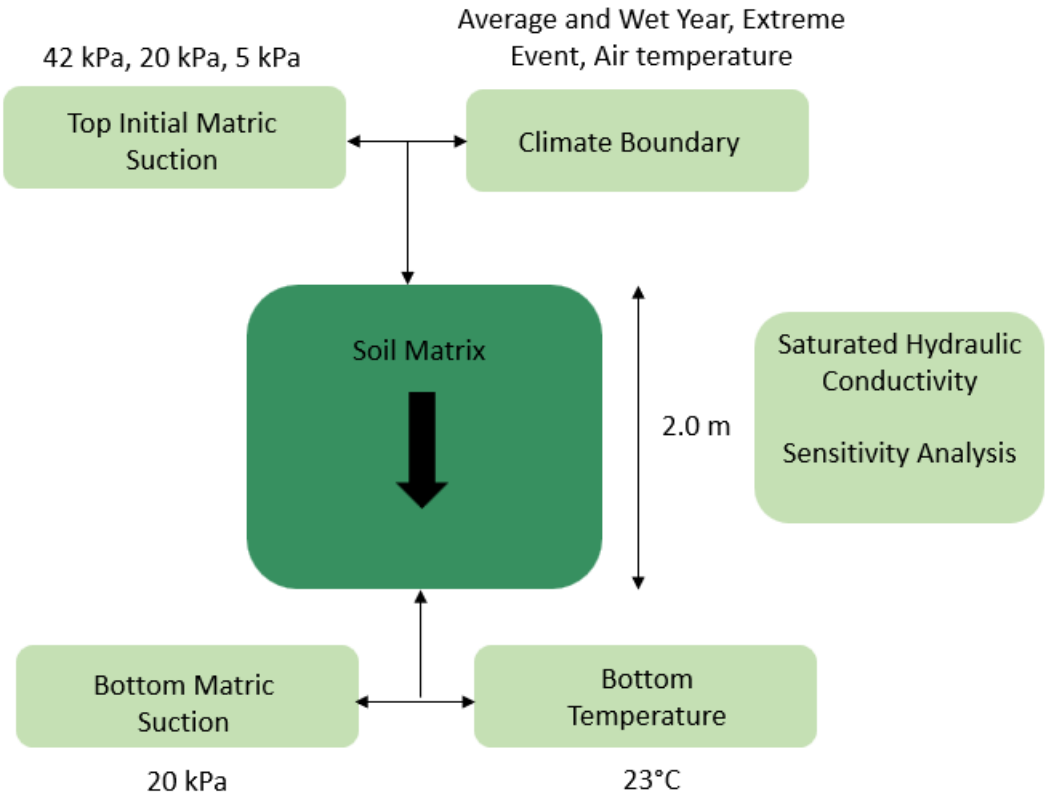

Figure 3.3.1 - Overall Net Infiltration Model Schematic

The following sections detail all scenarios and input parameters used to represent realistic surface flux boundary conditions. Derivations and reasoning behind choosing all input parameters is also provided.

3.3.1. Model Scenarios

To provide reasonable variability and range in surface flux boundary conditions for use in a reactive transport model, different meteorological scenarios are typically modelled: average year, wet year, and an extreme precipitation event. Sensitivity analyses are also considered to understand the sensitivity of the system. Parameters such as wind speed, net radiation, and relative humidity were only available for the years 2017 to 2018. A significant data gap was found where the entire month of June 2017 is missing both net radiation and relative humidity. Section 3.3.5.2 and Section 3.3.5.3 describe the statistical analysis used to derive these missing values. Details of each model scenario are described in the following sections.

Average and Wet Year

Precipitation records obtained for this project contain daily precipitation records from 1980 – 2020. Annual cumulative precipitation was assessed from 2000 – 2020, where the geometric mean of annual precipitation was found to be 357 mm. The year with the largest annual precipitation between the years 2000 and 2020 was found to be 2016 with a total of 507 mm. 2017 was chosen to represent a wet year with an annual total of 379 mm (accounting for snow water equivalent), and 2018 was chosen as a representative average year with a total annual precipitation of 308 mm. Each year was chosen within the realm of available meteorological data.

Extreme Precipitation Event

Days with the largest recorded precipitation were identified as potential candidates for further analysis. The largest recent event recorded on August 24, 2008 saw a daily total precipitation of 29.4 mm. Wind speed data was not available for this date, therefore an event with a total of 28.8 mm which was recorded on August 23, 2017 was chosen for further analysis.

It is widely known that the rainfall intensity used in numerical modelling can affect resulting infiltration and runoff calculations. Ideally hourly infiltration analysis would be completed. Hourly data from site contained numerous quality issues, such as negative and missing values.

In each meteorological scenario, a base case simulation is assessed, named DHM, which utilizes the average field saturated hydraulic conductivity of all valid double head method Guelph permeameter results. Additional sensitivity analyses are utilized to understand the effect of initial matric suction and k_{fsat} on the overall water balance.

Table 3.3.1 - Timeline for Simulation Periods

	Extreme Event	**2017**	**2018**
Start	August 22	May 1	April 26
End	August 25	October 13	September 19
Number of Days	4	166	147

All models were run for two consecutive years to stabilize the initial conditions that were assumed based on field measurements. All results are taken from the second year of analysis.

Simulation days provided in time series assessments of results are linked to the corresponding calendar date in Table 3.3.2 and should be used when reviewing time series plots of water balance results.

Table 3.3.2 - Summary of Simulation Day and Calendar Date

2017 Simulation		2018 Simulation	
Simulation Day	**Calendar Date**	**Simulation Day**	**Calendar Date**
166	May 1, 2017	141	April 26, 2018
171	May 6, 2017	146	May 1, 2018
176	May 11, 2017	151	May 6, 2018
181	May 16, 2017	156	May 11, 2018
186	May 21, 2017	161	May 16, 2018
191	May 26, 2017	166	May 21, 2018
196	May 31, 2017	171	May 26, 2018
201	June 5, 2017	176	May 31, 2018
206	June 10, 2017	181	June 5, 2018
211	June 15, 2017	186	June 10, 2018
216	June 20, 2017	191	June 15, 2018
221	June 25, 2017	196	June 20, 2018
226	June 30, 2017	201	June 25, 2018
231	July 5, 2017	206	June 30, 2018
236	July 10, 2017	211	July 5, 2018
241	July 15, 2017	216	July 10, 2018
246	July 20, 2017	221	July 15, 2018
251	July 25, 2017	226	July 20, 2018
256	July 30, 2017	231	July 25, 2018
261	August 4, 2017	236	July 30, 2018
266	August 9, 2017	241	August 4, 2018
271	August 14, 2017	246	August 9, 2018
276	August 19, 2017	251	August 14, 2018
281	August 24, 2017	256	August 19, 2018
286	August 29, 2017	261	August 24, 2018
291	September 3, 2017	266	August 29, 2018
296	September 8, 2017	271	September 3, 2018
301	September 13, 2017	276	September 8, 2018
306	September 18, 2017	281	September 13, 2018
311	September 23, 2017	286	September 18, 2018
316	September 28, 2017	287	September 19, 2018
321	October 3, 2017	-	-
326	October 8, 2017	-	-
331	October 13, 2017	-	-
332	October 14, 2017	-	-

3.3.2. GEOMETRY

SoilCover carries out one-dimensional analyses which assumes the majority of infiltration follows a vertical path downward through a specific depth of soil. No effect of slope is assessed. In-situ measurements of physical characterization and hydraulic properties were taken to a depth of 25 cm. These properties were extended through a 2.0 m tall soil column within the model.

3.3.3. INITIAL AND BOUNDARY CONDITIONS

Initial and boundary conditions in water balance simulations can have a large effect on the overall results. Initial and boundary conditions have been chosen to represent in-situ measurements of various parameters in order to create a base case scenario. Additional alterations to base case values will be made in order to conduct sensitivity analyses.

In-situ matric suction is used as the initial condition at the top of the soil column within SoilCover. Matric suction was measured in-situ using jet fill tensiometers installed at a depth of 0.25m to 0.45 m, where readings were monitored during the day while on site. Steady-state readings free of interference ranged from 30 kPa – 54 kPa. The geometric mean of steady state field measurements was found to be 42 kPa, which will be used as the initial measurement for the top of the soil column. In order to understand how the water balance is affected by changes in matric suction, two additional starting conditions will be applied to the top initial condition in a sensitivity analysis; 5 kPa and 20 kPa will be used. These were chosen to progressively saturate the top node of the simulation past the air entry value of the material.

Initial temperature is also specified for the soil column. The recorded air temperature for the first day of the simulation was used as the initial temperature condition at the top of the soil column. The bottom temperature condition for the soil column is set at 23°C, which was measured in-situ during the site investigation at a depth of 0.6 m within the Guelph permeameter hole used at test location UA-19 TL1. This measurement is consistent with the results of Bao et al. (2022).

Top and bottom nodes in each model require a boundary condition to complete each simulation. The SoilCover software provides different options for boundary condition inputs to suit different needs. In this model, the top boundary condition is input as a rainfall intensity, where the daily precipitation for each meteorological scenario is used. Bottom boundary conditions in each

simulation are set as a matric suction of 20 kPa and were chosen based on typical values found in waste rock piles.

3.3.4. SOIL PARAMETERS

Geotechnical and hydrological properties are essential when modelling infiltration. In-situ and laboratory measurements of soil properties are used to simulate the water balance for different scenarios. Table 3.3.3 contains all values of average physical soil properties used in numerical simulations.

Table 3.3.3 - Soil Parameters Used in Numerical Simulations

Parameter	Average	Source
Field Saturated Hydraulic Conductivity (cm/s)	2.4E-6	Field Derived
Specific Gravity	2.79	Lab Derived
Porosity	0.29 (S2)	Lab Derived
Coefficient of Volume Change (kPa^{-1})	9.1E-6	Geo-Analysis (1997)
SWCC Function	S2	Lab Derived
Thermal Conductivity Function	95% quartz	Geo-Analysis (1997) using Johansen (1975)
Mass Specific Heat for Specific Heat Function (J/kgC)	850	Geo-Analysis (1997)

Field Saturated Hydraulic Conductivity

12 tests were performed in-situ from 0.17m to 0.68 m depth on the surface of the Main Dump East. Both the double head method and single head method were used to determine the field saturated hydraulic conductivity. Two test locations (UA19-TL1 and UW17-BH2) had positive

results using the double head method, therefore the lowest of the measurements at UW17-BH2 , which was found to be 6.8E-9 m/s will be used in simulations as a sensitivity assessment. The average of the two double head method results was found to be 2.4E-8 m/s and will be used as an additional sensitivity parameter. To understand the progression of infiltration with changes in flow characteristics, two values were assumed and applied to the model, which were KSAT1 and KSAT2. This information is summarized in Table 3.3.3 below:

Table 3.3.4 - Field Saturated Hydraulic Conductivity Values Used in Simulations

KFSAT ID	DHM	GTP6	KSAT1	KSAT2
KFSAT (cm/s)	2.4E-6	6.8E-7	5E-6	5E-5
Source	Guelph Permeameter	Guelph Permeameter	Assumed Value	Assumed Value
Representation	Average of Double Head Method	Double Head Method Result for GTP6	Increase by one-quarter magnitude from DHM.	Increase by one order of magnitude from DHM.

Porosity

Values of porosity used in numerical simulations were assumed to be equivalent to the saturated volumetric water content of the applied soil-water characteristic curve to prevent any mathematical discontinuities (Jubinville 2013).

Coefficient of Volume Change

Volume change can be quantified using constitutive relationships describing the change in volume of air, water, and total volume in a four-phase unsaturated soil system (Wilson, 1990). The coefficient of volume change (m_v) is used in each relationship to describe the decrease in

soil volume per unit applied pressure, or the volumetric strain per unit applied stress (Sivakugan and Das, 2010).

Sands typically have little to no significant volume change as a result of changes in the degree of saturation and matric suction; therefore, the coefficient of volume compressibility will be smaller than those found for expansive clays and oil sands tailings. Geo-Analysis (1997) provides default values for pre-determined materials. For a normally consolidated sand, m_v was estimated to be 9.1E-6 kPa^{-1} and will be used as a base case for this material.

Thermal Conductivity Function

A soil's ability to transmit heat is necessary to quantify heat and moisture flow through soils. The rate at which a soil can transmit this heat is dependant on the vertical temperature gradient and the thermal conductivity of the specific material (Geo-Analysis 1997). The thermal conductivity function is used within SoilCover to numerically estimate the relationship between the volumetric water content and the thermal conductivity of the material. SoilCover uses the equation proposed by Johansen (1975), where the user has the choice of choosing pre-selected overall weighted quartz percentage to best describe your input material. Based on the grain size distribution and the nature of the waste rock sampled, the suggested weighted quartz percentage of 0.95 for sands will be used in the thermal conductivity function. Overall water balance results have been shown to be insensitive to changes in assumed quartz contents (Geo-Analysis 1997).

Volumetric Specific Heat Function

Volumetric heat capacity of soil is defined as the amount of stored heat required to change the soil's internal temperature by one degree Celsius (Jumikis 1977, Geo-Analysis 1997). SoilCover requires the volumetric specific heat function, which is the relationship between the volumetric water content and the volumetric specific heat of a soil. SoilCover estimates this as the product of the mass specific heat and the dry density of the soil. All SoilCover calculations are used to estimate the volumetric specific heat function.

3.3.5. METEOROLOGICAL DATA

This thesis will reference two different meteorological data sets. The first henceforth referred to as “EQUIS” was the original dataset provided by CIRNAC, the second referred to as ‘External” was provided by an external consultant. The EQUIS dataset contained daily and hourly meteorological records but contained negative precipitation readings and periods of 30 days with consistent missing records. Errors in this data set were attributed to the use of the tipping bucket as a precipitation gauge, where errors were exasperated during the winter months due to the mechanical operation of the bucket. The external dataset contains daily records of precipitation and other meteorological parameters in addition to values of hourly wind speed. Extensive effort by the external consultant was placed into applying statistical methods to fill gaps in the data, and to eliminate any anomalies. Precipitation records from the external consultant are used for all analyses.

It is important to note that it has been demonstrated by Abdulnabi et al. (2016) and Jubinville (2013) that rainfall intensity and resolution can affect runoff volume predictions. Hourly meteorological data is expected to provide a more accurate water balance than a daily resolution, but it has been shown that SoilCover’s daily resolution has been able to predict field measurements of water balance with confidence. The external dataset provided precipitation records in a daily intensity; therefore, daily rainfall intensity will be used to assess infiltration. SoilCover provides the option to specify the time range of which precipitation is applied. Rainfall will be applied to the model using the assumption that all rainfall occurs between 4:00 and 20:00.

3.3.5.1. GAP FILLING USING STATISTICAL CORRELATIONS

Both data sets were missing key information for the entirety of June 2017. EQUIS meteorological records were missing all input parameters, whereas the External Dataset was missing wind speed, relative humidity, and net radiation. A nearby weather station (Grum Meteorological Station) was also missing this data from the EQUIS dataset. June is a key period for evaluating water balance as evaporative fluxes are prominent during this time; therefore, single parameter correlations were performed to fill in the remaining gaps for all missing meteorological parameters.

To estimate relative humidity, two methods were used. First a single parameter correlation was completed, and the second utilized estimations developed by Allen et al. 1998 which focuses on using the dew point temperature. To estimate net radiation, single parameter correlations were completed. These correlation analyses were assessed for all meteorological parameters (air temperature, wind speed, relative humidity, and net radiation) in the summer months of July and August 2017, as well as June, July, and August of 2018. The following sections contain the results of this correlation analysis.

3.3.5.2. Statistical Correlations for Relative Humidity

The first estimation of relative humidity was performed using Allen et al. 1998's method. This estimation has assumed that in most cases, the maximum, average, and minimum air temperatures can be used to calculate each corresponding benchmark vapour pressure (Allen et al. 1998). This allows for the estimation of the relative humidity using Equations 13 to 15. One of the key assumptions in this method is the equivalence of the dewpoint temperature to the minimum daily temperature. The actual vapour pressure of each scenario is calculated using the average and minimum (dewpoint) air temperature for the corresponding day respectively.

$$RH_{mean} = \frac{e_a}{e_s} \, x \, 100 \quad [13]$$

$$e_a = 0.6108 * exp\left[\frac{17.27 * \ T_{min}}{T_{min} + 237.3}\right] \quad [14]$$

$$e_s = 0.6108 * exp\left[\frac{17.27 * T}{T + 237.3}\right] \quad [15]$$

RH_{mean} = mean daily average relative humidity (%)

e_a = Actual vapour pressure

e_s = Saturation vapour pressure

T_{min} = minimum daily air temperature (°C), assumed to be equal to dew point temperature

Furthermore, the results of the correlation analysis were used to estimate the relative humidity using known parameters in the dataset for June 2017. The cor() function in the base R package was used to calculate Pearson correlation coefficients for July and August of 2017. These values are presented in Figure 3.3.2 and Figure 3.3.3.

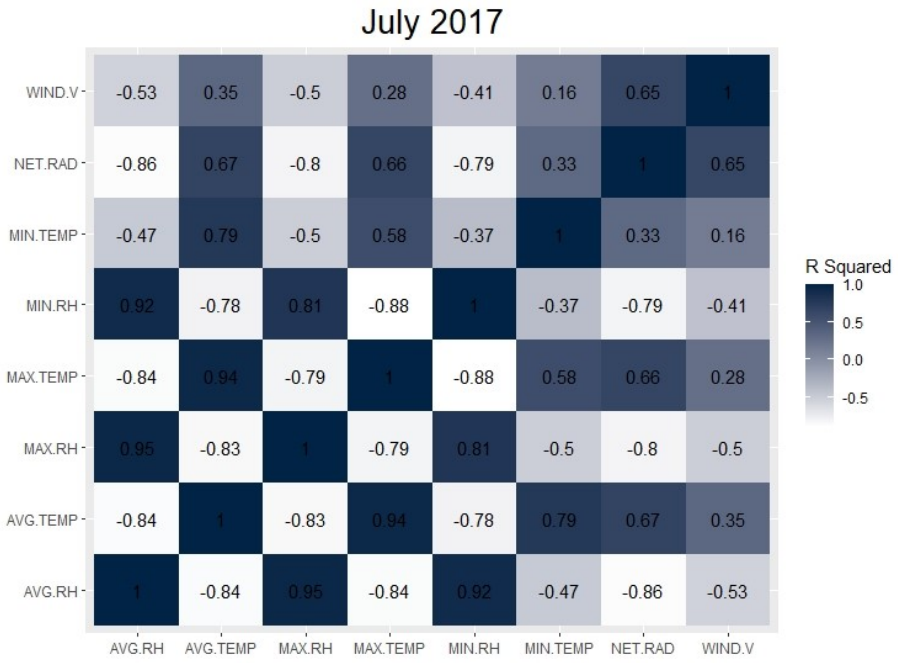

Figure 3.3.2 - Statistical Correlations of Meteorological Parameters in July 2017

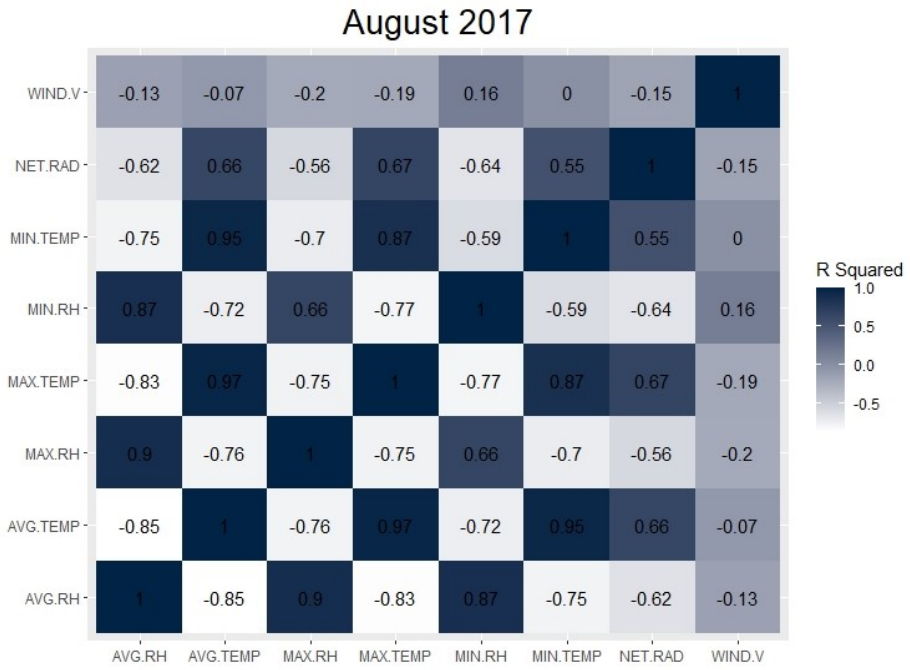

Figure 3.3.3 - Statistical Correlations of Meteorological Parameters in August 2017

This analysis showed that there are several statistically significant correlations between known parameters and a range of values for relative humidity during the summer of 2017. In July 2017, the largest correlations with known measurements were between minimum relative humidity and maximum temperature (-0.88), and the lowest correlation was attributed to minimum RH and wind speed (-0.41). In August 2017, the highest correlation was observed to be between average RH and average air temperature (-0.85) and the lowest being between average RH and wind speed (-0.13) which is expected.

Minimum, maximum, and average values of relative humidity were also highly correlated between each other with correlation coefficients ranging from 0.81 to 0.95 in July, and 0.66 – 0.90 in August. This correlation analysis also showed that net radiation had significant correlations to the full range of humidity versions tested in July of 2017, where this is less so in August of 2017.

To understand if these trends are similar for the month of June, statistical correlations were measured for the month of June 2018. Results of this analysis are contained in Figure 3.3.4.

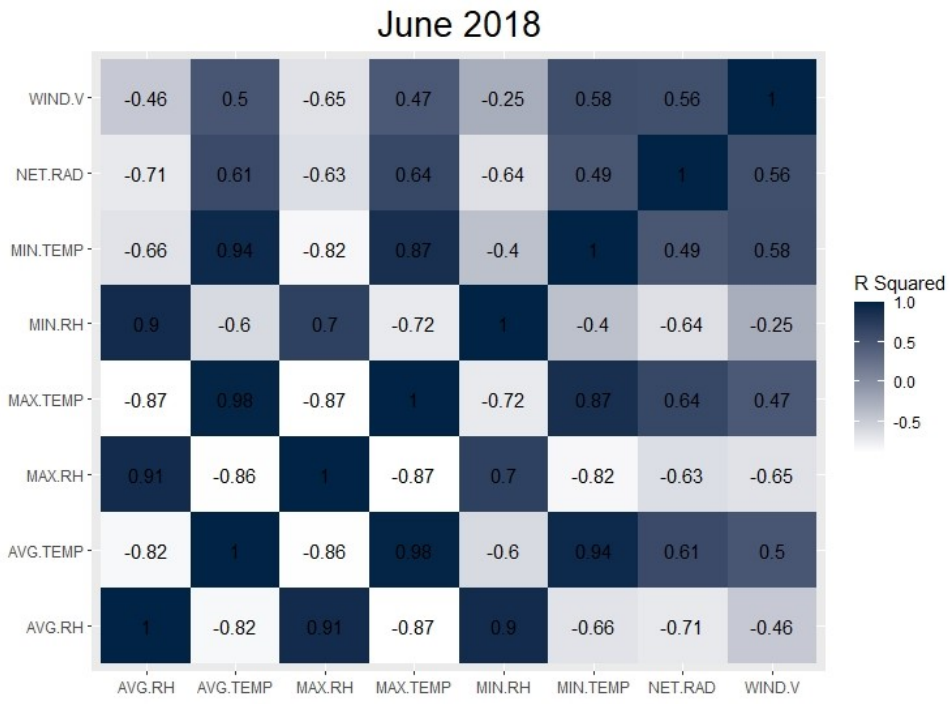

Figure 3.3.4 - Statistical Correlations for Meteorological Parameters in June 2018

Examining the correlations derived for June 2018 show similar correlation trends to those performed in July and August of 2017, where statistically significant (-0.40 to -0.87) relationships were found in the range of maximum, minimum, and average relative humidity. Less statistically significant relationships are seen in the month of June compared with the July and August 2018 counterparts. In June 2018 the range of relative humidity measurements were seen to be highly correlated to one another, where the largest correlation coefficient value between each relative humidity measurement was 0.91, which occurred within in each relative humidity trend. Linear regression was performed to predict daily average, maximum, and minimum relative humidity based on June 2018 data. Results of each linear regression analysis can be found in Appendix B. Relative humidity based on linear regressions with maximum daily temperature and the correlated average daily relative humidity from June 2018 data was used to determine data for the month of June 2017.

As previously stated, the Allen et al. 1998 method was used to calculate the daily relative humidity based on dew point temperature. Figure 3.3.5 contains the time series of both correlated and calculated values of average, maximum, and minimum relative humidity values. It can be seen that the calculated values tend to predict a higher relative humidity value than the correlated

values which has a smaller range of relative humidity values than previous recorded years. It is also observed that the two datasets show different trends with time.

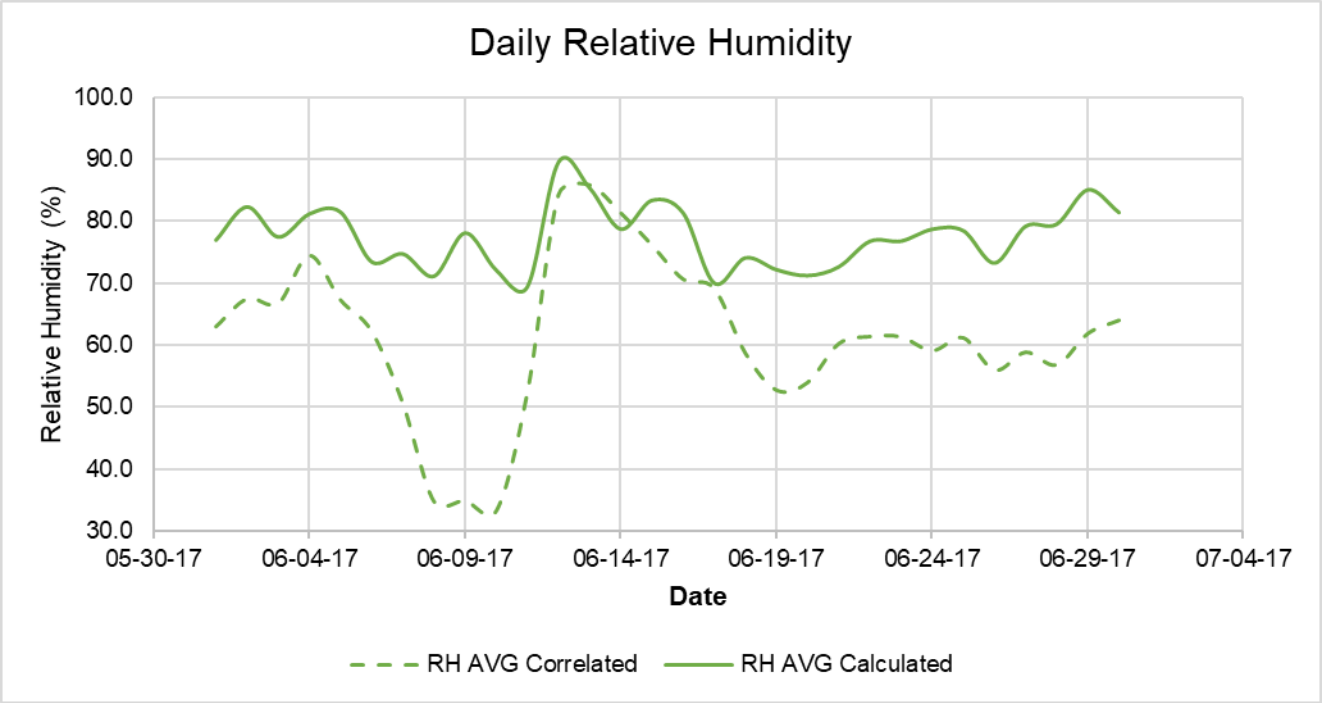

Figure 3.3.5 - Calculated and Correlated Daily Average, Minimum, and Maximum Relative Humidity June 2017

Due to the difference in the datasets, the correlated values will be used as the baseline level used in the 2017 simulations.

3.3.5.3. Statistical Correlations for Daily Net Radiation

Correlation coefficient values determined for July 2017 and August 2017 showed statistically significant correlations between net radiation and other meteorological parameters. These are shown in Figure 3.3.2 and Figure 3.3.3. In July 2017, the largest correlation was observed to be between net radiation and the average relative humidity (-0.86). Average air temperature and maximum air temperature were the largest correlations between net radiation and directly measured parameters, with a coefficient value of 0.67 and 0.66 respectively. Similar correlations were seen between these parameters in August of 2017, where the largest correlation to net radiation was maximum air temperature and average air temperature with correlation coefficient values of 0.67 and 0.66 respectively.

Some of the strongest correlations seen with net radiation were relative humidity. To see the difference in predicted values based on different correlations, net radiation was predicted for June 2017 using average and maximum daily temperature in addition to average relative humidity. Figure 3.3.6 contains values using each linear regression using data from June 2018.

It can be seen that daily net radiation correlated based on daily average and maximum temperatures was reasonably similar. Values predicted based on average relative humidity produces consistently lower net radiation values but followed the same trend as those predicted with daily temperatures. To reduce the propagation of estimation errors within the dataset, correlations made with daily temperatures were used in analyses.

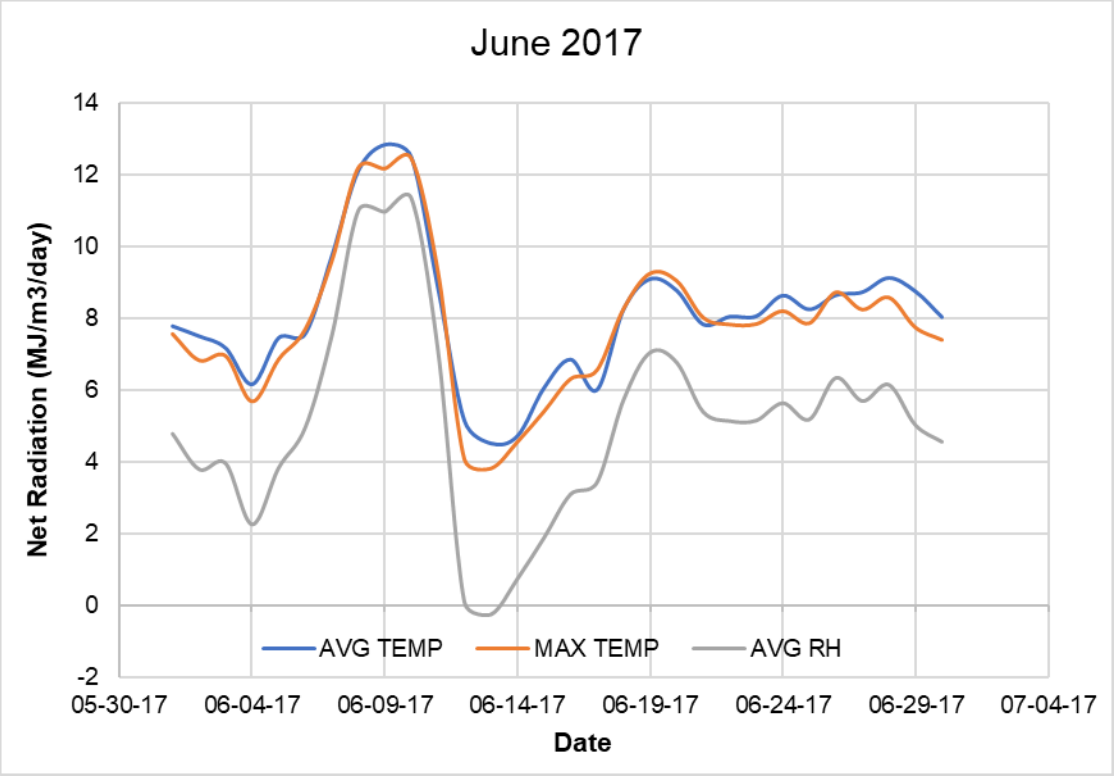

Figure 3.3.6 - Correlated Net Radiation June 2017

3.3.6. Meteorological Parameters

All atmospheric data was collected from an existing weather station located on top of the Main Dump East, located approximately 110 meters from the general test area. Atmospheric readings are captured at a height of approximately 2 m above the ground surface. Data available from the

Main Dump climate station contained daily precipitation records from 1980 to 2020. Average daily parameters were recorded, with wind speed being recorded hourly. Table 3.3.5 contains all meteorological parameters used in each model scenario. The following sections contain detailed derivations of specific meteorological parameters, which includes the Snow Water Equivalent (SWE) data for the Main Dump East.

Table 3.3.5 - Summary of Meteorological Parameters Used for Numerical Analysis

Parameter	2017	2018	Extreme Event	Source
Precipitation (mm)	Daily Total			External Data Set
SWE (mm)	Applied as surcharge of 4.53 mm/day from May 1 to May 15	Applied as surcharge of 6.8 mm/day from April 26 to May 11	Not Applicable	Yukon Government Snow Survey Reports from 2017 - 2018
Air Temperature	Daily Average			EQUIS Data Set
Soil Temperature	Hourly Records			External Data Set
Net Radiation (W/m^2)	Daily Average			EQUIS Data Set
Relative Humidity (%)	Daily Average			EQUIS Data Set
Wind Speed (m/s)	Daily Average			External Data Set

3.3.6.1. TEMPERATURE

Air temperature and soil temperature were recorded on the Main Dump East from 2003 to 2020. As temperatures rise in the spring, snow cover acts as an insulative cover which keeps the soil temperature below increasing atmospheric temperatures, creating a lag between soil and atmospheric temperature equalization (Gold (1963); Goodrich (1982); Zhang (2005)). It is important to quantify this lag, as frozen ground is assumed to have negligible infiltration capacity in soils with temperatures below 0°C. Three soil temperature sensors were installed at the climate station on the Main Dump East, where two are currently operational. T2 sensor is installed at a depth of 10 cm and T3 is installed at a depth of 30 cm. To ensure the entire sample depth of 20 cm achieve temperatures greater than 0°C, the temperatures from T2 were used to determine simulation days where the ground temperature is consistently greater than 0°C. Figure 3.3.7 contains both the average daily atmospheric and soil temperatures for the years 2017 and 2018 on the Main Dump East. Soil temperature data was not available through February 2, 2017 to April 31, 2017.

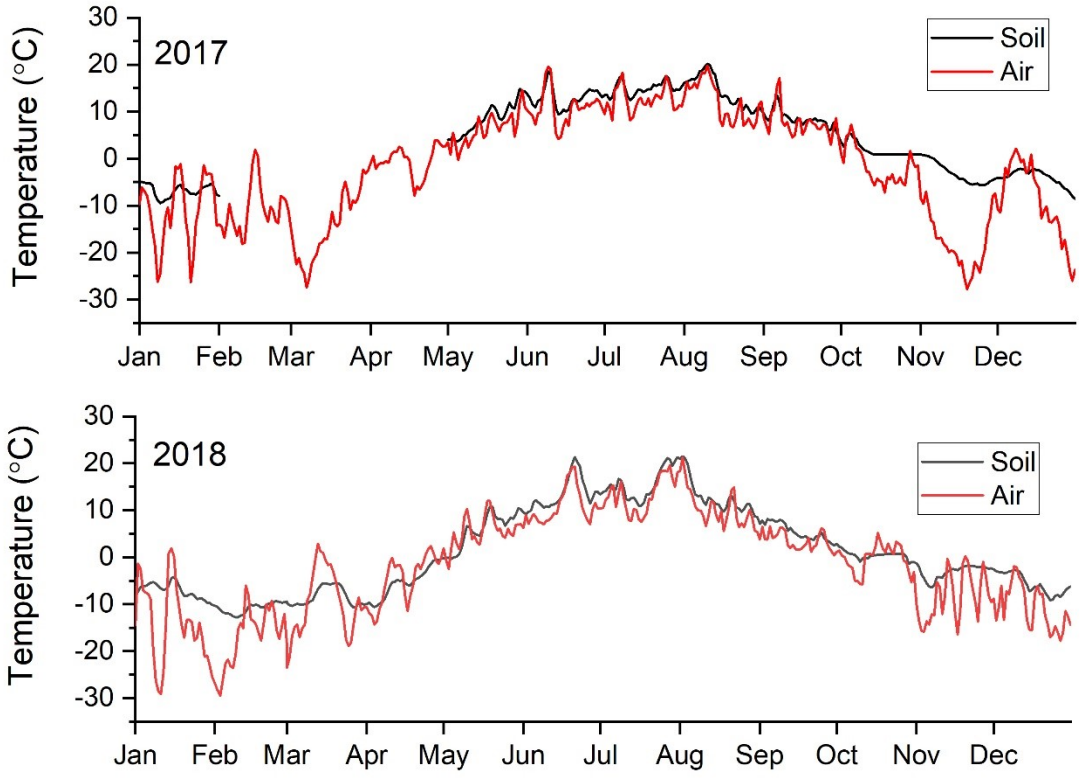

Figure 3.3.7 - Average Daily Soil and Air Temperature for 2017 and 2018

Differences observed between soil and air temperatures are congruent with the accepted insulative properties of snowpack's during seasonal variations in temperature. There are periods of time during the winter months where the snow cover maintains the internal temperature of the soil while atmospheric temperatures decline with the arrival of winter. There are two periods of time identified in Figure 3.3.7 where the soil temperature is maintained lower than the atmospheric temperature during simulation periods, but these periods are very brief. Data from each sensor indicate that the soil temperature is quick to respond to atmospheric temperatures starting in May and June. To ensure that the soil is not frozen during numerical analysis, dates where the temperature is consistently above 0°C were chosen for simulation. Table 3.3.1 contains the periods of simulation for each year chosen.

3.3.6.2. Snow Water Equivalent

Data for snowpack depth from the meteorological station on the Main Dump was deemed non-reliable due to the use of a tipping bucket device to record snow water equivalent. Limited manual measurements of the snowpack depth over time on the surface of the Main Dump also result in minimal data; therefore, additional research was needed to determine the SWE for winter months. Previous water balance studies conducted by Janowicz et al. (2006) at Faro Mine utilized the Prairie Blowing Snow Module (PBSM) and an energy balance method to determine the snow losses and SWE, respectively. In 1995, SWE was predicted to reach a peak of 75 mm before snowmelt, and in 2006, predicted to accumulate 100 mm of SWE before majority of snowmelt occurred (Janowicz et al. (2004), Janowicz et al. (2006)). Beginning of snow melt was predicted to occur around April 16 in 1995 and during the month of May in 2005.

Historical snowpack depth at the Faro Airport was provided by Environment Canada, indicating an average of 23 cm at the end of March for the years 2017 and 2018. No information was provided on the snowpack relative density, therefore a SWE estimation of 66.8 mm was made using the estimation method developed by Strum et al. (2010), assuming a tundra climate regime as determined by the study's climate classification. Although this data was available for Faro Airport, there is a significant difference in elevation between the Main Dump surface and the Faro Airport; therefore, Yukon Snow Survey records from 2015 - 2020 were used to gather SWE for surrounding stations at similar elevations to the study site (Government of Yukon, 2015 -

2020). All SWE measurements and estimations are contained in Table 3.3.6 with all locations and elevations. Table 3.3.7 contains statistical analysis for each snow survey report analyzed.

Table 3.3.6 - Snow Water Equivalent Measurements from 2017 and 2018 Yukon Snow Survey Reports

Year	Location	Elevation (m)	March Start (mm)	March End (mm)	April End (mm)
2017	**Mount Berdoe**	1035	118	103	70
	Hoole River	1036	121	123	90
	Twin Creeks	900	133	170	44
2018	**Mount Berdoe**	1035	87	135	118
	Hoole River	1036	109	133	86
	Twin Creeks	900	118	123	102

Table 3.3.7 - Statistics on Snow Water Equivalent Measurements 2017 and 2018

Year	March Start (mm)	March End (mm)	April End (mm)
2017	124 ± 7.9	129 ± 34.4	68 ± 23.1
2018	104 ± 15.9	130 ± 6.4	102 ± 16.0

Snow survey records for each location were available for the beginning and end of March, as well as the end of April. Based on the start date of each simulation year, the appropriate SWE measurement was applied. For 2017, the simulation start date was May 1, therefore the

geometric mean of SWE measurements for the end of April 2017 were used to estimate the SWE applied in numerical simulations. The geometric mean of SWE measurements for 2017 was determined to be 68.0 mm at the end of April, and for 2018, the SWE estimate for the end of April was found to be 102 mm. The SWE estimated using source locations, excluding the Faro Airport measurement, will be applied evenly over a 15-day period at the start of each year when temperatures are consistently above 0°C each year (O'Kane 1995). For 2017, this surcharge is equivalent to 4.53 mm/day and for 2018, the SWE will be applied as a 6.8 mm/day precipitation surcharge.

Losses due to sublimation, wind, and saltation can be significant when determining an appropriate SWE (Mott et al. (2018), Reba et al. (2012), Pomeroy & Li, (2000), Sexstone et al. (2016)). Snowpack losses are a function of many site-specific parameters including wind velocity, net radiation, temperature, relative humidity, surface terrain, various snow surface properties, and snowfall depth (Mott et al. 2018, Sexstone et al. 2016). Sublimation is one of the main snow removal processes and is highly influenced by wind velocity (Janowicz et al. 2004, Li & Pomeroy, 1997). Previous studies by Li and Pomeroy (1997) have shown that insignificant snow loss is seen where wind velocities do not exceed on average 9.9 m/s for wet snow, and 7.7 m/s for dry snow. This observation was confirmed by analyses performed by Janowicz et al. (2006) where wind speeds rarely exceeded 6 m/s on the surface of the Main Dump and resulted in 1.5% loss of SWE.

To determine if there is potential for significant snowpack loss, hourly windspeed records for dates contributing to snowpack development were considered. To isolate timelines that had the potential to support and maintain the growth of the snowpack, dates with soil temperatures less than 0°C were used for further analysis. These dates were taken from the year previous to that being simulated, as well as those dates at the beginning of the simulation year that contributed to the growth of the snowpack. In 2017 this period was identified to be from October 13, 2016, to May 1, 2017, and for the simulation conducted for 2018, this period was found to be November 9, 2017, to April 26, 2018. Hourly wind speed records are contained in Figure 3.3.8.

Over 4000 hourly wind speed records were fit each year using a lognormal distribution which is shown in Figure 3.3.8. Mean wind speed was calculated for 2017 and 2018 was found to be 1.89 m/s and 1.91 m/s respectively, and the standard deviation was determined to be 1.66 m/s and

1.67 m/s respectively. Of 4824 wind speed records, it was found that during snowpack development days for the 2017 simulation, only 0.8% of hourly wind speed exceeded 7.7 m/s, and only 0.04% exceeded 9.9 m/s. The same trend is shown for the same analysis performed for the 2018 simulation year, where only 0.8% exceeded 7.7 m/s and 0.06% exceeded 9.9 m/s. This is an insignificant portion of readings contributing to blowing snow sublimation, but to ensure thorough investigation of the windspeed events is conducted, the duration of large wind speed events was investigated.

All days during each timeframe were assessed for windspeed duration where windspeeds exceeded 7.7 m/s. The longest wind event greater than 7.7 m/s was recorded to last 5 hours, where the longest duration of winds exceeding 9.9 m/s lasted 2 hours. Each of these measurements occurred on December 31, 2016, and January 6, 2017, respectively. All other large wind speed records occurred in 1 – 3-hour durations. indicating this was an isolated event. Similar trends were observed in the 2018 snowpack windspeed records, showing that there should be minimal migration of the snowpack across the surface of the Main Dump East.

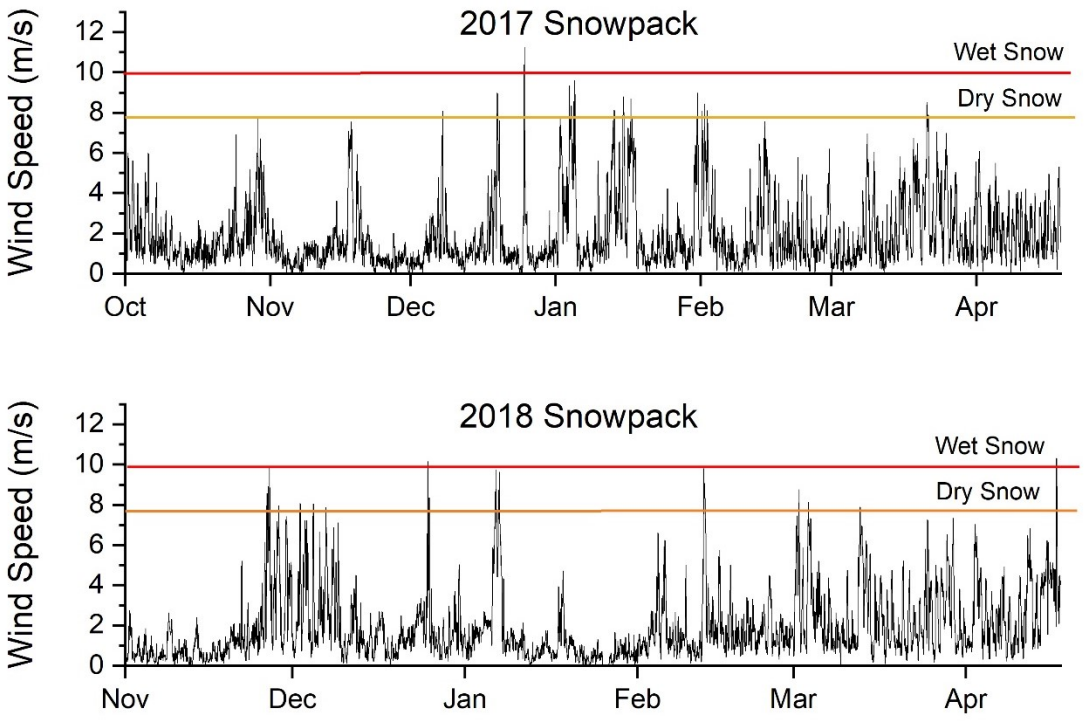

Figure 3.3.8 - Wind Speed Records Contributing to Snowpack Development for Numerical Simulations in 2017 and 2018

Blowing sublimation will be considered a negligible loss, but sublimation due to latent heat exchange can still be considered a significant loss term. Furthermore, measurements of snow depth from snow survey reports (Yukon, 2015 – 2017) consider all losses when recording physical on-site measurements therefore no additional losses will be considered during each simulation scenario. Lastly, any losses during the 15-day melt period are also assumed to be negligible based on these results.

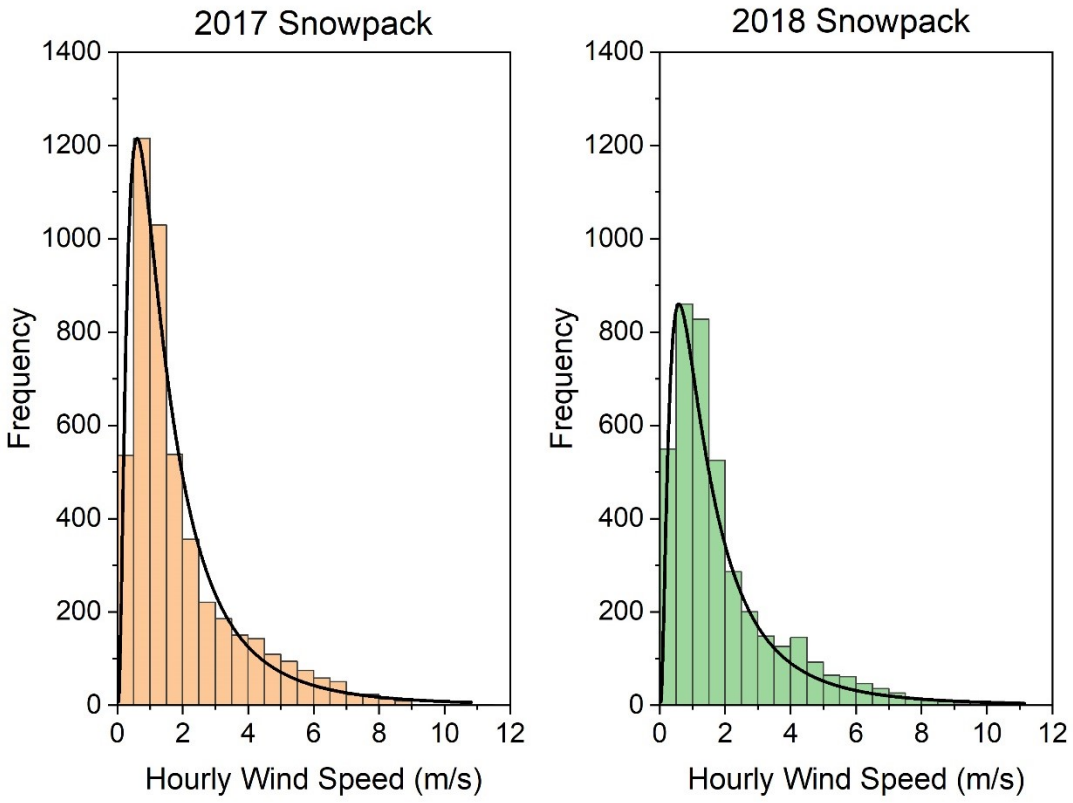

Figure 3.3.9 - Statistical Analysis of Hourly Wind Speed Records Contributing to Snowpack Development

3.3.7. MODEL VALIDATION

University of Waterloo conducted an extensive in-situ investigation where test pits and boreholes were completed in 2017 (Bao et al. 2020). Instrumentation was installed in UW17-BH1, -BH2, and -BH3 to measure volumetric water content, pore-gas concentrations of O_2 and CO_2, temperature, and air permeability (Bao et al. 2020). Laboratory tests were conducted to characterize the behavior of test pit samples. Results of the measured in-situ seasonal behavior

and soil characterization will be used to qualitatively validate the measured soil parameters of the surface materials, as well as the results of water balance simulations. Observations made during site investigations will also be used to validate the large-scale behavior of the surface materials.

CHAPTER 4. PRESENTATION AND DISCUSSION OF FIELD AND LABORATORY RESULTS

This chapter outlines all final numerical results from field, laboratory, and numerical analysis. Each section contains specific details of each analysis and any points of interest that were present during analysis.

4.1. FIELD RESULTS

In this section, final numerical results for the field saturated hydraulic conductivity, in-situ density as well as in-situ matric suction values are presented. Details of the analysis are also provided for context of numerical results.

4.1.1. GUELPH PERMEAMETER RESULTS

Numerical analysis using the double head method resulted in negative field saturated hydraulic conductivities for several permeameter tests. This was a result of severe heterogeneity in the waste rock where the bulb of field saturated water developed (SoilMoisture, 2012). Theoretical principles that characterize how the bulb of water saturates in sub surface soils relies on having a homogeneous soil below the permeameter (SoilMoisture, 2012). Calculation of k_{fsat} and $\emptyset_m$ (matric flux potential) are highly dependent on the ratio of flow rates Q_1 and Q_2; therefore, if the soil properties are not equal at each location of flow readings, both parameters can result in negative values (Elrik et al. 1989). Therefore, a negative k_{fsat} is indicative of a heterogeneous soil.

To correct this value, the single head method was used to analyze test locations yielding negative values of hydraulic conductivity. The double head method, which was used on site, required recording the steady state flow resulting from two different initial head measurements. So, to satisfy the single head method, each individual test with a different head measurement was analyzed separately using the single head method. Results of both single head results at the same depth were arithmetically averaged to determine the k_{fsat} at a specific depth for each test location. The averaged k_{fsat} is reported as the field saturated hydraulic conductivity for that test.

Analysis of saturated hydraulic conductivity requires classification of soil texture according to the Richard's Analysis. An α^* variable is assigned based on various descriptions of structure, and textures of certain soils. Based on site observations and the resulting grain size distribution from laboratory analysis, Type 4 was thought to observe the best match for the soil type being tested, which is attributed to coarse and gravely sands with highly structured soils containing large cracks and/or macro pores (SoilMoisture 2012). Due to the heterogenous nature of waste rock and observations of non-steady flow during in-situ testing, an α^* of 0.36 was assigned to the surface waste rock material.

Results for UW17-BH2 (GTP1), UW17-TP2 (GTP2 & GTP3), and UA19-TL1 (GTP5) all required the single head average method. This result was expected, as during GPT2 near UW17-TP2, non-steady flow was indicated through dramatic increases and decreases in flow rate around the 13-minute mark. These observations showed that there were most likely small-scale preferential flow paths through the subsurface of the waste rock at a starting depth of 0.137 m at that location. This conclusion is supported by the evidence of preferential flow paths observed on the surface of the waste rock. Table 4.1.1 contains the field saturated hydraulic conductivity of each sample and test location using α^* of 0.36.

Table 4.1.1 - Results of Guelph Permeameter Testing

Test ID	**GPT1**	**GPT2**	**GPT3**	**GPT4**		**GPT5**	**GPT6**	
K_{fs} (m/s)	$8.4x10^{-7}$	$1.4x10^{-6}$	$5.8x10^{-7}$	$1.3x10^{-6}$	4.1-8	$8.6x10^{-7}$	2.5E-6	6.8E-9
Test Method	Single	Single	Single	Single	Double	Single	Single	Double
Depth of Installation (m)	0.61	0.185	0.43	0.38		0.23	0.22	
Test Location	UW17-BH2	UW17-TP2	UW17-TP2	UA19-TL1		UA19-TL1	UW17-BH2	

Laboratory measurements of saturated hydraulic conductivity were completed by Bao et al. (2020b) using both fine and coarse fractions, with materials passing 2.00 mm and 9.5 mm respectively. It is unknown what density these samples were prepared to during constant and

falling head permeameter tests. Geometric mean of saturated hydraulic conductivity of the fine fraction was found to be $1.7x10^{-6}$ m/s, where maximum and minimum values of $3.3x10^{-7}$ m/s and $4.5x10^{-6}$ m/s were measured. It was found that the magnitude of saturated hydraulic conductivity varied based on the location that the samples were taken. The magnitude of these results is reasonable for waste rock materials. Results of Guelph permeameter measurements determined by the double head method were one order of magnitude smaller than the minimum laboratory measurements conducted by Bao et al. (2020b). This difference in magnitude is expected considering the samples processed by Bao et al. (2020b) contained less fines and may have been tested at a lower dry density than achieved in surface materials. Trafficking and grading of the surface is likely to have contributed to the reduction in saturated hydraulic conductivity at the surface.

4.1.2. MATRIC SUCTION

Constantly changing weather conditions on site resulted in decreased suction with increasing humidity; therefore, steady state readings were considered for further analysis. During GPT4 located at UA19-TL1, decreases in suction were observed during the permeameter test. The tensiometer was installed at a depth of 0.52 m and a depth of 0.48 m. Responses were recorded over time, and a total decrease of 6 kPa was observed once steady state flow conditions were achieved.

Maximum suction values at all tensiometers on September 1, 2019 ranged from 30 kPa to 54 kPa, with a geometric mean of 42 kPa at steady-state. Noticeable decreases over the day were noted as humidity started to increase with increased cloud cover and weather events, but these values were not considered for further analysis as the moisture content was unknown.

Matric suction was measured in-situ with varying volumetric water content near UW17-TP1 and UW17-TP2 to varying depths (0.3 m, 0.6 m, and 0.9 m) (Bao et al. 2020b). During dry periods with low rainfall, matric suction at 0.3 m depth was found to reach a maximum value of approximately 50 kPa during September 2018. This is comparable to the average steady-state value found during September of 2019, which was measured to be 42 kPa.

4.1.3. In-Situ Density

In-situ density was measured using the principles of the sand cone density method, where the volume of the removed material is measured with an equivalent material. The density values were fairly consistent between test locations, with a maximum difference of 3.4%. Table 4.1.2 contains the results for each sample.

Table 4.1.2 - In-Situ Bulk Density

Sample ID	**UA-S1**	**UA-S2**	**UA-S3**
In-Situ Bulk Density (kg/m^3)	2253.1	2319.6	2173.6
Test Volume (m^3)	0.00124	0.00145	0.00114
Average Bulk Density (kg/m^3)	2243.2		

4.2. Laboratory Results

This section contains all results from the laboratory analyses conducted from October 2019 to March 2020, and subsequent testing of soil-water characteristic curves in 2021. A comprehensive summary of all results obtained from laboratory experiments are provided in Table 4.2.1.

Table 4.2.1 - Summary of Soil Classification Parameters from Dry Sieve Results

Parameter	S1	S2	S3	Average
G_s	2.80	2.80	2.76	2.79
D_{60} (mm)	5.4	6.0	3.5	5.0
D_{30} (mm)	0.62	0.7	0.56	0.7
D_{10} (mm)	0.10	0.11	0.08	0.10
C_u	54.0	54.5	43.8	50
C_c	0.71	0.74	1.12	0.98
LL (%)	30.7	32.5	31.8	31.7
PL (%)	23.3	24.1	22.3	23.2
PI (%)	7.4	8.4	9.5	8.4
w (%)	4.39	5.00	3.56	4.32
n	0.23	0.21	0.24	0.23
e	0.30	0.27	0.32	0.30
S (%)	40.1	52.0	31.0	41.0
USCS Classification	SP-SM Poorly graded sand with silt and gravel	SP-SM Poorly graded sand with silt and gravel	SW-SC Well graded sand with clay and gravel (Or silty clay and gravel)	SP-SM Poorly graded sand with silt and gravel

4.2.1. MOISTURE CONTENT

Moisture contents were assessed for both of the pail samples and the sand cone density samples taken from each test location. Pail samples ranged from 4.46 % to 5.52 %, where the sand cone samples ranged between 3.56 % to 5.00 %. The two sample types yielded gravimetric water contents within close agreement to each other for each sample location. Table 4.2.2 contains each in-situ moisture content measurement.

Table 4.2.2 - In-Situ Moisture Content

Moisture Content	Sample 1	Sample 2	Sample 3
Pail (%)	4.72	5.52	4.46
Sand Cone Density Sample (%)	4.39	5.00	3.56

4.2.2. GRAIN SIZE DISTRIBUTION

Results from both sieve and hydrometer analysis were used to compile final grain size distributions for each sample location and sieve type. These results are contained in Figure 4.2.1. Following the USCS soil classification system, an average representation of all dry sieve samples contains few cobbles (2%), approximately 39% gravel, 51% sands, and 8% clay and silt. Coefficient of curvature (C_c) and uniformity (C_u) were calculated for each sample, where C_u varied from 43.8 to 54.5, and Cc ranging from 0.74 to 1.12. Samples 1 and 2 are classified as a poorly graded sand with silt and gravel, whereas the third sample is a well graded sand with clay / silt and gravel according to the amount of material less than 4.75 mm and the coefficients previously mentioned. Variability between samples was small, which is reflected in the closeness of the coefficient of curvature to the well graded and poorly graded classification boundary. All samples had a significant fine fraction, where materials smaller than 4.75 mm ranges from 55.9% – 65.0% of the total mass, which will determine the governing mechanisms behind unsaturated flow through waste rock matrix materials.

Wet sieve results were also determined using a sand cone density sample taken from UW17-TP2. Looking at Figure 4.2.1, it can be shown that the wet sieve had similar proportions of course fraction materials but contained an increased amount of fine sand, silt, and clay. This sample had no cobbles, approximately 41% gravel, 40.6% sands, and 18.4% silts and clays. C_u and C_c were found to be 317 and 1.27 respectfully, indicating a well graded soil (Das and Sivakugan 2015). The USCS soil classification system categorizes the wet sieve sample as a clayey sand with gravel (SC). The wet sieve sample also indicated that there is a significant portion of the soil matrix less than 4.75 mm in diameter, amounting to 59% of the total sample.
It is clear that there were two different results in regard to the amount of fine fraction found in each sample. Wet sieve results indicated a fine fraction of 18.4% where the measured clay sized

particles were found to be approximately 3.5% of the entire sample. Dry sieves indicated a fine fraction of 9.1% which contained approximately 1.5% clay. When comparing the two, it is observed that the wet sieve measured double the fine fraction of the dry sieve, and the sand measured using wet sieving was 10% lower than that using dry sieving. This indicates that the fine fraction was mostly agglomerated on the sand fraction, where washing the sample removed the agglomerates and measured their presence as a fine fraction. Wet sieving methods can also generate a greater fine fraction than present in-situ due to physical and chemical methods of soil degradation (Shokouhi and Williams 2017; Le Bissonnais 1996). Slaking, differential swelling and physio-chemical dispersion can all affect the measurements of the fine fraction (Shokouhi and Williams 2017). Slaking is a process by which entrapped air caused by rapid wetting can break apart the fine fraction and was found to be less prevalent in samples with higher clay contents (Le Bissonnais 1996). Differential swelling can result in microcracking of silts and clays due to large rapid changes in moisture content (Le Bissonnais 1996). The last of the most prominent effects on the grain size distribution is physio-chemical dispersion or flocculation. Presence of polyvalent and monovalent ions within the soaking solution can affect the surface chemistry of clay particles. If a net negative charge remains within the soil-water system, repellant forces can generate microaggregate degradation (Le Bissonnais 1996). Overall, the wet sieve shows that there is a larger presence of fines within the soil matrix than originally measured with the dry sieve.

Dominant unsaturated flow mechanisms have been correlated to parameters derived from the grain size distribution. Empirical evidence collected by Barbour et al. (2016) shows that all three test locations, with both wet and dry sieve results, can be said to be “soil-like” in behavior as greater than 20% by weight of each sample passes through the 2 mm sieve (Barbour et al. 2016; Bao et al. 2020b). Having a soil-like behavior indicates that moisture flux through the waste rock will be transported dominantly through the fine matrix under capillary suction, and gravity driven flow will occur in larger sized pores during large infiltration events (Barbour et al. 2016; Bao et al 2020b). Furthermore, classifications of waste rock put forth by Herasymuik (1996) suggest additional criteria for determining rock-like or soil-like behaviors from GSD parameters. Soils with greater than 40% passing the 4.75 mm sieve will have capillary suction driving unsaturated flow (Herasymuik 1996; Barsi 2017).

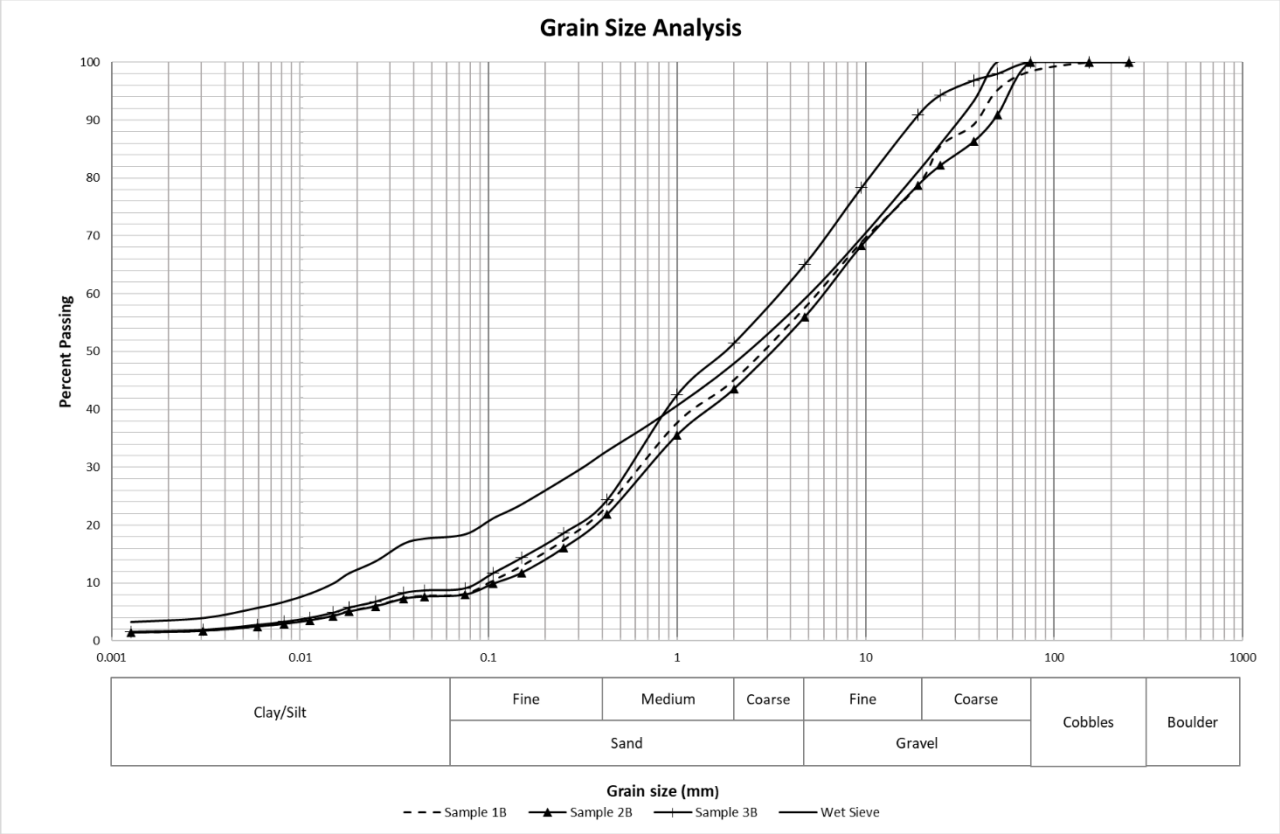

Figure 4.2.1 - Grain Size Distributions Using Dry and Wet Sieving Methods

Previous site investigations conducted by Bao et al. (2020b) in 2017 provided grain size distributions for test pit samples ranging from 0.5 to 4 m in depth on the surface of the Main Dump East. A bimodal fit was used to characterize particle size trends of over 20 samples, where it was observed that approximately 35% of each sample passed through the 4.75 mm sieve. Dry sieve results showed that surface samples were composed of 56% - 65% fine fraction, and 59% of wet sieve sample was composed of the fine fraction. Furthermore, grain size distributions for all matrix materials smaller than 4.75 mm from UW and UA samples are compared in Figure 4.2.2. Test pit samples from 2017 showed and approximate increase of 2% difference in the clay sized fraction looking at the dry sieve, and the wet sieve showed approximately 8% increase. Both the comprehensive and fine fraction grain size distributions show that there is an increased fine fraction in addition to clay and silt fraction found on surface samples which is to be expected. This is likely to be attributed to physical and chemical breakdown and weathering of materials on the surface when exposed to meteoric events, traffic, and maintenance of the surface materials over time.

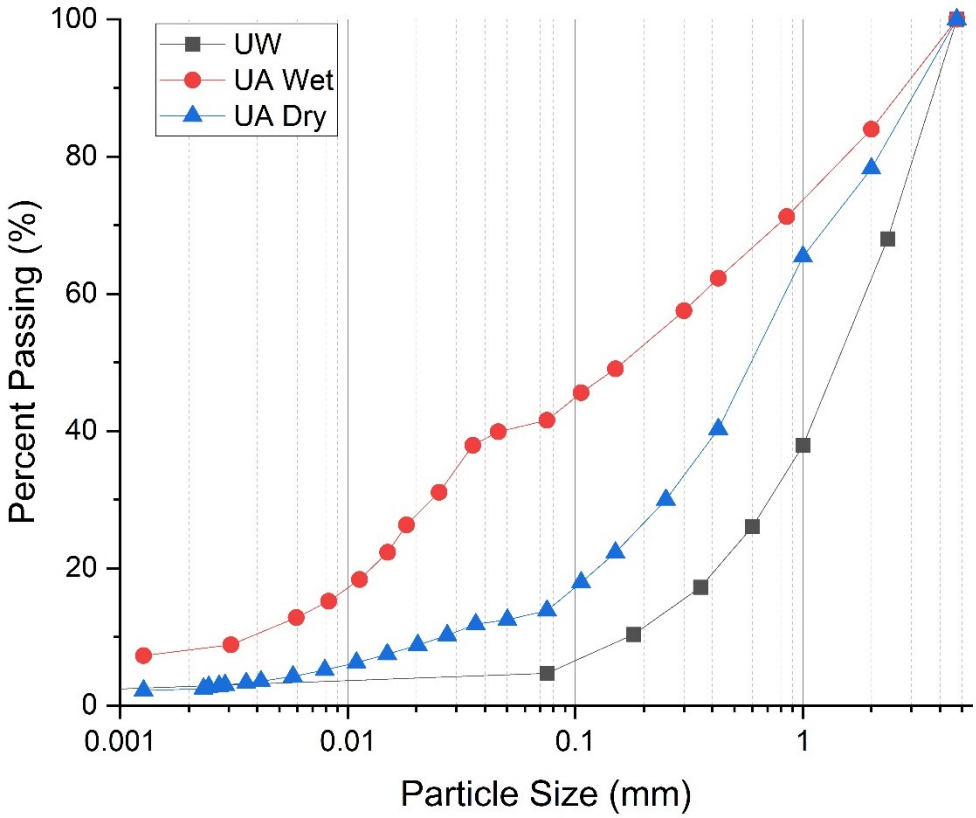

Figure 4.2.2 - Comparison of Fine Fractions of University of Alberta and University of Waterloo Samples

4.2.3. HYDROMETER

Although numerical results of the hydrometer analysis are contained in the previous section, certain observations of the fine fraction were made during the hydrometer test and wet sieve preparation. Soil chemistry can play a large part in soil structure and geochemical reactions that affect the flow of water over time. Along with the amount of clay in a soil matrix, the surface chemistry of clay-sized particles can either disperse or flocculate clays, creating a more or less permeable soil. During sample agitation and dispersion, a metallic sheen was observed in the slurry which is shown in Figure 4.2.3.

This may indicate that some silt and clay sized particles are either metallic specs from degrading gravel and cobbles, or precipitates from in-situ geochemical reactions. Interactions of both clays and metallic clay-sized particles with precipitation over time can produce precipitates or could create a dispersed soil structure that reduces infiltration variably with time.

Figure 4.2.3 - Observations of Metallics During Hydrometer Experiments

4.2.4. ATTERBERG LIMITS

Liquid and plastic limit tests were conducted for waste rock matrix materials smaller than 0.425 mm. A linear trend between the blow count and moisture content of each trial was found with R^2 values ranging from 0.90 to 0.94. Liquid limits for each sample were plotted against plasticity index to characterize the behavior of fines. Results are contained in Figure 4.2.4. Little sample variability was seen between Samples 1 and 2, where fines are classified as ML, plotting below the A-Line. Sample 3 plotted above the A-Line (CL), indicating inorganic silts and clays with medium plasticity (Das and Sivakugan, (2015). Results from this investigation are similar to those reported by Azam et al. (2007) which found a liquid limit ranging from 23-40, and a plasticity index ranging from 5-10 for waste rock matrix materials from Golden Sunlight Mine located in Montana, USA.

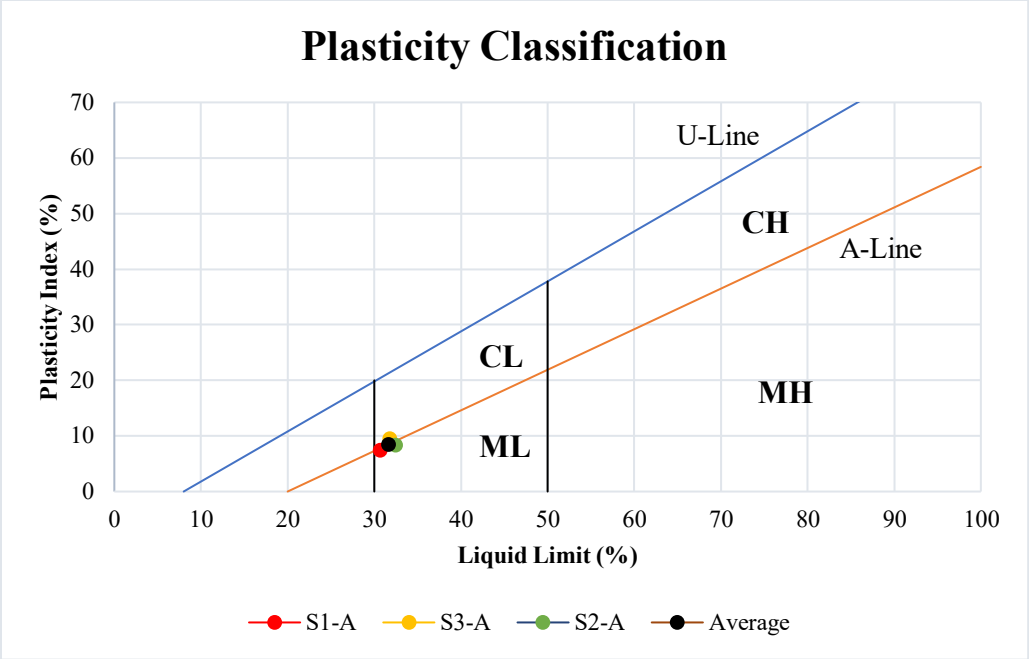

Figure 4.2.4 - Plasticity Chart for Waste Rock Samples

4.2.5. Unsaturated Flow Characteristics

The soil water characteristic curve was measured over the period of 3 months using the hanging column method at lower values of suction (0.1 – 4 kPa) and by applying positive air pressure to the sample at higher values of suction (5 kPa – 95 kPa). Figure 4.2.5 contains the results of each curve from UA laboratory experiments as well as UW test pit materials.

One of the most important unsaturated flow characteristics of soil matrix is the air entry value (AEV). Samples S1 and S2 had an AEV of 12.9 and 13.0 respectively. Sample S3 had an air entry value of 6.2, which is lower than that measured for S1 and S2. It is thought that during the saturation process, S3 experienced piping, creating a macropore within the sample and draining the soil sample at a faster rate than S1 or S2.

In-situ measurements of matric suction with changes in volumetric water content were recorded at UW17-TP1 and UW17-TP2 at varying depths (0.3 m, 0.6 m, and 0.9 m) (Bao et al. 2020b). Looking at Figure 4.2.5, it can be shown that the air entry value for UW samples was significantly lower than that of surface samples. Existence of preferential flow paths and an

increase in coarse fractions beneath surface materials are thought to contribute to a lower air entry value, when compared with laboratory measurements from this study. Increased presence of fines in the surface samples will increase the air entry value according to the capillary suction theory presented by (Taylor, 1948). As the pore radii decreases, the equivalent capillary suction needed to drain those pores increases, resulting in a higher air entry value. Furthermore, the density of surface samples in laboratory experiments was much larger than that completed for UW samples. Smaller pore diameters created during compaction require higher values of matric suction to reduce the volumetric water content. This results in a shallower trend towards desaturation which is evident when comparing UW and UA SWCC curves.

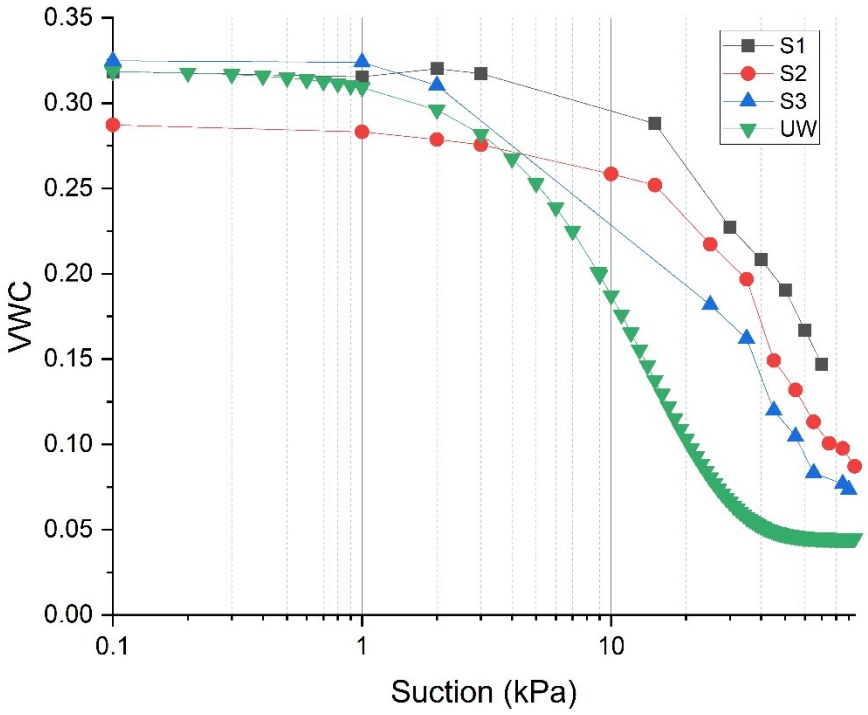

Figure 4.2.5 - Laboratory Derived Soil-Water Characteristic Curves for UA and UW Samples

Unsaturated flow is highly dependent on the in-situ moisture content. As the moisture content reduces, availability of moisture within pore spaces is decreased, resulting in a decreasing trend in hydraulic conductivity. Fredlund et al. (1994) developed a method to determine the permeability function using the SWCC for a variety of soil types over a large suction range, knowing the SWCC and saturated hydraulic conductivity for each sample. Built-in functions within SoilCover software were used to facilitate calculations resulting in each permeability

function for the average sample. To anchor the permeability functions, a saturated hydraulic conductivity of $2.4x10^{-8}$ m/s was chosen as it is the average of both double head permeability measurements. Figure 4.2.6 contains the permeability functions for both SWCC curves S1 and S2 anchored at the previously specified value. The permeability functions will change as the permeability changes during sensitivity analyses.

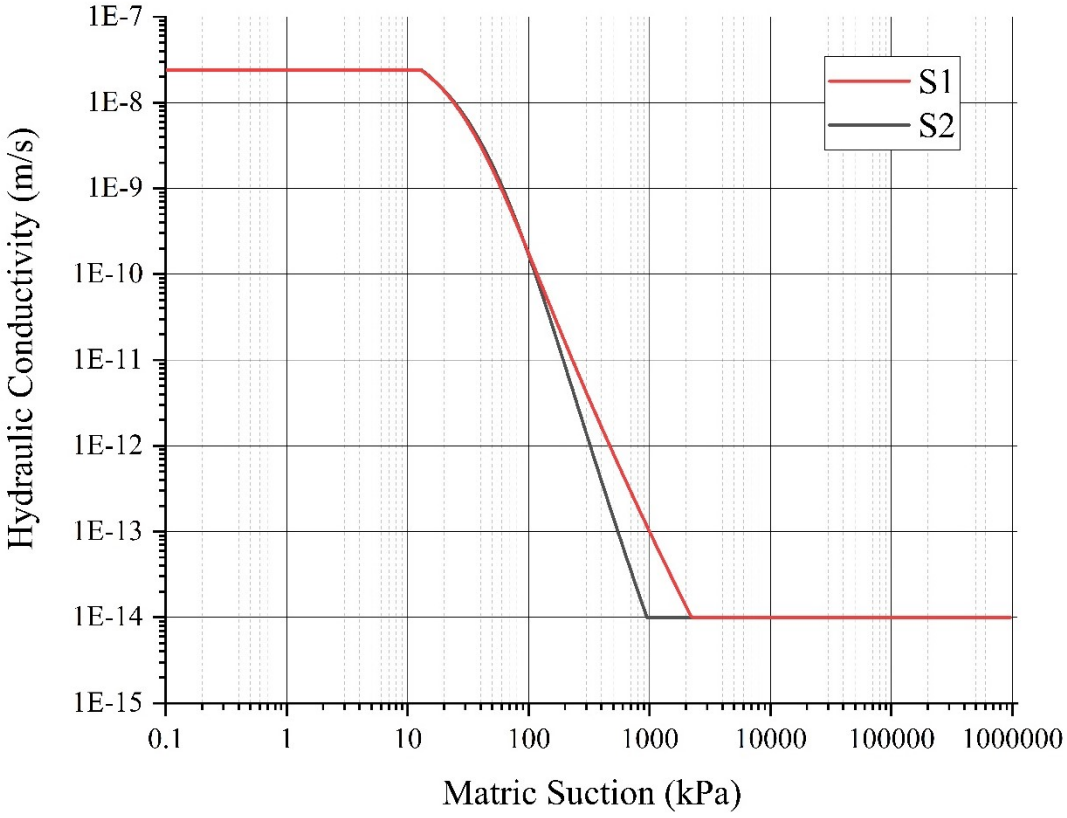

Figure 4.2.6 - Permeability Functions Using Fredlund, Huang, and Xing (1994) Estimation Method

CHAPTER 5. PRESENTATION AND DISCUSSION OF WATER BALANCE RESULTS

Three precipitation conditions were chosen to understand the variance in surface flux boundary conditions. Sensitivity analyses were conducted in SoilCover to quantify the effect of various soil parameters on the resulting water balance (i.e. initial saturation and k_{fsat}). Table 5.0.0.1 and Table 5.0.0.2 contain a summary of all water balance parameters for both 2017 and 2018 simulation periods. Water balance parameters for the extreme event analysis is provided in Table 5.0.0.3. The following sections provide a summary and discussion of the results.

A total of 308 mm of precipitation was applied to the average year model. For each baseline case, the net infiltration, runoff, and actual and potential evaporation was found. The ratio between the potential evaporation and the average annual precipitation was found to be 1.2 for 2018 for the baseline case (DHM). Using the climate classification provided within the GARD Guide (INAP 2009) shown in Figure 5.0.1, this results in a climate classification between semi-arid and arid, which is expected for the northern climate in the Yukon.

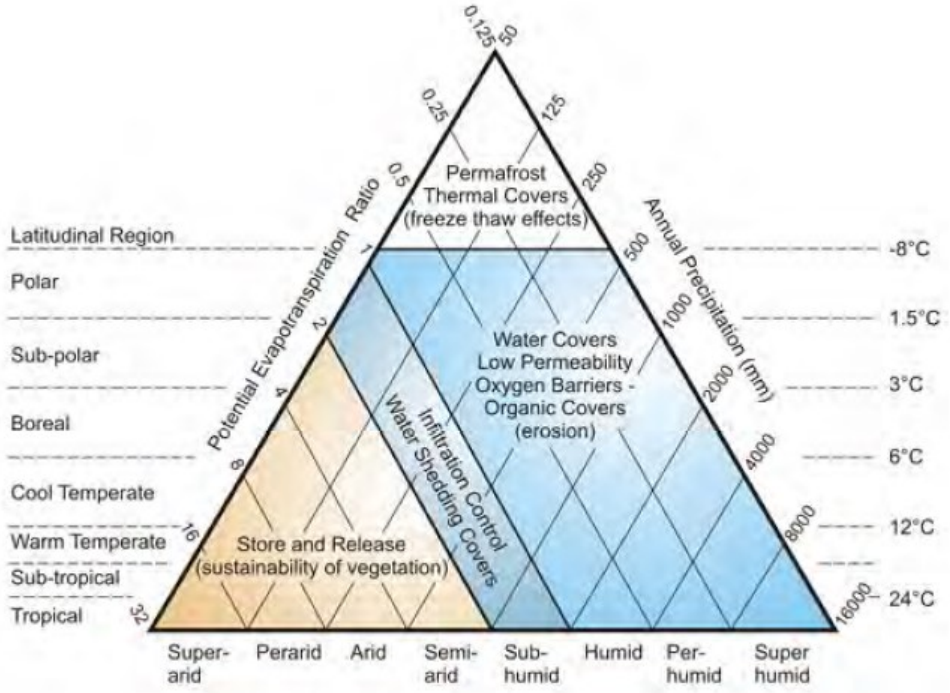

Figure 5.0.1 - Tri-Parameter Climate Plot for Cover Type Selection (INAP 2009)

Table 5.0.0.1 - Summary of Water Balance Parameters for 2018 Simulation of an Average Year

Scenario	K_{sat}	Initial Matric Suction	Precipitation	Final Infiltration		Runoff		Actual Evaporation	Potential Evaporation	PE/AE
	(cm/s)	(kPa)	(mm)	(mm)	(%)	(mm)	(%)	(mm)	(mm)	
DHM	$2.40x10^{-6}$	42	308	45.2	11.8	43.1	14.0	219.9	356.1	1.6
		20		42.6	11.1	44.9	14.6	220.6	356.1	1.6
		5		42.3	11.1	45.2	14.7	220.7	356.1	1.6
GTP6	$6.80x10^{-7}$	42		16.7	4.4	105.2	34.1	186.3	355.9	1.9
		20		11.0	2.9	108.8	35.3	188.4	355.9	1.9
		5		7.9	2.1	110.9	36.0	189.4	355.9	1.9
KSAT1	$5.00x10^{-6}$	42		67.0	17.5	7.1	2.3	234.1	356.1	1.5
		20		66.2	17.3	7.7	2.5	234.3	356.1	1.5
		5		66.3	17.3	7.6	2.5	234.3	356.1	1.5
KSAT2	$5.00x10^{-5}$	42		38.4	10.0	1.0	0.3	268.8	355.9	1.3
		20		37.6	9.8	0.8	0.3	269.7	355.9	1.3
		5		38.4	10.0	1.0	0.3	268.8	355.9	1.3

Table 5.0.0.2 - Summary of Water Balance Parameters for 2017 Simulation of a Wet Year

Scenario	K_{sat}	Initial Matric Suction	Precipitation	Final Infiltration		Runoff		Actual Evaporation	Potential Evaporation	PE/AE
	(cm/s)	(kPa)	(mm)	(mm)	(%)	(mm)	(%)	(mm)	(mm)	
DHM	$2.40x10^{-6}$	42	379	59.2	15.5	48.5	12.8	271.2	371.8	1.4
		20		57.7	15.1	49.6	13.1	271.5	371.8	1.4
		5		57.2	15.0	49.8	13.2	271.9	371.8	1.4
GTP6	$6.80x10^{-7}$	42		26.0	6.8	116.6	30.8	236.3	371.9	1.6
		20		19.9	5.2	121.7	32.1	237.2	371.9	1.6
		5		17.2	4.5	123.9	32.7	237.8	371.9	1.6
KSAT1	$5.00x10^{-6}$	42		77.0	20.1	13.6	3.6	288.3	371.7	1.3
		20		76.6	20.0	13.8	3.6	288.5	371.7	1.3
		5		76.5	20.0	13.7	3.6	288.6	371.7	1.3
KSAT2	$5.00x10^{-5}$	42		59.3	15.5	48.4	12.8	271.2	371.9	1.4
		20		52.0	13.6	0.1	0.0	326.7	371.6	1.1
		5		52.0	13.6	0.1	0.0	326.7	371.6	1.1

Table 5.0.0.3 -Summary of Water Balance Parameters for the Extreme Event Simulation

Scenario	K_{sat}	Initial Matric Suction	Precipitation	Final Infiltration		Runoff		Actual Evaporation	Potential Evaporation	PE/AE
	(cm/s)	(kPa)	(mm)	(mm)	(%)	(mm)	(%)	(mm)	(mm)	
DHM	$2.40x10^{-6}$	42	28.8	13.6	47.3	12.3	42.6	2.9	2.9	1.0
		20		13.6	47.1	12.3	42.8	2.9	2.9	1.0
		5		13.6	47.1	12.3	42.8	2.9	2.9	1.0
GTP6	$6.80x10^{-7}$	42		7.1	24.6	18.8	65.4	2.9	2.9	1.0
		20		7.1	24.5	18.9	65.5	2.9	2.9	1.0
		5		6.8	23.6	19.1	66.4	2.9	2.9	1.0
KSAT1	$5.00x10^{-6}$	42		19.6	68.1	6.3	21.8	2.9	2.9	1.0
		20		19.6	68.0	6.3	21.9	2.9	2.9	1.0
		5		19.6	68.1	6.3	21.8	2.9	2.9	1.0
KSAT2	$5.00x10^{-5}$	42		13.4	46.5	12.5	43.4	2.91	2.93	1.0
		20		25.9	89.9	0.0	0.0	2.91	2.91	1.0
		5		25.9	89.9	0.0	0.0	2.91	2.91	1.0

5.1. NET INFILTRATION

Results of net infiltration for baseline scenarios (DHM) and sensitivity analyses are presented in this section. Both saturated hydraulic conductivity and initial matric suction were used as sensitivity parameters. Results computed for 2017 and 2018 yearly analyses as well as the extreme event are presented as total values and time series trends.

2018 – Average Year

Results of cumulative net infiltration for the 2018 water balance simulations are contained in Figure 5.1.1. Total infiltration ranges from 2.1% to 17.3%, found with cases GTP6 and KSAT1 respectfully (i.e., 6.8×10^{-7} cm/s and 5×10^{-6} cm/s). Increasing the hydraulic conductivity by one-quarter of magnitude between DHM and KSAT1 (i.e., from 2.4×10^{-6} cm/s to 5×10^{-6} cm/s) showed a 7% increase in net infiltration, from an average of 11.4 mm to 17.3 mm. As expected, the amount of total infiltration decreased with decreasing saturated hydraulic conductivity. Generally, as the saturated hydraulic conductivity increased, the total amount of infiltration increased with higher infiltration capacity. KSAT2 was the scenario with the highest saturated hydraulic conductivity that was tested. It was expected that infiltration would increase compared with the baseline case DHM, but final values of infiltration were computed to be equal. It is thought that the increase in saturated hydraulic conductivity allowed for additional evaporation from the soil matrix, which reduces the amount of infiltration.

A time series of each simulation is provided in Figure 5.1.3. It can be shown that the largest infiltration event happens within the first 15 days, where snowmelt was applied to the system to account for the freshet season. All infiltration events are shown to happen in direct response to the applied rainfall intensity, where the magnitude of each infiltration event looks proportional to the applied rainfall. The saturated hydraulic conductivity clearly affects the amount of final infiltration observed. Further investigations on an hourly timescale should be used to quantify the soils response to infiltration events to understand if there is an hourly lag between the applied precipitation and the infiltration itself.

Final values of net infiltration in all cases show that there is little change when initial conditions are altered between 42 kPa and 5 kPa matric suction. The largest change in net infiltration between cases was observed in GTP6 simulations. Decreasing the matric suction from 42 kPa to 5 kPa resulted in a decrease of 8.8 mm, which accounts for 2.8% of the total annual precipitation.

2017 – Wet Year

Infiltration patterns found during the wet year simulation are similar to those found for average year simulations in 2018. Values of year-end infiltration are summarized in Figure 5.1.2. For the base case scenario (DHM), average final infiltration computed across three initial matric suction conditions was found to be 58 mm, which accounts for 15.3% of the total annual precipitation. This is expected to be reasonable for the material type and properties within northern arid climates. The wet year (2017) was found to produce 4% more infiltration that the average year (2018).

Values of saturated hydraulic conductivity that were tested ranged from $5x10^{-5}$ cm/s to $6.8x10^{-7}$ cm/s. When increasing the hydraulic conductivity of the waste rock by one quarter magnitude in relation to baseline (DHM), the computed infiltration increased to an average of 76.7 mm, which accounts for 20.2% of the total input precipitation. Increasing the saturated hydraulic conductivity by one order of magnitude saw a 7 mm reduction in predicted infiltration compared with the baseline (DHM) scenario. The lowest in-situ measurement of hydraulic conductivity (GTP6) resulted in a total annual infiltration of 5.5 mm which is only 1.45% of the total annual infiltration.

As expected, as the field saturated hydraulic conductivity decreased, less net infiltration occurred. In the case of KSAT2, it was expected that due to the increase in k_{fsat}, computed values of net infiltration would be larger than that computed for the baseline case (DHM). Results for KSAT2 simulations in 2018 computed final infiltration equal to that found in the baseline case.

A time series representation of infiltration for the wet year is shown in Figure 5.1.3. Patterns observed in the time series data show similar trends to that computed for the average year, where infiltration occurs in direct response to daily precipitation events. As seen in 2018, the largest infiltration event occurs during the freshet season when snowmelt is applied to the system.

Comparing the results computed for 2017 and 2018, similar values of infiltration were observed, where the total amounts of infiltration for DHM computations were found to be 50 mm and 45 mm respectively. No large difference in infiltration was observed.

Just as computed for 2018 water balance simulations, the matric suction did not have a significant effect on the predicted net infiltration cases of DHM and KSAT1. A visible effect of

matric suction was seen in GTP6 and KSAT2 simulations, where approximately 1% and 7% difference exist respectively between cases with an initial matric suction values of 42 kPa and 20 kPa. Time series of computed infiltration also show small differences due to initial suction conditions in GTP6 and KSAT2 cases.

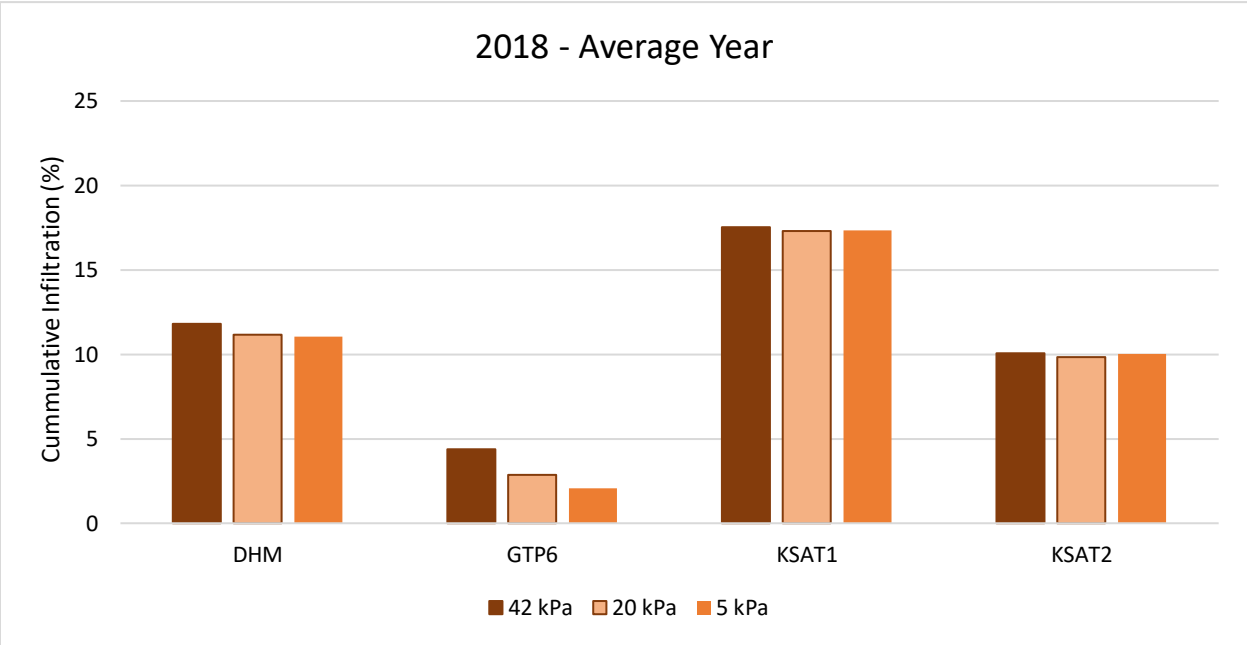

Figure 5.1.1 - Final Infiltration for 2018 Analyses

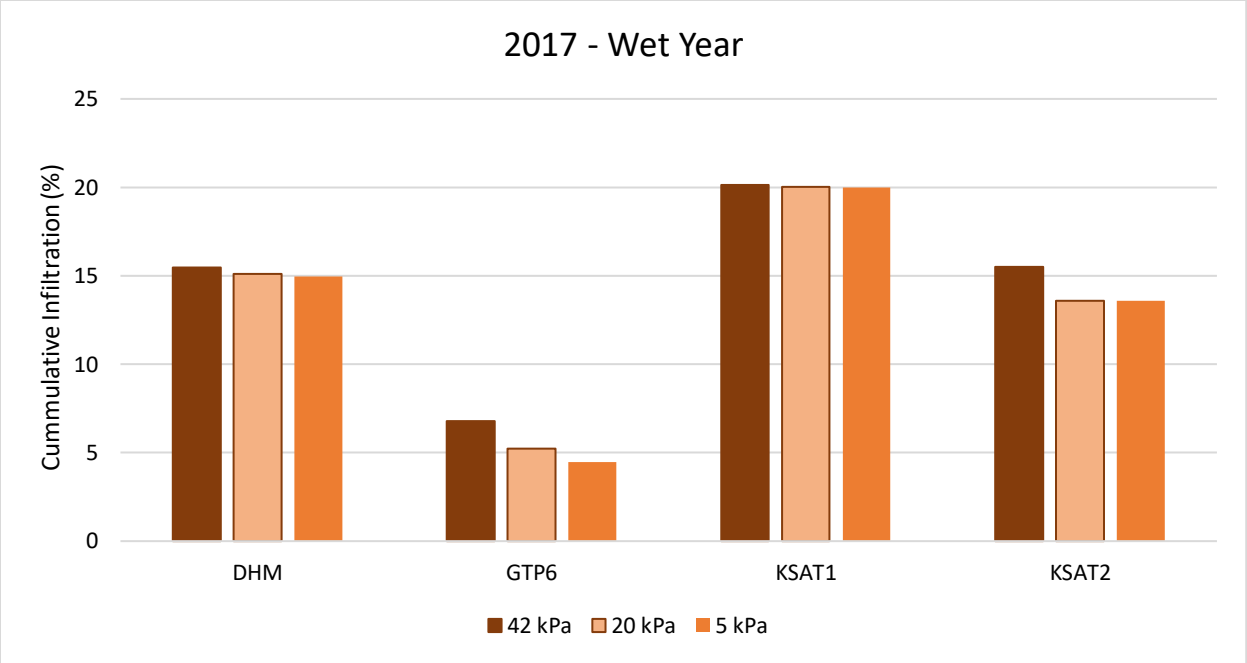

Figure 5.1.2 – Final Infiltration for 2017 Analyses

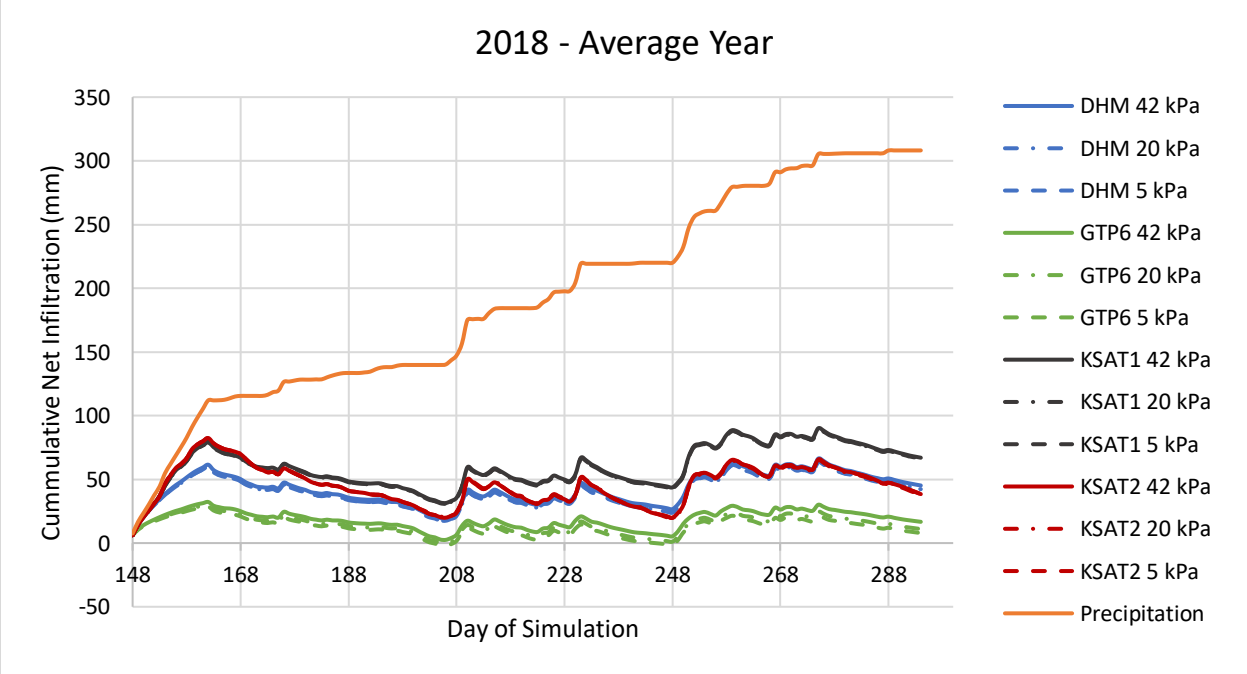

Figure 5.1.3 - Time Series Infiltration for 2018 Baseline Case

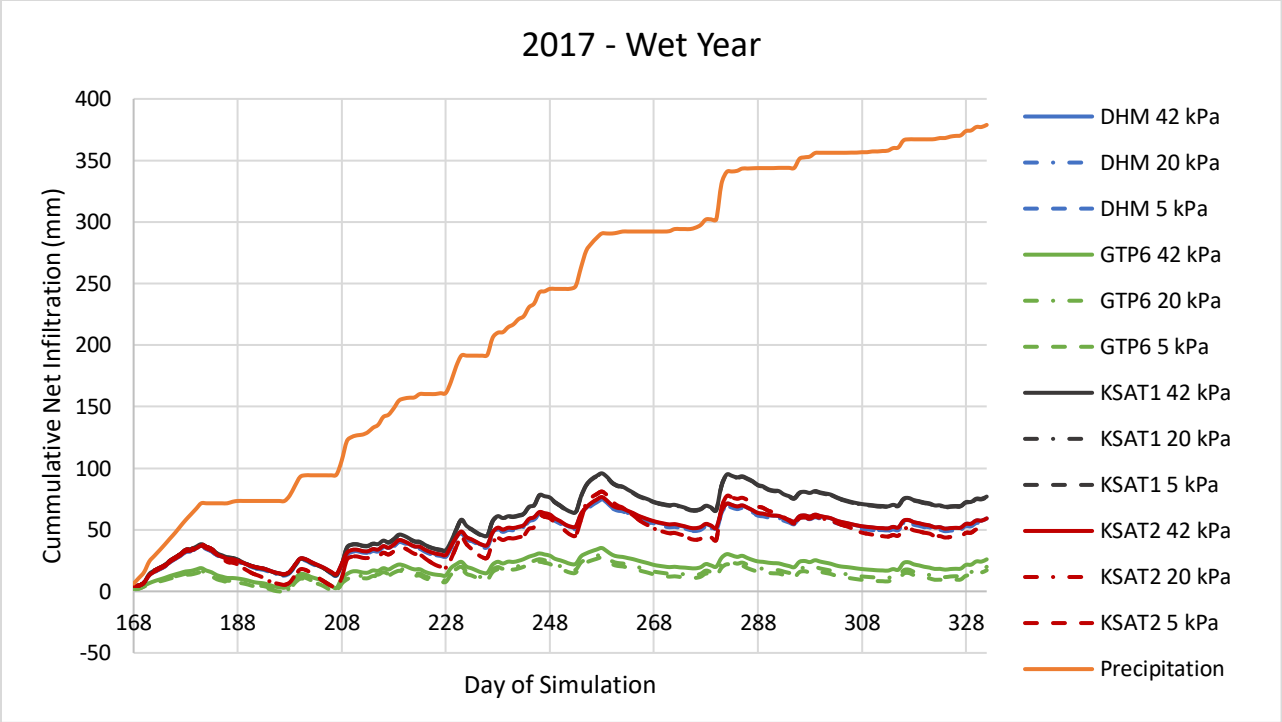

Figure 5.1.4 - Time Series Infiltration for 2017 Baseline Case

Extreme Event

Infiltration was quantified for the largest precipitation event identified within the year 2017. A total of 28.8 mm of rainfall fell over a 24-hour period.

Figure 5.1.5 contains a summary of the net percolation computed for the extreme event.

Net infiltration computed for the baseline case using a saturated hydraulic conductivity of 2.4x10-6 cm/s (DHM) was an average of 40% across all initial matric suction conditions. As the saturated hydraulic conductivity decreases, the resulting net infiltration decreases as expected. An average of 36.4% net infiltration was computed for the lowest saturated hydraulic conductivity (GTP6), which is reduced by approximately 3.6% compared with the baseline assessment. When increasing the saturated hydraulic conductivity by half an order of magnitude (i.e., from 2.4x10-6 cm/s to 5x10-6 cm/s), values of net infiltration computed increased by 21%, resulting in an overall net infiltration of 68%. Applying a further increase to the saturated hydraulic conductivity by one order of magnitude resulted in varying ratios of net infiltration for each initial matric suction condition. It is shown in

Figure 5.1.5 that an initial matric suction condition of 42 kPa results in 46.5% infiltration, which is comparable to the results found for the baseline case. Decreasing initial matric suction to 20 kPa resulted in net infiltration values of 89%, which is 1.9x values computed with a higher matric suction. This may be a result of a decreased infiltration capacity in a more desaturated state compared with that found for 20 kPa and 5 kPa.

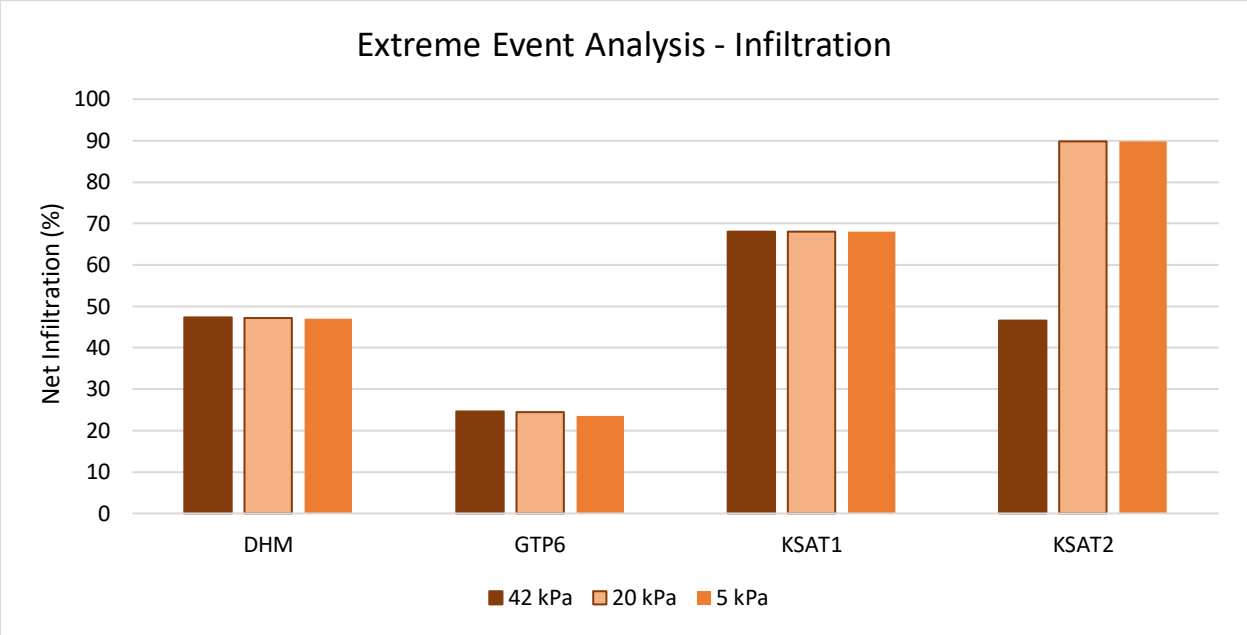

Figure 5.1.5 – Final Infiltration for Extreme Event Analysis

Understanding the extent of infiltration during extreme events is important, as climate change is increasing the frequency and severity of extreme rainfall events. Material properties used to represent surface waste rock materials do not reflect the increase in hydraulic conductivity that can exist within preferential flow paths. Preferential flow paths can facilitate further infiltration and provide a larger availability of water for geochemical reactions. Results of this extreme event show that infiltration of such events can range from 36% to 89% depending on the saturated hydraulic conductivity and initial matric suction condition. Depending on the distribution of such preferential flow paths, greater infiltration than what was computed may occur in-situ.

It has been shown that net infiltration during extreme events is sensitive to the saturated hydraulic conductivity of the system, and in some cases the initial matric suction condition. It is

important to note that the results from this extreme event analysis are conducted at a daily intensity. Conducting similar analyses at an hourly timescale may yield more accurate proportions of the fate of water within the soil-atmosphere system.

Results of average and wet year infiltration, as well as results presented above for the extreme event analysis show that a significant volume of infiltration can occur on the surface of the Main Dump at the Faro Mine Complex. When comparing the average year baseline infiltration compared with the extreme event, the computed net infiltration increased by approximately 30%. This is important to note as the frequency and magnitude of these infiltration events are predicted to increase with climate change over time. This trend towards more extreme events can increase the infiltration beyond the 30% computed during this study. In-situ measurements of water quality from the Main Dump have shown that the volume of infiltration events contribute to the recharge of contaminants into the environment (Bao et al. 2020b, Bao et al. 2022). Freshet seasons and extreme rainfall events can drive contaminant flushing through the Main Dump during summer months which affects the overall concentrations of the contaminants of concern seasonally (Bao et al. 2020b, Bao et al. 2022).

5.1.1. VALIDATION OF INFILTRATION

Bao et al. (2020b) measured volumetric water content at varying depths (1.0, 2.0, and 3.0 ,) within borehole UW17-BH2. Notable changes in volumetric water content were observed during periods where greater than 10 mm of rainfall was measured on site. This is reflected in the time series plots of infiltration computed for both 2017 and 2018 simulation periods contained in Figure 5.1.3 and Figure 5.1.4, where only larger rainfall events generated notable infiltration.

Calculated values of the local meteoric water line (LMWL) determined by Bao et al. (2020b) were plotted against measured values of stable water isotopes. This indicated that there is rainfall-dominated seepage into North Fork Rose Creek, which flows near the toe of the Main Dump. It is thought that infiltration as a result of rainfall contributes to contaminant flow through the waste rock storage facility over time.

5.2. RUNOFF

One of the most important water balance parameters used for the design, operation, and closure of the waste rock storage facility is runoff. Most water management plans, and long-term operations such as water treatment involve quantifying and managing water that has been in contact with PAG material. Runoff is also one of the most important water balance parameters when calculating net infiltration.

Generally, the amount of runoff generated in unsaturated soils is dictated by the infiltration capacity of the material. When rainfall intensity exceeds the hydraulic conductivity of the soil, rainfall in excess of the hydraulic conductivity is shed as runoff (Abdulnabi 2018). The following section summarizes the computed values of runoff occurring for average and wet years, as well as during an extreme event.

2018 – Average Year

Simulations were run for an average precipitation year, where baseline values of runoff found for DHM simulations was found to be 43 mm, which accounts for 14.3% of the total annual precipitation. Table 5.0.0.1 contains the computed values of runoff for all 2018 scenarios. The maximum and minimum values of runoff were computed to be 0.8 mm and 111 mm, which accounts for 0.3% and 36% respectively. In general, it was observed that when the material was assigned lower values of hydraulic conductivity, the resulting runoff increased as expected. Virtually no runoff was predicted for simulations using a saturated hydraulic conductivity of $5x10^{-5}$ cm/s. It is shown that the saturated hydraulic conductivity has a large effect on the resulting volume of runoff generated over time.

2017 – Wet Year

During a wet year, runoff was predicted to account for 13% of the total annual precipitation during the baseline analysis case (DHM). As expected, lower values of saturated hydraulic conductivity produced larger volumes of runoff due to a reduction in the soil's infiltration capacity. Computations completed for GTP6 predicted an average of 120.7 mm of runoff, which amounts to 31.8% of the total annual precipitation. Decreasing the saturated hydraulic conductivity by approximately half and order of magnitude (i.e., from $2.4x10^{-6}$ cm/s to $6.8x10^{-7}$ cm/s) increased runoff generation by 20%, which is a significant volume when considering the

surface area of the entire facility. Increasing the saturated hydraulic conductivity decreased the amount of runoff as expected due to the increase in infiltration capacity. Runoff generation was predicted to total 13.7 mm for KSAT1 which is only 3.6% of annual precipitation.

Generally, there was no significant effect on runoff computations due to changes in initial matric suction conditions. As observed during infiltration analyses, matric suction was seen to affect results of GTP6 and KSAT2 the most. In the case of GTP6, as the initial matric suction condition reduced to 5 kPa, the predicted runoff increased by 7 mm, which is 6% of the average total runoff generated for GTP6 cases. KSAT2 observed the largest effect on the runoff prediction. When an initial condition of 42 kPa matric suction was used, runoff generation was estimated to be equal that of the baseline case (DHM) of 48 kPa. When matric suction was reduced to 20 kPa and 5 kPa, almost no runoff was computed. This indicates that the saturated hydraulic conductivity at a further unsaturated state is lower than the rainfall intensity applied, resulting in runoff. When the matric suction is dropped, the rainfall intensity becomes less than the saturated hydraulic conductivity and allows for further infiltration.

Time series of runoff generation is provided in Figure 5.2.1 and Figure 5.2.2 It is observed that runoff events are generated in direct response to increases in rainfall intensity over the simulation period. The magnitude of each response decreases as the saturated hydraulic conductivity increased, which is expected.

When comparing the average and dry year analyses, it was shown that the baseline value of runoff in the average year was comparable to that of the wet year, where runoff was computed to be 11% and 13% respectively. Maximum values of runoff generated during 2018 and 2017 were 111 mm and 124 mm respectively, which were both computed for GTP6 assuming an initial value of matric suction of 5 kPa. Runoff predicted during each case is comparable to each yearly water balance. For annual precipitation total greater than that used in 2017, there may be larger differences in runoff generation due to increased number and intensity of predicted storm events.

Extreme Event

Runoff for an extreme event occuring in August of 2017 was quantified for each simulation scenario. Figure 5.2.3 contains a summary of runoff computed for each extreme event analysis. Total runoff values during the baseline scenario DHM (i.e., 2.4×10^{-6} cm/s) were computed to be

42% of the total precipitation event, which is a significant portion of the water balance. No significant effect of initial matric suction was observed on the runoff values for the baseline case. When decreasing the saturated hydraulic conductivity by half an order of magnitude (i.e., from $2.4x10^{-6}$ cm/s to 6.8x10-7 cm/s) resulted in an increase in runoff. 65.5% of the total precipitation event is shed as runoff during scenartio GTP6, which is a significant portion of the water balance. Increasing the saturated hydraulic conductivity by a quarter magntidue (i.e. from 2.4x10-6 cm/s to 5x10-6 cm/s), resulted in a reduction in runoff by approximately 50% which was expected. Increasing the saturated hydraulic conductivity can result in an increased infiltration capacity which allows for greater volumes of infiltration and subsequent reduction in runoff. The reduction in runoff by 50% shows that the system is sensitive to the saturated hydraulic conductivity.

Different volumes of runoff were predicted for the KSAT2 case, where the initial matric suction condition did affect the result. The saturated hydraulic conductivity for KSAT2 was increased by one order of magnitude (i.e., from 2.4x10-6 cm/s to 5x10-5 cm/s). When an initial matric suction conditon of 42 kPa was used, a value of runoff was predicted. For initial conditions of 20 kPa and 5 kPa, there was no runoff predicted. This indicates that the saturated hydraulic conductivity associated with the infiltration capcity of the material at those conditions is larger than the rainfall intensity applied to the system, assuming a unit gradient applied to the system. These results indicate that the in-situ conditons and the variety in surface properties over the Main Dump can allow for a range of runoff conditions. Runoff quantities along the surface can range

from 0 mm to 19 mm, which account for 0% and 65.5% of the total precipitation event respectively.

Quantifying the total runoff during these events is critical as it directly impacts the final value of net infiltration, which subsequently drives geochemical reacitons within the Main Dump over time. Comparing the total runoff in extreme events to that found during the entire year, the

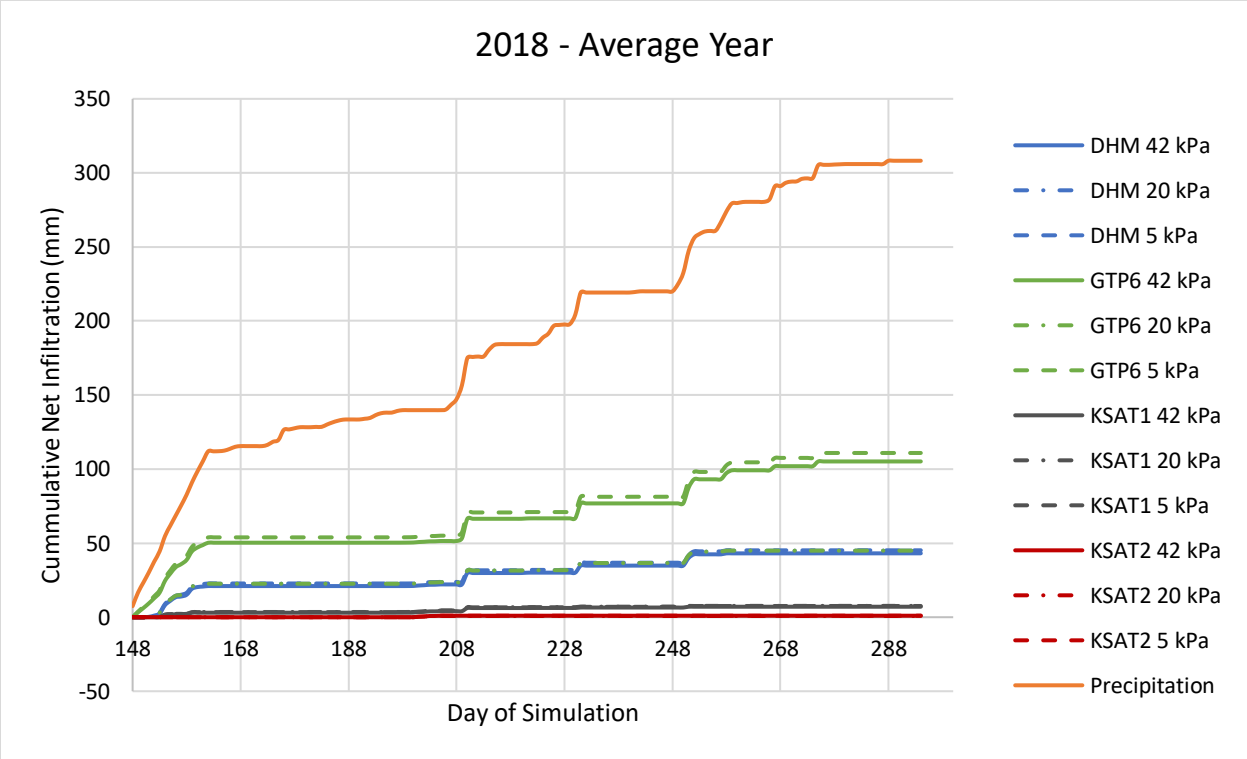

Figure 5.2.1 - Time Series Runoff for 2018 Simulations

proportion of water shed as runoff is increased by almost 30%, which is similar to that found for the magnitude of infiltration. As mentioned in Section 5.1, the increase in frequency and severtiy of these extreme events have an effect on the resulting water quality produced by the waste rock storage facility over time. Climate change may result in increased runoff, which in a one-dimensional water balance system is assumed to be prevented from infiltration.

If the surface is sufficiently sloped, the runoff may be prevented from infiltrating into the waste rock downslope over time or could potentially result in infiltration downslope of the origin point (Mu et al. 2015, Zhao et al. 2015, Morbidelli et al. 2018). For all model scenarios (wet and average years, as well as extreme events), more detailed analysis and in-situ measurements

should be made to capture these features and measure their in-situ quantities to validate the computations performed in this study. The fate of runoff should also be traced to understand if runoff shed during rainfall and as a result of the freshet season infiltrates further downslope or on side slopes which contribute to the persistence of geochemical reactions. A two-dimensional seepage analysis should be used to inform on the fate of runoff if a notable slope exists. Furthermore, an hourly model interval should be used to compute the water balance results for extreme events, as the infiltration capacity of the soil has been shown to depend highly on the time interval used to compute runoff (Abdulnabi 2018).

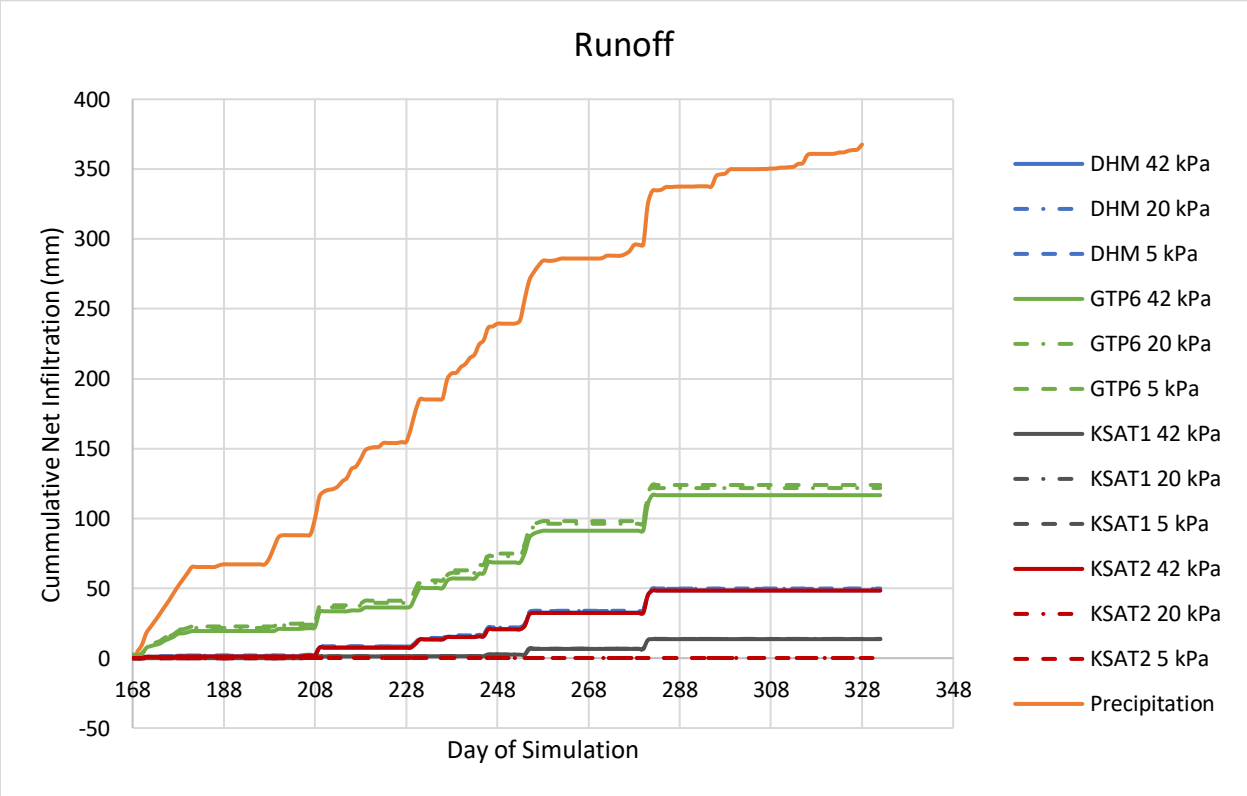

Figure 5.2.2 - Time Series Runoff for 2017 Simulations

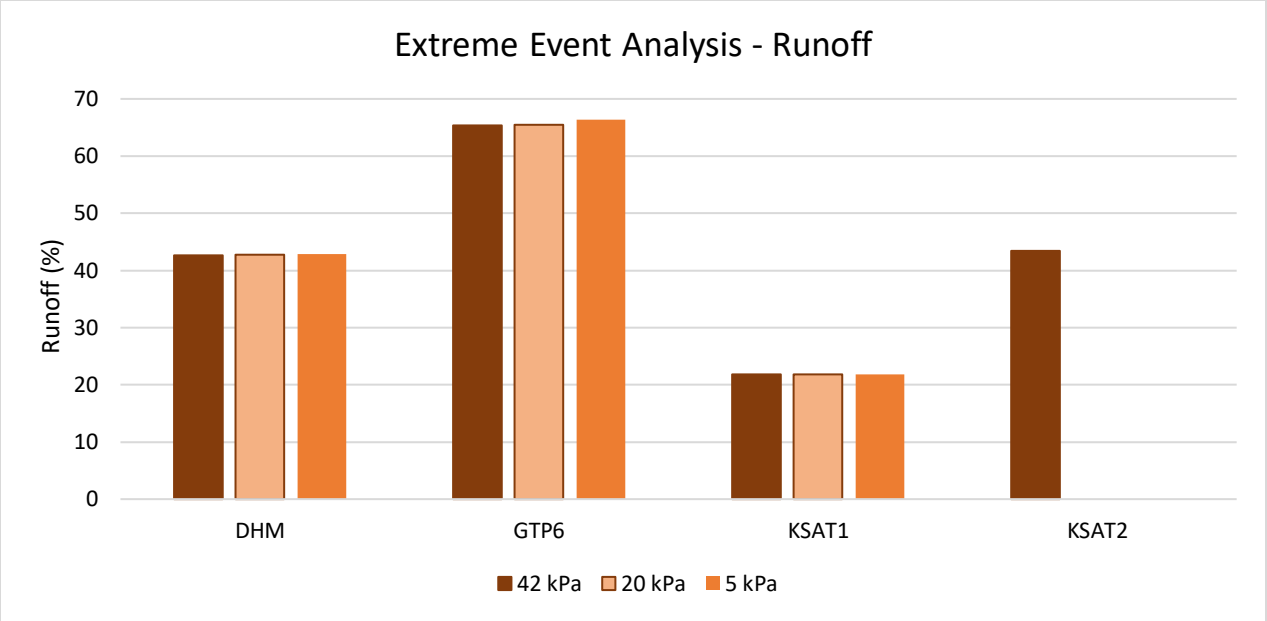

Figure 5.2.3 -Summary of Runoff for Extreme Event Analysis

5.2.1. Validation of Runoff

Looking at photographs taken during periods of runoff on the surface by Bao et al. (2020b), it is shown that runoff is generated, and was observed to pond within local depressions and/or participate in surface flows. Figure 3.1.4 in Section 3.1.1 of this thesis shows a preferential flow path that exhibited surface flow towards the depression in the surface of the waste rock dump. No measurements of surface runoff volumes or flow rates have been measured; therefore, evidence of previous surface runoff is used to validate the presence of runoff in each numerical simulation.

5.3. Evaporation

2018

Actual and potential evaporation were computed for the average year analysis conducted during 2018. Figure 5.3.1 contains a time series plot of actual evaporation for all simulations completed for the 2018 year, where the trend seems fairly linear over the simulation period. Average baseline values of actual evaporation for the DHM case was found to be 220.6 mm across all

initial suction conditions, which accounts for approximately 71.6% of the total annual precipitation. Actual evaporation varied between sensitivity cases, where the lowest computed value was 189 mm during GTP6 which accounts for 61% of the total annual precipitation. The highest value of actual evaporation was found using the highest saturated hydraulic conductivity of $5x10^{-5}$ cm/s (KSAT2) which was found to be 269 mm, accounting for 87.3% of the total precipitation. It is thought that by reducing the saturated hydraulic conductivity, the soil matrix makes water more available for evaporation, which increases the amount of actual evaporation from the soil matrix. Increasing the saturated hydraulic conductivity by half an order of magnitude (i.e., from $2.4x10^{-6}$ cm/s to $5x10^{-6}$ cm/s), the actual evaporation increased by 14 mm, which is a 4.5% of the annual applied precipitation.

Potential evaporation was calculated and was found to be consistent amongst all simulations. Values of potential evaporation were computed to be 356 mm, which exceeds the baseline actual evaporation by 56 mm. The ratio of potential evaporation to actual evaporation was calculated for all simulation cases. Values ranged between 1.3 and 1.9 from KSAT2 and GTP6 respectively. This shows that as the saturated hydraulic conductivity increases, the computed amounts of actual evaporation become closer to the computed potential evaporation which is expected.

Results of computed actual evaporation show that the overall climate is arid, where the actual evaporation can reach 87% of the total annual precipitation. This is expected for arid northern climates at higher elevations. It can be shown that the system is sensitive to changes in saturated hydraulic conductivity, where total volumes of actual evaporation can range by 20%. No significant changes in actual evaporation were observed when altering the initial matric suction condition in each scenario. The heterogeneity observed over the surface will contribute a wide range of actual evaporation rates over time.

2017

Values of actual and potential evaporation were computed for the 2017 simulation period. Figure 5.3.2 contains the time series of actual evaporation for the wet year analysis. Average total actual evaporation (AE) for the baseline case (DHM) was computed to be 272 mm, which accounts for 71.6% of the total precipitation. Total annual potential evaporation (PE) was computed to be 372 mm which amounts to 98% of the total input precipitation. The ratio of potential evaporation to actual evaporation for all 2017 simulations ranged from 1.1 to 1.6, corresponding to KSAT2 and

GTP6 simulations respectively. The ratio of PE to AE was expected for the location of the waste rock storage facility. Northern climates tend to have arid climates where the PE is equal to or exceeds the actual evaporation potential. Time series of actual evaporation for 2017 simulation period is provided in Figure 5.3.2. Actual evaporation rates are fairly constant over the time frame of the simulation period.

Comparing both the evaporation rates between the average year and wet year, 2018 and 2017 respectively), similar trends were found in each simulation period. Baseline actual evaporation found during DHM scenarios were both computed to be 71.6% of the annual precipitation, which resulted in 220.6 and 272 mm of evaporation for 2018 and 2017 respectively. This was expected as the wet year applies a larger amount of precipitation to the system which was shown to evaporate at the same ratio as the average year. Maximum and minimum values correspond to the same relative amount for each input precipitation, where both 2018 and 2017 showed a range of actual evaporation from approximately 60% - 87%. When the saturated hydraulic conductivity increased, the relative amount of total annual precipitation resulting in evaporation increased in both simulation periods. Altering initial matric suction conditions in both years resulted in no notable change in actual evaporation. The saturated hydraulic conductivity was observed to be the most important soil parameter that affects actual evaporation within the system.

It was observed that the saturated hydraulic conductivity had a significant effect on the water balance. Meteorological parameters also have an effect on the overall water balance of a soil-atmosphere model. Net radiation is one of the most important meteorological parameters to compute actual evaporation for a soil system.

Results of computed actual evaporation show that actual evaporation is controlling the net percolation compared to runoff. Over 70% of the precipitation within the soil-atmosphere system is being lost to evaporation, compared with a maximum of approximately 30% lost to runoff. In detailed analyses, it will be important to carefully characterize meteorological and physical properties of the soil-atmosphere system (i.e., net radiation and saturated hydraulic conductivity) to properly estimate the actual evaporation from the surface of the Main Dump.

Extreme Event

Evaporation for an extreme event identified in August of 2017 was computed and is summarized in Table 5.0.0.3. As expected, for all simulation cases, the actual evaporation rate was essentially equal to the potential evaporation rate, where there was little variance between alterations made of the saturated hydraulic conductivity as well as the initial matric suction condition. This was expected, as the increase in the degree of saturation associated with large rainfall events increases the availability of water within the soil matrix. Figure 2.3.2 in Section 2.3.3 of this thesis visualizes the concept of water availability with the soil matrix. This resulted in larger actual evaporation rates computed for each extreme event scenario.

Quantities of actual and potential evaporation for extreme events resulted in almost 3 mm of the total 28.8 precipitation event, which accounts for 10% of the extreme event. When comparing this to the yearly totals, the total evaporation is significantly lower in evaporation, by approximately 62% when comparing against the baseline average year scenario (DHM).

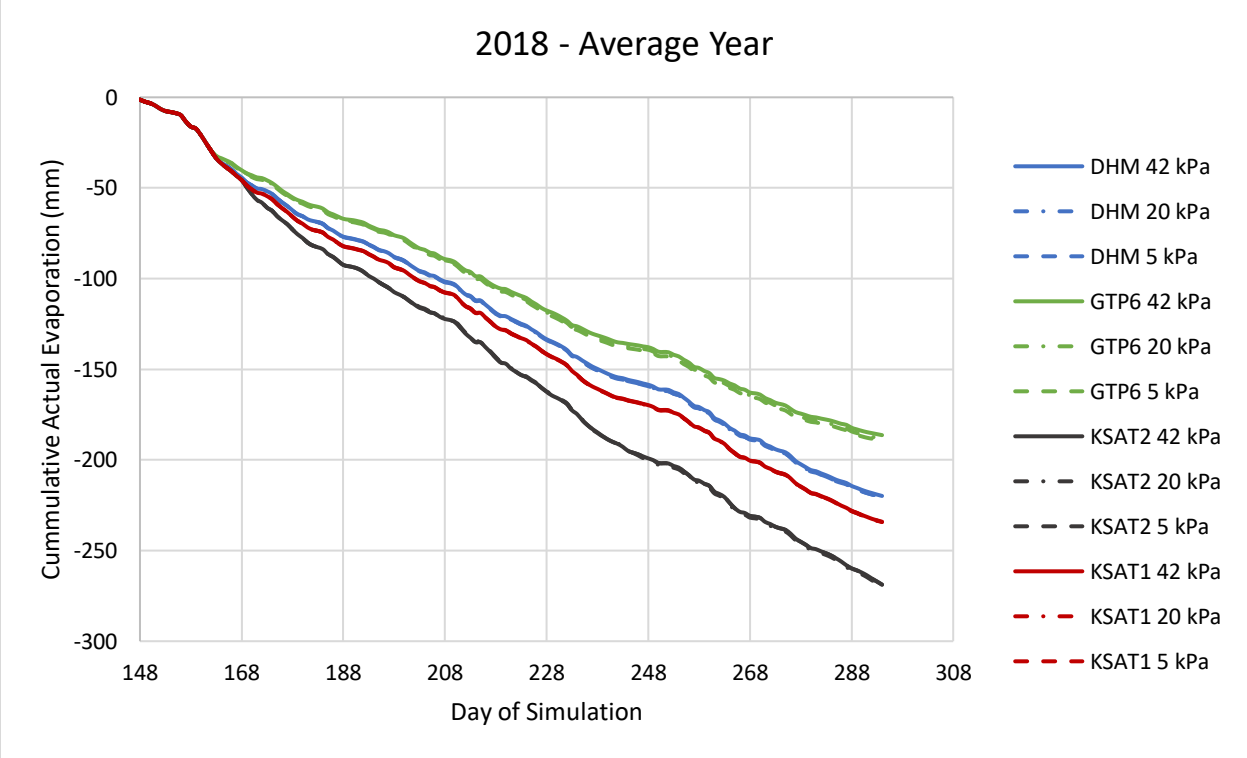

Figure 5.3.1 - Time Series Actual Evaporation for 2018 Simulation

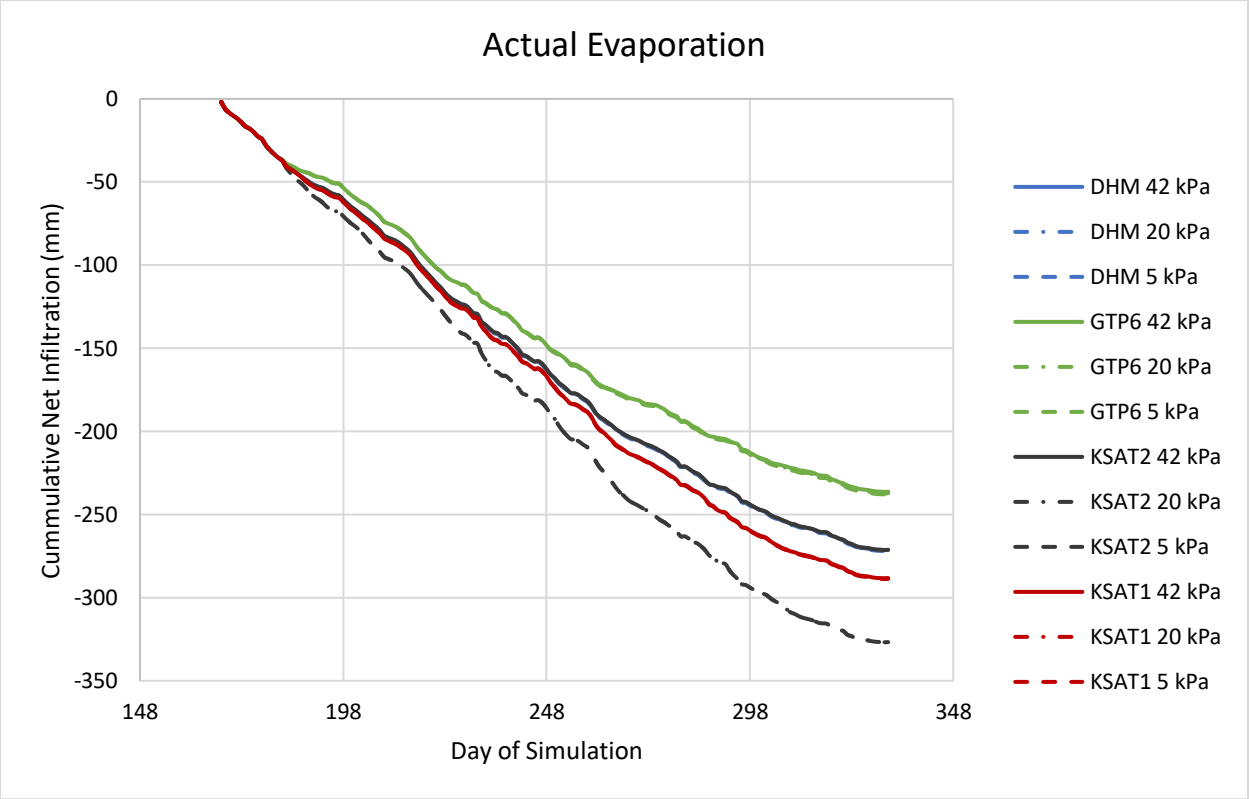

Figure 5.3.2 - Time Series Actual Evaporation for 2017 Simulation

5.3.1. VALIDATION OF EVAPORATION

Bao et al. (2020b) utilized $\delta^{18}O$ and $\delta^{2}H$ as tracers of water through test pits UW17-TP1 and UW17-TP2. The local evaporation line (LEL) was measured in-situ by recording 24-hour measurements of pan evaporation from the surface of the Main Dump between September 18 – 28, 2018. Results showed that in UW17-TP1, the measured potential pan evaporation had a strong correlation to the local evaporation line. This indicates that the evaporation rate from shallow waste rock materials was closely related to the potential evaporation rate when water is available. Computed values of actual evaporation from surface materials during baseline and increased saturated hydraulic conductivity (DHM and KSAT2) showed that over 70% of available water within the soil matrix results in evaporation. Actual evaporation from soil surfaces is a difficult parameter to estimate. Further work should be done to confirm the evaporation rate using methods such as eddy covariance.

5.4. SUCTION PROFILES

Profiles of matric suction were computed for both the 2017 and 2018 simulation periods at 5-day intervals. All matric suction profiles can be found in Appendix B.

Figure 5.4.1 and Figure 5.4.2 contain suction profiles computed for the DHM case using an initial matric suction value of 42 kPa for both 2018 and 2017 respectively. Matric suction for both 2017 and 2018 simulations were observed to be similar in behaviour. The first 20 days during freshet (Day 141 to 161) showed the top 1.0 m of the soil column progressively becomes saturated, where the matric suction falls below the air entry value of the material, which was measured to be 13 kPa. After the freshet period, the soil column starts to desaturate, where the largest changes take place in the top 0.5 m of the soil column. For the remainder of the simulation period, the top 0.5 m remains mostly desaturated. The least change over the entire simulation period occurs deeper within the soil column where for the majority of the simulation period the soil remains slightly desaturated around 20 kPa matric suction.

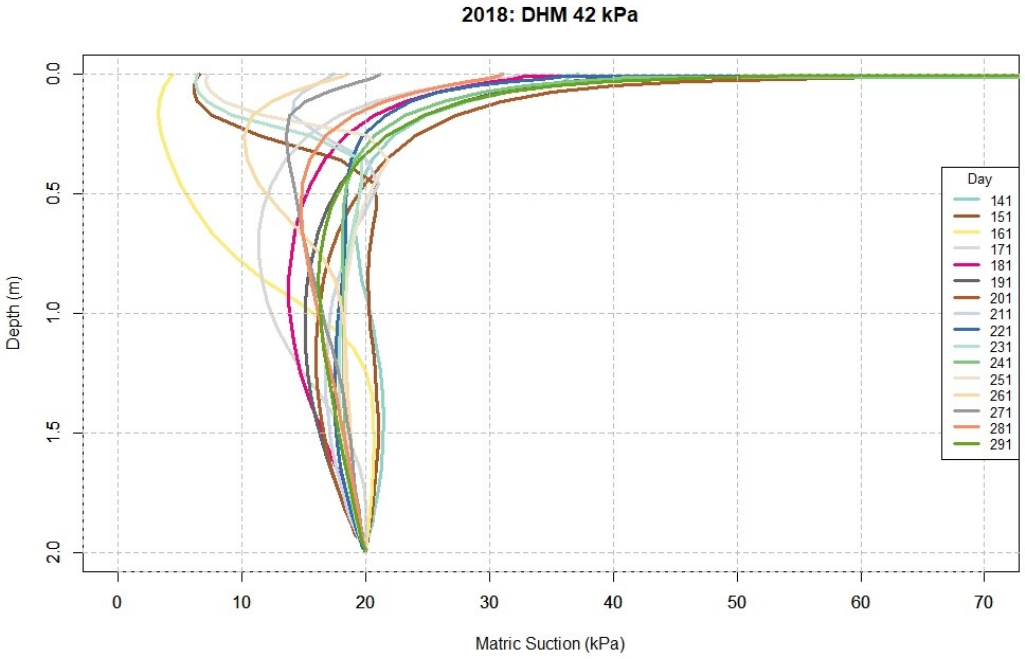

Figure 5.4.1 - Matric Suction Profile for DHM 42 kPa 2018 Simulation

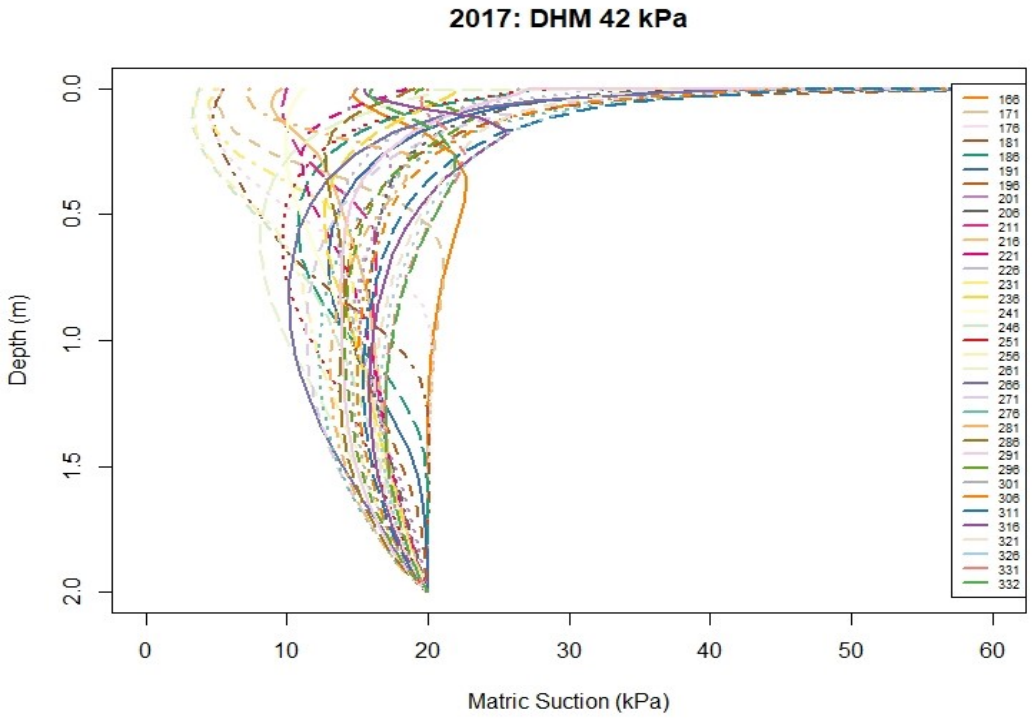

Figure 5.4.2 - Matric Suction Profile for DHM 42 kPa 2017 Simulation

2018 – Average Year

Looking at matric suction profiles for baseline simulations (DHM), profiles became progressively more saturated with depth when matric suction increased which is expected. For DHM 5 kPa scenario, the profile remains saturated until Day 201. The remainder of the year starts to desaturate the profile gradually to approximately 17 kPa.

Saturation profiles for GTP6, where the saturated hydraulic conductivity was decreased by half an order of magnitude (i.e., from 2.4x10-6 cm/s to 6.8x10-7 cm/s), generally saw the most change over the simulation period in the top 0.5 m. Assuming an initial matric suction of 42 kPa, the top 1.5 m of the soil column progressively became more saturated over time, decreasing by approximately 10 kPa over the simulation period. This bottom 1.5 m remained unsaturated. Increasing the initial matric suction to 20 kPa and 5 kPa had significant change to the bottom 1 m of the soil profile. Both profiles had insignificant change in saturation, and remained stable over the simulation period but remained close to saturation over time. Most significant changes

remained within the top 0.5 m of the soil profile. With a lower saturated hydraulic conductivity, it is expected that deep infiltration is not the primary transport and is supported by expected behaviours.

When increasing the saturated hydraulic conductivity (DHM to KSAT2), it was observed that the saturation profile remains fully unsaturated even during freshet. Changing initial conditions of matric suction had minimal effect over the simulation period. No significant change was seen in the bottom 1.5 meters of saturation profile.

All profiles for the average year show that the first 15 days result in the largest decrease in matric suction as a result of the freshet applied to the system.

2017 – Wet Year

Baseline simulations for the wet year using a saturated hydraulic conductivity of $2.4x10^{-6}$ cm/s showed increased saturation throughout the entire soil profile compared with the average year simulations, which is expected. The top 0.75 m of the soil profile experiences the largest changes in matric suction over time. Freshet season was shown to impact the soil column to a depth of approximately 1 m. After freshet, the soil column continues to progressively saturate to Day 181, and subsequently desaturate for the remainder of the simulation period. Decreasing the initial matric suction condition also resulted in increased saturation over time. Between a depth of 1.0 m and 1.5 m, the soil column becomes progressively saturated as the initial matric suction is decreased. The lowest value of matric suction achieved for the baseline is approximately 5 kPa, which is comparable to that found for the average year simulations.

Saturation profiles were also seen to be affected by the saturated hydraulic conductivity as expected. When decreasing the saturated hydraulic conductivity from $2.4x10^{-6}$ cm/s and $6.8x10^{-7}$ cm/s and applying a matric suction of 42 kPa, the saturation profile is comparable to the same one computed in 2018 simulations. Soil beneath 0.5 m depth within the computed column remains below the air entry value of the material, essentially maintaining desaturation. The bottom 1.5 m also progressively saturates over time, non-linearly through the soil column. Decreasing the initial matric suction to 20 kPa and 5 kPa had similar patterns to those found for equivalent 2018 simulations. Top 0.75 m experience the largest changes, and freshet season is shown to have a less severe impact on the water balance.

Increasing the saturated hydraulic conductivity from 2.4x10-6 cm/s to 5x10-5 cm/s (DHM and KSAT2) also changed the saturation profile. It was observed that the saturation profile remains fully unsaturated even during freshet, which is a similar trend found in the average year simulation. Changing initial conditions of matric suction had minimal effect over the simulation period. No significant change was seen in the bottom 1.5 meters of saturation profile.

Extreme Event

Figure 5.4.2 contains the suction profile for the extreme event, which occurred on Day 281 of the simulation period. It can be shown that the matric suction decreases to approximately 8 kPa, which compared to the AEV of the material, indicates that the material is saturated during this infiltration event. The overall infiltration event reaches a depth of approximately 0.25 m, where the soil column beneath this point remains unsaturated at a value of matric suction below 13 kPa.

5.4.1. VALIDATION OF SOIL PROFILES

Bao et al. (2020b) has conducted an extensive research program to determine the fate of water throughout the Main and Intermediate waste rock dumps. The program utilized stable isotopes of water ($\delta^{18}O$ and $\delta^{2}H$) to trace the source and fate of water. Pore water samples from boreholes UW17-BH1, UW17-BH2, and UW17-BH3, in addition to test pits UW17-TP1 and UW17-TP2 were collected. Samples were tested both in laboratory settings using centrifugation, and in-situ using SWSS sampling methods.

Water samples taken from depths of 0.5 and 1.0 m suggest that the source of the pore water at those depths is due to rainfall. Samples taken from deeper elevations within the waste rock pile (2.0, 3.0, and 4.0 m) were less influenced by rainfall, suggesting minimal infiltration reaches such elevations. Spatial variability in rainfall influence was found in pore water samples. Rainfall recharge was observed to be lower in UW17-TP2 than UW17-TP1. Bao et al. (2020b) suggests that increased fines content was found near UW17-TP2 than UW17-TP1 and observed increased runoff in the area of UW17-TP2 where samples were taken in September of 2019 for this research study. These findings and observations are consistent with results of infiltration analyses and are supported by matric suction profiles computed during water balance modelling.

Volumetric water content was monitored at varying depths (1.0, 2.0, and 3.0 m) within borehole UW17-BH2. Changes in volumetric water content due to rainfall events were measured to a depth of 2.0 m in borehole UW17-BH2, and to depths of 7 m in UW17-BH3. Matric suction profiles generated during this study show that the largest influence of infiltration was shown at a depth of 1.0 m which is shallower compared with in-situ measurements. The 2.0 m soil column used in the numerical model consisted of finer materials sampled at the top 25 cm of the waste rock dump. It is expected that the presence of preferential flow paths in-situ can more easily transport infiltration to deeper elevations within the waste rock pile, increasing the volumetric water content and decreasing the matric suction over time.

CHAPTER 6. SUMMARY, CONCLUSIONS, AND RECOMMENDATIONS

6.1. SUMMARY

A parametric study was conducted to quantify and qualify net infiltration through the surface of the Main Dump at Faro Mine. The effect of soil parameters such as the initial matric suction and saturated hydraulic conductivity was tested to understand variation in net percolation. The following objectives were used to achieve this goal:

1) Characterize physical properties of surface waste rock samples.
2) Characterize hydrology of the surface of the waste rock dump,
3) Assess the net percolation through the surface of the Main Dump.

To achieve the first objective, a field study was conducted to measure in-situ properties of waste rock materials that control unsaturated / saturated seepage within the soil-atmosphere interaction. Measurements of saturated hydraulic conductivity, matric suction, and density were taken in the Fall of 2019. Samples of waste rock were taken for additional laboratory analyses. Index testing was performed to understand the geotechnical performance of the surface materials. This included grain size distributions, specific gravity, and Atterberg limits. The overall nature of the surface materials were found such that the fine matrix materials dominated the flow of water when experiencing unsaturated flow. Soil-water characteristic curves were used to measure the volumetric water content of the soil in response to changes in matric suction.

The second objective was met by observing in-situ behaviour and analyzing site specific meteorological data. Evidence of runoff, evaporation, and preferential flow was observed on the surface of the Main Dump during field investigations. Furthermore, meteorological data was used to characterize the overall climate of the site and develop a reliable dataset to be used for further numerical modelling.

Lastly, an existing finite element soil – atmosphere model, SoilCover, was used to quantify and qualify net percolation for three meteorological scenarios: wet year, average year, and an extreme event. Physical and hydrological properties found for the surface materials were used to compute values of net percolation. Sensitivity analyses using both soil and meteorological parameters were conducted to provide a range of net percolation values. The effect of several water balance parameters on the net infiltration was also discussed.

6.2. CONCLUSIONS

In this study, several stages of analyses were used to quantify net percolation through the surface of the Main Dump. Four different values of saturated hydraulic conductivity were used to determine a range of net percolation values during a wet year, average year, and an extreme event. Each analysis was conducted assuming one of three initial matric suction values to understand the effect of the initial conditions on the overall water balance. Final values of net percolation were computed, along with values of runoff, actual evaporation, and potential evaporation. Specific conclusions found during this study are presented below:

1) Net Percolation:
    a. Baseline values were found to be 15% and 20% in 2017 and 2018 respectively,
    b. Range of values predicted for average and wet years fell between 2.1% and 20% for all sensitivity cases,
    c. Extreme event was computed to allow 47% of infiltration in the average case, and ranged between 25 % and 90% for all sensitivity cases

2) Runoff:
    a. Baseline values of runoff were found to be 11% and 13% in the average and wet year respectively,
    b. Minimum and maximum values were computed to be 0% and 36% throughout both average and wet years
    c. Extreme event resulted in 12% of runoff during the average case, and ranged from 0% to 66% throughout all sensitivity cases

3) Actual Evaporation
    a. Potential evaporation exceeded actual evaporation in all wet year and average year scenarios,
    b. Baseline AE for average and dry year scenarios was computed to be 71 %,
    c. Range in actual evaporation for average and dry years was found to be between 60% and 86%,

d. Extreme event resulted in 10% of actual evaporation for both baseline and all sensitivity cases tested. Potential evaporation was equal to actual evaporation for all cases,
e. Actual evaporation was found to be similar to findings of in-situ studies conducted by Bao et al. (2020). When water is available within the soil matrix, the evaporation rate is essentially equal to that of the potential evaporation.

4) Suction Profiles
    a. The largest changes happened within the top 0.5 meters of the soil column, where the deepest effect of infiltration was computed to occur at 1.0 m below the surface,
    b. Freshet season caused the largest changes in matric suction and generated the largest portion of infiltration. The remainder of the year progressively desaturates until the temperatures become less than 0°C.

Overall, it was shown that the system is extremely sensitive to the saturated hydraulic conductivity. For the majority of simulations, the initial value of matric suction was not a large factor; however, for simulations using a saturated hydraulic conductivity of $5x10^{-5}$ cm/s (KSAT2), it was shown that the initial value does have a notable impact on computed values of runoff, evaporation, and net infiltration.

Good agreement between numerical simulations and in-situ measurements of evaporation and infiltration were found when compared to Bao et al. (2020b). One main difference in results between the two studies lies within the depth of infiltration events. Bao et al. (2020b) has measured influence of infiltration to a depth of 2 – 3 meters within UW17-BH2. It is thought that the preferential flow paths that exist beneath the surface facilitate movement of infiltration at faster rates than capable within the numerical model. Preferential flow paths are known to have saturated hydraulic conductivities much greater than the surrounding soil matrix, which allows for movement of water deeper through the waste rock pile. Evaporation rates were seen to be within good agreement with the local evaporation line measured by Bao et al. (2020b).

Similar patterns in water balance parameters between the wet and average year were computed. When lowering the saturated hydraulic conductivity, runoff increased, and infiltration decreased,

and the opposite was observed when increasing the saturated hydraulic conductivity as expected. One case where these trends were not all observed was for simulations conducted using a saturated hydraulic conductivity of $5x10^{-5}$ cm/s. For average and wet year simulations, it was expected that the infiltration would increase due to an increase in the saturated hydraulic conductivity, but the opposite happened for both average and wet years.

6.3. RECOMMENDATIONS

There were several assumptions and limitations applied to the water balance simulations conducted in this study which occurred at varying stages during the analysis.

Results of water balance modelling show that in-situ measurements of saturated hydraulic conductivity have a large effect on the resulting net infiltration. It is known that there is spatial variability of fines content and soil structure on the surface of the Main Dump. Additional double-ring infiltrometer tests should be conducted at a larger number of locations across the surface of the Main Dump to build a more complete database of in-situ saturated hydraulic conductivity. These measurements should be compared with the results of the Guelph permeameter testing previously completed as part of this study.

In-situ waste rock structure is one of the most important defining factors of infiltration. In-situ measurements of soil-water characteristic curves should be completed to confirm laboratory derived measurements. This will also quantify the spatial variability in unsaturated seepage across the surface of the Main Dump.

An important factor when performing numerical analysis includes calibrating results to field measurements of various parameters such as runoff and evaporation. It is recommended that future work be done to directly measure runoff depths generated during storm events. Additionally, actual evaporation should be directly measured from the surface of the waste rock storage facility. Measuring actual evaporation has been a challenge for many years and it is one of the most difficult parts of the water balance to accurately determine. Many methods have been suggested such as Bowen's ratio and others. Eddy Covariance is to be a significant steppingstone in directly measuring actual evaporation. Measuring multiple rainfall events over the course of a

summer on top of a waste rock dump may lead to more accurate water balance estimations. Currently, an eddy covariance tower is operating on the surface of the Main Waste Rock Dump. To properly quantify actual evaporation, the eddy covariance tower needs to be deployed during multiple rainfall events occurring during summer months to capture evaporation rates when they are at their highest.

One of the limitations when applying SoilCover is the time interval used for assessing the water balance. Current model properties allow for water balance calculations at a daily time scale. It has been shown that an important factor in runoff generation is the rainfall intensity and the time scale of which it is calculated. It is recommended that hourly rainfall and meteorological data be cleaned and used for numerical modelling on an hourly timescale to quantify runoff with time.

Additional analyses should be completed to determine extreme events based on several return periods and durations. Decisions on which extreme events and values of such extreme events should be informed based on downscaled climate change predictions. Current database of precipitation data was not large enough to determine return periods of larger than 1 in 2 years; therefore, external datasets should be used to determine such rainfall intensities.

One of the largest challenges during this study was found to be the gaps in meteorological data over extended periods of time. Having a consistent data set with all necessary meteorological data is an important factor in achieving an accurate water balance estimation. It is understood that this is not an easy feat in practice but should be worked towards and prioritized going forward.

BIBLIOGRAPHY

Abdulnabi, A., Jubinville, S., & Wilson, G. W. 2016. A Case Study of Numerical Prediction of Rainfall Runoff for Soil Cover Systems. Proceedings of the 69th Canadian Geotechnical Conference, Vancouver, Canada. October 2 – 5 2016.

Abdulnabi, A. 2018. Prediction of Rainfall Runoff in Geoenvironmental Engineering Practice. Doctoral Dissertation, University of Alberta, Edmonton, Alberta.

Allbright, W.H., Gee, G.W., Wilson, G.V., and Fayer, M.J. 2002. Alternative Cover Assessment Project Phase I Report. Publication No. 41183, Desert Research Institute, Nevada, USA.

Allen, R.G., Pereira, L.S., Raes, D., Smith, M. 1998. Crop evapotranspiration – Guidelines for computing crop water requirements – FAO Irrigation and drainage paper 56.

ASTM D1556.Standard test method for density and unit weight of soil in place by sand-cone method.

ASTM D2216-19.Standard test methods for laboratory determination of water (moisture) content of soil or rock by mass.

ASTM D4318-17. Test methods for liquid limit, plastic limit, and plasticity index of soils.

ASTM D4914. Standard test methods for density of soil and rock in place by the sand replacement method in a test pit.

ASTM D6913-17. Standard test methods for particle size distribution (gradation) of soils using sieve analysis.

ASTM D7928-17. Standard test method for particle size distribution (gradation) of fine-grained soils using the sedimentation (hydrometer) analysis.

ASTM D854-14. Standard test method for specific gravity of soil solids by water pycnometer.

Assouline, S. 2013. Infiltration Into Soils: Conceptual Approaches and Solutions. Water Resources Research, **49**: 1755 – 1772.

Azam, S., Wilson, G., Herasymuik, G., Nichol, C., and Barbour, L. 2007. Hydrogeological behaviour of an unsaturated waste rock pile: A case study at the golden sunlight mine, Montana, USA. Bulletin of Engineering Geology and the Environment, **66**(3): 259-268, doi:10.1007/s10064-006-0077-7.

Bao, Z., Bain, J., Holland, S.P., Wilson, D., Mackenzie, P., Ptacek, C.J., Blowes, D.W. 2020a. Faro Waste Rock Project: Characterizing geochemical heterogeneity in sulfide – and carbonate – rich waste rock. Applied Geochemistry, **121**: 104691.

Bao, Z., Blowes, D.W., Ptacek, C.J., Bain, J., Holland, S.P., Wilson, D., Wilson, G.W., & MacKenzie, P. 2020b. Faro waste rock project: Characterizing variably saturated flow behavior through Full-Scale Waste-Rock dumps in the continental subarctic region of northern canada using field measurements and stable isotopes of water. Water Resources Research, **56**(3): 1-24. doi:10.1029/2019WR026374.

Bao, Z., Bain, J., Holland, S.P., Wilson, D., Ptacek, C.J., and Blowes, D.W. 2022. Hydrogeochemical Response of a Variably Saturated Sulphide – Bearing Mine Waste – Rock Pile to Precipitation: A Field Scale Study in the Discontinuous Permafrost Region of Northern Canada. Water Resources Research, **58**: e2021WR031082.

Barbour, S.L., and Fredlund, D.G. (1989). Mechanics of osmotic flow and volume change in clay soils. Canadian Geotechnical Journal, **26**: 551-562.

Barbour, S.L., Hendry, M.J., Carey, S.K. 2016. High-resolution profiling of the stable isotopes of water in unsaturated coal waste rock. Journal of Hydrology, **534**, 616 – 629.

Barsi, D. 2017. Spatial Variability of Particles in Waste Rock Piles. Master's Dissertation, University of Alberta, Edmonton, Alberta.

Bond, J. D. 2001. Quaternary geology and till geochemistry of the anvil district (parts of 105K/2, 3, 5, 6 and 7), central Yukon Territory (Bulletin 11 Edition), Exploration and Geological Services Division, Yukon, Indian and Northern Affairs Canada.

Brooks, R.H., and Corey, A.T. 1964. Hydraulic Properties of Porous Media, No. 3. Colorado State University, Fort Collins, Colorado.

Campbell, G.S. 1974. A Simple Method for Determining Unsaturated Conductivity from Moisture Retention Data. Soil Science, **117**(6), 311 – 314.

Carey, S.K., Barbour, S.L., and Hendry, M.J. 2005. Evaporation from a waste-rock surface, key lake, Saskatchewan. Canadian Geotechnical Journal, **42**: 1189-1199. doi:10.1139/T05-033.

Cash, A. 2014. Structural and hydrologic characterization of two historic waste rock piles. Master's dissertation, University of Alberta, Edmonton, AB.

Climate Atlas of Canada. (2019). BCCAQv2 Climate Data Model, version 2, accessed from: https://climateatlas.ca/data/city/243/annual_meantemp_2030_85/line.

Das, B.M., and Sivakugan, N. 2015. Fundamentals of Geotechnical Engineering, Fifth Edition. Cenage Learning, Boston, MA, USA.

Edlefsen, N.E., and Anderson, A.B.C. 1943. Thermodynamics of soil moisture. Hilgardia, **15**(2): 31 – 298.

Elrik, D.E, Reynolds, W.D., and Tan, K.A. 1989. Hydraulic Conductivity Measurements in the Unsaturated Zone Using Improved Well Analyses. Groundwater Monitoring and Remediation, **9**(3): 184 – 193.

Fayer, M.J. 2000. UNSAT-H Version 3.0: Unsaturated soil water and heat flow model, theory, user manual, and examples. Pacific Northwest Lab (PNNL), Richland, Washington, United States.

Flerchinger, G.N., and Saxton, K.E. 1989. Simultaneous Heat and Water Model of Freezing Snow-Residue-Soil System I. Theory and Development. American Society of Agricultural Engineers, **32**(2): 565 – 571.

Flerchinger, G.N., Baker, J.M., and Spaans, E.J.A. 1996. A Test of the Radiative Energy Balance of the SHAW Model for Snowcover. Hydrological Processes, **10**: 1359 – 1367.

Fredlund, D.G., and Xing, A. (1994). Equations for the soil-water characteristic curve. Canadian Geotechnical Journal, **4**(31): 521-532.

Fredlund, D.G., Xing, A., and Huang, Shangyan. 1994. Predicting the permeability function for unsaturated soils using the soil-water characteristic curve . Canadian Geotechnical Journal, **4**(31): 533-546.

Fedlund, D.G., and Gitirana, G. Jr. 2005. Unsaturated Soil Mechanics as a Series of Partial Differential Equations. Proceedings of the International Conference on Problematic Soils, May 25 – 27, Eastern Mediterranean University, Famagusta, N. Cyprus.

Fredlund, D. G., Rahardjo, H., and Fredlund, M. D. 2012. Unsaturated soil mechanics in engineering practice. John Wiley & Sons, Hoboken, New Jersey.

Freeze, A. R. 1969. The mechanism of natural ground-water recharge and discharge 1. one-dimensional, vertical, unsteady, unsaturated flow above a recharging or discharging ground-water flow system. Water Resources Research, **5**(1): 153-171.

Freeze, A.R. and Cherry, J.A. 1979. Groundwater, Prentice-Hall Inc, Englewood Cliffs, New Jersey.

Geo-Analysis 2000 Ltd. 1997. SoilCover Version 4.0., 202 Kerr Rd. Saskatoon, Saskatchewan, Canada.

Gold, L. W. 1963. Influence of the snow cover on the average annual ground temperature at Ottawa, Canada. International Association of Hydrological Sciences (IAHS), Publication 61: 82-91.

Goodrich, L. E. 1982. The influence of snow cover on the ground thermal regime . Canadian Geotechnical Journal, **19**: 421-432.

Green, W. H., and Ampt, G. A. 1911. Studies in soil physics. part 1. the flow of air and water through soils. Journal of Agricultural Science, **4**: 1-24.

Healy, R.W. 1990. Simulation of solute transport in variably saturated porous media with supplemental information on modifications to the U.S. Geological Survey's computer program VS2D. Department of the Interior, US Geological Survey, **90**: No. 4025.

Herasymuik, G. M. 1996. Hydrogeology of a sulphide waste rock dump. Master's Dissertation, University of Saskatchewan, Saskatoon, Saskatchewan.

Horton, R. E. 1933. The role of infiltration in the hydrologic cycle. Transactions, American Geophysical Union, **14**: 443-460.

International Network for Acid Prevention, (INAP). 2019. Global Acid Rock Drainage Guide (GARD Guide).http://www.gardguide.com/.

Janowicz, J.R., Hedstrom, N.R., and Granger, R.J. 2004. Investigation of Anvil Range Mining Corporation (Faro) Waste Dump Water Balances: Preliminary Water Balance. Report prepared for SRK Consulting Inc. on behalf of Deloitte & Touche Inc. January 2004.

Janowicz, J.R., Hedstrom, N.R., Granger, R.J. 2006. Investigation of Anvil Range Mining Corporation (Faro) Waste Dump Water Balance - Final Water Balance. Report prepared for SRK Consulting Inc. on behalf of Deloitte & Touche Inc. August 2006.

Johansen, O. 1975. Thermal Conductivity of Soils. Cold Regions Research and Engineering Laboratory, U.S Army Corps of Engineers, Hanover.

Joshi, B. 1993. A finite element model for the coupled flow of moisture and heat in soils under atmospheric forcing. Master's Dissertation, University of Saskatchewan, Saskatoon, Saskatchewan, Canada.

Jubinville, S. 2013. Prediction of Rainfall Runoff for Soil Cover Modelling. Master's Dissertation, University of Alberta, Edmonton, Alberta, Canada.

Jumkis, A.R. 1977. Thermal Geotechnics. Ruger University Press, New Brunswick, N.J.

Kale, R. V., and Sahoo, B. 2011. Green-ampt infiltration models for varied field conditions: A revisit. Water Resources Management, **25**: 3505-3536.

Kinsel, W.G., 1980. CREAMS, a field scale model for chemical runoff and erosion from agricultural management systems. Volumes I, II, and III. Conservation Report 26, USDA – SEA: 643.

Lahmira, B., Lefebvre, R., Aubertin, M., and Bussière, B. 2016. Effect of heterogeneity and anisotropy related to the construction method on transfer processes in waste rock piles. Journal of Contaminant Hydrology, **184** : 35-49. doi:10.1016/j.jconhyd.2015.12.002.

Le Bissonnais, Y. 1996. Aggregate stability and assessment of soil crustability and erodibility: I. Theory and methodology. European Journal of Soil Science, **67**: 1-21.

Li, L., and Pomeroy, J.W. 1997. Estimates of threshold wind speeds for snow transport using meteorological data. Journal of Applied Meteorology and Climatology, **36**(3): 205-213.

Macdonald, E.H. 2007. Handbook of Gold Exploration and Evaluation, Chapter 3: Climate. Institute of Materials, Minerals & Mining, Woodhead Publishing Limited, Cambridge England.

Marshall, B. 2019. Facts and figures 2019: The State of Canada's Mining Industry. Retrieved from https://mining.ca/wp-content/uploads/2020/01/FF-English-Web-1.pdf.

Machibroda, R.M. 1994. Soil evaporative flux modelling of layered cover systems. Master's Dissertation, University of Saskatchewan, Saskatoon, Saskatchewan, Canada.

Morbidelli, R., Saltalippi, C., Flammini, A., and Govindaraju, R.S. 2018. Role of slope on infiltration: A review. Journal of Hydrology, **557**: 878 – 886.

Mu, W., Yu, F., Li, C., Xie, Y., Tian, J., Liu, J., and Zhao, N. 2015. Effects of Rainfall Intensity and Slope Gradient on Runoff and Soil Moisture Content on Different Growing Stages of Spring Maize. Water, **7**: 2990 – 3008.

Nahir, M. 2019. Faro Mine Rehabilitation Project. Presented at the BC MEND ML/ARD Annual Workshop June 4 – 5, 2008, Manitoba, Canada.

Newman, G.P. 1995. Heat and mass transfer in unsaturated soils during freezing. Master's Dissertation, University of Saskatchewan, Saskatoon, Saskatchewan, Canada.

Nordstrom. D.K. 2012. Models, validation, and applied geochemistry: Issues in science, communication, and philosophy. Applied Geochemistry, **27**: 1899 – 1919.

Ojha, C. S. P., Berndtsson, R., and Bhunya, P. 2008. Engineering Hydrology. Oxford University Press, Oxford, United Kingdom.

O'Kane, M. 1995. Instrumentation and Monitoring of an Engineered Soil Cover System for Acid Generating Mine Waste. Master's Dissertation, University of Saskatchewan, Saskatoon, Saskatchewan.

Penman, H.L. 1948. Natural evaporation from open water, bare soil and grass. Proc. Roy. Soc. London A193: 120 – 146.

Philip, J.R., and de Vries, D.A. 1957. Moisture movement in porous materials under temperature gradients. Transactions American Geophysical Union, **38**(2): 222 – 232.

Pigage, L. C. 2004. Bedrock geology compilation of the anvil district (parts of NTS 105K/2,3,5,6,7, and 11), Central Yukon Geological Survey Bulletin 15.

Pomeroy, J.W., and Li, L. 2000. Prairie and arctic areal snow cover mass balance using a blowing snow model . Journal of Geophysical Research, **105**(D21), 26,619-26,634.

Price, W. A. 2003. Challenges posed by metal leaching and acid rock drainage, and approaches used to address them. Mineralogical Association of Canada: Environmental aspects of mine waste short course series: 1-10

Reba, M. L., Pomeroy, J., Marks, D., and Link, T. E. 2012. Estimating surface sublimation losses from snowpacks in a mountain catchment using eddy covariance and turbulent transfer calculations. Hydrological Processes, **26**(24): 3699-3711. doi:10.1002/hyp.8372.

Richards, L.A. 1931. Capillary Conduction of Liquids Through Porous Mediums. Physics, **1**(5): 318.

Robertson Geoconsultants. 1996a. Anvil Range Mining Complex – integrated comprehensive abandonment plan – volume 1 – Background, Report No. 033001/3, prepared for Anvil Range Mining Corporation, Vancouver.

Robertson Geoconsultants. 1996b. Anvil Range Mining Complex – integrated comprehensive abandonment plan – Volume 2 – Site Characterization, Report No. 033001/3, prepared for Anvil Range Mining Corporation, Vancouver.

Robertson, A. 2019. Managing risk: Doing, checking, and checking the checkers for tailings, water and waste management. Proceedings of the *Design and Assessment of Mine Waste Short Course,* University of Alberta Geotechnical Centre, Edmonton, Alberta.

Scanlon, B.R., Christman, M., Reedy, R.C., Porro, I., Simunek, J., and Flerchinger, G.N. 2002. Intercode comparisons for simulating water balance of surficial sediments in semiarid regions. Water Resources Research, **38**(12): 1323, doi:10.1029/2001WR001233.

Schroeder, P.R., Dozier, T.S., Zappi, P.A., McEnroe, B.M., Sjostrom, J.W., and Peyton, R.L. 1994. The Hydraulic Evaluation of Landfill Performance (HELP) Model: Engineering Documentation for Version 3. EPA/600/R-94/168b, September 1994, U.S. Environmental Protection Agency Office of Research and Development, Washington, DC.

Sexstone, G.A., Clow, D.W., Stannard, D.I., and Fassnacht, S.R. 2016. Comparison of methods for quantifying surface sublimation over seasonally snow-covered terrain . Hydrological Processes, **30**(19): 3373-3389. doi:10.1002/hyp.10864.

Shokouhi, A., and Williams, D.J. 2017. Volume change behaviour of mixtures of coarse coal reject and tailings. Mining Technology, **126**(3): 163 – 176.

Simunek, J., and van Genuchten, M.Th. 1999. Using the HYDRUS-1D and HYDRUS-2D codes for estimating unsaturated soil hydraulic and solute transport parameters. Characterization and measurement of the hydraulic properties of unsaturated porous media, **1**: 523-1.

Simunek, J., van Genuchten, M.Th., and Sejina, M. 2006. The HYDRUS Software Package for Simulating Two-and Three Dimensional Movement of Water, Heat, and Multiple Solutes in Variably-Saturated Media, Version 1.0, PC Progress, Prague, Czech Republic.

Simunek, J., Sejina, M., Saito, H., Sakai, M., and van Genuchten, M.Th. 2009. The HYDRUS-1D Software Package for Simulating the One-Dimensional Movement of Water, Heat, and Multiple Solutes in Variably-Saturated Porous Media. Version 4.08, Department of Environmental Sciences, University of California Riverside, Riverside, California.

Sivakugan, N., and Das, B. M. 2010. Geotechnical engineering: A Practical Problem-Solving Approach. Ross Publishing, Fort Lauderdale, FL.

Smith, L and Beckie, R. 2003. Hydrologic and geochemical transport processes in mine waste rock. Environmental aspects of mine waste short course series, Mineralogical Association of Canada: 51-72.

SoilMoisture Equipment Corp. (SoilMoisture). 2012. Operating instructions for 2800 series guelph permeameter. December 2012.

SoilVision Systems Ltd. 2014. SVFLUX 1D/2D/3D saturated / unsaturated finite element groundwater seepage modelling theory manual. Saskatoon, Saskatchewan, Canada.

Sturm, M., Taras, B., Liston, G.E., Derksen, C., Jonas, T., and Lea, J. 2010. Estimating snow water equivalent using snow depth data and climate classes. Journal of Hydrometeorology, **11**: 1380-1394, doi:10.1175/2010JHM1202.1.

Swanson, D.A. 1995. Predictive modelling of moisture movement in engineered soil covers for acid generating mine waste. Master's Dissertation, University of Saskatchewan, Saskatoon, Saskatchewan, Canada.

Swanson, D. A., Barbour, S. L., Wilson, G. W., and O'Kane, M. 2003. Soil-atmosphere modelling of an engineered soil cover for acid generating mine waste in a humid, alpine climate. Canadian Geotechnical Journal, **40**: 276-292, doi:10.1139/T02-116.

Swanson, D.A and O'Kane, M. 1999. Application of unsaturated zone hydrology at waste rock facilities: Design of soil covers and prediction of seepage. Proceedings of American Society of Mining and Reclamation, 517-526. doi:10.21000/JASMR99010517

Tami, D., Rahardjo, H., Leong, E-C., and Fredlund, D.G. 2004. Design and laboratory verification of a physical model of sloping capillary barrier. Canadian Geotechnical Journal, **41**: 814 – 830.

Taylor, D. W. 1948. Fundamentals of soil mechanics. John Wiley and Sons, New York City, New York.

Tingjun Zhang. 2005. Influence of the seasonal snow cover on the ground thermal regime: An overview. Reviews of Geophysics, **43**(4), RG4002-n/a, doi:10.1029/2004RG000157.

Trach, D. 1994. Moisture uptake within the root zone. Master's Dissertation, University of Saskatchewan, Saskatoon, Saskatchewan, Canada.

Wilson, E. M. 1974. Engineering Hydrology Second Edition. MacMillan Press Ltd, doi:10.1007/978-1-349-02417-9.

Wilson, G. W. 1990. Soil Evaporative Fluxes for Geotechnical Engineering Problems. Doctoral Dissertation, University of Saskatchewan, Saskatoon, Saskatchewan, Canada.

Wilson, G.W., Fredlund, D.G. and S.L. Barbour. 1994. Coupled soil-atmosphere modelling for soil evaporation. Canadian Geotechnical Journal, **31**: 151-161.

Verburg, K., Ross, P.J., and Bristow, K.L. 1996. SWIMv2.1 User Manual, Divisional Report 130. CSIRO Division of Soils, Canberra, Australia.

Zhao, Q., Li, D., Zhuo, M., Guo, T., Liao, Y., and Xie, Z. 2015. Effects of rainfall intensity and slope gradient on erosion characteristics of the red soil slope. Stochastic Environmental Research and Risk Assessment, **29**: 609 – 621.

APPENDIX A – WATER BALANCE FIGURES

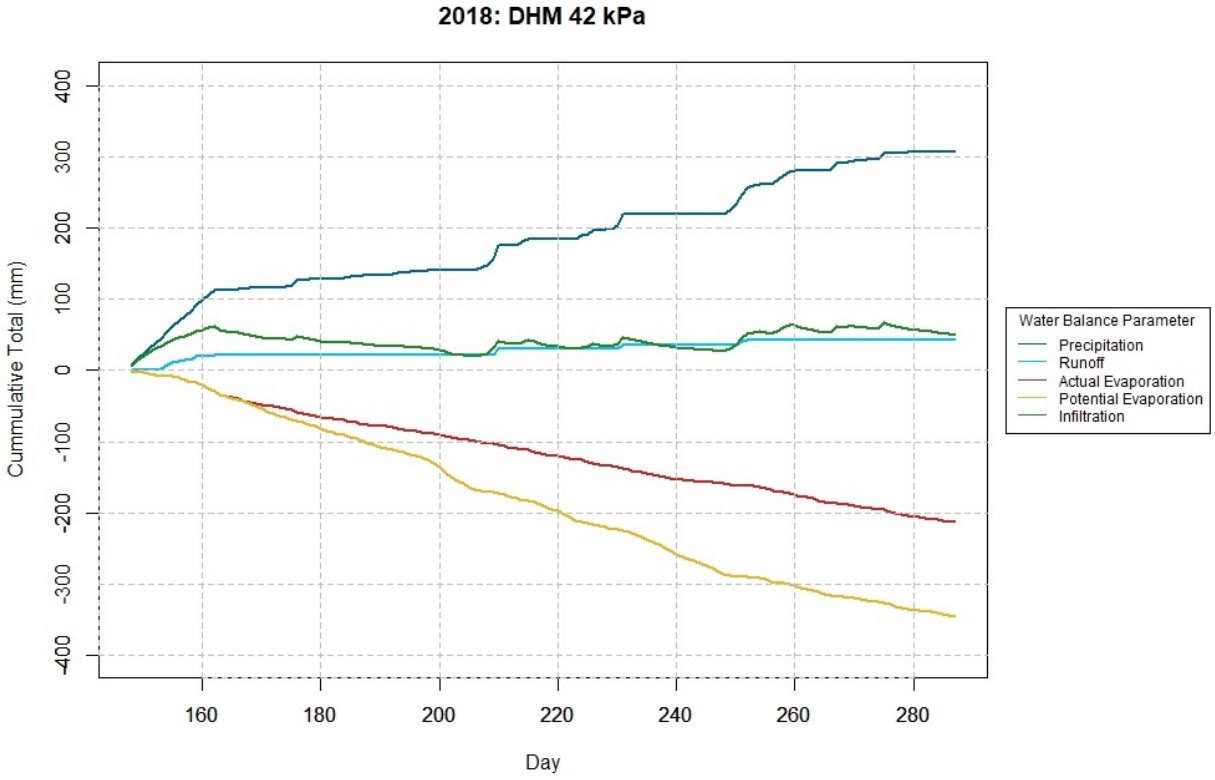

Figure A. 1 – Water Balance 2018 DHM 42 kPa

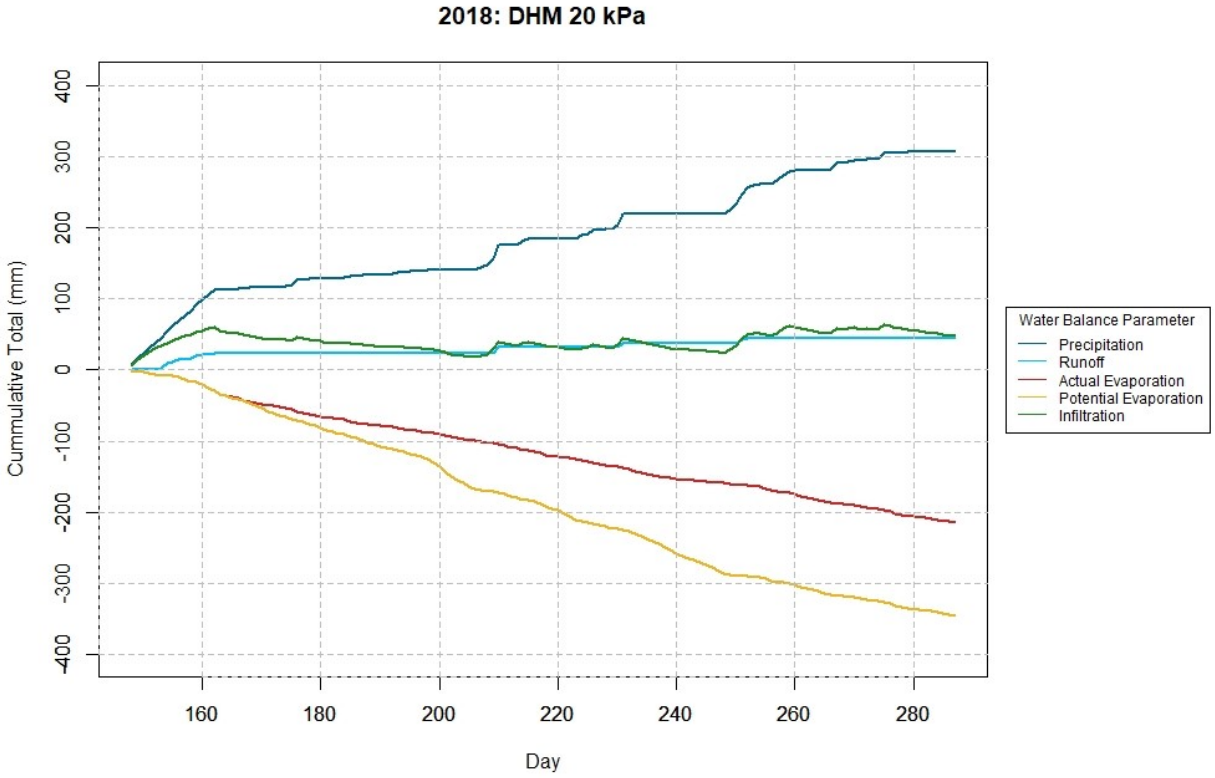

Figure A. 2 - Water Balance 2018 DHM 20 kPa

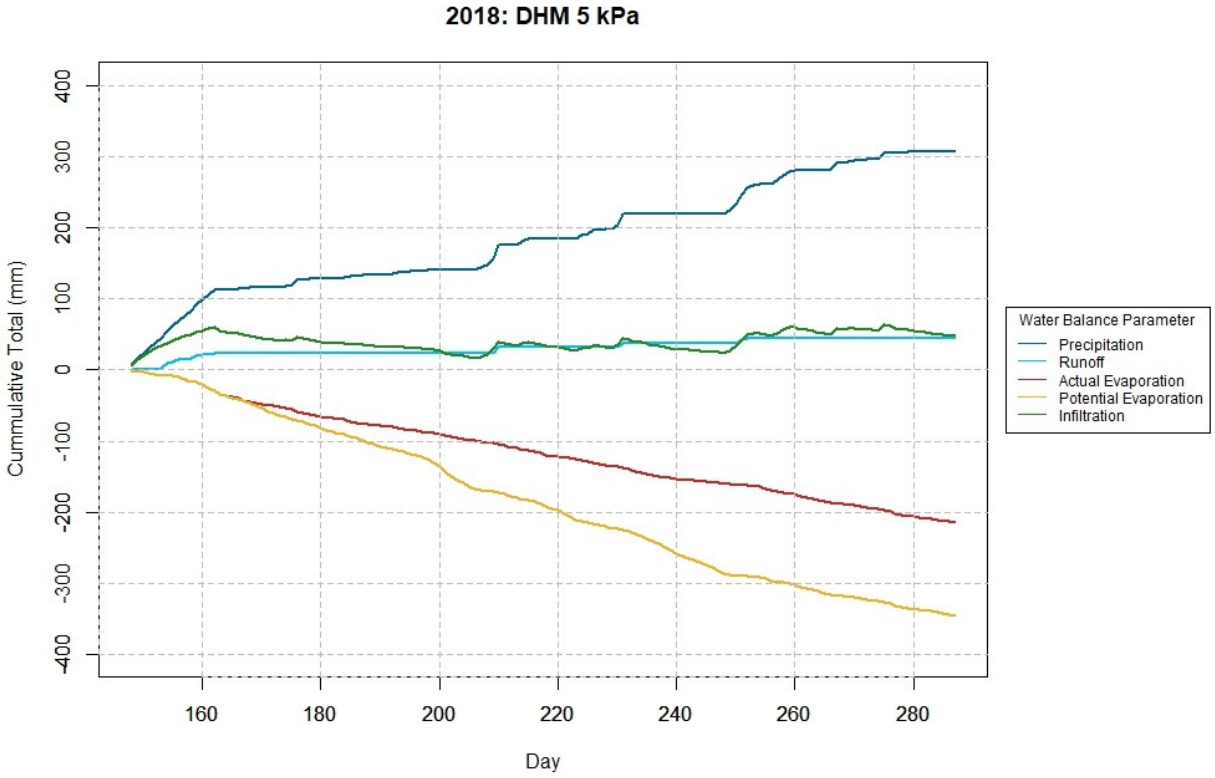

Figure A. 3 - Water Balance 2018 DHM 5 kPa

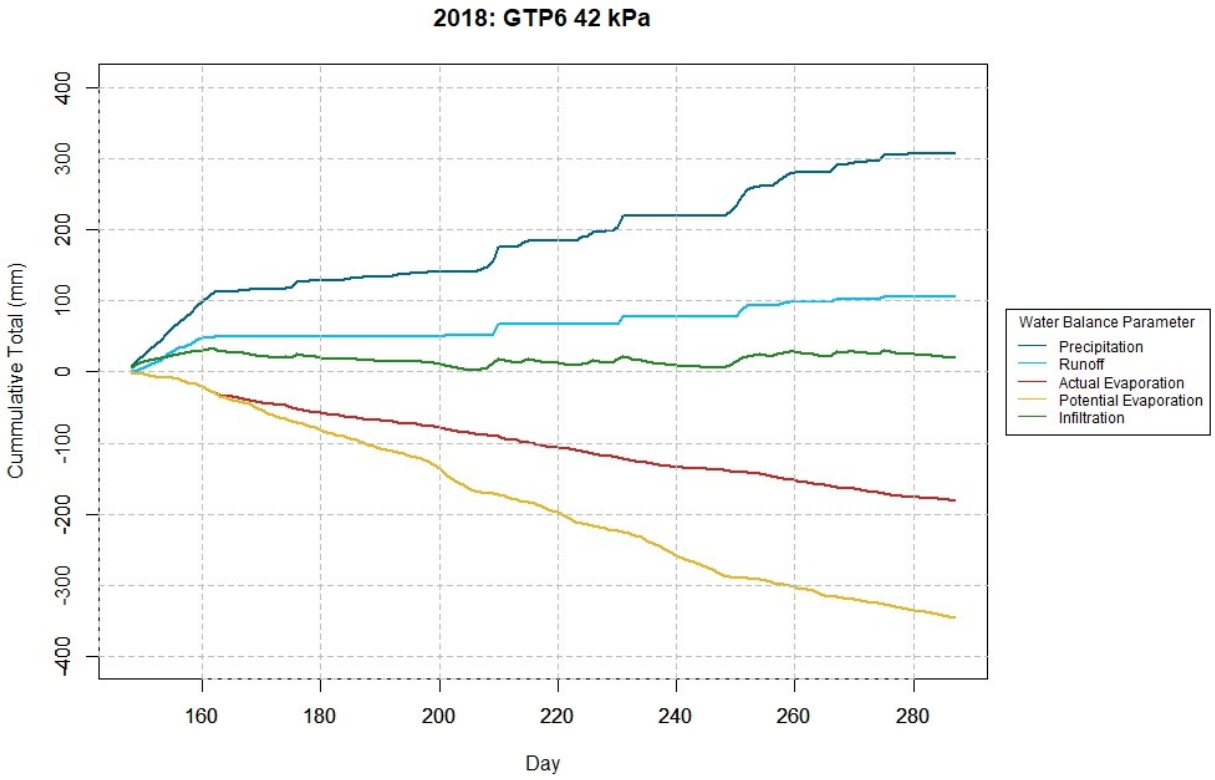

Figure A. 4 - Water Balance 2018 GTP6 42 kPa

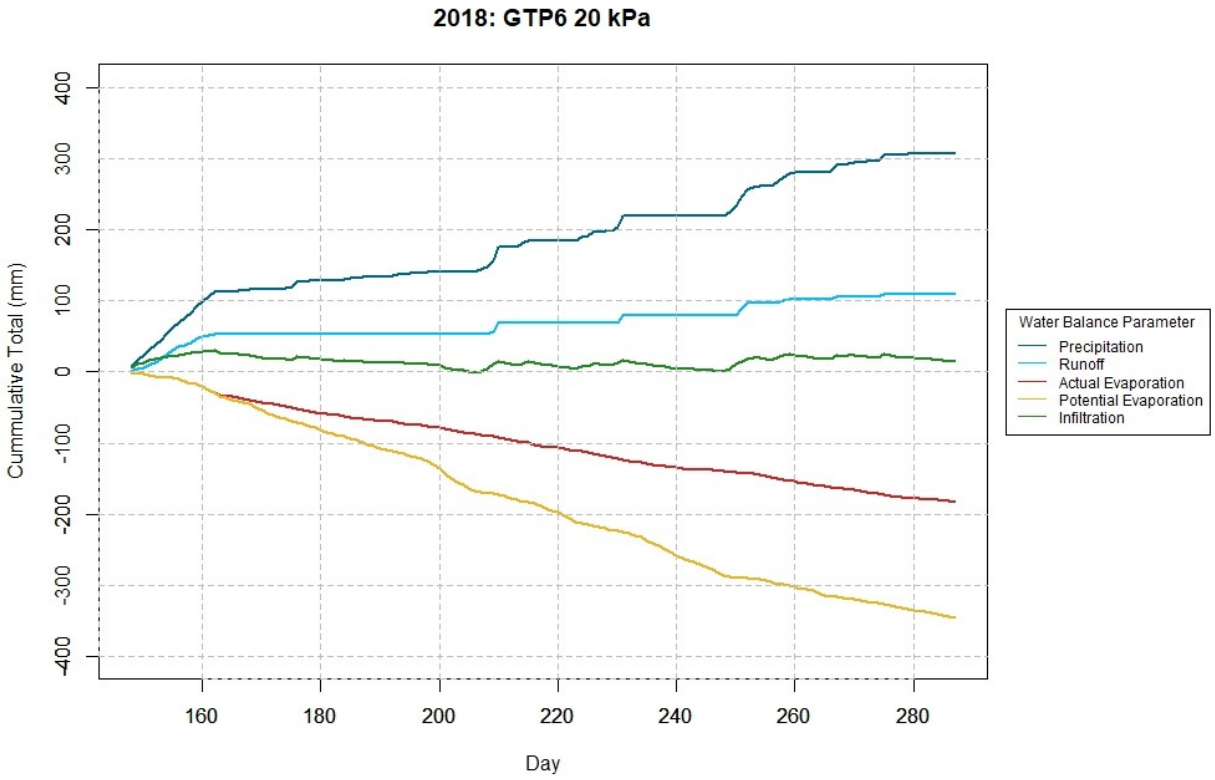

Figure A. 5 - Water Balance 2018 GTP6 20 kPa

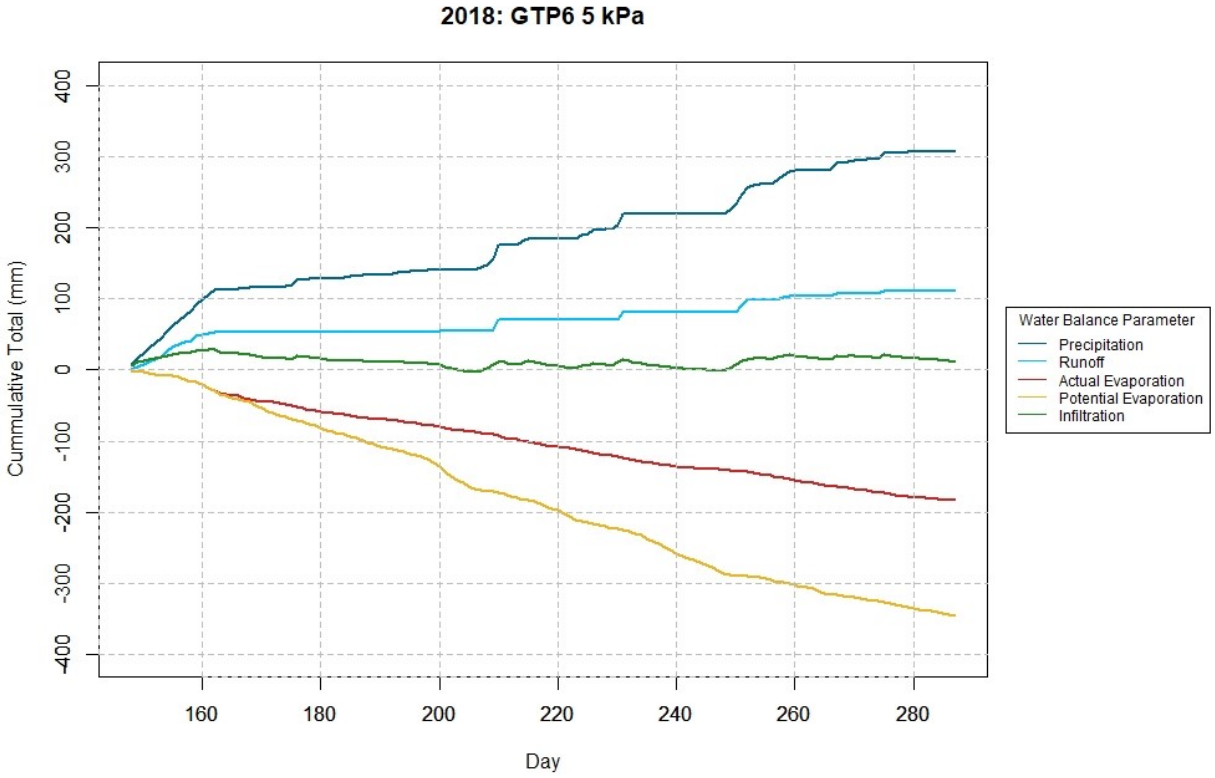

Figure A. 6 - Water Balance 2018 GTP6 5 kPa

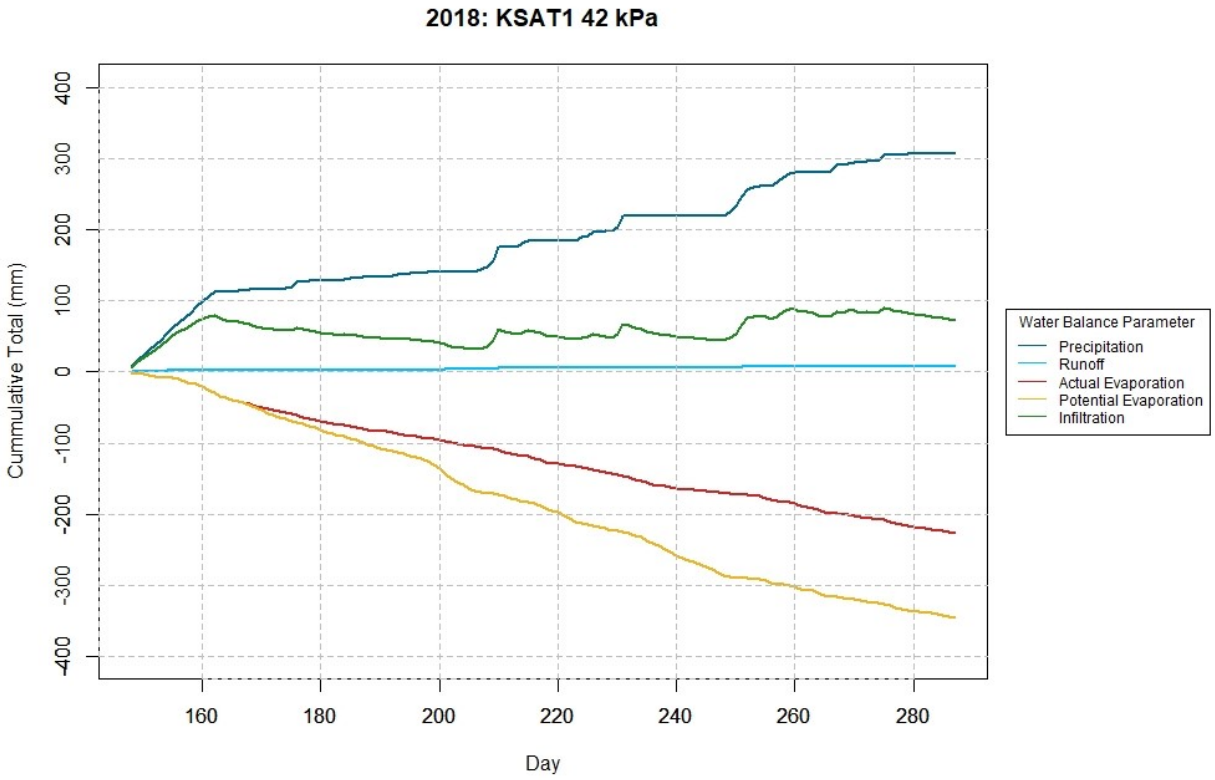

Figure A. 7 - Water Balance 2018 KSAT1 42 kPa

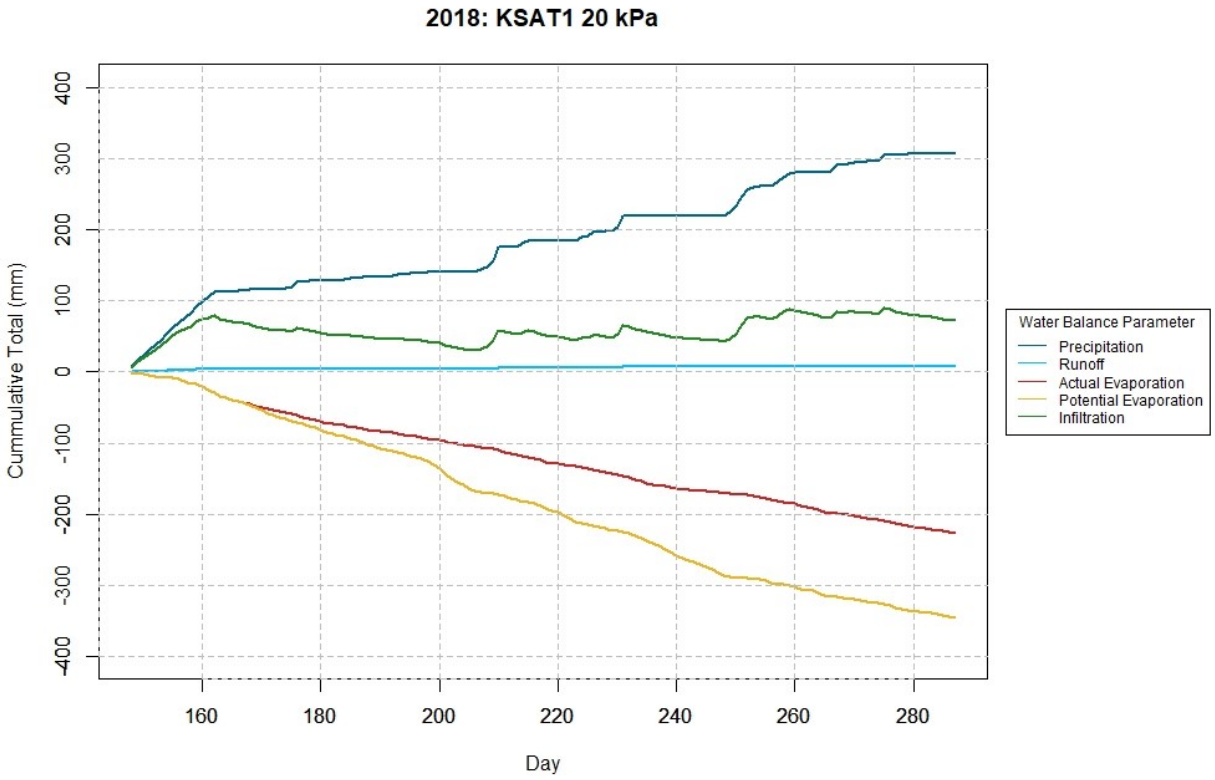

Figure A. 8 - Water Balance 2018 KSAT1 20 kPa

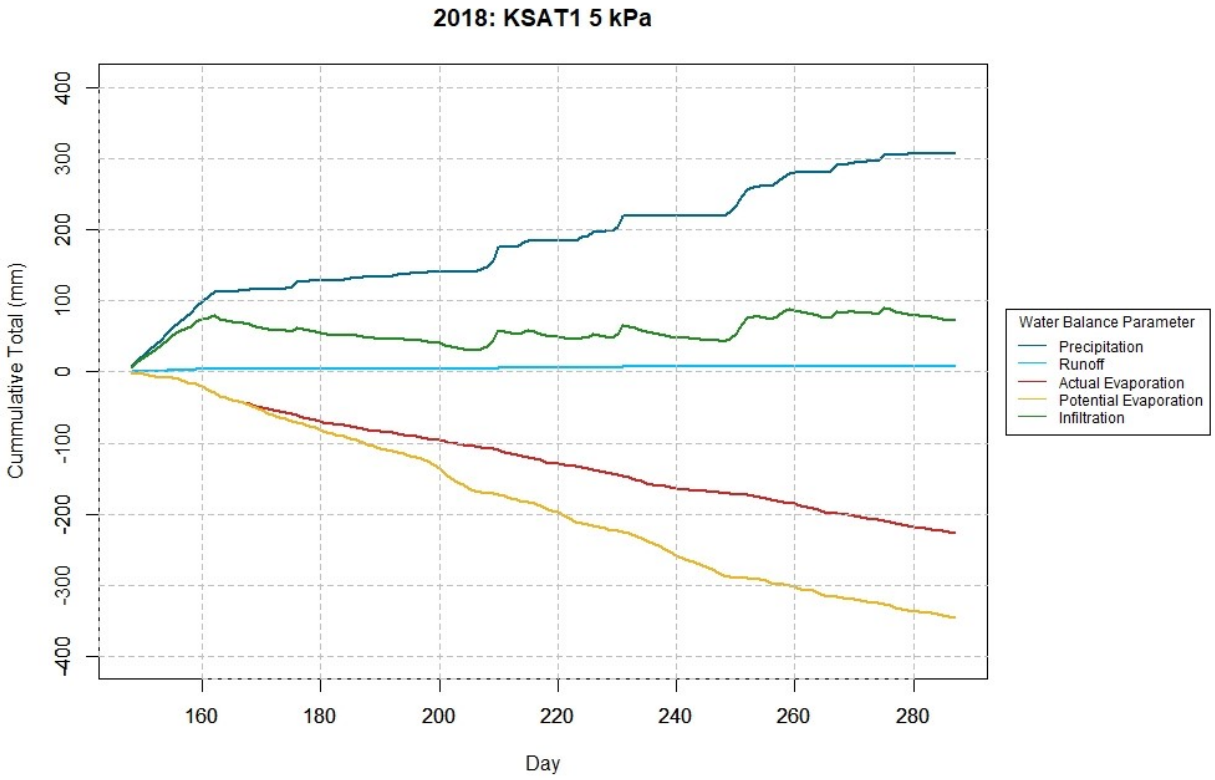

Figure A. 9 – Water Balance 2018 KSAT1 5 kPa

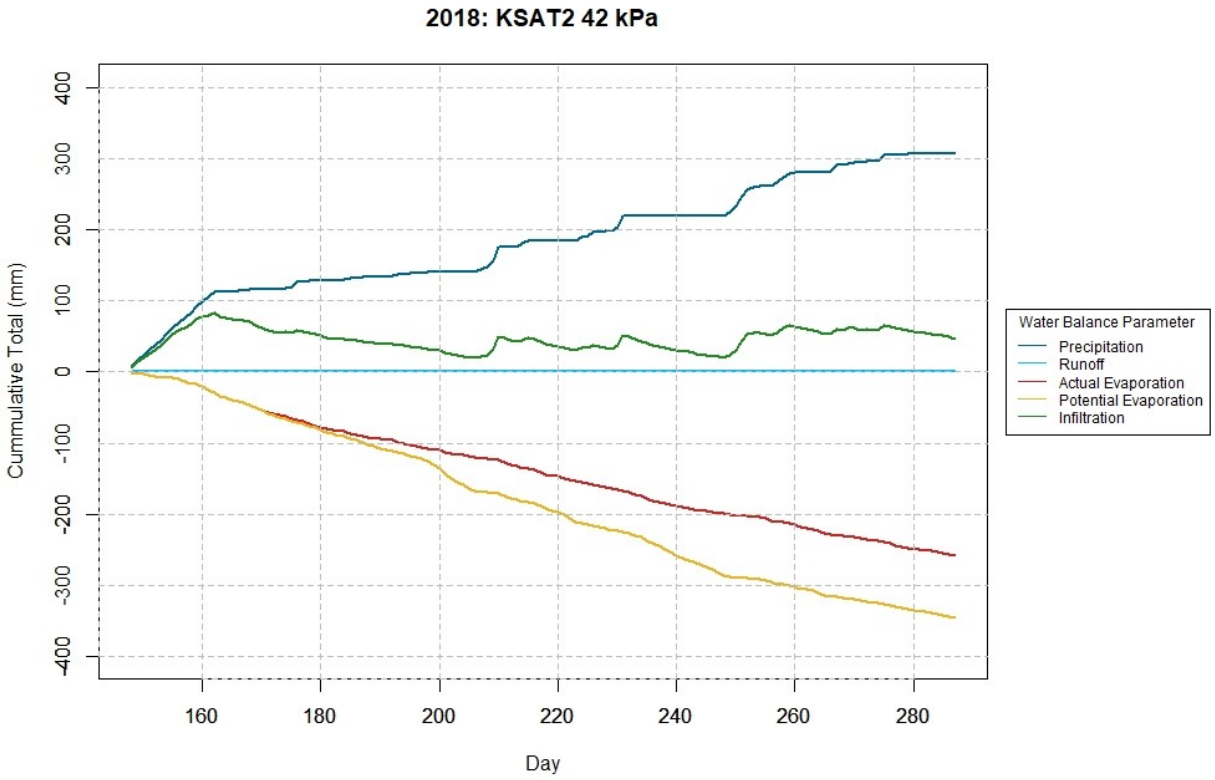

Figure A. 10 – Water Balance 2018 KSAT2 42 kPa

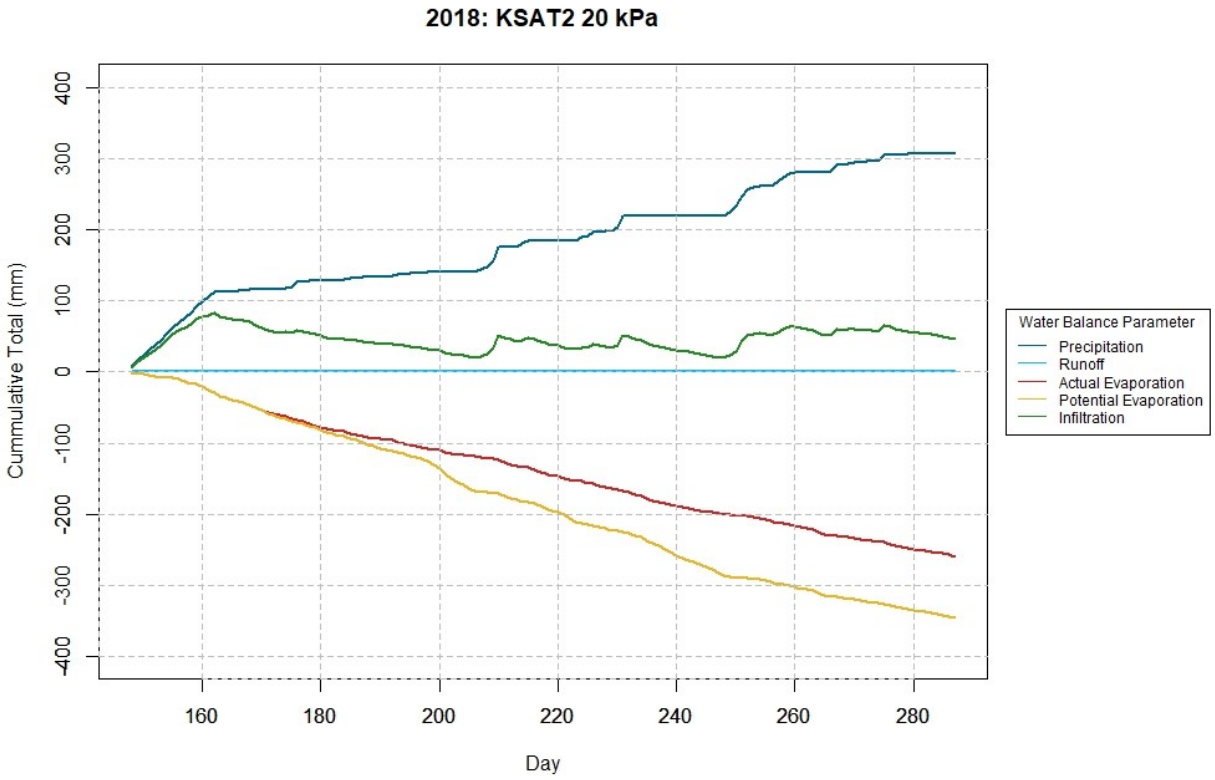

Figure A. 11 – Water Balance 2018 KSAT2 20 kPa

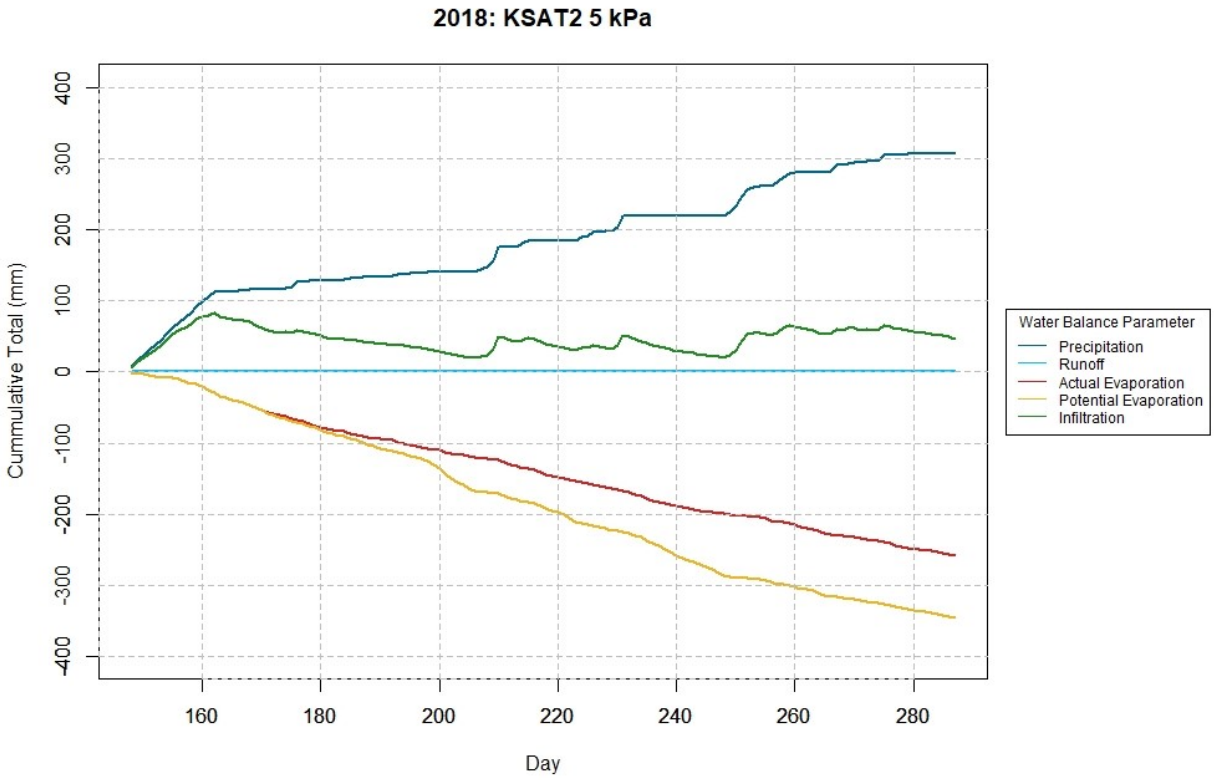

Figure A. 12 - Water Balance 2018 KSAT2 5 kPa

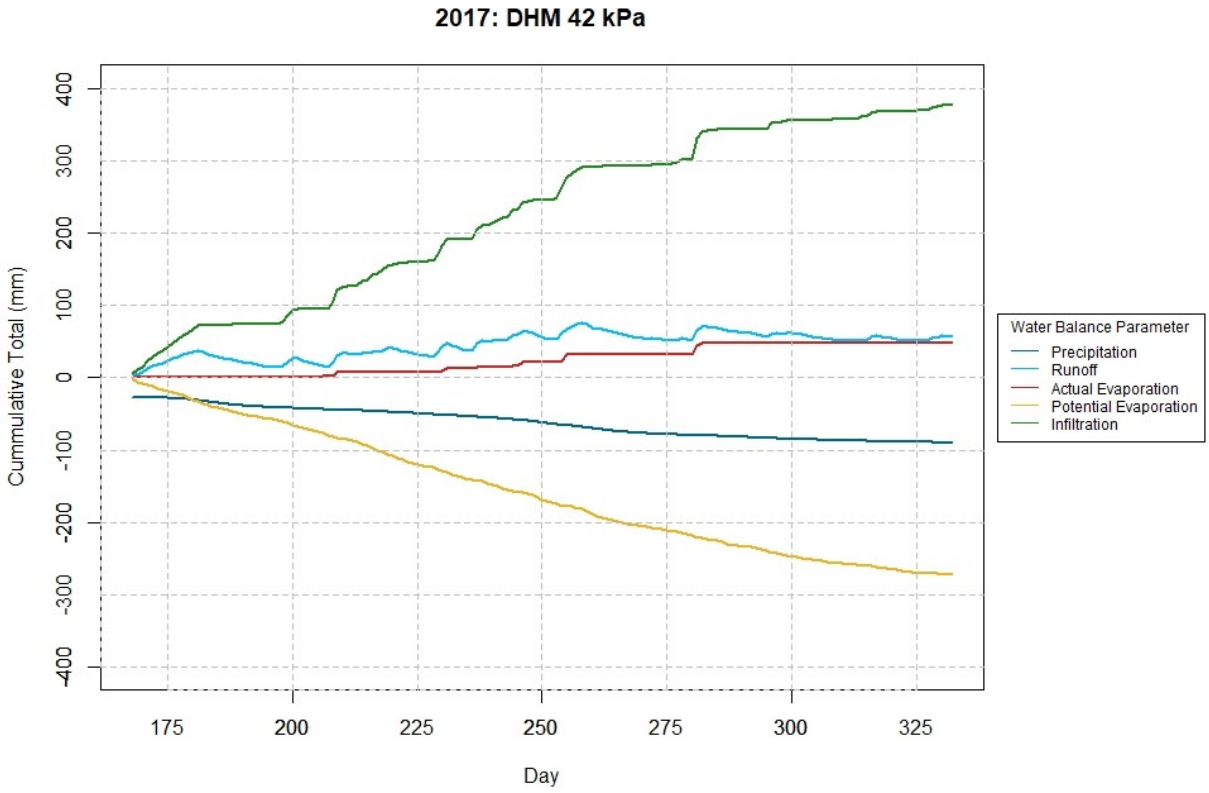

Figure A. 13 - Water Balance 2017 DHM 42 kPa

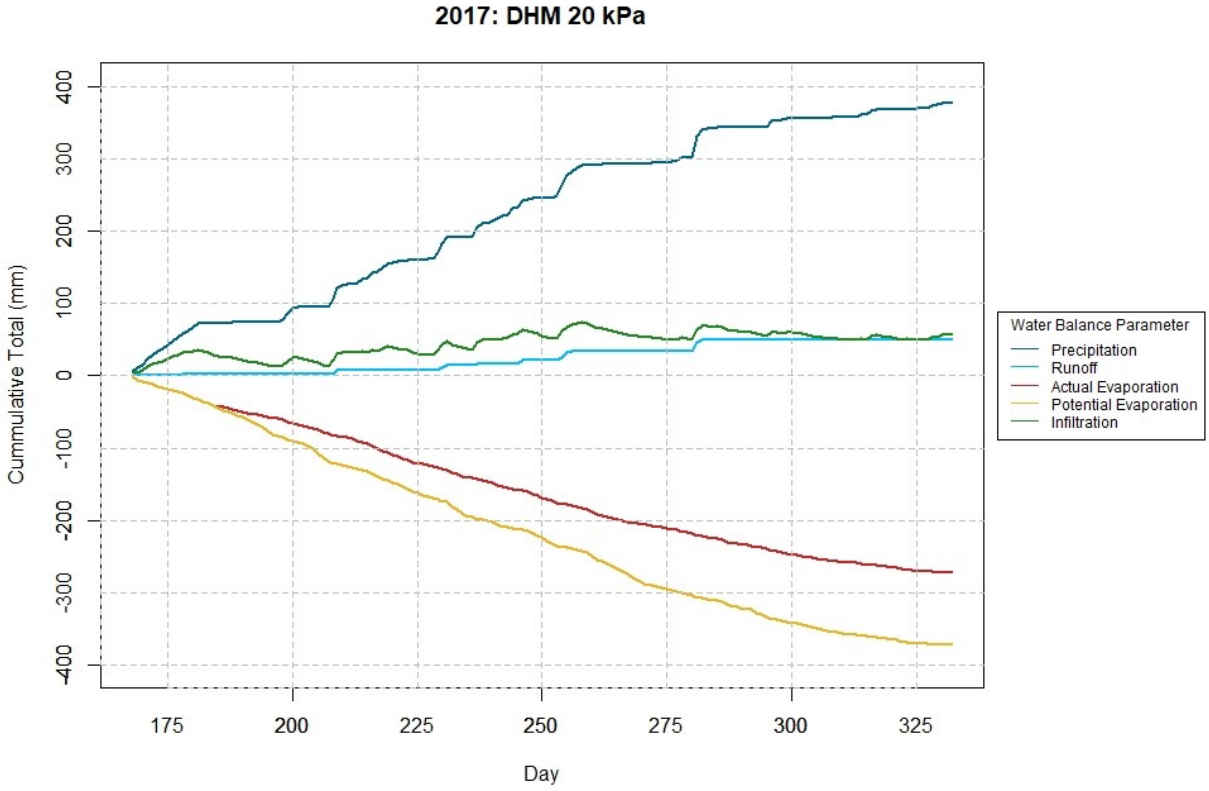

Figure A. 14 - Water Balance 2017 DHM 20 kPa

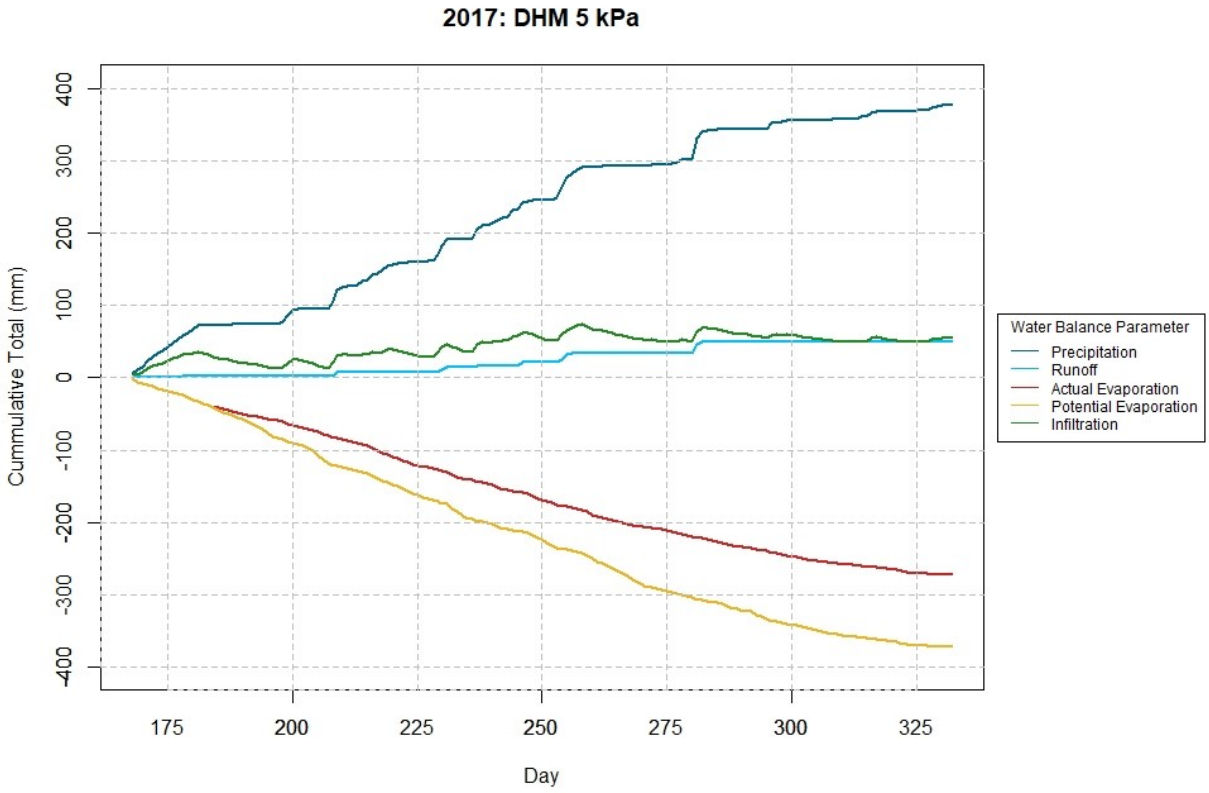

Figure A. 15 - Water Balance 2017 DHM 5 kPa

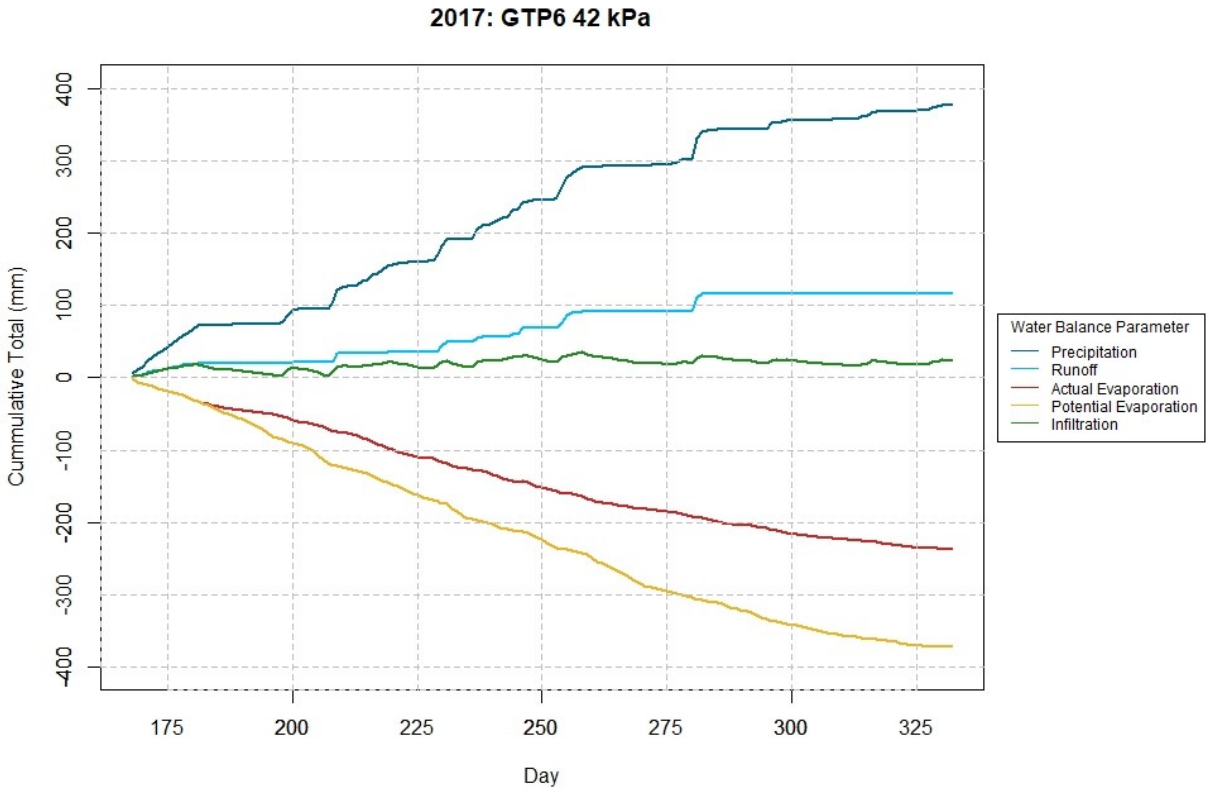

Figure A. 16 - Water Balance 2017 GTP6 42 kPa

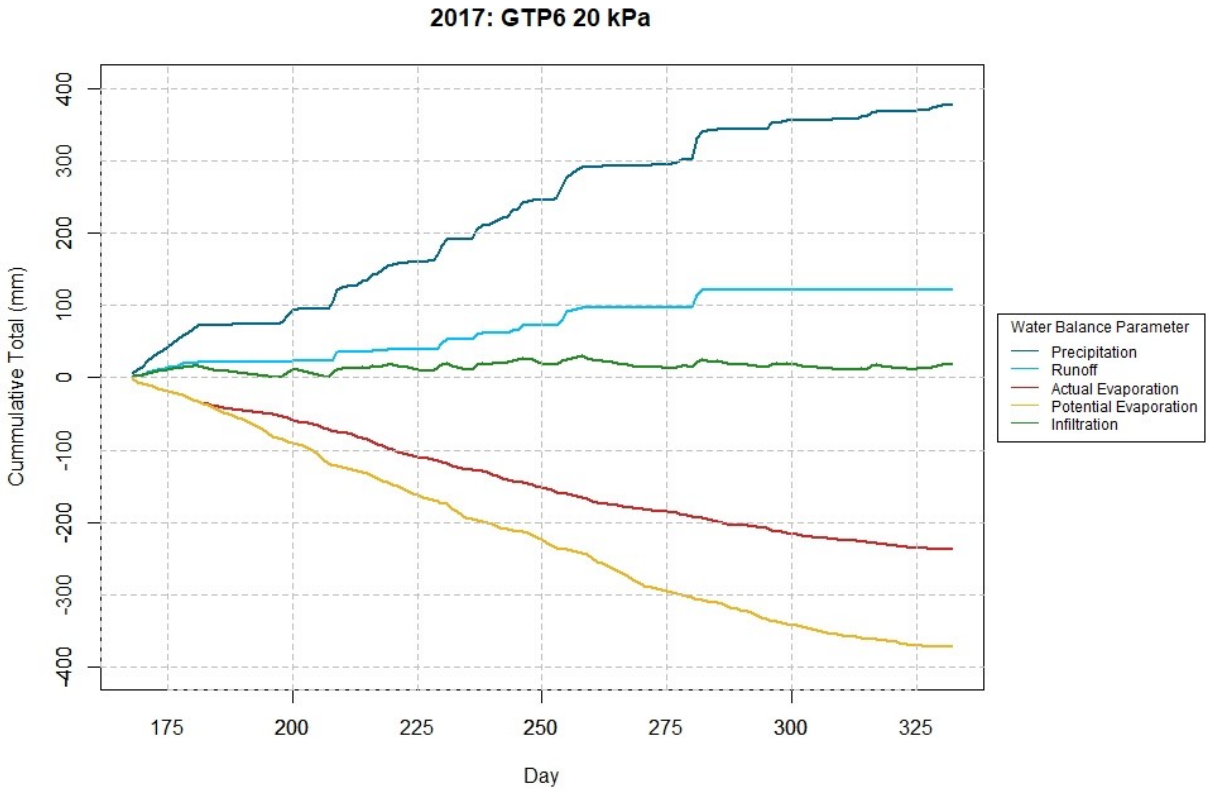

Figure A. 17 - Water Balance 2017 GTP6 20 kPa

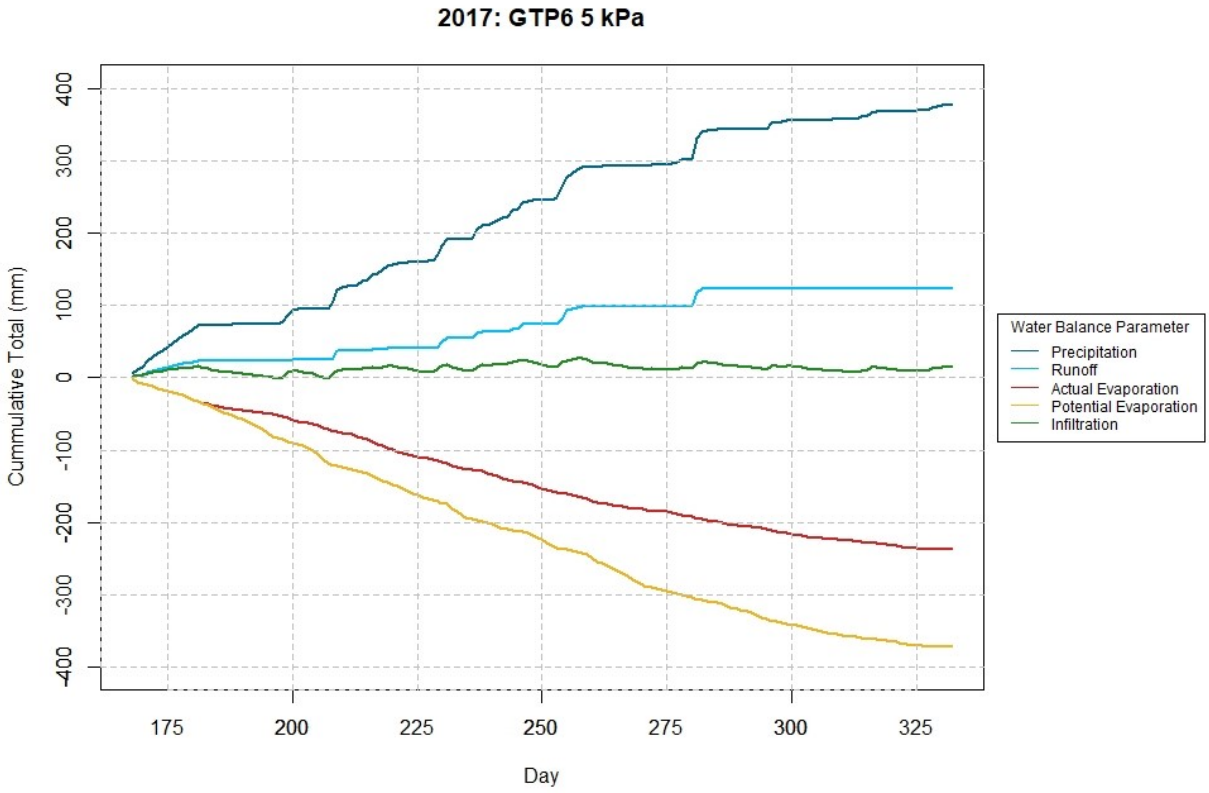

Figure A. 18 - Water Balance 2017 GTP6 5 kPa

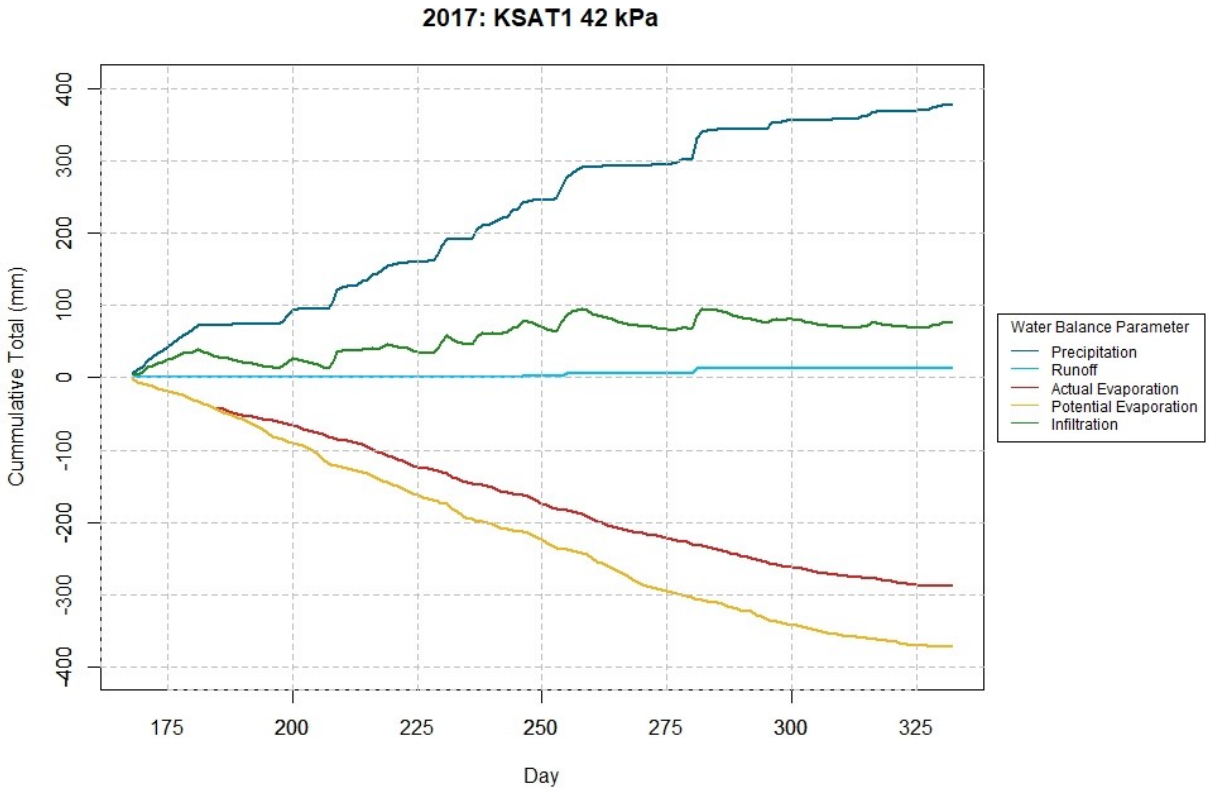

Figure A. 19 - Water Balance 2017 KSAT1 42 kPa

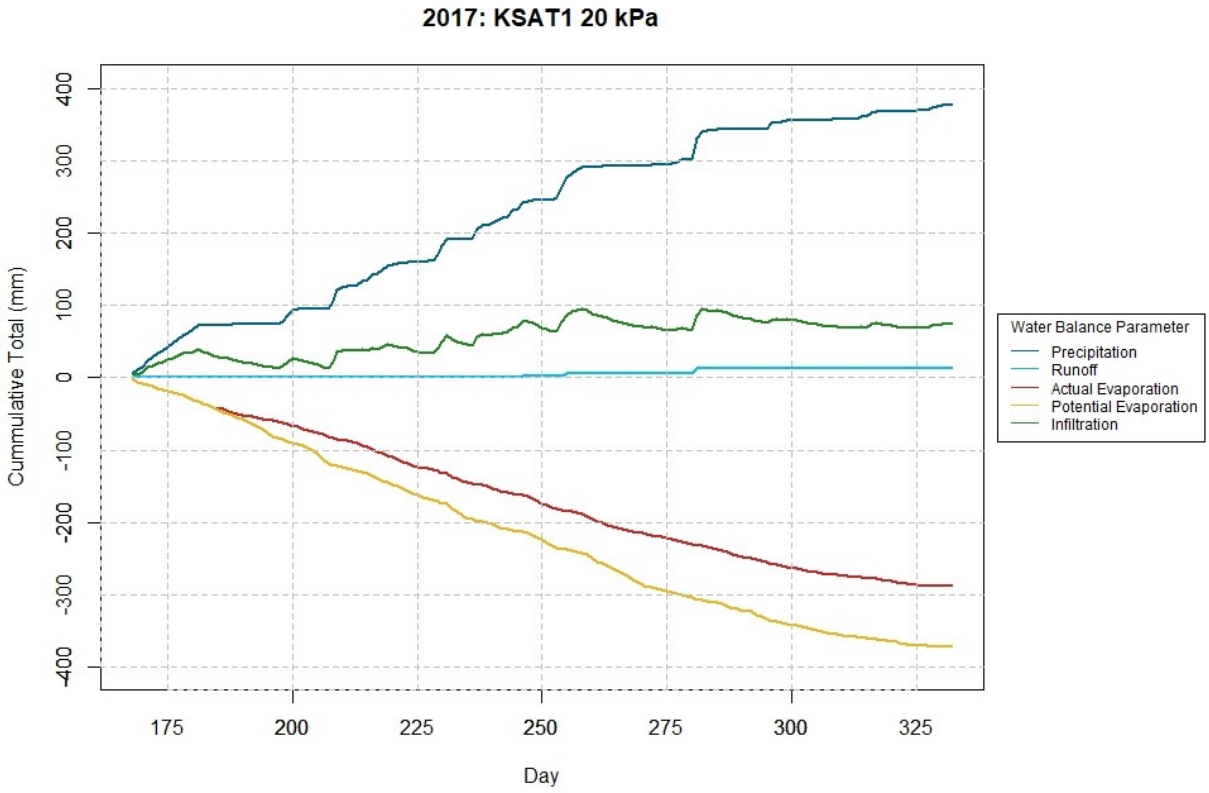

Figure A. 20 - Water Balance 2017 KSAT1 20 kPa

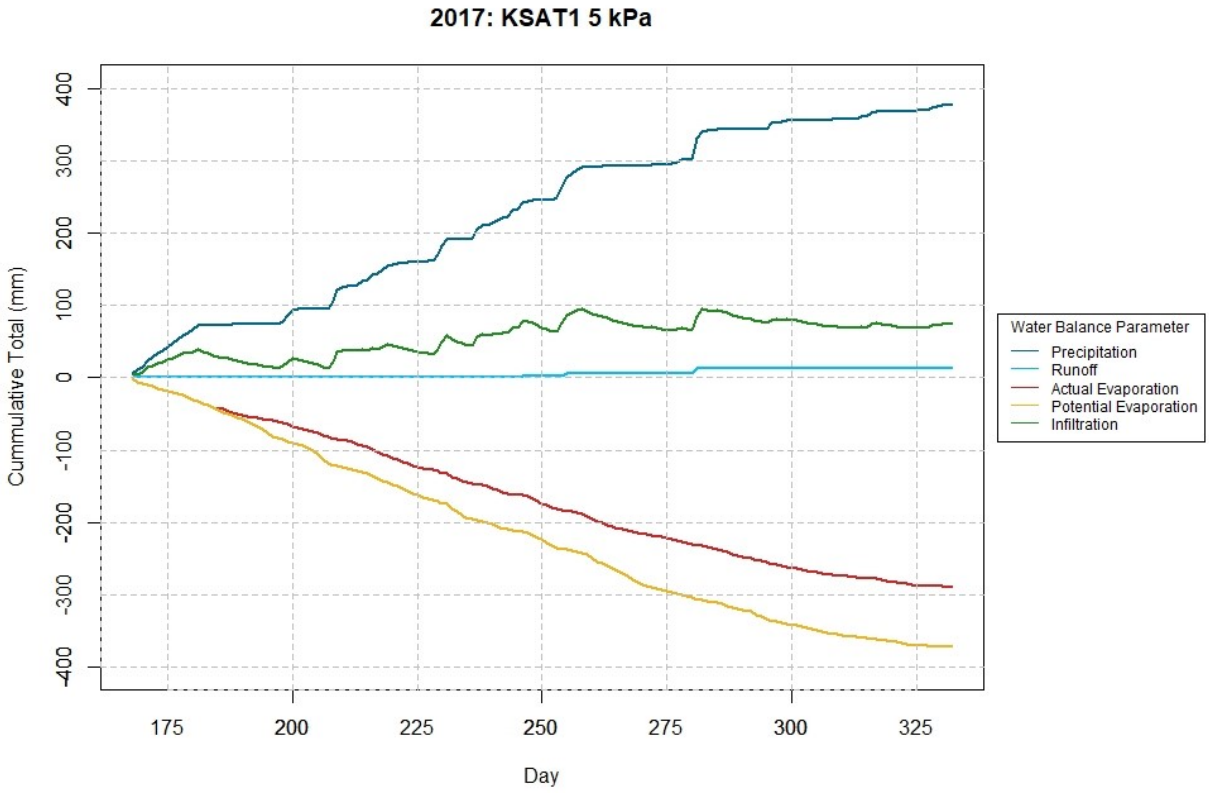

Figure A. 21 - Water Balance 2017 KSAT1 5 kPa

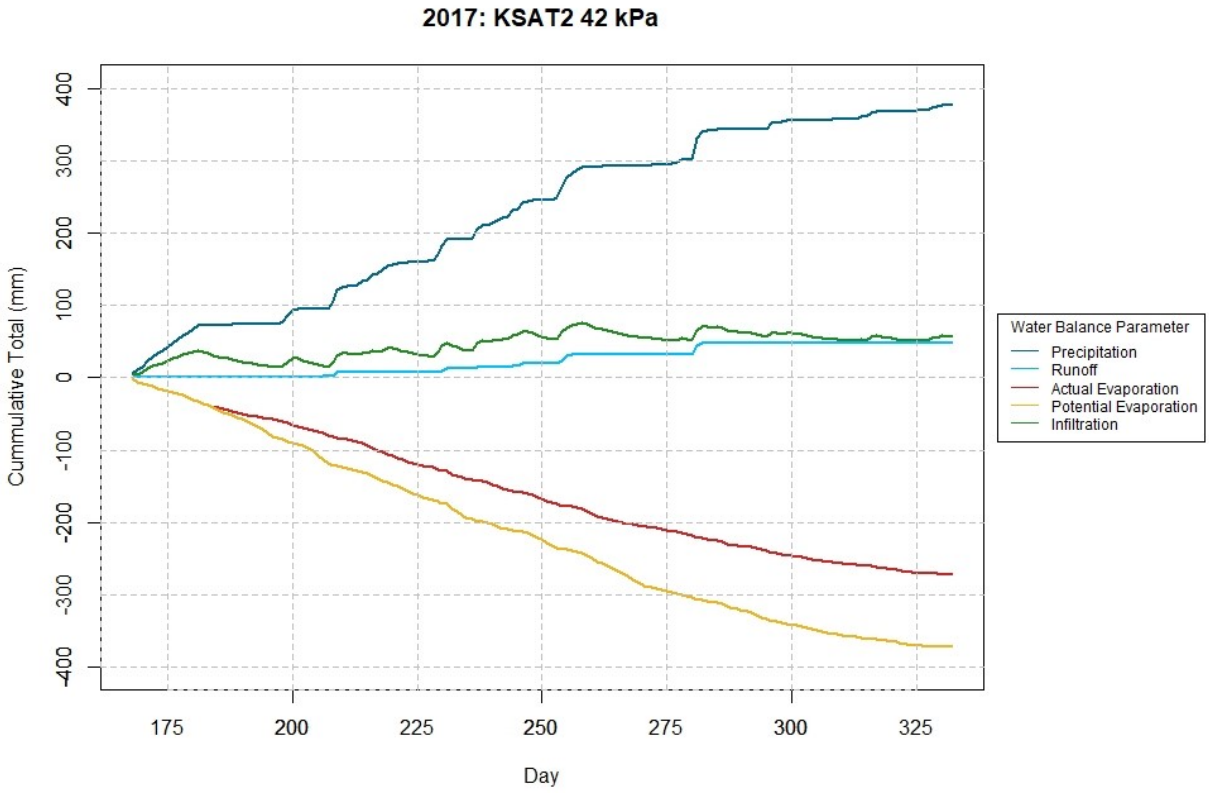

Figure A. 22 - Water Balance 2017 KSAT2 42 kPa

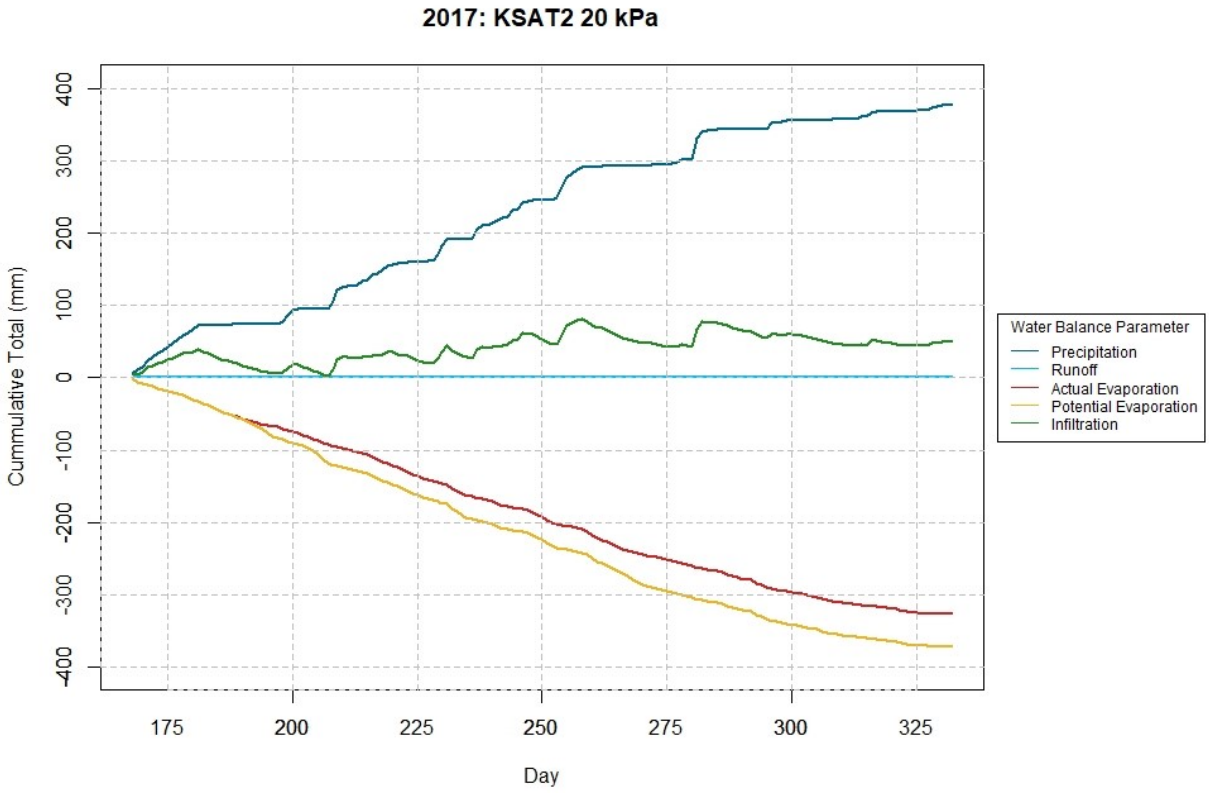

Figure A. 23 - Water Balance 2017 KSAT2 20 kPa

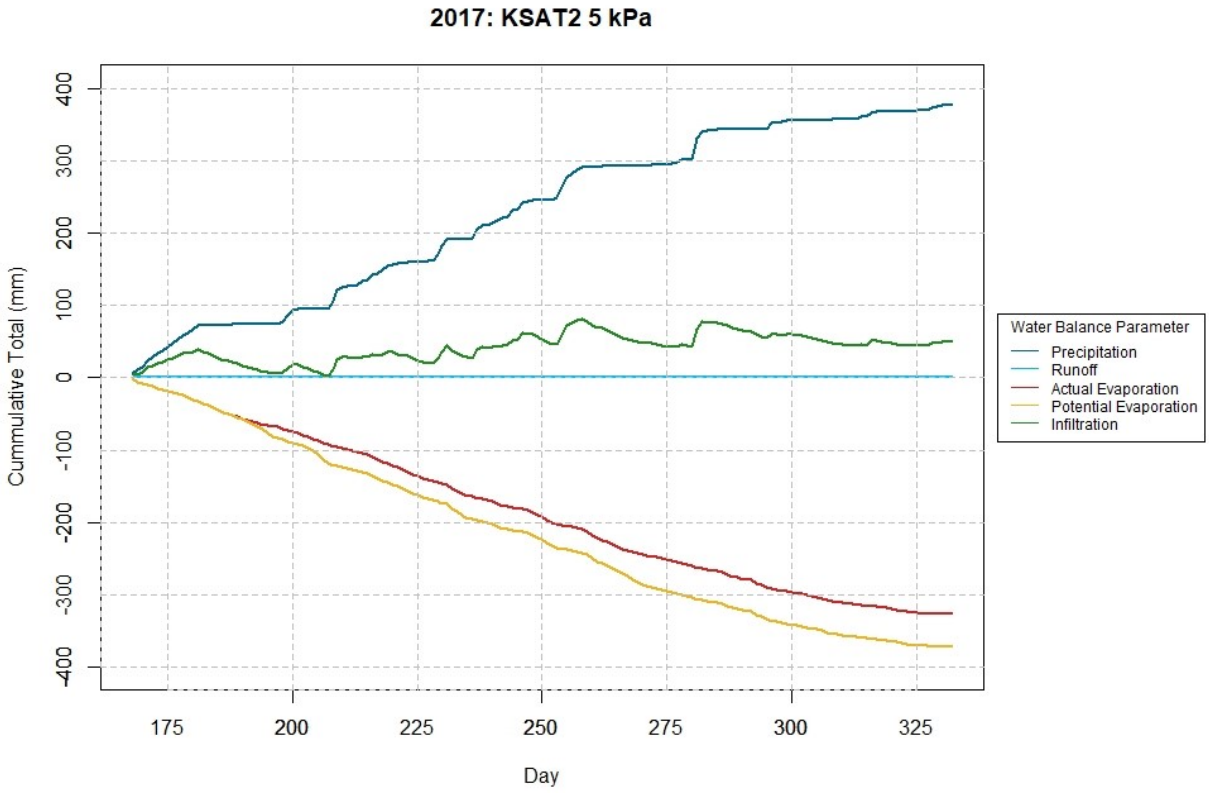

Figure A. 24 - Water Balance 2017 KSAT2 5 kPa

APPENDIX B – SUCTION PROFILES

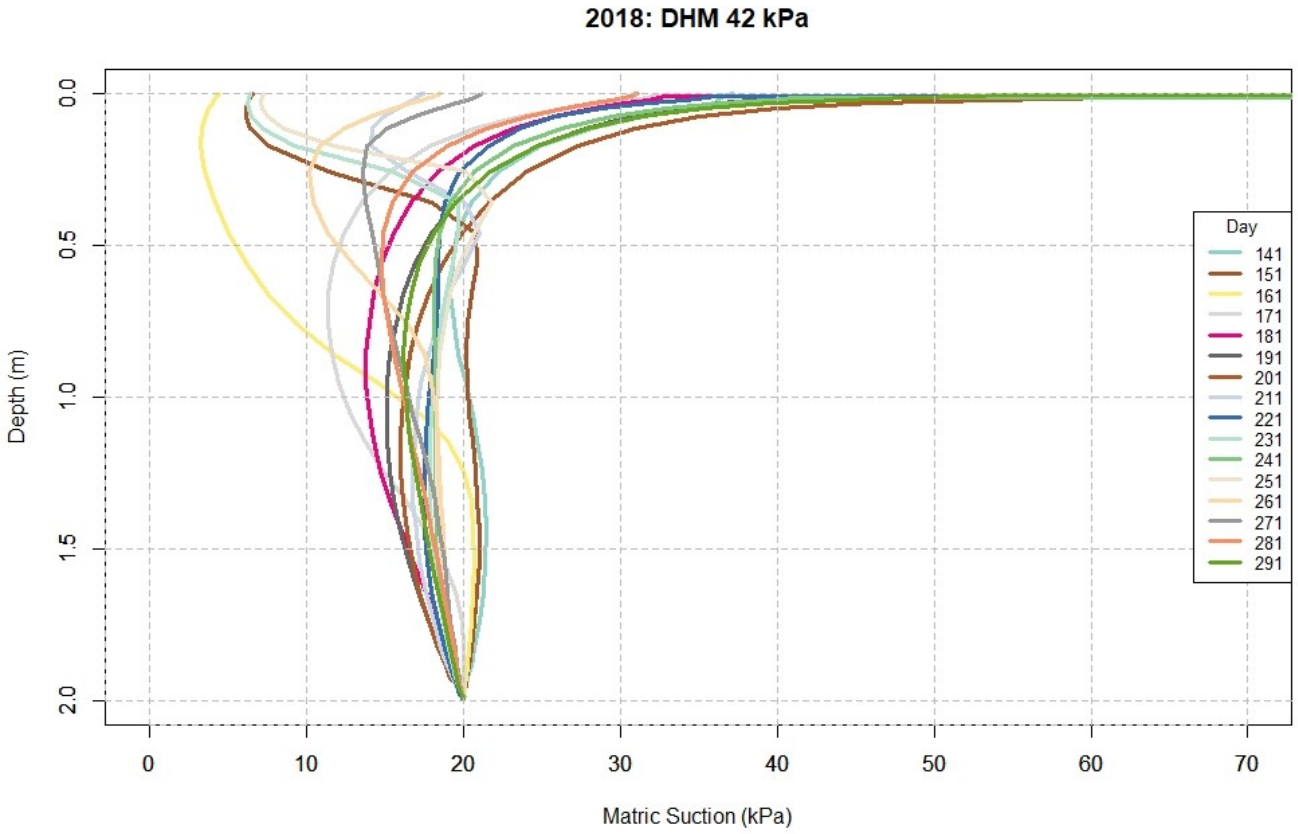

Figure B. 1 - Matric Suction Profile 2018 DHM 42 kPa

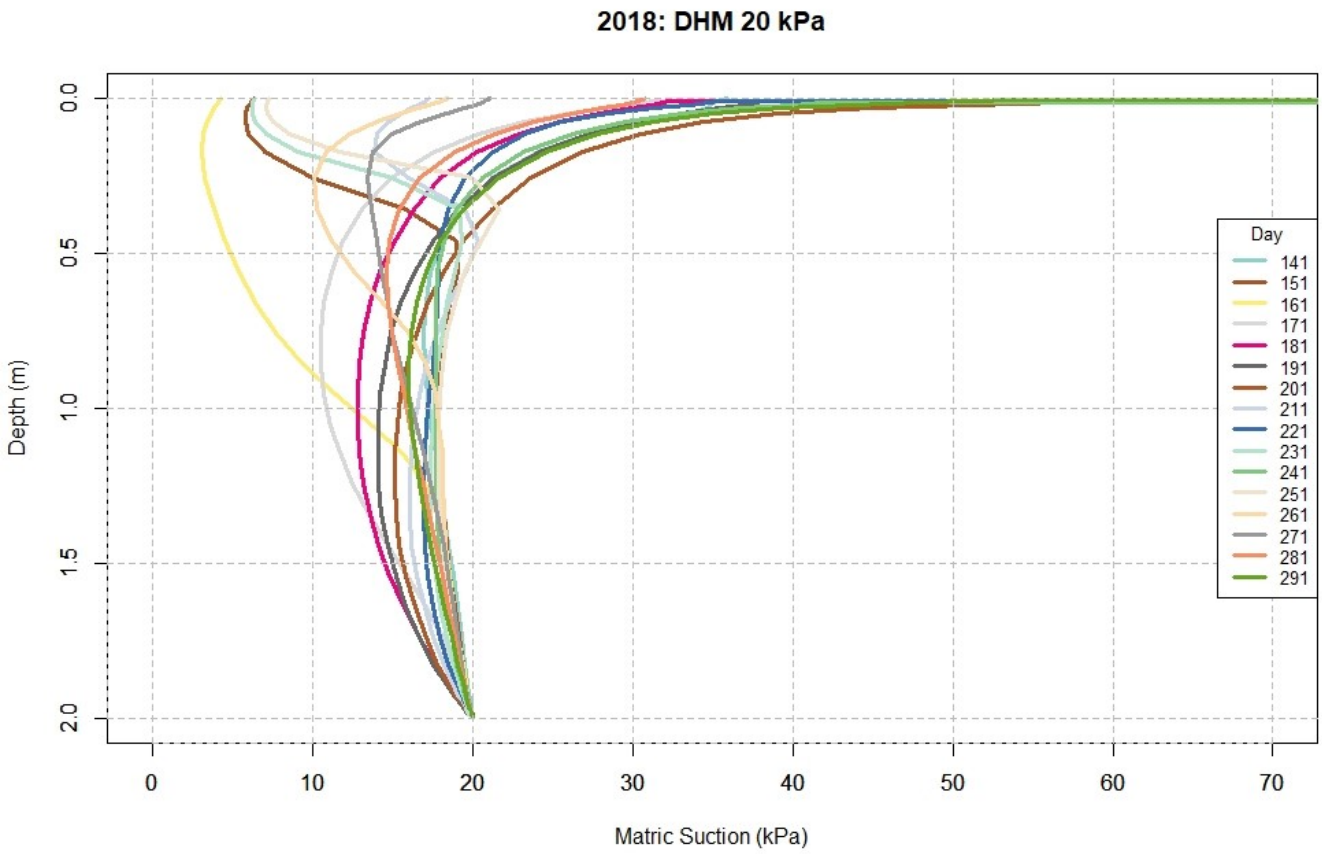

Figure B. 2 - Matric Suction Profile 2018 DHM 20 kPa

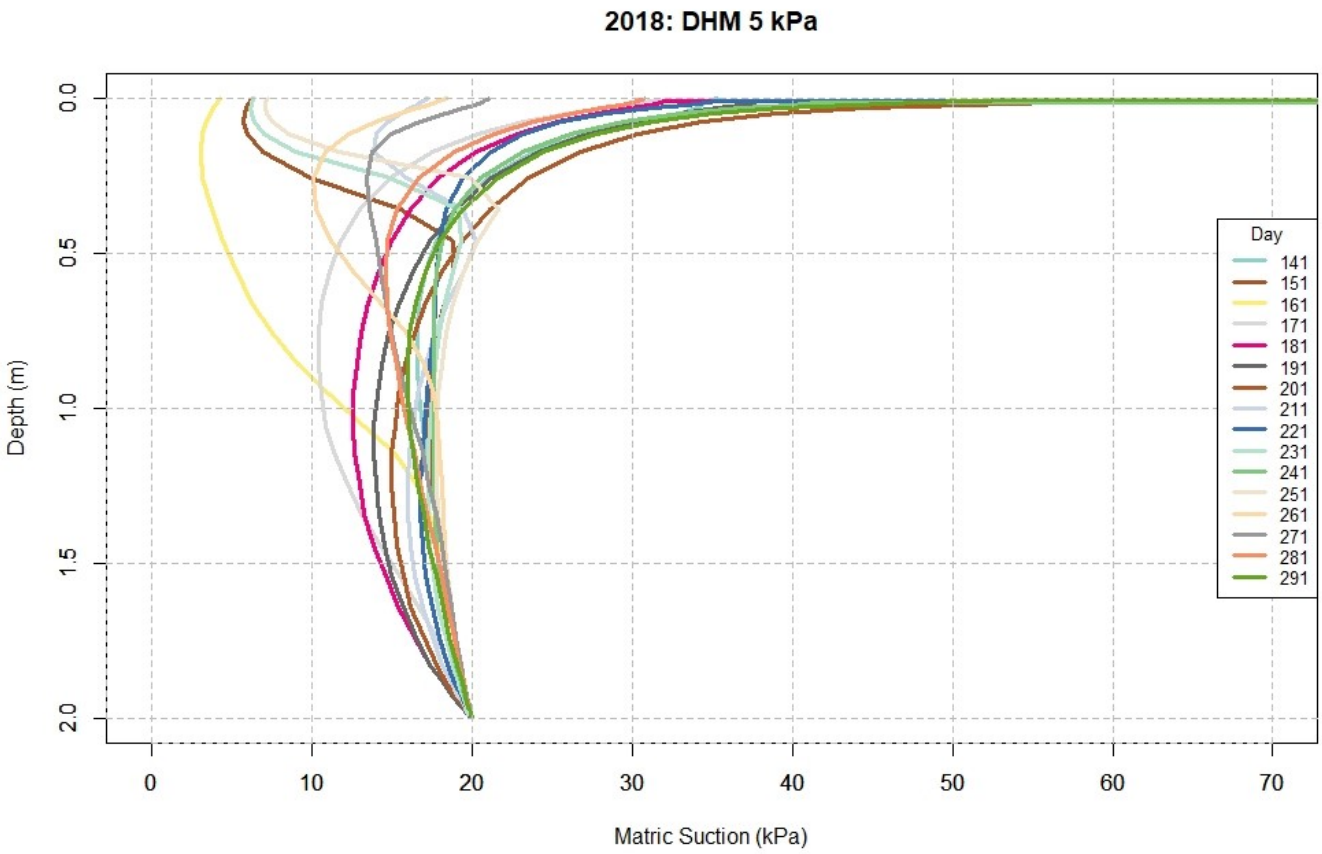

Figure B. 3 - Matric Suction Profile 2018 DHM 5 kPa

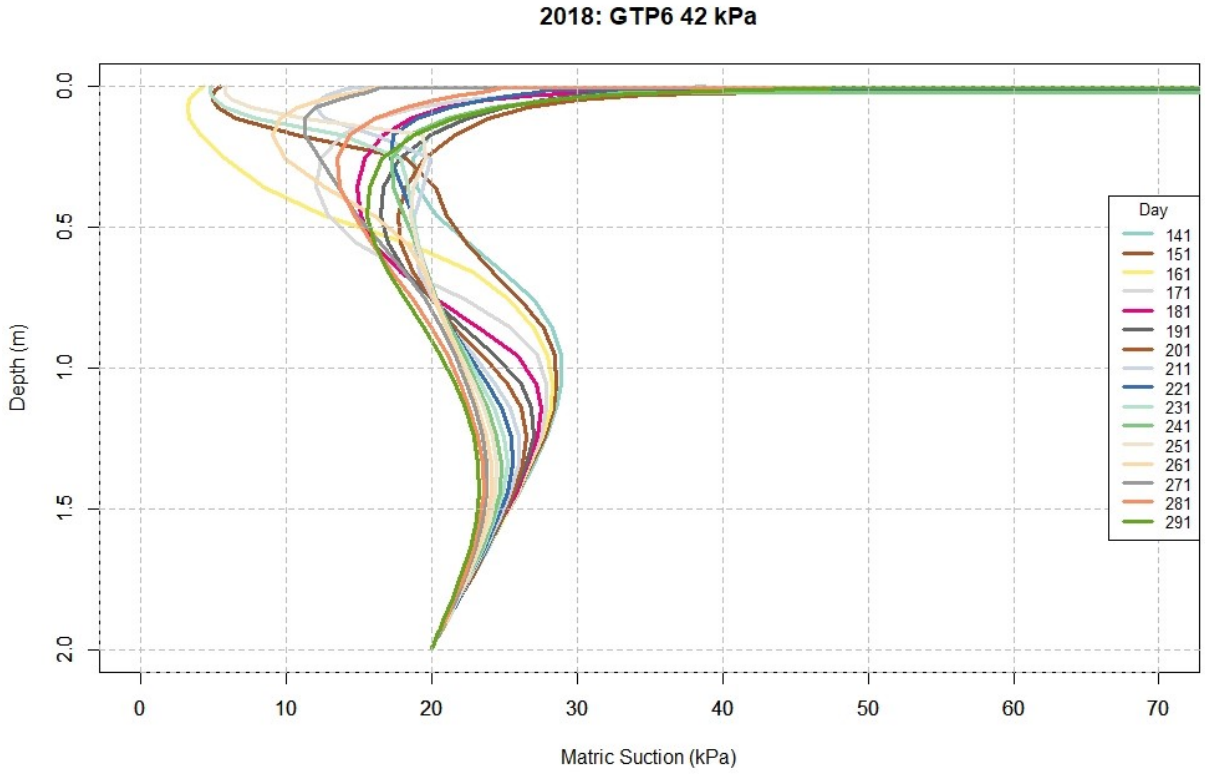

Figure B. 4 - Matric Suction Profile 2018 GPT6 42 kPa

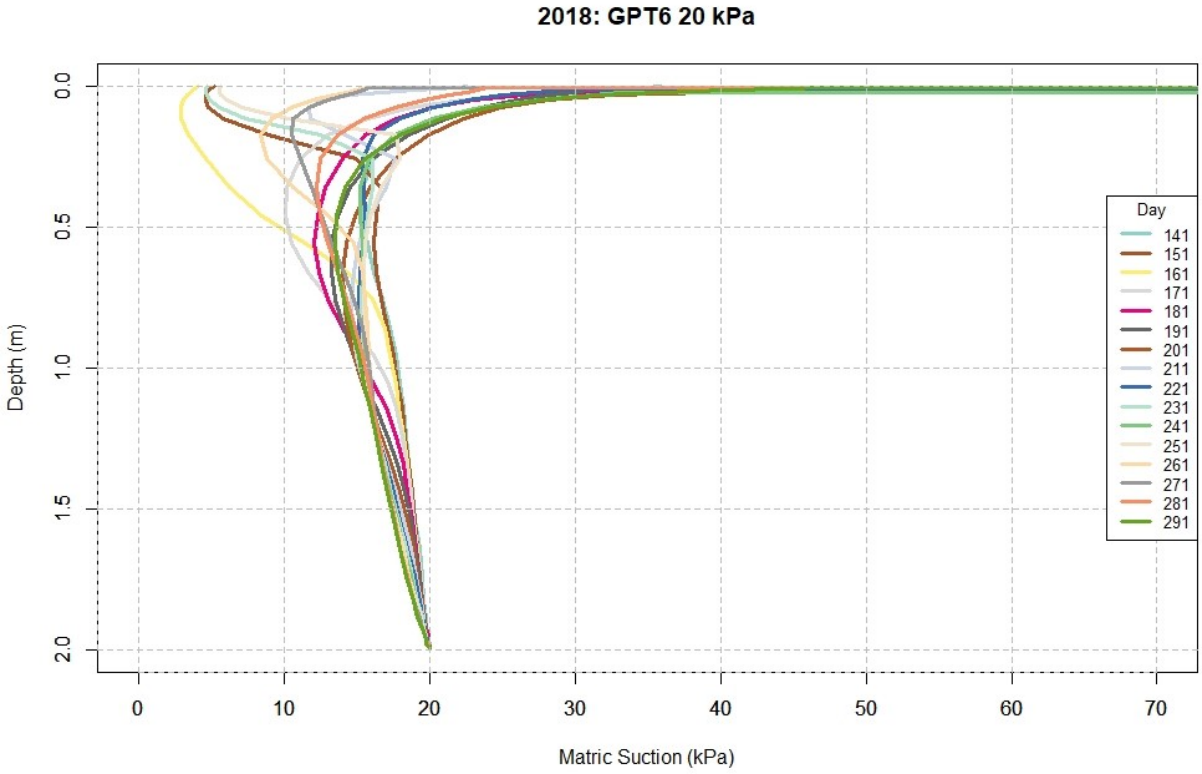

Figure B. 5 - Matric Suction Profile 2018 GTP6 20 kPa

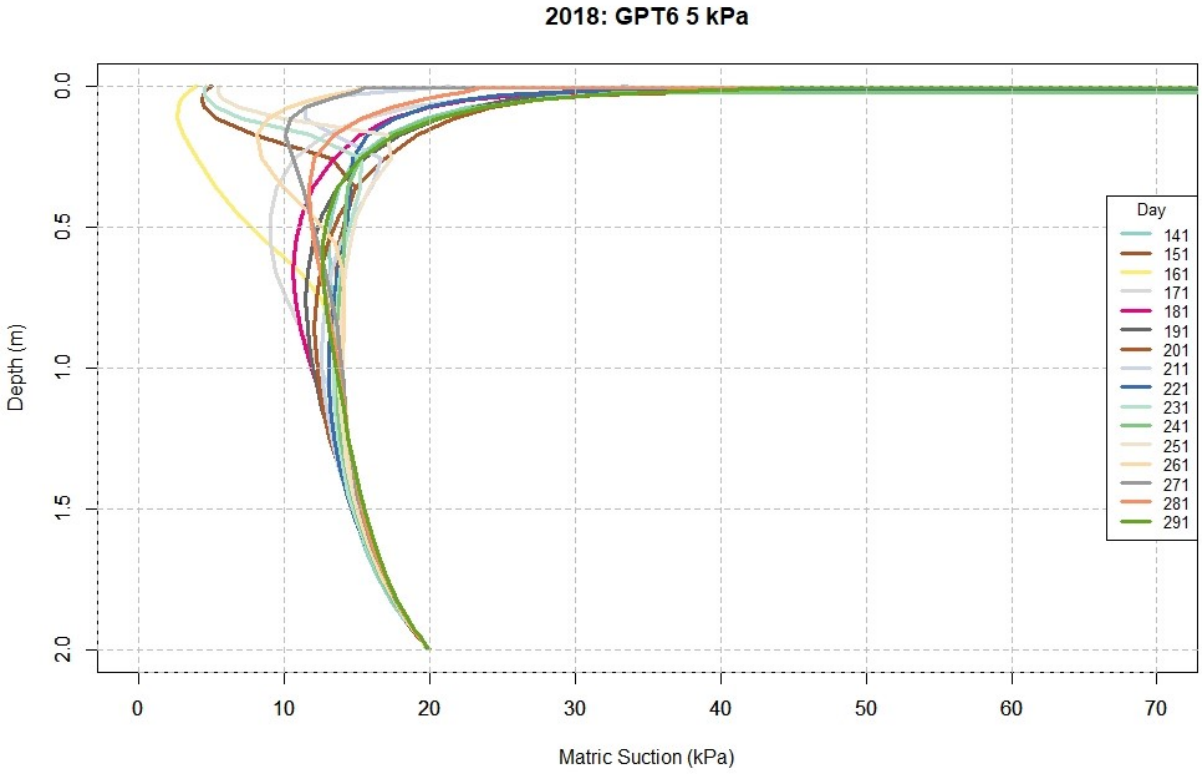

Figure B. 6 - Matric Suction Profile 2018 GPT6 5 kPa

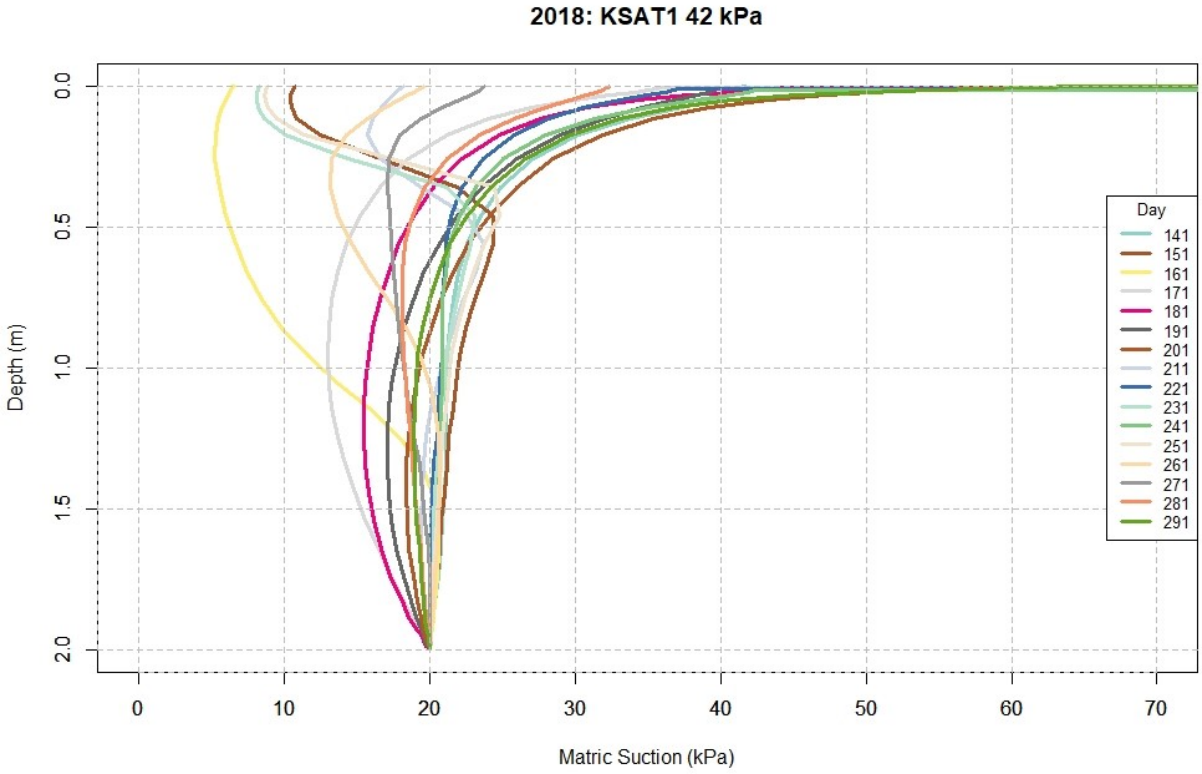

Figure B. 7 - Matric Suction Profile 2018 KSAT1 42 kPa

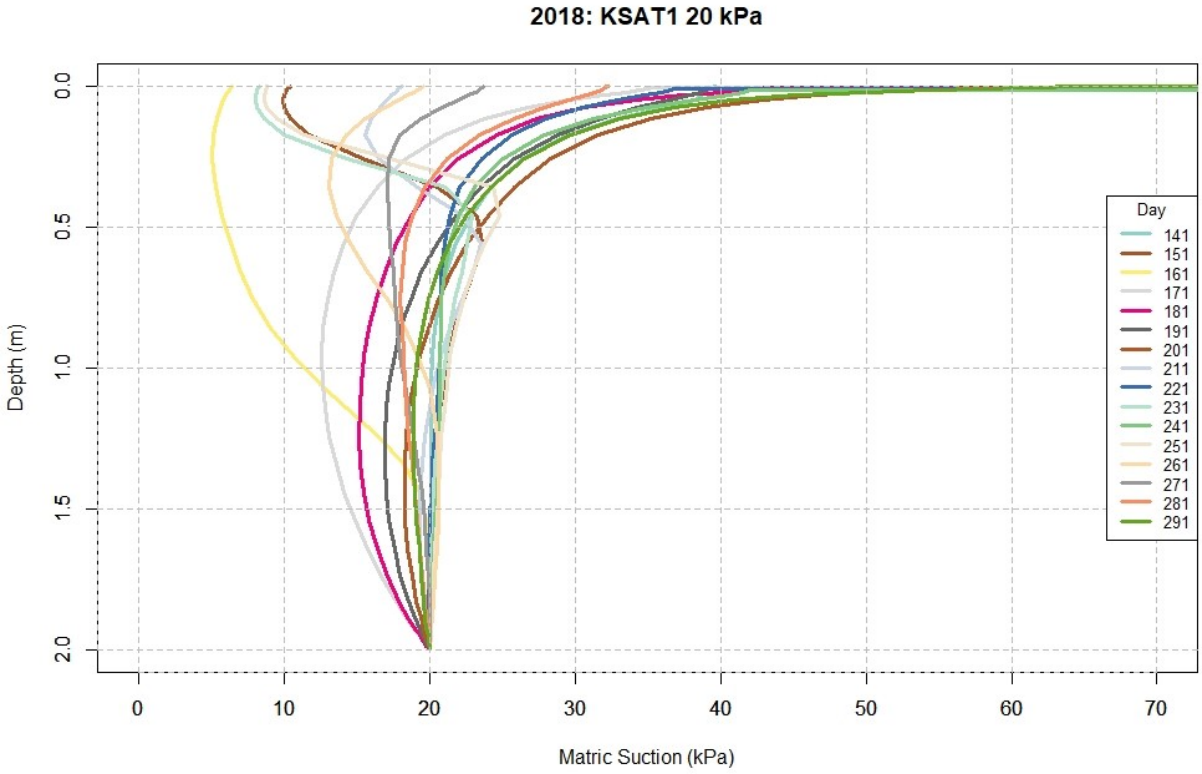

Figure B. 8 - Matric Suction Profile 2018 KSAT1 20 kPa

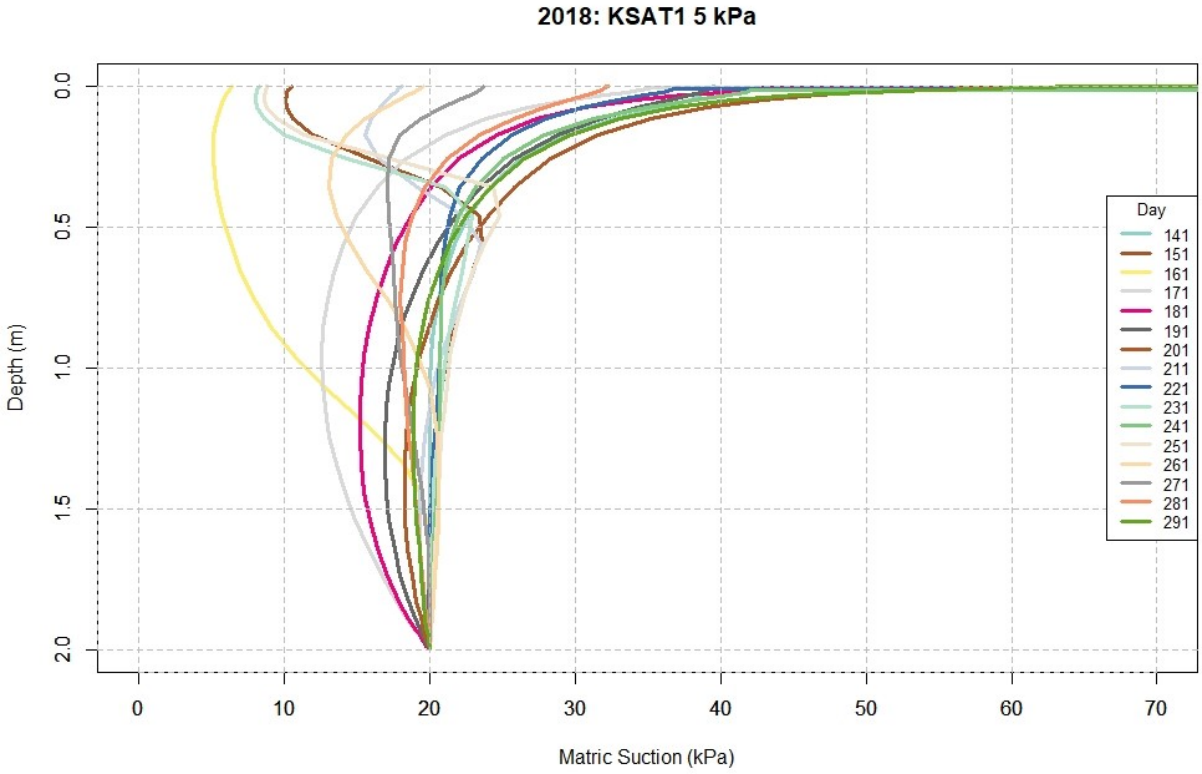

Figure B. 9 - Matric Suction Profile 2018 KSAT1 5 kPa

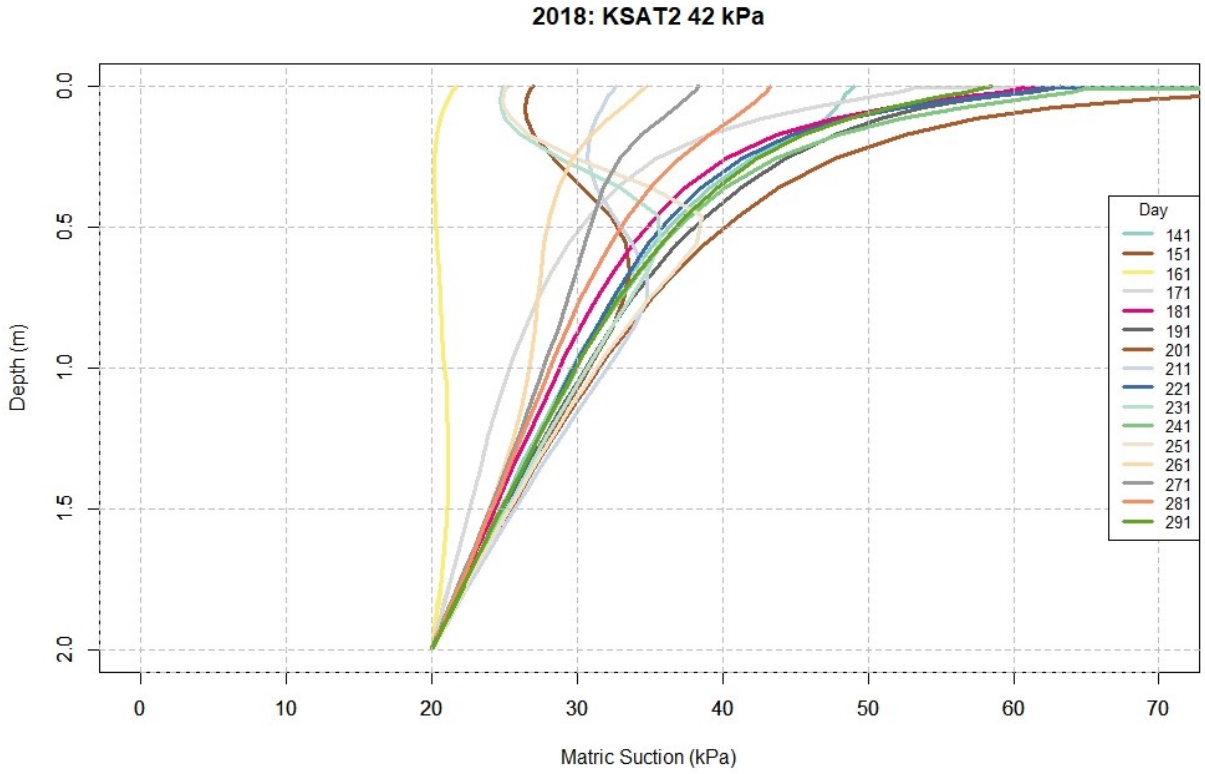

Figure B. 10 - Matric Suction Profile 2018 KSAT2 42 kPa

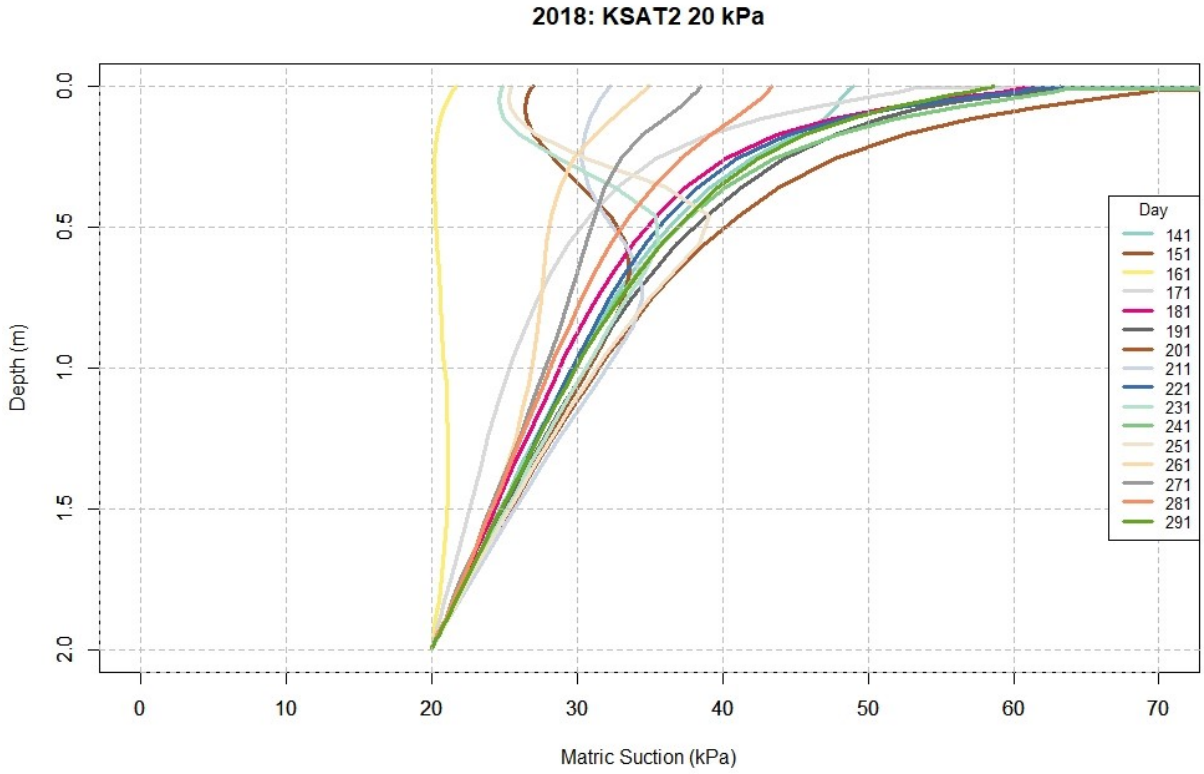

Figure B. 11 - Matric Suction Profile 2018 KSAT2 20 kPa

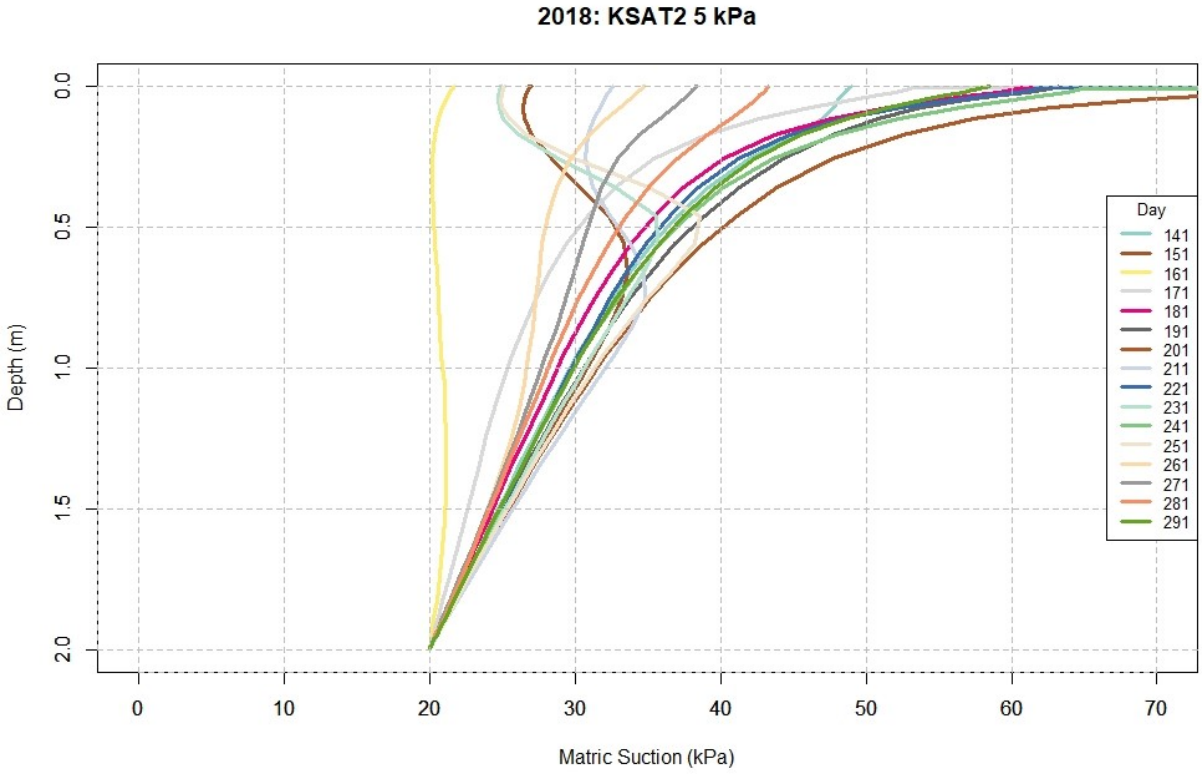

Figure B. 12 - Matric Suction Profile 2018 KSAT2 5 kPa

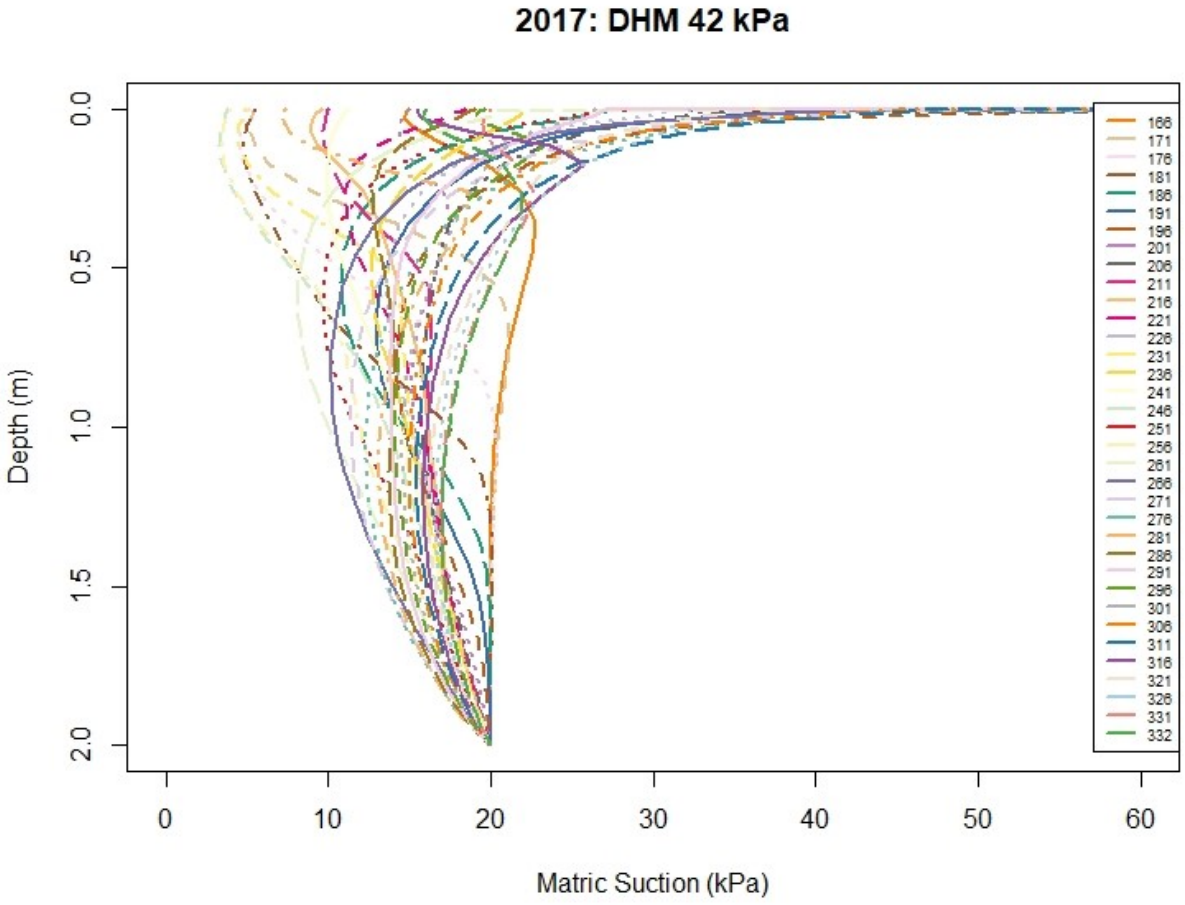

Figure B. 13 - Matric Suction Profile 2017 DHM 42 kPa

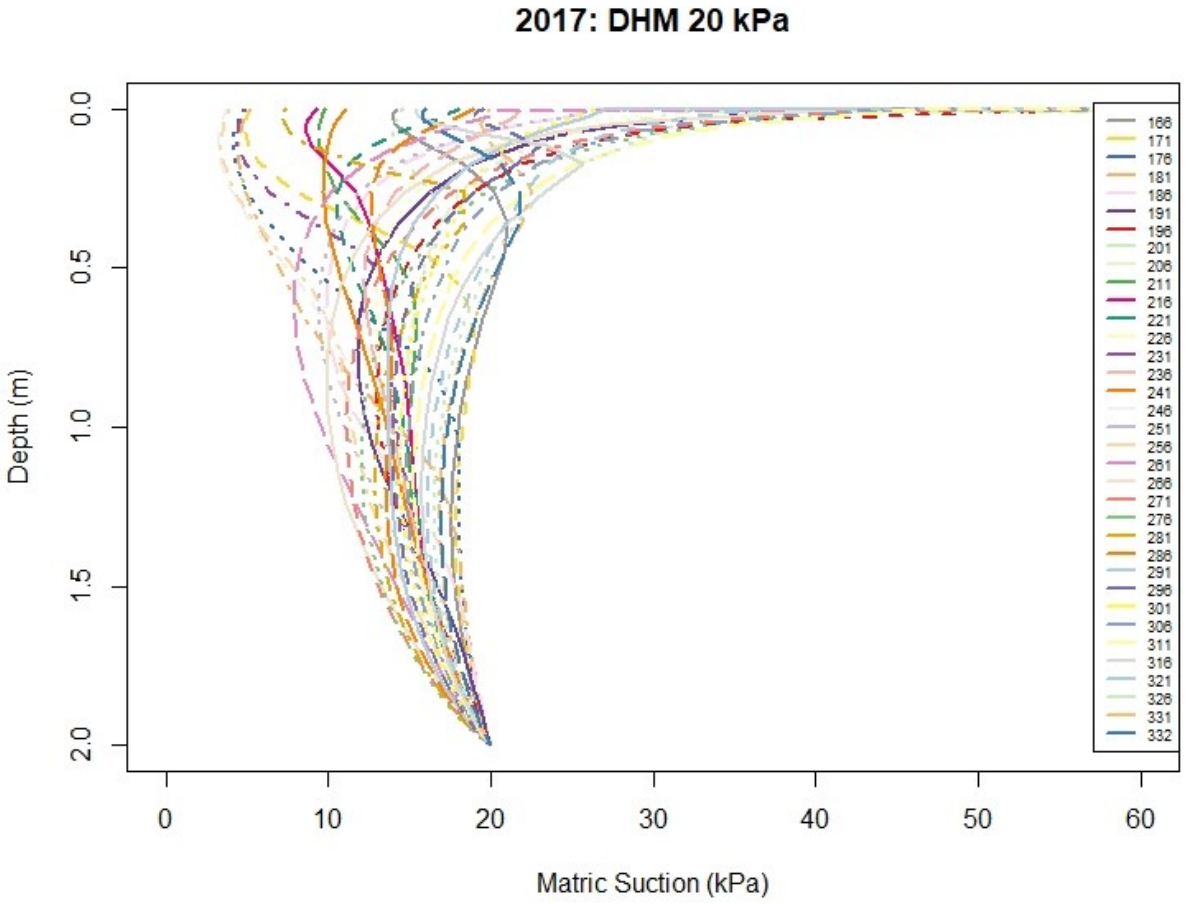

Figure B. 14 - Matric Suction Profile 2017 DHM 20kPa

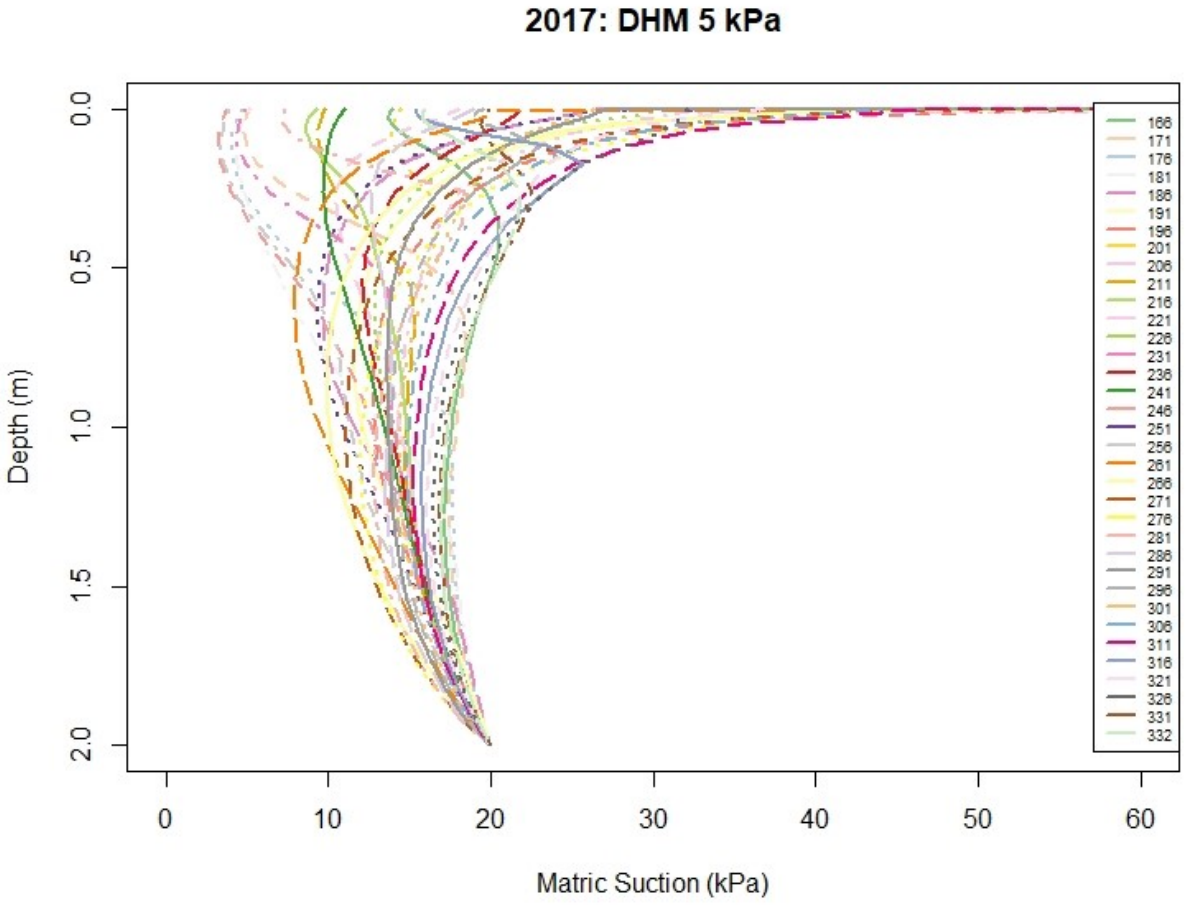

Figure B. 15 - Matric Suction Profile 2017 DHM 5 kPa

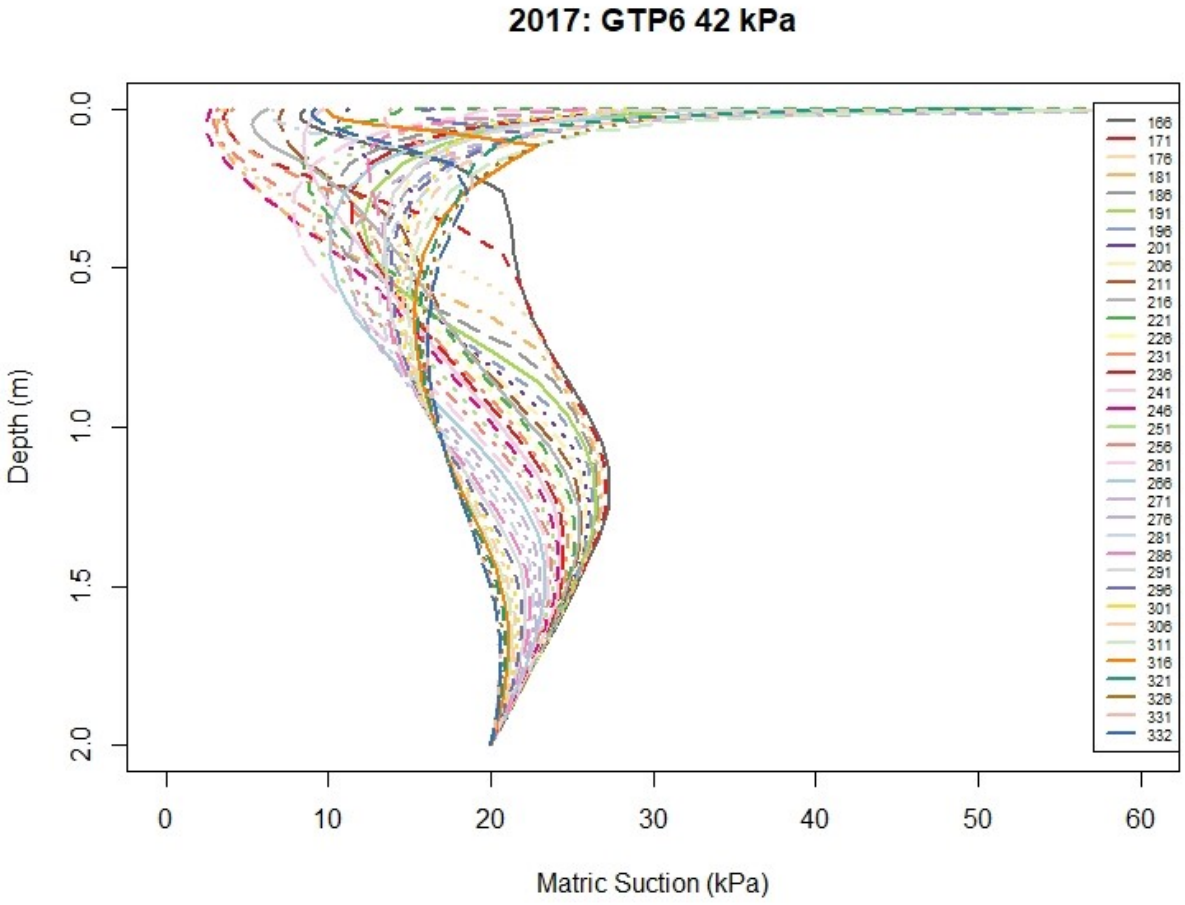

Figure B. 16 - Matric Suction Profile 2017 GTP6 42 kPa

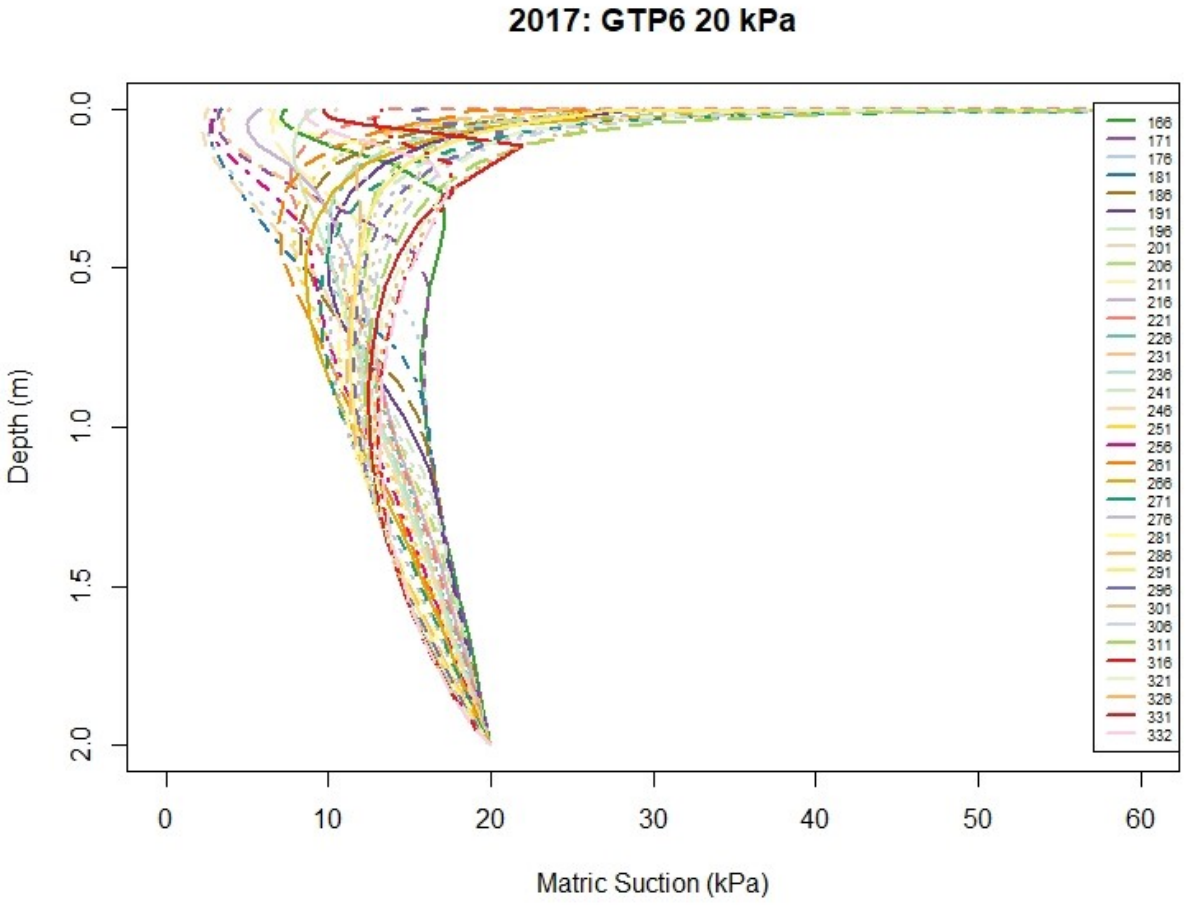

Figure B. 17 - Matric Suction Profile 2017 GTP6 20 kPa

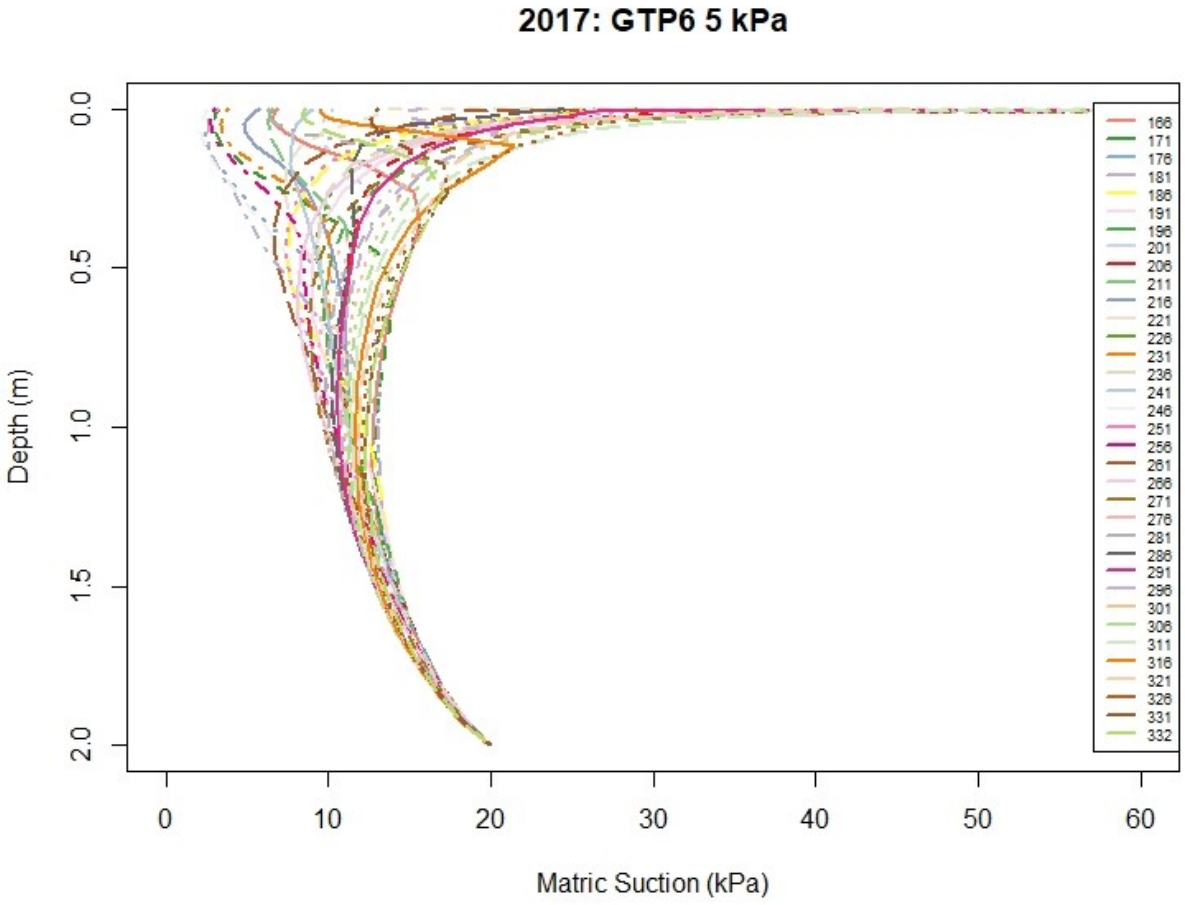

Figure B. 18 - Matric Suction Profile 2017 GTP6 5 kPa

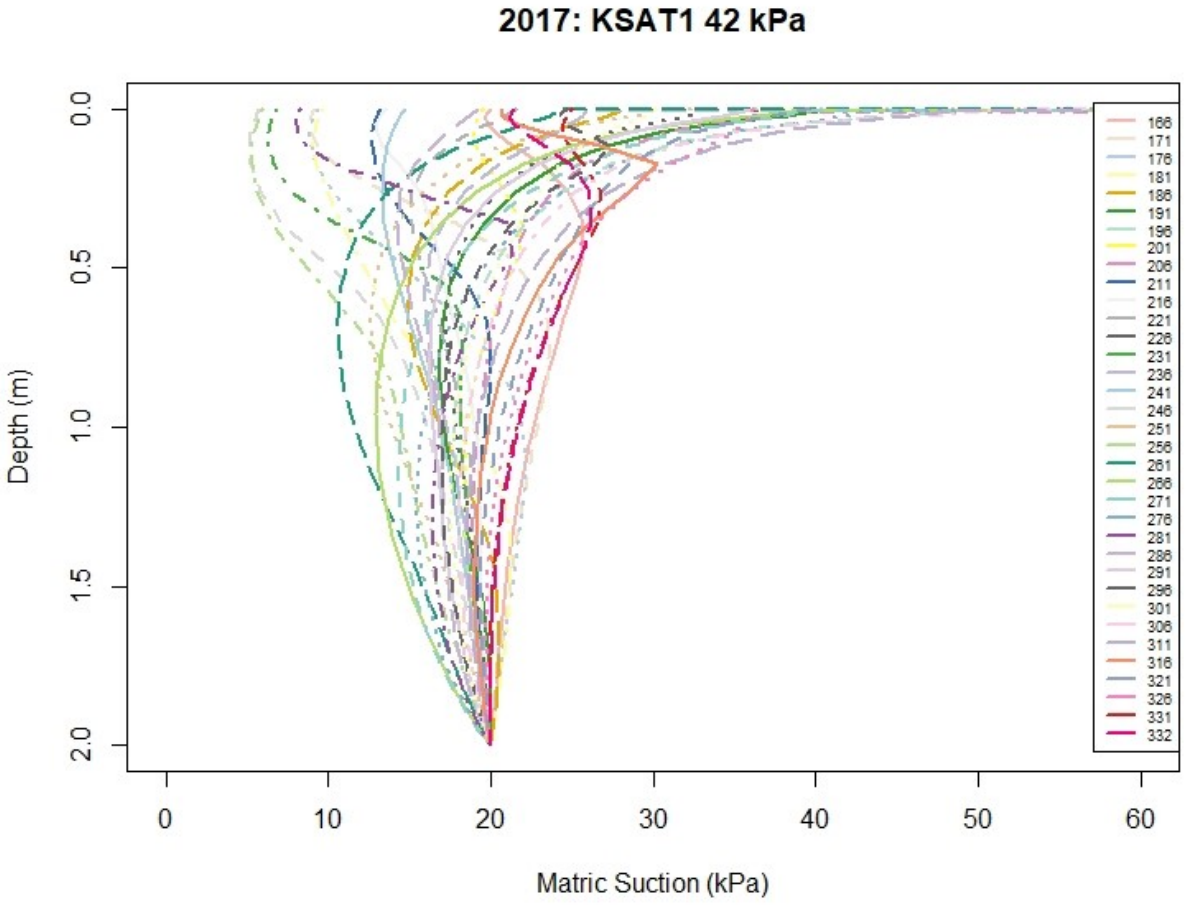

Figure B. 19 - Matric Suction Profile 2017 KSAT1 42 kPa

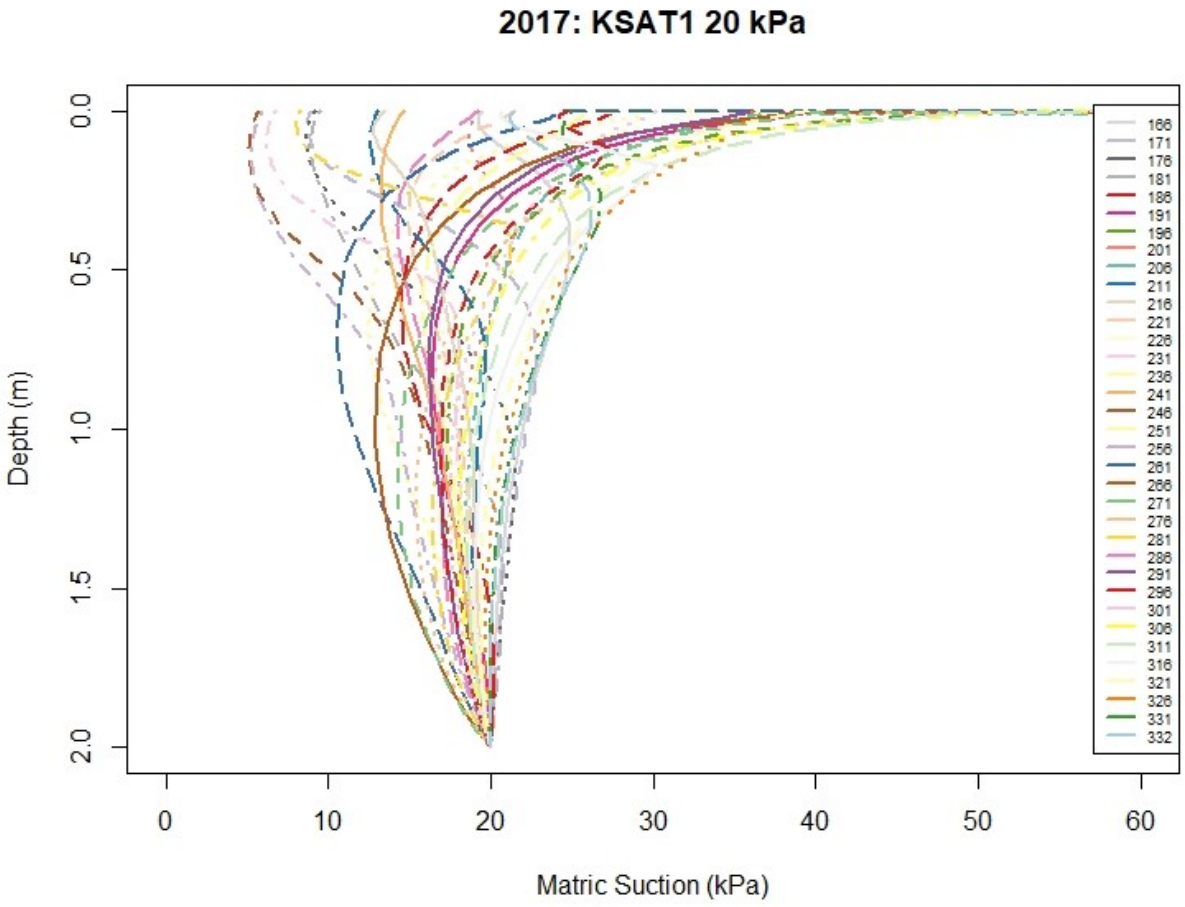

Figure B. 20 - Matric Suction Profile 2017 KSAT1 20 kPa

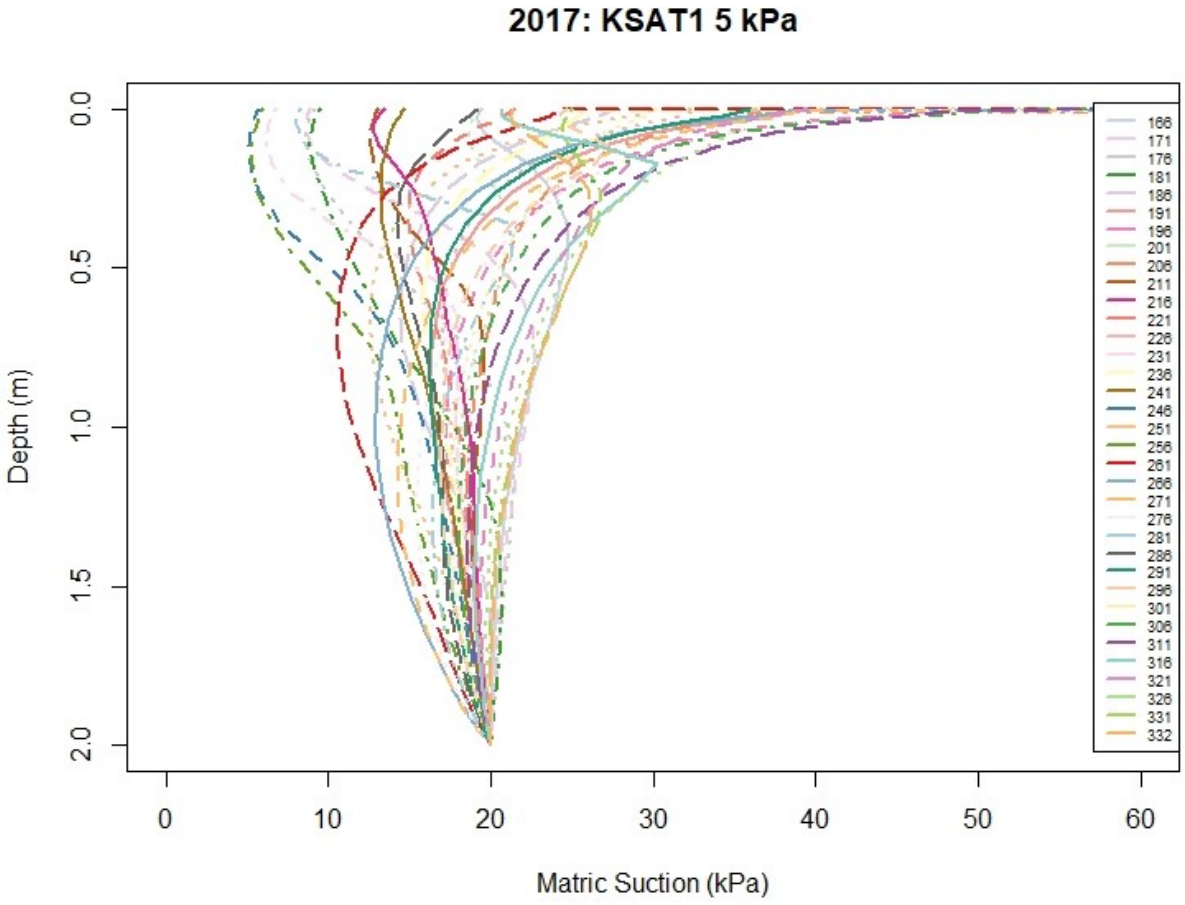

Figure B. 21 - Matric Suction Profile 2017 KSAT1 5 kPa

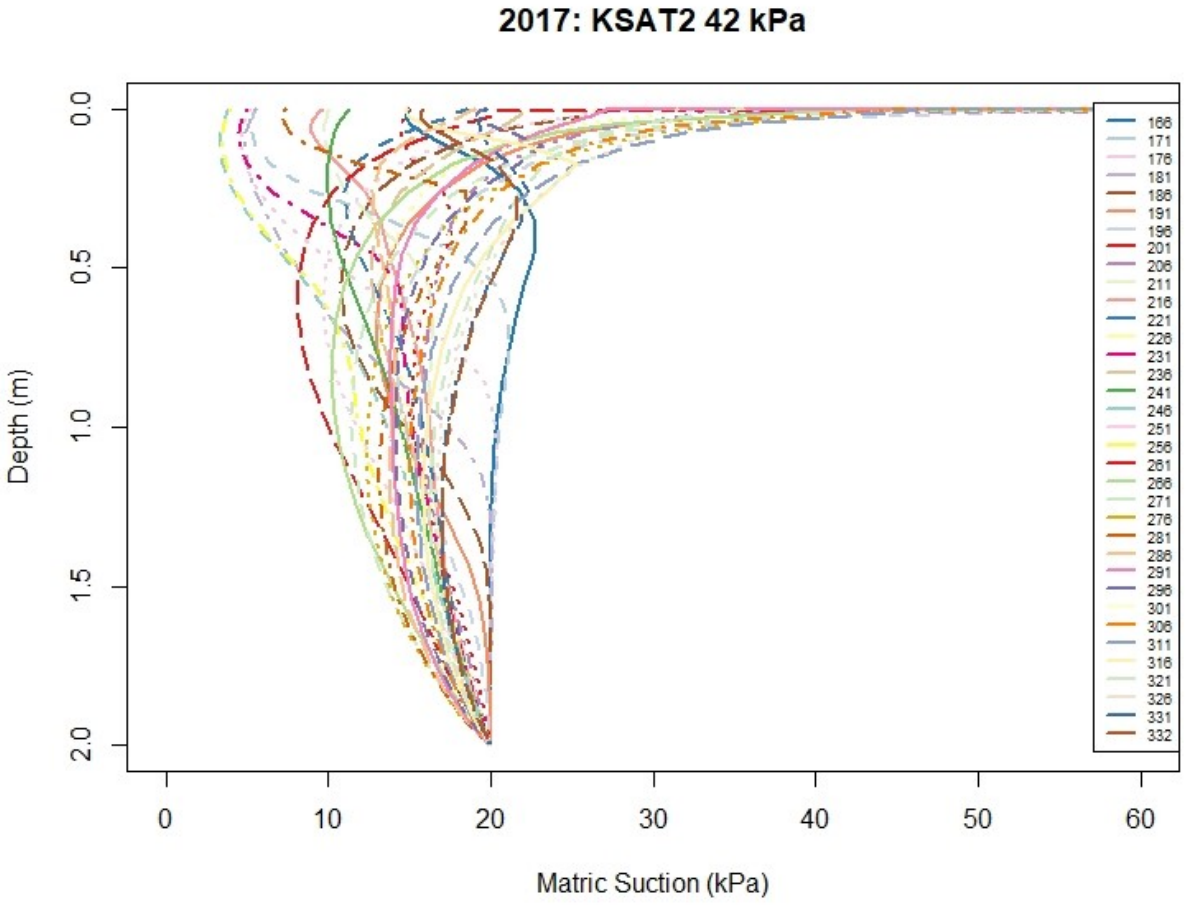

Figure B. 22 - Matric Suction Profile 2017 KSAT2 42 kPa

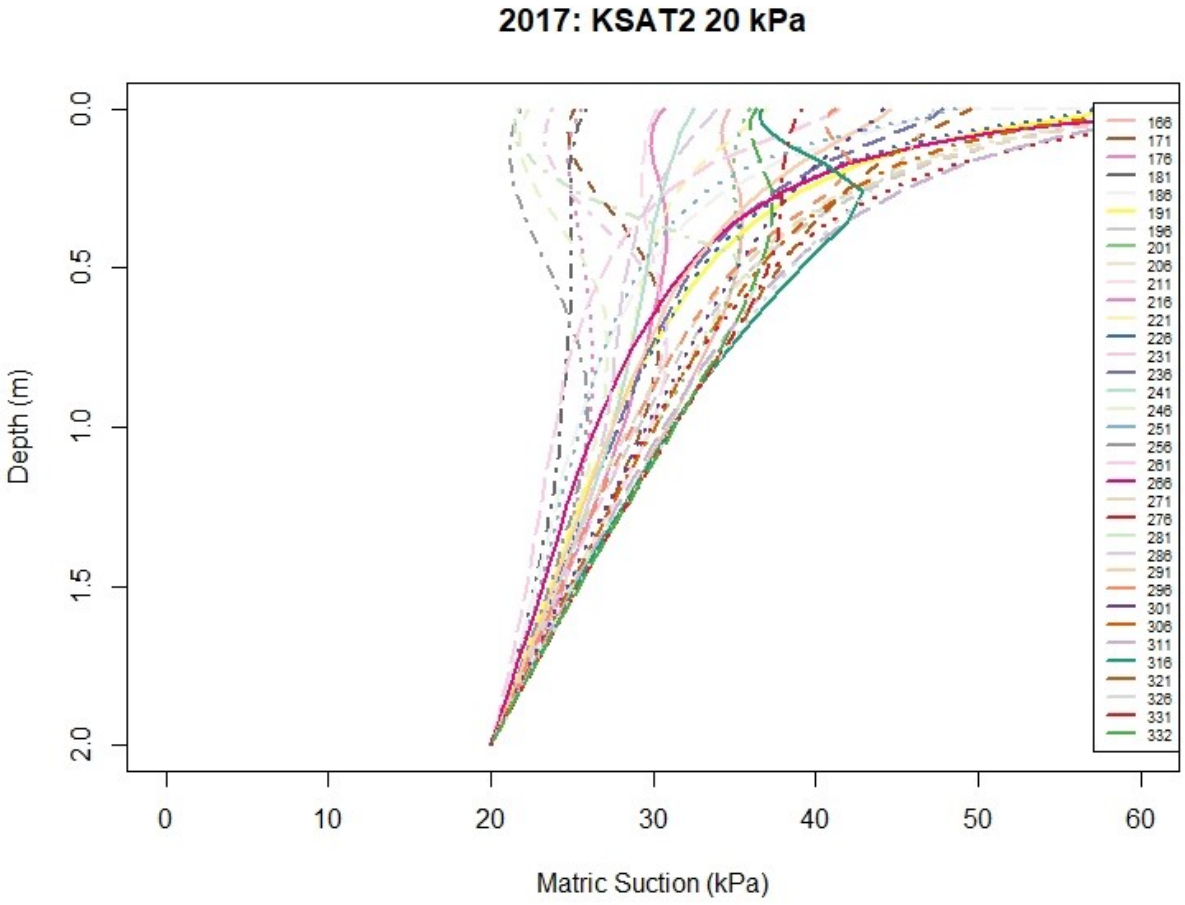

Figure B. 23 - Matric Suction Profile 2017 KSAT2 20 kPa

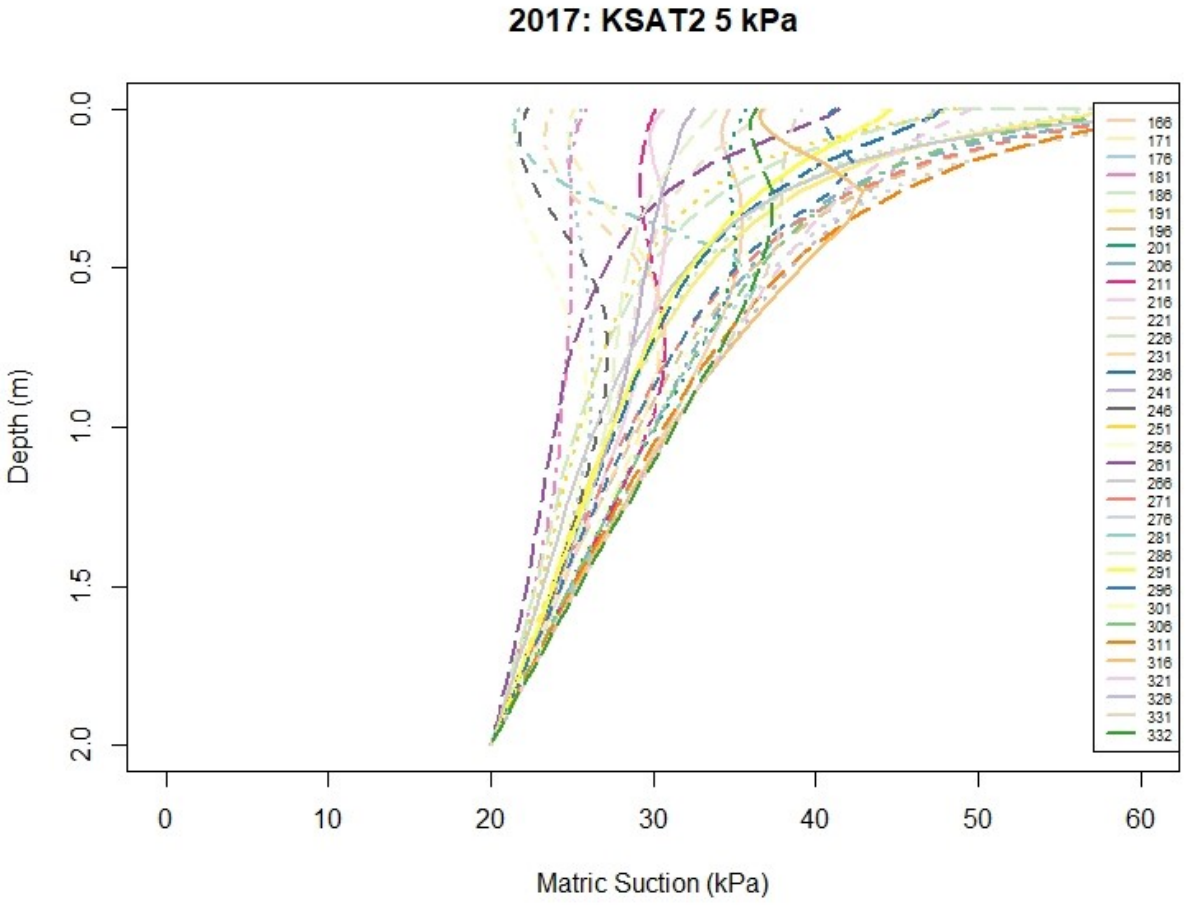

Figure B. 24 - Matric Suction Profile 2017 KSAT2 5 kPa